Understanding and Mitigating Transport Limitations in Thick Sintered Battery Electrodes

A Dissertation

Presented to

The Faculty of the School of Engineering and Applied Science

University of Virginia

In partial fulfilment

Of the requirements of the degree

Doctor of Philosophy in Chemical Engineering

By

Ziyang Nie

March 2022

Abstract

Lithium-ion (Li-ion) battery has been widely used in different applications. To further improve the energy and power density of Li-ion battery, approaches on developing new materials and by cell engineering are now being investigated by scientists. Conventional Li-ion battery electrodes are composite consist of active material, conductive carbon and polymer binder. Recently, another form of electrodes has been developed and reported by different groups. These electrodes are fabricated by thermal treatment of active material pellets and are called "sintered electrode". Compared to composite electrodes, sintered electrodes have greater thickness, no carbon and polymer additives and thus can improve the energy density at the cell level. However, a thicker electrode also indicates that the ion transport in liquid phase becomes the limiting factor for high-rate charge/discharge. Therefore, it is necessary to understand the ion transport and further improve the cell performance.

In this thesis, we first focused on studying the ion transport of cells with sintered $Li_4Ti_5O_{12}$ (LTO) anode and sintered $LiCoO_2$ (LCO) cathode. The cells had different electrode thickness and were discharged at different rate/current density. For such thick electrodes, the energy density advantage was further established. The limitation to deliver capacity at high rate was clearly evident. However, the detailed evidences that gave rise to this resistance were challenging to assign. Thus, to study the Li^+ distribution and track the movement of Li^+ during charge/discharge process, *operando* neutron imaging was used and the results were further studied with numerical tools. These results confirmed our hypothesis that the ion transport in electrolyte phase was the limiting factor of the reduced capacity at high charge/discharge rate.

After understanding the transport limitation, we further move towards on mitigating the resistance. Different approaches have been investigated. The first approach was to focus on electrode engineering by controlling the microstructure using ice-templating. With that technique, electrodes with aligned pores were fabricated, and we further confirmed that the ion transport in electrolyte phase was facilitated. The second approach was to use high concentration/conductivity electrolyte to mitigate Li^+ depletion during fast charge/discharge. Then the two methods were combined to further boost the cell performance. As a result, the cell with high concentration/conductivity electrolyte and ice templated electrodes showed 69 % improvement in discharge capacity retention compared to the cell with commercial electrolyte and non-templated electrodes.

At last, in addition to cell engineering, $TiNb_2O_7$ (TNO) anode material was synthesized and evaluated in sintered electrode system. TNO has a higher gravimetric and volumetric energy density than LTO used in previous experiments and can be an option to increase the energy density of the cell. Based upon the report, direct substitution of TNO for LTO can improve the anode capacity by 32 %. This results in either improved cell capacity or reduced electrode thickness which also mitigates the ionic transport resistance.

Table of Contents

Chapter 1

Introduction

1.1 Lithium-ion (Li-ion) battery

The overall trend for energy consumption is always increasing since the industrial revolution.[1] Up until now, most of the energy is still provided by burning of the fossil fuels such as oil, natural gas and coal.[1] However, the use of fossil fuels has caused some serious environmental problems and fossil fuels themselves are not sustainable due to the time scale needed to generate them. Thus, with the increasing demand of energy, new renewable energy sources are becoming more and more important. A challenge of these renewable energy sources is that the energy production is not stable and will be affected by the weather or seasonal changing. Thus, it is difficult to adjust the energy output in accordance with the energy demand which is also always changing.[2-4] Therefore, energy storage techniques are needed. Currently, the most used energy storage method is the pumped hydro storage, but this technique requires specific landform. So, other types of storage are also considered. One of the options is the electrochemical storage methods such as flow battery and li-ion battery, the latter one will be the focus of this work.[5,6]

Li-ion battery is gaining more and more research interest not only because it can be used in grid scale energy storage, but also because its excellent performance in electric vehicles (EVs) and portable electronics such as cell phones and laptops. EVs are now a growing market as they are zero emissions and are also supported by many governments. Although they have been a competitor to gasoline cars, the mileage range and the charging time are still challenges. For portable electronics, as they are now an essential part of modern daily work and life, the increasing demand also needs further development of the batteries. Thus, investigating li-ion batteries with a higher energy and power density is necessary and can be beneficial.

The history of Li-ion battery can be date back to 1965 when TiS_2 was proposed to be the cathode material paired with Li metal anode.[7] Later, the anode was substituted by carbonaceous materials due to the safety issue of metallic Li and the cathode was replaced by $LiCoO_2$ (LCO), which has a higher operating voltage.[8,9] After several years of development, the first commercial Li-ion battery was released in 1991 by Sony, in which LCO and graphite were used as electrode active materials.[10] In 2019, as Li-ion battery has become an important part of people's life, the three pioneers in this work, John B. Goodenough (discovered LCO and $LiFePO_4$ cathode), M. Stanley Whittingham (explained intercalation effect), and Akira Yoshino (developed carbonaceous anode) were awarded the Nobel Prize of Chemistry.[11]

1.2 Fundamentals of Li-ion battery

The discharge of a Li-ion cell is a typical galvanic cell with some unique features. The fundamental structure of a Li-ion cell is shown in Fig. 1.1.[12] The basic components in a cell include a porous cathode, a porous anode, a porous separator to avoid internal short of the cell and all components are soaked in the liquid electrolyte. The electrolyte contains lithium salt, which usually is $LiPF_6$, dissolved in organic solvent.

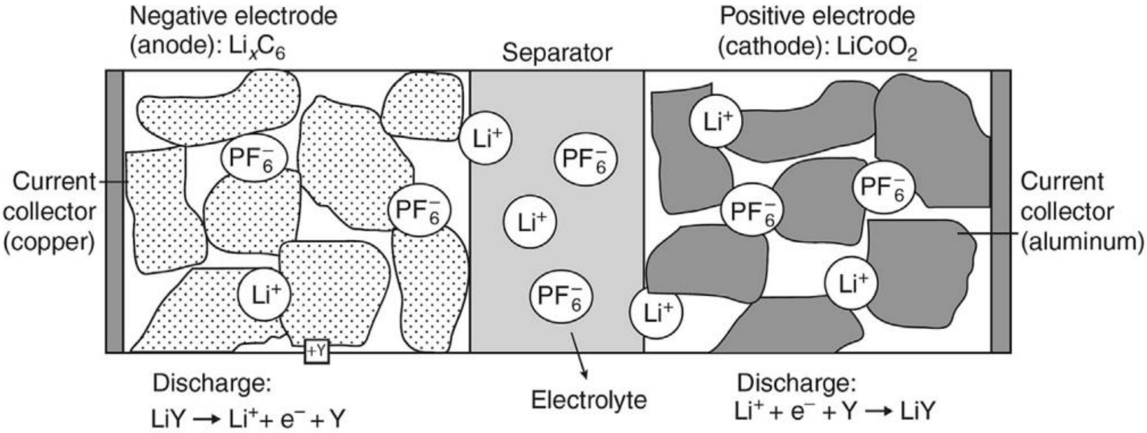

Fig. 1.1. Basic structure of a Li-ion cell.[12]

In Fig 1.1, the anode material is carbon lithium intercalation compounds and the cathode material is $LiCoO_2$, both of which are commonly used in commercial batteries. During discharge, Li^+ are released from the crystal structure of anode active material, penetrate through the solid-electrolyte interface (SEI) formed on the anode particles, go into the electrolyte phase in the pores. Then, the ions diffuse through the porous structure from anode to separator to cathode, and reach the cathode active material particle surface. In some cases, there is also a layer of cathode-electrolyte interface formed on the cathode surface, and the Li^+ need to pass through this layer and finally enter the solid phase of cathode active material.[13,14] In the meantime, to balance the charge, electrons will move from the anode active material, pass through the conductive matrix of the anode and reach the current collector. Then from the outer circuit, the electrons move to the cathode current collector and pass through the cathode conductive matrix and combine with the cathode active material. The movement of electrons will provide energy to appliances that connected to the cell in the outer circuit. For charge, every process is reversed.[13]

The charge/discharge process results in a voltage curve which relates the cell voltage with the charge/discharge capacity, and can also be related to the state of charge of the active material in the cell. The shape of the curve is a reflection of multiple factors. At slow rate, the shape was determined by the intrinsic property of the active material used in the cell,[15] which is a result of the electrochemical potential of the material. To obtain the voltage curve of a certain active material, this material is usually paired with Li metal, which has a constant voltage during lithiation/delithiation, and cycled using a slow rate. This cell is usually called a half cell, and the resulting profile shows the voltage vs. Li/Li^+. While two different materials (no Li metal in the cell) are paired, the configuration is called a full cell, and the voltage profile is a combination of the half cell curves of the two materials. At high charge/discharge rate, factors other than the intrinsic material property start to play a role. Some factors are: the Li^+ diffusion in solid phase,[16] Li^+ diffusion in liquid electrolyte phase[17] and electronic conductivity of the electrode matrix.[18] At high current density, one or more factors can be the limitation of the capacity delivered and thus result in worse performance of the cell. An example showing the charge/discharge profiles of Li/LCO half cell at different current density is displayed in Fig. 1.2. The limit factor of the cell system investigated in this thesis will be discussed in more details in Chapter 2 and 3.

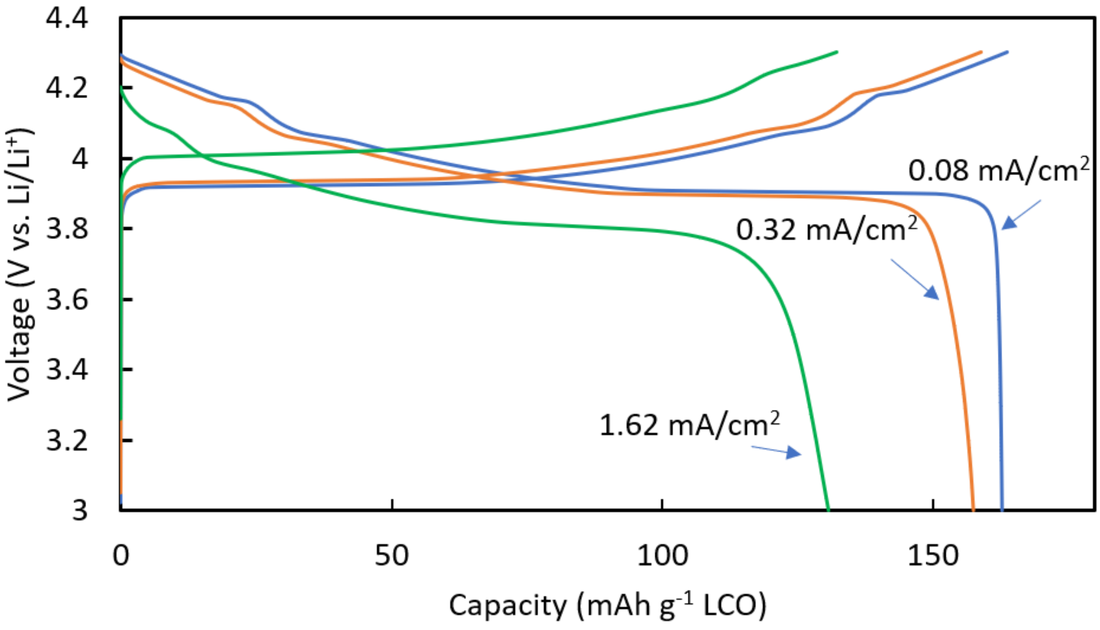

Fig. 1.2. Charge/discharge profiles of Li/LCO cell at different current densities.

1.3 Li-ion battery electrodes

1.3.1 Composite electrodes

The electrode structure in Fig. 1.1 is simplified to highlight the porous structure and active material particles. In real application, the electrode is composed of active material, conductive carbon additive and polymer binder (Fig. 1.3a).[19,20] As introduced in section 1.2, the active material is the source of electrochemical capacity and determines the fundamental property of a Li-ion cell. The carbon additive is used to provide electronic conductive matrix for the movement of electrons. The polymer binder helps to connect different particles in the electrode and maintain its integrity.

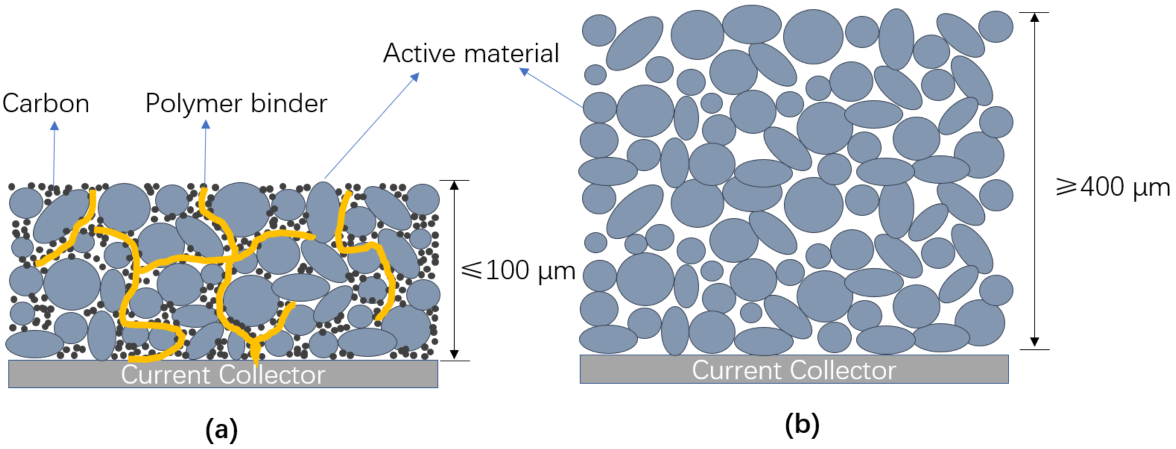

Fig. 1.3. Schematic of structures for (a) composite electrode, (b) sintered electrode.

Composite electrodes have been widely used in both research and commercial product. However, there are still challenges for these electrodes. One of the challenges is the thickness of the composite. To fabricate a composite electrode, a slurry that contains active material, carbon and polymer binder with a solvent, which usually is n-methyl-2-pyrrolidone, is cast on a metal sheet which is used as current collector. Thus, the electrode is usually thin with a thickness less than 100 μm.[17,21] However, to improve the energy density of a cell, thicker electrodes are preferred. A schematic is shown in Fig. 1.4. For thin electrodes, stack structures are used to increase the total amount of active material. If thicker electrodes are used, the number of stacks can be reduced and certain layers of current collectors and separators can be gotten rid of. As a result, the total amount of active material is increased and so does the capacity at a cell level.[22] For composite electrode, increase the thickness will result in delamination of the electrode from the current collector.[23] To solve this problem, efforts such as using foam as current collector[24] or adjusting the slurry property and use 3D printing[25] have been made and still need further investigation.

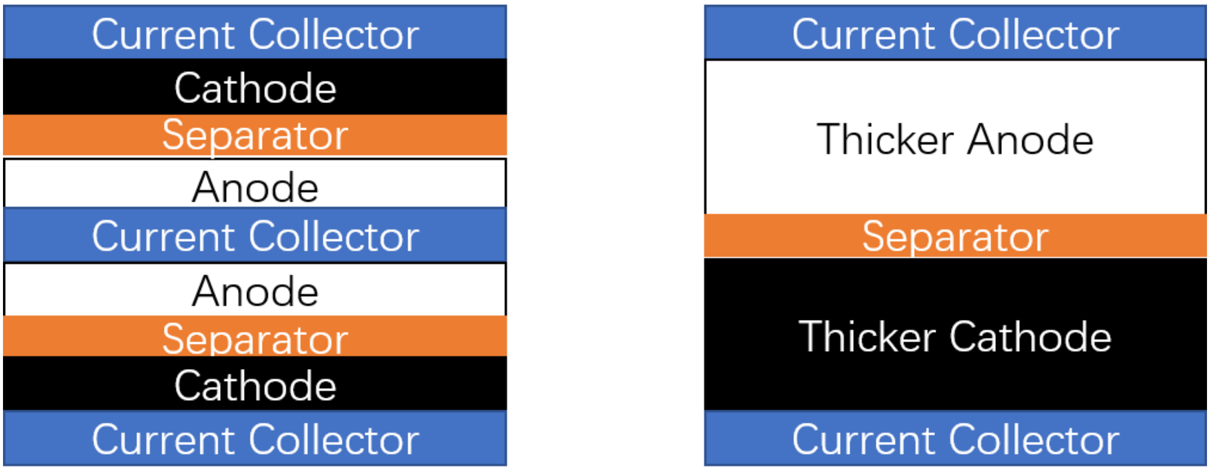

Fig. 1.4. Cell stacks with thin electrodes (left) and thick electrodes (right).

Another challenge for composite electrode is the tortuosity. Composite electrode has three different components with different particle morphology (Fig. 1.3a). The carbon and polymer additives are electrochemically inert but take a certain volume in the electrode, which act as a barriers when the ions are moving in the porous structure of the electrode. Besides, the electrode is usually calendared before cell fabrication to reduce porosity. As a result, the tortuosity of composite electrode is high compared to random packed spheres.[26,27] For thin electrode, this may not be a limiting factor, but if the electrode thickness increases, the high tortuosity will be a resistance for ion transport in electrolyte phase. To reduce the tortuosity, different alignment techniques have been reported. Some methods include: magnetic alignment of emulsion-based slurries[28] and inversion phase template.[23] The resulting electrodes showed greater thickness and lower tortuosity, and also with a good rate capability during electrochemical test. However, the aligned porosity electrodes usually had a higher porosity, indicating a lower volumetric energy density compared to regular composite electrodes.[23,28]

1.3.2 Sintered electrodes

As it is challenging to fabricate thick composite electrodes, another method has been proposed, which is to use thermal treatment to anneal the active materials. The resulting electrode is composed of sintered active materials and thus is called “sintered electrodes”.[29,30] The structure of sintered electrode is shown in Fig. 1.3b. Compared to composite electrode, sintered electrode does not have carbon and polymer additives, indicating that its tortuosity is close to random packed spheres and is lower than the composite electrode.[31] Besides, as the electrode integrity is maintained by the sintered matrix of active material, these electrodes can be made much thicker. Thus, the energy and power density of cells with sintered electrodes should be better. Previous reports have shown that the capacity at the cell level was greatly improved with sintered electrodes.[29,30] However, there are also some challenges for this technique.

1.3.3 Challenges for sintered electrodes

1.3.3.1 Volume change of the active materials

The first challenge is the volume change of active material during lithiation/delithiation. This volume change is the property of active material and is inevitable during the cell cycling. Some extreme cases have been found in conversion type of materials like Si and Ge, which have a volume change of >250 %.[15] For intercalation type material, the volume change is usually a few percent. The data of some intercalation materials are shown in Table 1.1.[29,32,33] For composite electrode, the effect of active material volume change can be mitigated by the polymer binder and the cycle life of the cell can be maintained. However, the particle level crack has also been observed in composite electrode.[32] For sintered electrode, as the electrode pellet is purely sintered active materials, the volume change can result in internal stress and cause the damage of the pellet. So it is an important factor to be considered. In our previous work, we have cycled LTO/LCO cells with sintered electrode and the results were promising.[30] For cathode, LCO was chosen due to the lower volume change compared to other cathode material. For anode, LTO is known as the "zero-strain" material, which means the volume change effect is negligible,[34] indicating it is a perfect material for sintered electrode. Other cathode materials have also been investigated by our group and other researchers, showing a certain amount of volume change could be tolerable in sintered pellets.[35,36] Another option for anode material was explored in this thesis and will be discussed in Chapter 6.

Table 1.1. Volume change of some electrode materials after lithiation/delithiation[29,32,33]

Lithium storage compound	Volume strain ΔV/V0
Cathode	
$LiCoO_2$ (LCO)	1.9%
$LiFePO_4$ (LFP)	6.6%
$LiMn_2O_4$ (LMO)	7.3%
$LiNiO_2$ (LNO)	2.8%
$LiNi_{0.3}Mn_{0.3}Co_{0.3}O_2$ (NMC333)	1.7%
$LiNi_{0.8}Co_{0.15}Al_{0.05}O_2$ (NCA)	5.0%
Anode	
C (graphite)	13.9%
$Li_4Ti_5O_{12}$ (LTO)	0.02%
$TiNb_2O_7$ (TNO)	7.2%

1.3.3.2 Electronic conductivity of sintered electrode

The second challenge of sintered electrode is the electronic conductivity. As shown in Fig. 1.1. The composite electrode has carbon network for electronic conduction. For sintered electrode, the electrons can only go through the matrix of active material particles. For most of the active materials, the conductivity is several orders of magnitude lower than the carbon,[37], indicating greater electronic resistance in cells with sintered electrodes. However, for some materials, the pristine form has a low electronic conductivity, but some studies have found that after slightly lithiation/delithiation, the conductivity can also increase by several order of magnitude.[38,39] For example, pristine LCO ($LiCoO_2$) has a conductivity of ~10^{-3} S cm^{-1}. A slightly delithiation ($Li_{0.96}CoO_2$) can increase the conductivity to ~10^{-1} S cm^{-1} and further delithiation ($Li_{0.55}CoO_2$) can result in a conductivity of ~10 S cm^{-1}.[38] LTO ($Li_4Ti_5O_{12}$) also shows a similar trend. Pristine LTO behaves like an insulator (10^{-8} S cm^{-1}) and slightly lithiation ($Li_{4.6}Ti_5O_{12}$) can increase the value to 2.5 S cm^{-1}.[39] This indicates by selecting proper material the limitation of conductivity can be mitigated for sintered electrode system. However, not all material has the property of conductivity increase. Materials such as LFP and LMO remains at low conductivity after delithiaion.[40,41] Thus, to use these materials in sintered electrode system, several methods such as doping[35] and conductive layer coating[42] could be used to pretreat the pristine material.

1.3.3.3 Ion transport in thick porous electrode

The third challenge is the ion transport in electrolyte phase. This is a general challenge for thick electrode,[17] but as sintered electrode can be made much thicker than composite electrode, it is an important factor needs to be considered.

The typical ion transport in thick sintered electrode is shown in Fig. 1.5a. To reach an active material particle, the Li^+ needs to pass through the tortuous pathway. Thus, the thicker the electrode is, the higher the ion transport resistance will be. To mitigate this resistance, one option is to apply templating method to fabricate electrodes with aligned pores (Fig. 1.5b). Some methods have been used for composite electrode discussed in section 1.3.1. The reported methods than can be used for sintered electrode include: wood templating,[43] ice templating[44] and laser processing.[45] Among them, the ice templated pellets will be investigated in this thesis in Chapter 4.

Another option to mitigate the transport resistance is to use high concentration and conductivity electrolyte. As shown in Fig. 1.5c, the long distance of Li^+ will result in a concentration gradient in electrolyte phase along the vertical direction (electron movement direction) of the porous electrode. If the gradient is large, Li^+ will be depleted in some regions and thus the Li^+ are no longer available for some active material particles.[46] Thus, an idea to mitigate this phenomenon is to increase the concentration of Li^+ in electrolyte phase (Fig. 1.5d), and also increase the conductivity to facilitate the ion diffusion. By doing so, the gradient is still existing, but Li^+ will be available in more regions near the current collector. To investigate the effect of Li^+ concentration in electrolyte phase, work has been done and presented in Chapter 5.

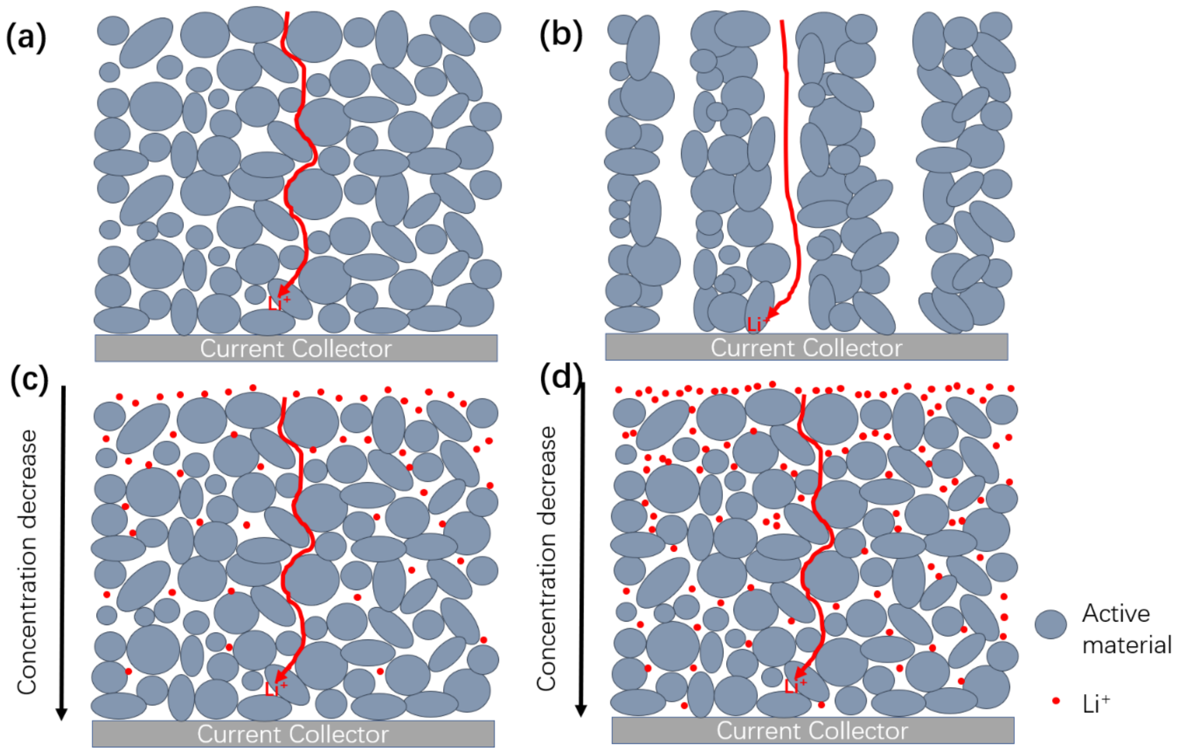

Fig. 1.5. Li$^+$ movement in electrolyte phase in (a) random packed particle matrix; (b) electrode with aligned pores and the Li$^+$ concentration gradient formed due to the Li$^+$ transport in (c) low concentration electrolyte and (d) high concentration electrolyte.

1.4 Objectives and summary of accomplishment

This dissertation studies the ion transport property of sintered electrode cells. Based on previous study in our group, LTO/LCO was chosen as the model system for investigation. Then, several ways to improve the rate capability and further improve the energy density at the cell level are explored.

Chapter 2 studied the ion transport of LTO/LCO cells with sintered electrodes of different thickness. Neutron imaging technique was used to track the movement in-situ and numerical tools was used to analyze and support the results. Chapter 3 further studied the ion transport sintered LTO/LCO cells at different discharge rate with the tools mentioned above. The results of these work first expanded the application of neutron imaging technique. And the transport property found in these studies reveals the limitation of thick sintered electrodes, or thick electrodes in general electrochemical systems. These findings are direct motivation for the following studies in this thesis to improve the ion transport and rate capability of the sintered electrode system. The work of these two chapters resulted publications in *Journal of Power Sources* and *Molecular Systems Design and Engineering*.

Chapter 4 explored the electrochemical performance of electrodes with aligned pores. These electrodes were fabricated by ice-templating technique and again the neutron imaging and numerical calculation were used to support the results. Chapter 5 used the high concentration/conductivity electrolyte in the sintered electrode system to investigate the cycling performance. The electrolyte showed the best performance was used with templated electrodes to further improve the rate capability. The work of these two chapters provides possible solutions of improving the performance for systems with transport limitations, which can be useful for researchers investigating similar approaches. The results were published in two papers in *Journal of The Electrochemical Society* and *Molecular Systems Design and Engineering*.

Chapter 6 considered a way to further increase the energy density at the cell level. For that purpose, a recently developed high energy density anode material TNO was tested in sintered electrode cells. This work expands the material selection for sintered electrode cell system, indicating the electrode material could be more flexible in future investigations. The work has been submitted.

By investigating these topics, this thesis provides insights for understanding and developing Li-ion cells with high energy and power density.

1.5 References

(1) Dale, S. BP statistical review of world energy. *British Petroleum Company* **2016**.

(2) Gielen, D.; Boshell, F.; Saygin, D.; Bazilian, M. D.; Wagner, N.; Gorini, R. The Role of Renewable Energy in the Global Energy Transformation. *Energy Strat. Rev.* **2019**, *24*, 38–50.

(3) Wong, L. A.; Ramachandaramurthy, V. K.; Walker, S. L.; Ekanayake, J. B. Optimal Placement and Sizing of Battery Energy Storage System Considering the Duck Curve Phenomenon. *IEEE Access* **2020**, *8*, 197236–197248.

(4) Krietemeyer, B.; Dedrick, J.; Sabaghian, E.; Rakha, T. Managing the Duck Curve: Energy Culture and Participation in Local Energy Management Programs in the United States. *Energy Res. Soc. Sci.* **2021**, *79* , 102055.

(5) Ibrahim, H.; Ilinca, A.; Perron, J. Energy Storage Systems—Characteristics and Comparisons. *Renew. Sustain. Energy Rev.* **2008**, *12*, 1221–1250.

(6) DOE Global Energy Storage Database, https://sandia.gov/ess-ssl/gesdb/public/statistics.html.

(7) Rüdorff, W. Inclusion of common metals into graphite and into metal chalcogenides. *Chimia* **1965**, *19*, 489–499.

(8) Yoshino, A. The Birth of the Lithium-Ion Battery. *Angew. Chem. Int. Ed Engl.* **2012**, *51*, 5798–5800.

(9) Mizushima, K.; Jones, P. C.; Wiseman, P. J.; Goodenough, J. B. Li_xCoO_2 (0<x<-1): A New Cathode Material for Batteries of High Energy Density. *Mater. Res. Bull.* **1980**, *15*, 783–789.

(10) Nishi, Y. The Development of Lithium Ion Secondary Batteries. *Chem. Rec.* **2001**, *1*, 406–413.

(11) Scientific Background on the Nobel Prize in Chemistry 2019 Lithium-Ion Batteries

(12) Kurzweil, P. Lithium Battery Energy Storage: State of the Art Including Lithium Air and Lithium Sulfur Systems. In *Electrochemical Energy Storage for Renewable Sources and Grid Balancing*; Elsevier, 2015; pp 269–307.

(13) Scrosati, B.; Garche, J. Lithium Batteries: Status, Prospects and Future. *J. Power Sources* **2010**, *195*, 2419–2430.

(14) Wang, Z.; Lee, J. Z.; Xin, H. L.; Han, L.; Grillon, N.; Guy-Bouyssou, D.; Bouyssou, E.; Proust, M.; Meng, Y. S. Effects of Cathode Electrolyte Interfacial (CEI) Layer on Long Term Cycling of All-Solid-State Thin-Film Batteries. *J. Power Sources* **2016**, *324*, 342–348.

(15) Nitta, N.; Wu, F.; Lee, J. T.; Yushin, G. Li-Ion Battery Materials: Present and Future. *Mater. Today* **2015**, *18*, 252–264.

(16) Smith, K.; Wang, C.-Y. Solid-State Diffusion Limitations on Pulse Operation of a Lithium Ion Cell for Hybrid Electric Vehicles. *J. Power Sources* **2006**, *161*, 628–639.

(17) Zheng, H.; Li, J.; Song, X.; Liu, G.; Battaglia, V. S. A Comprehensive Understanding of Electrode Thickness Effects on the Electrochemical Performances of Li-Ion Battery Cathodes. *Electrochim. Acta* **2012**, *71*, 258–265.

(18) Kondo, H.; Sawada, H.; Okuda, C.; Sasaki, T. Influence of the Active Material on the Electronic Conductivity of the Positive Electrode in Lithium-Ion Batteries. *J. Electrochem. Soc.* **2019**, *166*, A1285–A1290.

(19) Armand, M.; Axmann, P.; Bresser, D.; Copley, M.; Edström, K.; Ekberg, C.; Guyomard, D.; Lestriez, B.; Novák, P.; Petranikova, M.; Porcher, W.; Trabesinger, S.; Wohlfahrt-Mehrens, M.; Zhang, H. Lithium-Ion Batteries – Current State of the Art and Anticipated Developments. *J. Power Sources* **2020**, *479*, 228708.

(20) Marks, T.; Trussler, S.; Smith, A. J.; Xiong, D.; Dahn, J. R. A Guide to Li-Ion Coin-Cell Electrode Making for Academic Researchers. *J. Electrochem. Soc.* **2011**, *158*, A51.

(21) Singh, M.; Kaiser, J.; Hahn, H. Thick Electrodes for High Energy Lithium Ion Batteries. *J. Electrochem. Soc.* **2015**, *162*, A1196–A1201.

(22) Wu, J.; Zhang, X.; Ju, Z.; Wang, L.; Hui, Z.; Mayilvahanan, K.; Takeuchi, K. J.; Marschilok, A. C.; West, A. C.; Takeuchi, E. S.; Yu, G. From Fundamental Understanding to Engineering Design of High-Performance Thick Electrodes for Scalable Energy-Storage Systems. *Adv. Mater.* **2021**, *33*, e2101275.

(23) Wu, J.; Ju, Z.; Zhang, X.; Quilty, C.; Takeuchi, K. J.; Bock, D. C.; Marschilok, A. C.; Takeuchi, E. S.; Yu, G. Ultrahigh-Capacity and Scalable Architected Battery Electrodes via Tortuosity Modulation. *ACS Nano* **2021**, *15* (12), 19109–19118.

(24) Yang, G.-F.; Song, K.-Y.; Joo, S.-K. Ultra-Thick Li-Ion Battery Electrodes Using Different Cell Size of Metal Foam Current Collectors. *RSC Adv.* **2015**, *5*, 16702–16706.

(25) Wei, T.-S.; Ahn, B. Y.; Grotto, J.; Lewis, J. A. 3D Printing of Customized Li-Ion Batteries with Thick Electrodes. *Adv. Mater.* **2018**, *30*, e1703027.

(26) Thorat, I. V.; Stephenson, D. E.; Zacharias, N. A.; Zaghib, K.; Harb, J. N.; Wheeler, D. R. Quantifying Tortuosity in Porous Li-Ion Battery Materials. *J. Power Sources* **2009**, *188*, 592–600.

(27) Kehrwald, D.; Shearing, P. R.; Brandon, N. P.; Sinha, P. K.; Harris, S. J. Local Tortuosity Inhomogeneities in a Lithium Battery Composite Electrode. *J. Electrochem. Soc.* **2011**, *158*, A1393.

(28) Li, L.; Erb, R. M.; Wang, J.; Wang, J.; Chiang, Y.-M. Fabrication of Low-tortuosity Ultrahigh-area-capacity Battery Electrodes through Magnetic Alignment of Emulsion-based Slurries. *Adv. Energy Mater.* **2019**, *9*, 1802472.

(29) Lai, W.; Erdonmez, C. K.; Marinis, T. F.; Bjune, C. K.; Dudney, N. J.; Xu, F.; Wartena, R.; Chiang, Y.-M. Ultrahigh-Energy-Density Microbatteries Enabled by New Electrode Architecture and Micropackaging Design. *Adv. Mater.* **2010**, *22*, E139-44.

(30) Robinson, J. P.; Ruppert, J. J.; Dong, H.; Koenig, G. M., Jr. Sintered Electrode Full Cells for High Energy Density Lithium-Ion Batteries. *J. Appl. Electrochem.* **2018**, *48*, 1297–1304.

(31) Nie, Z.; Ong, S.; Hussey, D. S.; LaManna, J. M.; Jacobson, D. L.; Koenig, G. M., Jr. Probing Transport Limitations in Thick Sintered Battery Electrodes with Neutron Imaging. *Mol. Syst. Des. Eng.* **2020**, *5*, 245–256.

(32) Tsai, P.-C.; Wen, B.; Wolfman, M.; Choe, M.-J.; Pan, M. S.; Su, L.; Thornton, K.; Cabana, J.; Chiang, Y.-M. Single-Particle Measurements of Electrochemical Kinetics in NMC and NCA Cathodes for Li-Ion Batteries. *Energy Environ. Sci.* **2018**, *11*, 860–871.

(33) Guo, B.; Yu, X.; Sun, X.-G.; Chi, M.; Qiao, Z.-A.; Liu, J.; Hu, Y.-S.; Yang, X.-Q.; Goodenough, J. B.; Dai, S. A Long-Life Lithium-Ion Battery with a Highly Porous $TiNb_2O_7$ Anode for Large-Scale Electrical Energy Storage. *Energy Environ. Sci.* **2014**, *7*, 2220–2226.

(34) Ohzuku, T.; Ueda, A.; Yamamoto, N. Zero-strain Insertion Material of $Li[Li_{1/3}Ti_{5/3}]O_4$ for Rechargeable

Lithium Cells. *J. Electrochem. Soc.* **1995**, *142*, 1431–1435.

(35) Cai, C.; Koenig, G. M., Jr. Investigating Dopants to Improve Sintered LiMn2O4 Spinel Electrode Electrochemical Cycling Limitations. *Electrochim. Acta* **2022**, *401*, 139484.

(36) Elango, R.; Nadeina, A.; Cadiou, F.; De Andrade, V.; Demortière, A.; Morcrette, M.; Seznec, V. Impact of Electrode Porosity Architecture on Electrochemical Performances of 1 Mm-Thick LiFePO4 Binder-Free Li-Ion Electrodes Fabricated by Spark Plasma Sintering. *J. Power Sources* **2021**, *488*, 229402.

(37) Sánchez-González, J.; Macías-García, A.; Alexandre-Franco, M. F.; Gómez-Serrano, V. Electrical Conductivity of Carbon Blacks under Compression. *Carbon N. Y.* **2005**, *43*, 741–747.

(38) Ménétrier, M.; Saadoune, I.; Levasseur, S.; Delmas, C. The Insulator-Metal Transition upon Lithium Deintercalation from $LiCoO_2$: Electronic Properties and 7Li NMR Study. *J. Mater. Chem.* **1999**, *9* (5), 1135–1140.

(39) Young, D.; Ransil, A.; Amin, R.; Li, Z.; Chiang, Y.-M. Electronic Conductivity in the $Li_{4/3}Ti_{5/3}O_4$-$Li_{7/3}Ti_{5/3}O_4$ System and Variation with State-of-Charge as a Li Battery Anode. *Adv. Energy Mater.* **2013**, *3*, 1125–1129.

(40) Xu, Y.-N.; Chung, S.-Y.; Bloking, J. T.; Chiang, Y.-M.; Ching, W. Y. Electronic Structure and Electrical Conductivity of Undoped $LiFePO_4$. *Electrochem. Solid State Letters* **2004**, *7*, A131.

(41) Zhuang, Q.-C.; Wei, T.; Du, L.-L.; Cui, Y.-L.; Fang, L.; Sun, S.-G. An Electrochemical Impedance Spectroscopic Study of the Electronic and Ionic Transport Properties of Spinel LiMn2O4. *J. Phys. Chem. C Nanomater. Interfaces* **2010**, *114*, 8614–8621.

(42) Park, K. S.; Son, J. T.; Chung, H. T.; Kim, S. J.; Lee, C. H.; Kang, K. T.; Kim, H. G. Surface Modification by Silver Coating for Improving Electrochemical Properties of $LiFePO_4$. *Solid State Commun.* **2004**, *129*, 311–314.

(43) Lu, L.-L.; Lu, Y.-Y.; Xiao, Z.-J.; Zhang, T.-W.; Zhou, F.; Ma, T.; Ni, Y.; Yao, H.-B.; Yu, S.-H.; Cui, Y. Wood-Inspired High-Performance Ultrathick Bulk Battery Electrodes. *Adv. Mater.* **2018**, *30* (20), e1706745.

(44) Delattre, B.; Amin, R.; Sander, J.; De Coninck, J.; Tomsia, A. P.; Chiang, Y.-M. Impact of Pore Tortuosity on Electrode Kinetics in Lithium Battery Electrodes: Study in Directionally Freeze-Cast $LiNi_{0.8}Co_{0.15}Al_{0.05}O_2$(NCA). *J. Electrochem. Soc.* **2018**, *165*, A388–A395.

(45) Park, J.; Jeon, C.; Kim, W.; Bong, S.-J.; Jeong, S.; Kim, H.-J. Challenges, Laser Processing and

Electrochemical Characteristics on Application of Ultra-Thick Electrode for High-Energy Lithium-Ion Battery. *J. Power Sources* **2021**, *482*, 228948.

(46) Fuller, T. F.; Doyle, M.; Newman, J. Simulation and Optimization of the Dual Lithium Ion Insertion Cell. *J. Electrochem. Soc.* **1994**, *141*, 1–10.

Chapter 2

Probing Lithiation and Delithiation of Thick Sintered Lithium-ion Battery Electrodes with Neutron Imaging

2.1 Abstract

As lithium-on (Li-ion) batteries increase in their prevalence and the range of applications expands, there is a need to understand and exploit the limits of electrochemical performance. Probing the internal processes in Li-ion batteries provides insights into the electrochemical characteristics of the cells as well as information necessary for rational cell design. In this manuscript an *in situ* method, neutron imaging, is applied to Li-ion full cells to track the lithiation/delithiation processes in the electrodes during discharge. The electrodes comprise thick sintered films of only active material, which improves the number of discrete points that are mapped for net changes in neutron intensity through the electrode. The lithiation/delithiation processes are qualitatively consistent with calculations of the Li^+ concentration and discharge profiles of the cells. These results illustrate that neutron imaging can experimentally probe and confirm limitations in the electrochemical performance of Li-ion full cells, particularly those with thick electrodes.

The content of this chapter has been published in the following journal:

Nie, Z.; McCormack, P.; Bilheux, H. Z.; Bilheux, J. C.; Robinson, J. P.; Nanda, J.; Koenig Jr, G. M. Probing Lithiation and Delithiation of Thick Sintered Lithium-Ion Battery Electrodes with Neutron Imaging. *J. Power Sources* **2019**, *419*, 127-136.

2.2 Introduction

Lithium-ion (Li-ion) batteries have become a critical technology for many applications, including consumer electronics and electric vehicles.[1,2] Understanding the material and performance limits of different Li-ion materials and components requires an understanding of how they function while being electrochemically charged and discharged. A variety of techniques have been developed to probe the operating fundamentals at different lengths scales – for example in-situ transmission electron microscopy electrochemical cells can provide insights into very local changes within the surface and bulk of electroactive materials during lithiation/delithiation.[3] Other techniques such as high resolution x-ray diffraction provide detailed structural information during electrochemical processes, but generally average that information using contributions from a larger amount of material within the cell.[4] While the techniques described above provide insights into processes and changes occurring with the electroactive material, it can be challenging to derive insights into the impacts, if any, of the transport of Li^+ ions through the porous architecture of the battery electrodes. In some cases, for example when electrodes are relatively thick, transport of Li^+ through the porous electrode (and separator) architecture can limit the charge/discharge rate.[5,6] For electrodes or battery cells that are limited, or potentially limited, by these processes of Li^+ transport through the porous void regions filled with electrolyte, tracking the transport and distribution of Li^+ *in situ* during the charge and discharge processes is critical to understand the transport occurring within the cell.

Towards the goal of tracking the *in situ* distribution of and/or transport of Li^+ within a battery cell, a number of techniques have been deployed. Recently, x-ray phase imaging was employed to quantify and visualize salt concentration distributions in battery electrolytes.[7] This technique provides quantitative concentration profiles of the Li^+ in the electrolyte, but a specialized spectroelectrochemical cell was required and access to concentration information was restricted to between the electrode regions. X-ray tomography has also been used to visualize the distribution of conversion electrode materials *in situ*,[8] although more subtle compositional changes such as the electrolyte concentration profile and the lithiation/delithiation of intercalation materials is more challenging using this method. More recently, there have been a few reports of using neutron imaging to track the distribution of Li^+ within a Li-ion cell. The transmission of the neutrons is highly sensitive to the total amount of Li^+ (and more specifically the $^6Li^+$) the neutrons interact with as they pass through the cell to the detector,[9,10] and thus neutron radiographs have high sensitivity to Li^+ compositional changes in a battery cell. For example, the lithiation of a graphite cathode was quantitatively tracked *in situ* using neutron radiographs of a pouch cell.[9] In addition, neutron tomography can be used to determine the three-dimensional distribution of lithiation/delithiation of active material, although the timescale of image collection generally limits the cells to post cycling analysis or extremely low rates of charge/discharge.[11]

Although neutron imaging has the advantages of being highly penetrating which enables not having to assemble special custom cells for analysis, and highly sensitive to Li^+ which enables tracking the entire active region of both electrodes and the electrolyte, a report in the literature of a Li-ion battery full cell with two intercalation electrodes undergoing neutron imaging *in situ* during electrochemical charge or discharge has been lacking. One of the primary reasons for this is the resolution of the technique – with previous reports having pixel sizes of ~40 μm and resolution of ~75 μm, though resolution can be improved with the tradeoff of significant reductions in field of view.[9] This resolution and pixel size limits the number of thickness locations that can be independently assessed within the cell or electrodes, because electrode thicknesses for Li-ion batteries are frequently 100 μm or less.[12] However, recently there have been reports of Li-ion battery cells with thicker electrodes, in some cases many hundreds of micrometers thick.[13,14] The thick electrodes are produced via hydraulic pressing and sintering, which results in pores in the electrode free of inactive binder and conductive additive components and the lack of a more conventional composite electrode architecture removes the concern of electrode delamination. The use of a full cell with two intercalation electrodes mitigates the current density, thickness change, and cycling limitation complications of having one of the electrodes be lithium metal.[13] Herein, neutron imaging will be used to quantify the lithiation/delithiation processes of a Li-ion battery full cell, where the electrodes are comprised of sintered porous thin films of intercalation materials. The neutron radiographs will be evaluated in the context of simulations of Li^+ concentration profiles calculated using a porous electrode model.[15,16,17]

2.3 Materials and methods

2.3.1 Preparation of active material powders

$Li_4Ti_5O_{12}$ (LTO) active material powder used in the anode was purchased from a commercial supplier (NANOMYTE BE-10 from NEI Corporation). $LiCoO_2$ (LCO) powder used as the active material in the cathode was synthesized using previously reported procedures based on the co-precipitation of $CoC_2O_4 \cdot 2H_2O$ precursor and calcination with Li_2CO_3 salt in a furnace with an air atmosphere.[18] For the LCO synthesis, in brief:

Cobalt oxalate precursor was synthesized using 1800 mL 62.8 mM $Co(NO_3)_2 \cdot 6H_2O$ (Fisher Reagent Grade) and 1800 mL 87.9 mM $(NH_4)_2C_2O_4 \cdot H_2O$ (Fisher Certified ACS) first prepared as separate solutions using deionized water, and both were heated to 50 °C. Then, $Co(NO_3)_2 \cdot 6H_2O$ solution was poured into $(NH_4)_2C_2O_4 \cdot H_2O$ solution all at once. The solution was stirred at 800 rpm and maintained at 50 °C for 30 minutes. After that, the solid precipitate product was collected using vacuum filtration and rinsed with 4 L deionized water. The powder was dried in an oven exposed to the surrounding air atmosphere for 24 hours at 80 °C.

To convert the precursor to LCO final active material, the oxalate particles were mixed with Li_2CO_3 (Fisher Chemical) powder with a Li:Co ratio of 1.02:1. The mixture was calcined in Carbolite CWF 1300 box furnace under an air atmosphere by heating to 800 °C with a ramp rate of 1 °C min^{-1}. Upon reaching the target temperature of 800 °C, the heat supplied to the furnace was turned off and it was allowed to cool to ambient temperature without any control over the cooling rate. The resulting LCO material was ground by hand using mortar and pestle and was further milled using Fritsch Pulverisette 7 planetary ball mill. For the ball milling, LCO powder was mixed with 5 mm diameter zirconia beads and milled for 5 hours at 300 rpm. The detailed materials characterization of the LTO and LCO materials used in this study, as well as their electrochemical characterization in conventional composite electrodes, can be found in previous reports.[13,18,19]

2.3.2 Electrode preparation and battery fabrication

The electrodes used in neutron imaging experiments were porous sintered metal oxides that were comprised of only active material. Cathode and anode pellets were independently and separately prepared using the same procedure. First, 1 g active powder was mixed with 2 mL 1 wt.% polyvinyl butyral (Pfaltz& Bauer) dissolved in ethanol (Acros). Mortar and pestle were used to facilitate mixing the slurry, and the hand mixing was continued until all solvent was evaporated. Second, the mixture powder was loaded into a 13 mm Carver pellet die. For the cell with “thin” electrodes, 0.2 g powder was used for LCO and 0.22 g powder was used for LTO. For the cell with “thick” electrodes, 0.26 g powder was used for both anode and cathode. For all pellets, the powder was pressed within the pellet die with 12,000 lb_f for 2 minutes in a Carver hydraulic press. The pellets were carefully extracted from the die intact and were sintered in a Carbolite CWF 1300 box furnace under an air atmosphere. The program used consisted of ramping from 25 °C to 700 °C at 1 °C min^{-1}, holding at 700 °C for 1 hour, then cooling to 25 °C at 1 °C min^{-1}.

The electrodes, comprised of porous disks containing only sintered electroactive materials, were assembled into full cells within CR2032 coin cells. The LCO pellets were attached to the bottom plate of the cell (Fig. 2.1a) using carbon paste (1:1 weight ratio Super P carbon black (Alfa Aesar) to polyvinylidene difluoride (PVDF, Alfa Aesar) binder dissolved in N-methyl pyrrolidone (NMP, Sigma-Aldrich)) and dried for 12 hours in an oven in air at 80°C. The LTO pellets were pasted on the stainless steel spacer of the coin cell using the same paste and drying procedure (Fig. 2.1b). The pellets attached to stainless steel were then transferred into an Ar-filled glove box (O_2 and H_2O both <1 ppm) for the remaining coin cell assembly steps. LTO and LCO electrodes were paired together while separated by a Celgard 2325 polymer separator. 16 drops of electrolyte (1.2 M $LiPF_6$ in 3:7 ethylene carbonate:ethyl methyl carbonate, purchased from BASF) were added. Other coin cell parts to complete assembly included a stainless steel wave spring, a stainless steel top cap, and a Teflon gasket (Fig. 2.1c). As described above, a “thin” cell and a “thick” cell were assembled for evaluation, where the sintered electrodes were used for LTO/LCO full cells. The LTO/LCO-Thin cell had electrodes with thicknesses of 0.738 mm and 0.463 mm for LTO and LCO, respectively. The LTO/LCO-Thick cell had electrodes with thicknesses of 0.886 mm and 0.640 mm for LTO and LCO, respectively. Representative scanning electron micrographs (SEMs, FEI Quanta 650) of LCO and LTO sintered pellet electrodes can be found in the Appendix 1, Figure A1.1.

The coin cells were cycled galvanostatically at different C rates, where the C rate was based on the mass of LCO in the cell with an assumed capacity of 150 mAh g^{-1} LCO (e.g. 1 C was assumed to be 150 mA g^{-1} LCO). Electrochemical cycling was performed using a MACCOR battery cycler or Bio-Logic potentiostat, with the Bio-Logic used for all electrochemical cycling conducted concurrent with neutron imaging. The cut off voltage limits were 1.0 V-2.8 V for all cells and C rates evaluated.

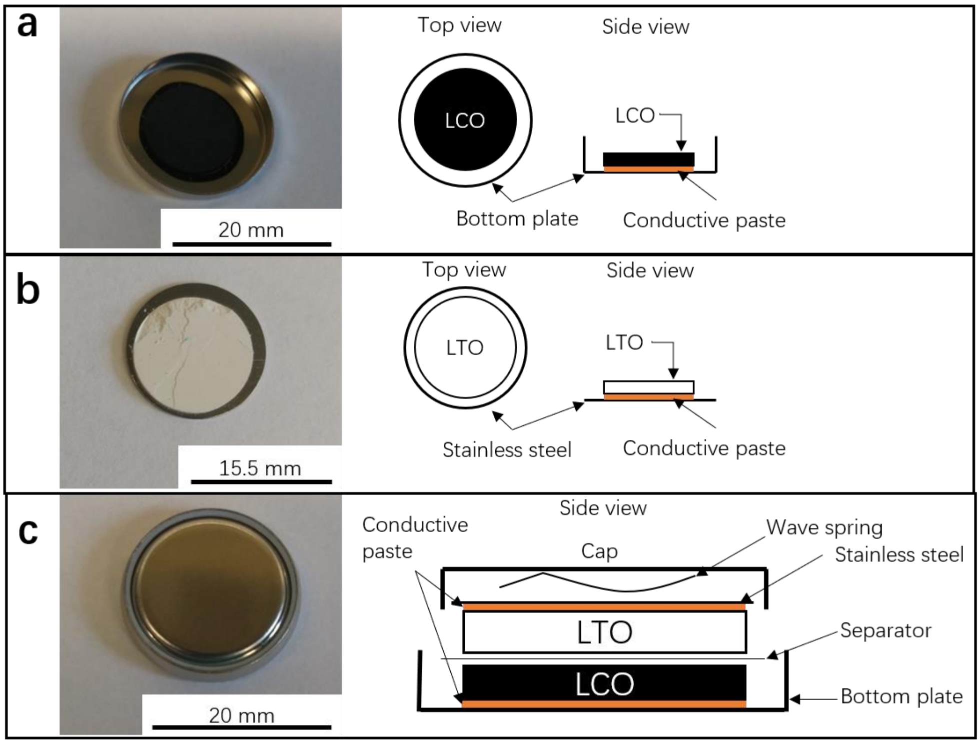

Fig. 2.1. (left) Photographs and (right) cartoon schematics depicting the different components and assembly of a CR2032 coin cell where both electrodes were sintered pellets. (a) Bottom plate with LCO pellet pasted within. (b) Spacer with LTO pellet pasted on top (note that LTO used in picture has noticeable cracks/defects on surface, while those used in cycled cells did not). (c) Final assembled coin cell (note that electrolyte and gasket are not shown in the schematic).

2.3.3 Neutron imaging

The neutron imaging experiment was carried out at the High Flux Isotope Reactor CG-1D beamline at Oak Ridge National Laboratory (ORNL).[20] A photograph showing the experimental setup with the coin cells in front of the scintillator detector can be found in Fig. 2.2a. An example of the raw radiograph taken of the cells in Fig. 2.2a can be found in Fig. 2.2b. To achieve sufficient neutron collection, each image was collected over a 35 second duration. This timescale was much shorter than the fastest discharge cycle that will be discussed in this report (for the fastest discharge each radiograph represents <0.07% of the total discharge time) which gave confidence that the image collection timescale gave sufficient temporal resolution for the processes being investigated. The raw radiograph was normalized using open beam and dark field corrections, and an example of a normalized transmission radiograph of the cells from the same experiment in Fig. 2.2b can be found in Fig. 2.2c. The goal of the neutron imaging was to track net changes in lithium concentration throughout the thickness of the cell during cycling, and thus the image data that will be discussed in the manuscript was further normalized relative to images collected before starting cycling (relative to the "no current" image). This normalization results in the cell components outside of the electrode region being approximately transparent because they are unchanged, while significant dark and bright contrast results in the electrode regions due to net Li^+ movement and Li^+ concentration changes. Darker regions correspond to lower transmission while brighter regions correspond to higher transmission relative to before cycling was initiated. Lithium is responsible for the majority of the attenuation (and thus decreases in neutron transmission) in the sample, and thus darker regions correspond to increased Li^+ concentration, while brighter regions correspond to decreased Li^+ concentration within the cell electrodes (relative to before cycling was initiated). In neutron images (normalized to “no current”) where grayscale is used, the dark/light contrast indicates net Li^+ concentration change as described above. In other cases a color scale for the changes in transmission, and correspondingly total Li^+ concentration, was used to show the distribution of changes in neutron transmission throughout the electrodes (see Fig. 2.2d, which is the adjusted image of the red box region in Fig. 2.2c, after normalizing relative to the no current image and using a color scale). The sample image in Fig. 2.2d was from the time point at the end of the C/30 discharge, which was chosen to illustrate the clear contrast between anode and cathode region with the net migration and insertion/deinsertion of Li^+ from the respective electrodes. In Fig. 2.2d, the electrode on the bottom (blue region) is LCO which has increased Li^+ concentration because the cell has been partially discharged and correspondingly the electrode on the top (red region) is LTO which has had a net decrease in Li^+ concentration. To extract the quantitative transmission information and maps of gradients in the z-direction in the cell (see Fig. 2.2d for z-direction), a 200-pixel wide line scan was used across the electrode area from bottom to the top. For both the LTO/LCO-Thin and LTO/LCO-Thick cells, the cells were charged to 2.8 V at a rate of C/100 before being shipped to ORNL. Then, after placing in the experimental setup in the neutron beam (Fig. 2.2a), the cells were charged again at a rate of C/50 to 2.8 V to recover any capacity that may have been lost to self-discharge during the 2 days between the charging at C/100 and the experiment at ORNL. Both cells were then discharged at a rate of C/30 while simultaneously collecting neutron radiographs. It is noted that due to exposure to the neutrons that some of the Co in the LCO becomes activated to ^{60}Co. ^{60}Co emits gamma rays and has a half-life of 5.27 years.[21,22] Thus, the cells used in the neutron imaging experiments cannot undergo post-testing materials characterization.

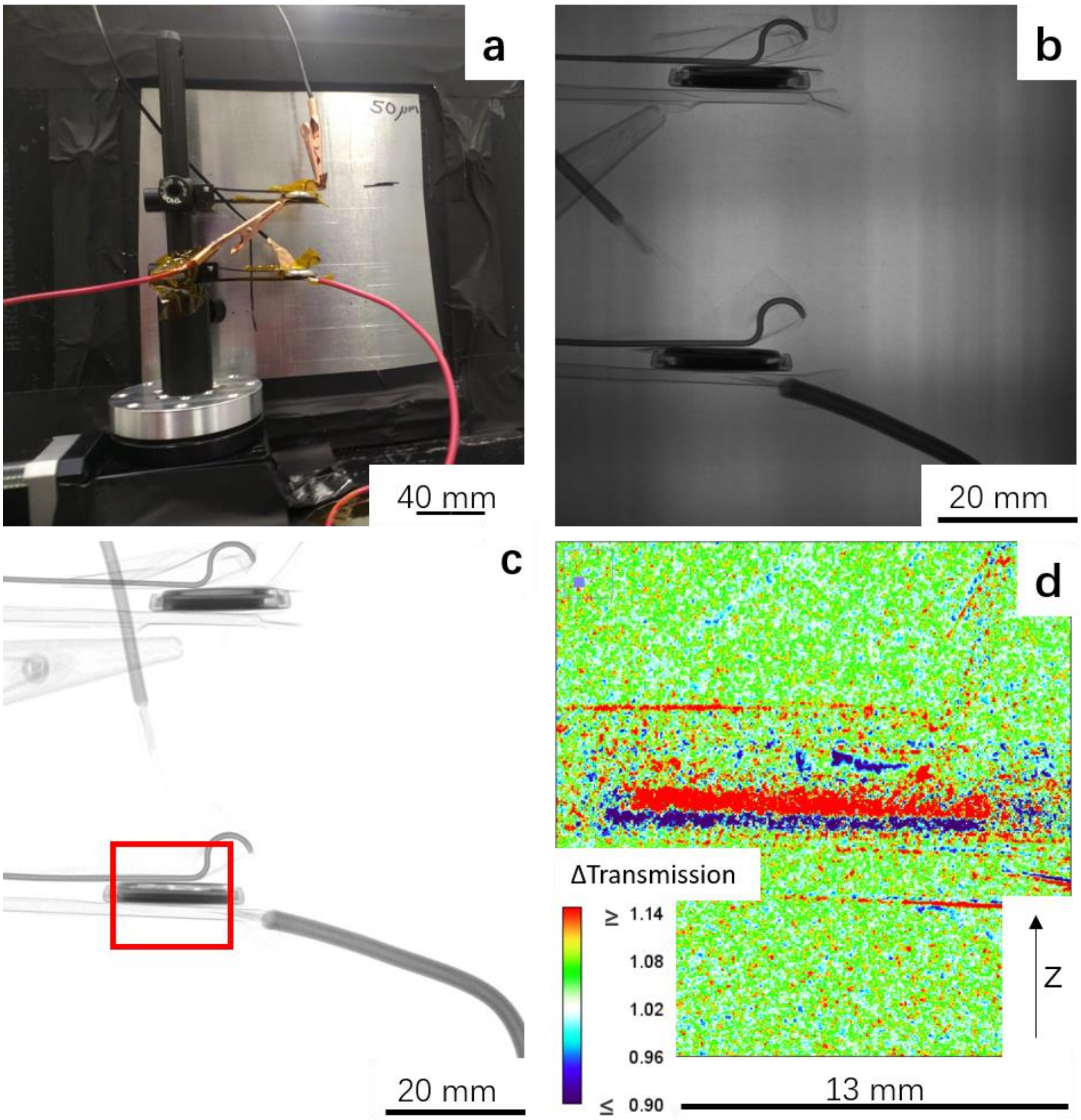

Fig. 2.2. (a) Photograph of neutron imaging experimental setup. Example neutron images depicting (b) raw collected radiographs, (c) transmission radiograph after normalizing using open beam and dark field radiographs, and (d) coin cell after normalizing relative to images collected before initiating

cycling and adding a color scale that corresponds to the relative change in neutron transmission. The image area in (d) is the same region as the red boxed region in (c). Inset in (d) is a color scale bar with the numerical value corresponding to the changes in relative neutron transmission at each pixel relative to the initiation of discharge. Black arrow on bottom right corner of (d) depicts the z-direction in the experiment, which is the length/depth dimension that is the focus of the Li^+ concentration profiles. Note that for (d) the brightest red regions have $\Delta T \geq 1.14$ and deepest blue regions have $\Delta T \leq 0.90$ and do not reflect the absolute maximum or minimum ΔT values. The color scale was truncated to best highlight the net change in the pixels throughout the electrode.

2.3.4 Model analysis

Experimental results were compared to calculations of electrochemical discharge of the cells conducted using the Dualfoil electrochemical model developed by Newman *et al.*[23] In particular, the Li^+ concentration profiles as a function of depth within the cell for both the liquid and the solid phase were extracted at different durations of discharge using the model, to compare to transmission profiles in the neutron radiographs. Details of the model have been discussed in detail in previous publications.[15-17,24] A brief introduction to the model can be found in Appendix 1.

2.4 Results and discussion

2.4.1 Neutron radiographs during discharge of thin cell

After charging the cell to 2.8 V, the LTO/LCO-Thin sintered electrode battery was discharged to 1.0 V at a rate of C/30. This rate corresponds to 0.98 mA and 0.74 mA cm^{-2}. The discharge voltage as a function of time can be found in Fig. 2.3a, and the total capacity delivered was 22.0 mAh, or 16.6 mAh cm^{-2}. LCO typically has a gradually sloping potential profile between 3.9 V (vs. Li/Li$^+$) and a cutoff voltage (typically <4.5 V, vs. Li/Li$^+$),[25] while LTO has a flat charge/discharge plateau at ~1.55 V (vs. Li/Li$^+$),[25] which would be expected to result in a sloping discharge curve between ~2.8 V (the upper cutoff for the cells in this study) and ~2.4 V.[26] As can be seen in Fig. 2.3a, the discharge profile has a gradual downward slope with the majority of the capacity between 2.5 V and 1.5 V. This discharge curve was consistent with an LTO/LCO cell, though with significant polarization. Thick sintered electrodes can have significant polarization due to the significant Li$^+$ transport distances[13] and due to electronic conductivity and cell resistance limitations, which will be discussed in further detail in Section 2.4.3. The discharge profile and capacity at C/30 was consistent with previous reports for LTO/LCO sintered electrode battery cells.[13]

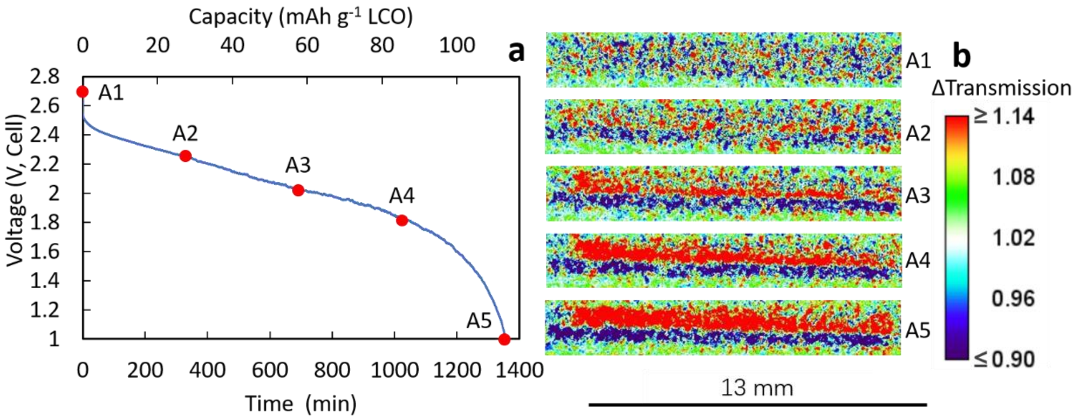

Fig. 2.3. (a) Discharge profile for the LTO/LCO-Thin cell. Time points A1-A5 are noted on the profile and correspond to the respective neutron images in (b). A1-A5 represent neutron radiographs that correspond to the times 0 min, 339 min, 678 min, 1017 min and 1357 min, respectively. The red and blue regions are the locations of the LTO and LCO electrodes, correspondingly. Inset in (b) is a color scale bar with the numerical value corresponding to the changes in relative neutron transmission at each pixel relative to the initiation of discharge. Note that for (b) the brightest red regions have $\Delta T \geq 1.14$ and deepest blue regions have $\Delta T \leq 0.90$ and do not reflect the absolute maximum or minimum ΔT values. The color scale was truncated to best highlight the net change in the pixels throughout the electrode.

Fig. 2.3b shows neutron radiographs taken at different points during the discharge of the LTO/LCO-Thin cell, with the color scale indicating the relative change in neutron transmission compared to just before discharge. At the initiation of discharge there was no significant change in pixel intensity in any region in the cell because the neutron transmission passing through different locations in the cell was not significantly different relative to the reference image taken before discharge. However, as the discharge proceeded, there was a clear red region that formed with a clear blue region below it, with a sharp step change between the two. The interface between the red and blue regions corresponded to the location of the separator between the LTO and LCO electrodes. The red region corresponded to the LTO electrode, and the blue region corresponded to the LCO electrode. As a function of discharge time/extent, the red region and blue region both extended further from the interface, though this was more noticeable with the red LTO top electrode. These changes in relative transmission were consistent with the net movement of Li^+ within the cell. As the cell discharges, the total amount of Li^+ within the electrolyte would be expected to stay constant (although the local concentration can vary significantly).[16] However, during the discharge the LTO will be delithiated from $Li_{4+y}Ti_5O_{12}$ back to $Li_4Ti_5O_{12}$ and simultaneously $Li_{1-x}CoO_2$ will be lithiated to $LiCoO_2$. Using the cell capacity of 22.0 mAh and assuming that at the end of discharge that the anode was uniformly of the composition $Li_4Ti_5O_{12}$ and the cathode was of the composition $LiCoO_2$, this means that when considering only the solid active material in the electrode the total concentration change in the LCO cathode material was 30.2 to 51.2 mol L^{-1} and the total concentration change in the anode LTO material was from 21.5 to 7.6 mol L^{-1}. This significant net concentration of Li^+ increase in the cathode and decrease in the anode, coupled with the large attenuation of neutrons absorbed by Li atoms due to its extremely large absorption coefficient,[9,10] resulted in the observed relative transmitted intensity changes in the neutron radiographs. The propagation of the changes in transmitted intensity from the separator towards the current collector, which provided the electrical path from the electrode to the external cell contacts (e.g., stainless steel components labeled in Fig. 2.1), as a function of the discharge time/extent (particularly in the LTO and less extreme for the LCO, as will be discussed in more detail in Section 2.4.3) indicated that Li^+ insertion into the cathode and deinsertion from the anode initially occurred on the separator/electrolyte side and propagated towards the current collector. This observation suggests that the electrochemical process was limited by the transport of the Li^+ through the porous electrode architecture, as has previously been described for thick electrode systems in general.[27] If the rate of lithiation/delithiation was limited by the solid state diffusion of Li^+ into/out of the individual active material particles, as is often the case in conventional and thinner Li-ion electrodes,[28] more uniform and gradual changes in transmitted intensity throughout the electrode thickness would be expected. It is noted that there was some heterogeneity in the transmitted intensity in the electrodes. For example, the red region consistent with delithiation of the LTO does not extend as far towards the current collector in the region on the far right at the end of discharge (see "A5" in Fig. 2.3b). The origins of this heterogeneity could be the result of multiple possibilities, including the heterogeneity of the LTO particles themselves, the temperature distribution during sintering of the electrode, and the stresses encountered and contact quality during processing the pellet into the coin cell. Understanding the causes of this heterogeneity will be the subject of future investigations.

2.4.2 Neutron radiographs during discharge of thick cell

The resulting discharge profile for the LTO/LCO-Thick cell can be found in Fig. 2.4a. The cell was charged to the same cutoff voltage of 2.8 V, discharged to the same cutoff voltage of 1.0 V, and was discharged at the same C rate of C/30 (though due to the higher loading the absolute current and current density was higher, at 1.26 mA and 0.95 mA cm^{-2}) as the LTO/LCO-Thin cell. The total capacity delivered was 17.2 mAh (12.9 mAh cm^{-2}). Note that this discharge capacity was 45.4% of the charge capacity of the cell, while for the LTO/LCO-Thin cell 75.4% of the charge capacity available was delivered during C/30 discharge. The polarization was also significantly greater in the LTO/LCO-Thick cell, with an average discharge voltage of 1.89 V, compared to the 2.03 V of the LTO/LCO-Thin cell. The only difference in the processing and fabrication of the LTO/LCO-Thick cell relative to the LTO/LCO-Thin cell was the greater thickness of the sintered electrodes. This suggested that the increased polarization and decreased capacity utilization was due to the longer diffusion paths of Li$^+$ through the tortuous electrodes in the LTO/LCO-Thick system.[13] A more detailed discussion to further support this outcome can be found in Section 2.4.3.

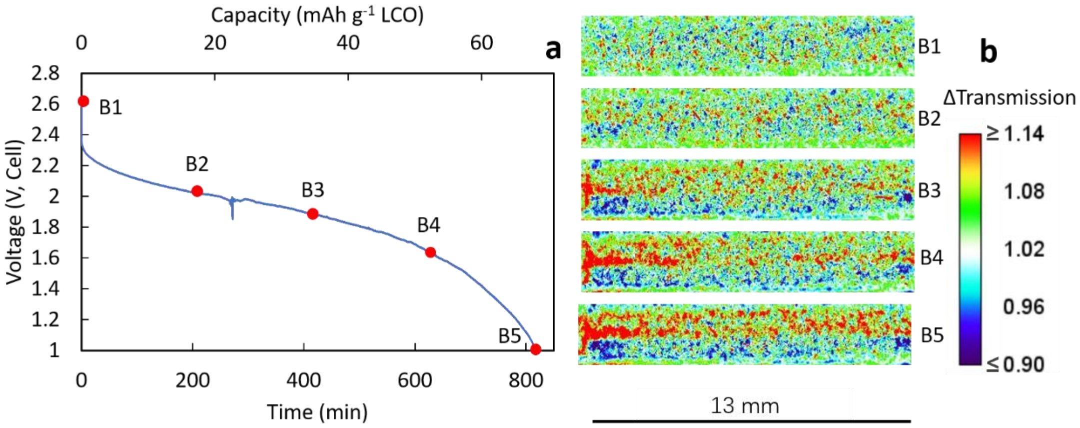

Fig. 2.4. Discharge profile for the LTO/LCO-Thick cell. Time points B1-B5 are noted on the profile and correspond to the respective neutron images in (b). B1-B5 are neutron radiographs that correspond to the times 0 min, 205 min, 409 min, 614 min and 819 min, respectively. The red and blue regions are the LTO and LCO electrode regions, correspondingly. Inset in (b) is a color scale bar with the numerical

value corresponding to the changes in relative neutron transmission at each pixel relative to the initiation of discharge. Note that for (b) the brightest red regions have $\Delta T \geq 1.14$ and deepest blue regions have $\Delta T \leq 0.90$ and do not reflect the absolute maximum or minimum ΔT values. The color scale was truncated to best highlight the net change in the pixels throughout the electrode.

The resulting neutron radiographs taken from different times during the LTO/LCO-Thick cell discharge can be found in Fig. 2.4b. The LTO/LCO-Thick cell images also appeared at the initiation of discharge to not have much variation in relative transmitted intensity, again due to there being no significant difference in neutron transmission relative to the cell before discharge. Careful inspection of the image sequence from B1-B5 results in qualitatively similar trends to the LTO/LCO-Thin cell; there was an interface of red/blue contrast that developed in the cell in the location near where the separator was located, and the blue and red regions both propagated away from the separator and towards the current collector. The red region (LTO electrode) was again on top and the blue region (LCO electrode) was again on the bottom, consistent with the net loss of Li^+ from LTO and gain of Li^+ by the LCO. The total thickness of the propagation of the red and blue regions, as well as the total change in contrast/attenuation, did not attain as great of an extent for the LTO/LCO-Thick system. This was consistent with the total extent of discharge being less, meaning that less total Li^+ (as a function of that available) was transferred across the LTO/LCO cell. This observation was also consistent with Li^+ transport through the electrode pores being the limitation to extracting the cell’s capacity, as the ability of the Li^+ to traverse the full distance of both electrodes was not successful at the C/30 rate.

2.4.3 LTO/LCO-Thin cell Li^+ composition comparison between experiment and calculation

To gain insights into the processes that limited the capacity and current density of the sintered electrode full cells, the Li^+ intercalation/deintercalation from the electrodes as a function of the depth within the cells (e.g., z-direction thickness location, see Fig. 2.2d) was assessed using the neutron imaging profiles. To obtain the transmission profiles, the average of transmission profile of 51 vertical pixel profiles for the LTO/LCO-Thin cell (and 59 for the LTO/LCO-Thick cell) were used to aid in averaging out local fluctuations and heterogeneity. The depth was captured from a location slightly below the LCO electrode to a location slightly above the LTO electrode to ensure the entire region where Li^+ concentration might change was sampled. For the LTO/LCO-Thin cell, this resulted in a sample region totaling 42 pixels (1430 μm). A neutron image highlighting the sample region can be found in the Appendix 1, Fig. A1.2a (and the relative transmission using a color scale in Fig. A1.2b). The corresponding sample region analyzed for the LTO/LCO-Thick cells can be found in Fig. A1.2c,d. The transmission profiles were fairly consistent across the “width” of the cells (for comparison of different locations see Appendix 1, Fig. A1.3), particularly in the LCO electrode region. As mentioned previously each pixel had been normalized relative to when the cells were first put in the path of the neutron beam after alignment (these profiles can be found in Appendix 1, Fig. A1.4a). However, the more appropriate comparison for the calculations was the change in transmission relative to the initiation of discharge (see Appendix 1, Fig. A1.4b, the impact of this change was relatively minor). Also, for easier comparison to calculations, the depth location in the cell was normalized by finding regions where the transmission did not change and assuming those areas represented the locations of the anode and cathode current collectors (also depicted in Appendix 1, Fig. A1.4b). After these data processing steps, the resulting profiles represented the change in neutron transmission relative to that observed at the initiation of the experiment as a function of the normalized depth between 0 and 1, where 0 represents the edge of the LCO electrode in contact with the current collector and 1 represents the location of the LTO electrode in contact with the current collector. The resulting transmission profile for the LTO/LCO-Thin electrode can be found in Fig. 2.5a.

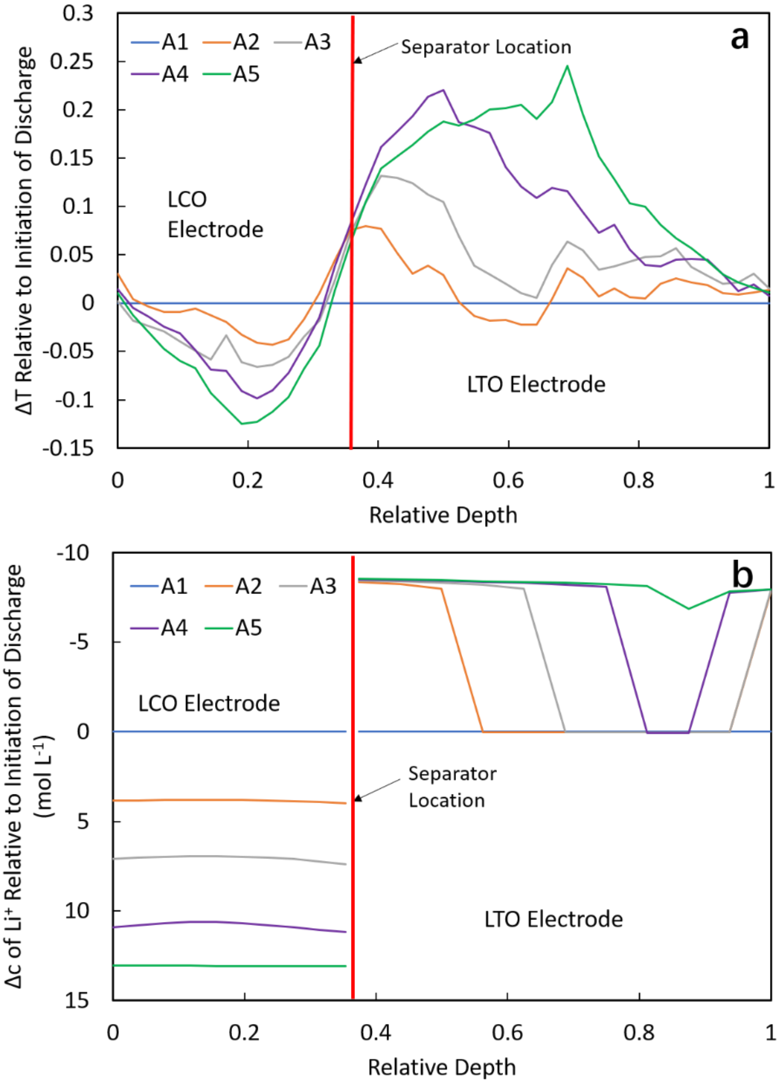

Fig. 2.5. LTO/LCO-Thin cell (a) experimental and (b) model results. The relative depth on the x-axis is the same for (a) and (b), and represents the thickness region normalized between the two electrodes (e.g., 0 is the connection of the LCO electrode to the current collector and 1 is the edge of the LTO electrode in contact with the current collector). Change in relative transmission intensity (ΔT) was determined from the neutron images collected during discharge for the A1-A5 timepoints corresponding to Fig. 2.3. Change in transmission intensity was relative to the image taken at the initiation of discharge (A1). Calculated change in Li^+ concentration (Δc) represents the difference between the total Li^+ concentration at that depth compared to the total concentration at the initiation of discharge (A1).

The change in transmission (ΔT) profiles as a function of time/extent of discharge for the LTO/LCO-Thin cell shown in Fig. 2.5a have a number of important features. First, overall the LCO electrode has a decrease in transmission and the LTO electrode has an increase in transmission relative to the initiation of discharge – this was consistent with the Li^+ net traversing from the LTO electrode to the LCO electrode during discharge. The LCO side has an approximately parabolic profile, with the bottom of the curve shape getting progressively lower as the discharge proceeds. This progression was consistent with a relatively uniform lithiation of the LCO electrode as a function of depth. It was suspected that the parabolic shape resulted from a combination of 1) the averaging of the transmission of the neutrons over multiple regions of the cell with each pixel due to the relatively large pixel size and 2) slight misalignment of the cell in the beam (collectively, contributions from outside the LCO electrode regions). Both of these effects would result in a parabolic profile, because at the current collector there would be no change in transmission expected, and near the separator the transmission would be expected to change in the opposite direction, thus averaging with those regions would result in the net parabolic profile. On the LTO side, uniform delithiation would be expected to also result in a parabolic shape due to contributions from outside the electrode region that was inverted relative to the LCO electrode because the LTO experienced deintercalation and loss of the highly attenuating Li^+. However, while the final state of the LTO electrode approximately resembled this outcome, the intermediate transmission profiles show a clear propagation of a transmission front from near the separator towards the current collector.

This front suggested the Li^+ was removed from the LTO electrode in a much less uniform manner relative to the LCO electrode’s intercalation with Li^+, where the LTO contributing the Li^+ during discharge started near the separator and came from progressively deeper depths in the electrode as a function of time/extent.

To gain further insights into the Li^+ distribution during the discharge of the LTO/LCO-Thin cell, calculations were performed using concentrated solution theory applied to the porous electrode model, as developed by Newman et al.[15,16,17] The relevant conservation equations can be found in the Appendix 1. A number of parameters were needed for the model, and they were either measured directly, found in the relevant literature, or assumed using approximations previously developed for the model. The detailed list of parameters can be found in Table 2.1. There have been multiple applications of this model using composite electrodes,[16,29] and two of the major differences that must be accounted for when using the sintered electrodes relative to the composite electrodes were that 1) the particles were not individually dispersed in the electrode and 2) the matrix conductivity in the electrode must come from the electroactive porous film itself rather than the carbon black/binder composite. For the first item, because the particle sintering was fairly mild (see Appendix 1, Fig. A1.1 for surface morphology) it was still assumed that the initial average particle size of the active material powders could be used for the electroactive particle diameters. For the second item, it was assumed that literature reports of the electronic conductivity after slight lithiation of LTO and delithiation of LCO could be used as the matrix conductivity.[30,31] The as-synthesized electronic conductivities of these materials were much lower, however with slight delithiation of LCO[30] and lithiation of

LTO[31] the electronic conductivity as reported in the literature significantly increased, particularly for LTO. The cells that were used had already been cycled a few times, meaning there should have been residual loss of Li^+ from LCO and gain of Li^+ by LTO even though the cell was fully charged at the beginning of the experiment. Using these conductivities also ignores resistance at grain boundaries, thus the electronic conductivities used likely represent a relatively high approximation. It is noted that calculations where the matrix conductivity was intentionally decreased for LTO and LCO electrodes did not impact the results interpretation until the conductivity was decreased by over two orders of magnitude, indicating there was a reasonable margin for the matrix electronic conductivities chosen. It is also noted that the cell internal resistance, extracted from experimental impedance spectroscopy measurements on the cells, were also quite high relative to conventional coin cells. It was suspected that this was due to resistance from the conductive paste and the quality of the contacts between the paste and both the sintered electrodes and the current collector.

Table 2.1. Battery parameters used in discharge calculations.

Parameters	LTO/LCO-Thin	LTO/LCO-Thick	Source
Thickness of negative electrode/LTO (m)	7.38×10^{-4}	8.66×10^{-4}	Measured
Thickness of separator (m)	2.5×10^{-5}	2.5×10^{-5}	Manufacturer
Thickness of positive electrode/LCO (m)	4.63×10^{-4}	6.40×10^{-4}	Measured
Bulk $LiPF_6$ concentration (mol m^{-3})	1200	1200	Manufacturer
Initial stoichiometric parameter, y for anode (y in $Li_{(4/3+y)}Ti_{(5/3)}O_4$)	0.64	0.39	Estimate from experimental capacities
Initial stoichiometric parameter, x for cathode (x in Li_xCoO_2)	0.58	0.75	Estimate from experimental capacities
Solid-state Li^+ diffusion coef. in anode (m^2 s^{-1})	1×10^{-12}	1×10^{-12}	Experimental data and Ref. Zaghib *et al.*[32]
Solid-state Li^+ diffusion coef. in cathode(m^2 s^{-1})	5×10^{-19}	5×10^{-19}	Ref. Geng *et al.*[33]
Radius of anode active particles (m)	1.7×10^{-7}	1.7×10^{-7}	Ref. Qi *et al.*[19]
Radius of cathode active particles (m)	1.5×10^{-7}	1.5×10^{-7}	Ref. Qi *et al.*[18]
Volume fraction of electrolyte in negative electrode	0.4	0.39	Based on measured porosity
Volume fraction of electrolyte in separator	0.39	0.39	Manufacturer
Volume fraction of electrolyte in positive electrode	0.36	0.31	Based on measured porosity
Conductivity of negative matrix (S m^{-1})	2	2	Ref. Young *et al.*[31]
Conductivity of positive matrix (S m^{-1})	0.3	0.3	Ref. Menetrier *et al.*[30]
Coulombic gravimetric capacity of negative material (mAh g^{-1})	175	175	Ref. Nitta *et al.*[25]
Coulombic gravimetric capacity of positive material (mAh g^{-1})	274	274	Ref. Nitta *et al.*[25]
Density of negative insertion material (kg m^{-3})	3485	3485	Theoretical crystal density, Ref. Kataoka *et al.*[34]
Density of positive insertion material (kg m^{-3})	5010	5010	Theoretical crystal density, Ref. Takahashi *et al.*[35]
Rate constant for negative reaction	8.7×10^{-6}	8.7×10^{-6}	Calculated based on Ref. He et al.[36]
Rate constant for positive reaction	4.3×10^{-7}	4.3×10^{-7}	Ref. Zhang *et al.*[37]
Internal resistance ($\Omega\cdot m^2$)	6.3×10^{-3}	1.6×10^{-2}	Experimental data
Bruggeman exponent	1.5	1.5	Assumed consistent with literature. Ref. Fuller *et al.*[16]

The simulated LTO/LCO-Thin cell discharge had a capacity of 20.3 mAh, in close agreement with the experimental value (the calculated and experimental discharge profiles can be found in the Appendix 1, Fig. A1.5). While the discharge capacity/time matched well, there was significantly more polarization in the experimental profile. It is suspected that the assumption on the matrix conductivity was one of the main simplifications that made the polarization difficult to match more quantitatively, because as the cell discharges the electronic conductivity could change significantly as a function of both depth and time. With the calculation, the Li^+ composition as a function of cell depth can be determined for both the liquid electrolyte phase and the solid electroactive material phase, as well as the sum of these concentrations (the calculated concentrations for the LTO/LCO-Thin cell can be found in Appendix 1, Fig. A1.6). The Li^+ concentration changes in both the liquid and solid phase will contribute to the resulting neutron transmission changes during discharge, however, the greatest calculated change in Li^+ in the liquid phase was <0.4 mol L^{-1} (see Fig. A1.6a), while the change in the solid phase was >10 mol L^{-1} in both electrodes (see Fig. A1.6b), and both phases occupy a similar volume fraction within the electrode. It is also noted that every constituent in the cell will contribute to the attenuation of the neutrons, however, the change in transmitted intensity relative to the initiation of discharge will only reflect changes in the dimensions of the cell components, which are expected to be negligible relative to the resolution of the neutron imaging, and changes in the composition within the cell. Other elements such as Co and Ti, while attenuating to neutrons, were not expected to have net transport that would change their compositional density within the cell to measurably impact the neutron radiographs. The change in Li^+ concentration (Δc) was calculated relative to the beginning of discharge, and the electrode depth was normalized by the total thickness, to make comparison of the calculated Li^+ profiles to the experimental neutron transmission profiles more straightforward.

The calculated change in Li^+ concentration through the cell thickness can be found in Fig. 2.5b. The Li^+ concentration scale has been inverted with increasing Li^+ going down instead of up to make comparison with the changes in neutron transmission more straightforward because decreased transmission corresponded with increased Li^+. The increase in the Li^+ concentration in the LCO electrode was uniform in the calculation across the LCO electrode thickness, with the extent of lithiation gradually increasing for all of the LCO material throughout the electrode as the discharge progressed. This was consistent with neutron transmission profiles. As discussed above, the parabolic shape resulted from regions of the cell that had unchanged or increasing transmission due to alignment and pixel averaging challenges. The peak in the transmission of the LCO electrode does slightly shift toward the current collector in the experimental profiles (Fig. 2.5a) indicating that there may have been slightly more lithiation near the separator in the LCO electrode, but the shift was not dramatic. In contrast, the LTO electrode has a fairly sharp transition where there was a region that goes from the separator into the electrode that has been completely delithiated (e.g., profile “A2” in Fig. 2.5b), a steep gradient in the extent of delithiation moving closer to the current collector, and then an area through the rest of the electrode thickness until reaching the current collector that was still fully lithiated and had not participated in the cell discharge. This gradient region propagates towards the current collector as the discharge proceeds, maintaining distinct regions that are either fully lithiated or fully delithiated. Also, at extents/durations of discharge “A3” and “A4” there was a second gradient region that propagated from the current collector towards the separator – and both gradients eventually disappeared at the end of discharge when the LTO electrode was completely delithiated throughout its thickness. Experimentally, the neutron transmission profiles within the LTO electrode also had an obvious sharp gradient region that propagated from the separator towards the current collector as a function of discharge time/extent. Such a gradient was consistent with Li^+ transport through the electrodes limiting the rate of discharge, which was not surprising given the large thickness of the electrodes. For the LTO/LCO-Thin electrode, the delithiation initiating from the current collector side of the LTO electrode was not observed experimentally. Lithium deintercalation will occur in the electrode at the locations with the lowest polarization. Within the LTO electrode, regions near the separator have the lowest ion transport polarization, while regions near the current collector have the lowest electron transport polarization.[38] As the lithiation gradient moved closer to the current collector, the polarization associated with the Li^+ moving all the way back to the separator (then subsequently through the current collector and LCO electrode) continued to increase. At some point the increased polarization due to ion transport associated with being even further from the separator in regions very near the current collector was balanced by the lower electronic resistance of being near the current collector, and the second delithiation front initiated near the current collector. While it was possible this occurred to an extent in the LTO/LCO-Thin cell, it was difficult to directly observe this second gradient in the neutron transmission profiles. This may have been due to limits in the experimental resolution, or may have also been due to the assumptions mentioned above on the matrix conductivity in the LTO electrode. If the LTO electronic conductivity of the matrix was effectively much higher, the second delithiation gradient initiating on the current collector side of the LTO electrode would not be expected.

2.4.4 LTO/LCO-Thick cell Li^+ composition comparison between experiment and calculation

The LTO/LCO-Thick cell was next analyzed for Li^+ intercalation/deintercalation during discharge. The transmission profiles during different discharge times/extents were processed using the same methods as described for the LTO/LCO-Thin cell (see Appendix 1, Fig. A1.7, A1.8), and the results can be found in Fig. 2.6a. The thickness was again normalized from 0 to 1, with 0 being the LCO current collector and 1 being the LTO current collector, although for the LTO/LCO thick cell that total distance in the cell was 1836 μm as opposed to 1430 μm. Looking at the electrodes on the whole, the average transmission in the LCO electrode decreased, while in the LTO electrode transmission increased, consistent with the net transfer of the highly attenuating Li^+ during discharge to lithiating the LCO after delithiating the LTO. For the LCO electrode in the LTO/LCO-Thick cell, the lithiation does not appear to be as uniform. There are two distinct regions closer to the current collector and closer to the separator that have significant decreases in transmission, consistent with lithiation in those regions. However, the mid region of the electrode does not have as large of a decrease in transmission, suggesting there was more significant lithiation/discharge of the LCO material closer to the two edges of the electrode and less lithiation towards the middle of the electrode thickness. While there was greater extent of lithiation nearer the ends of the electrode, there was not an observable gradient that moved through the electrode (in either direction) like the LTO electrode in the LTO/LCO-Thin cell case. Within the LTO electrode, there was a noticeable sharp gradient in the transmission profile that propagated from the separator towards the current collector, which was qualitatively consistent with the LTO/LCO-Thin cell. A new feature in the LTO/LCO-Thick cell LTO electrode, however, was a gradually increasing transmission near the current collector, suggesting delithiation in this region started fairly early during the discharge and Li^+ was extracted from this region as the discharge proceeded. The extent of the discharge of the LTO/LCO-Thick cell was much lower than the LTO/LCO-Thin cell (45.4% vs. 75.4%), thus the average net changes in transmission - increase in LTO electrode and decrease in LCO electrode – were lower for this cell.

The discharge of the LTO/LCO-Thick cell was also simulated using the same model as for the LTO/LCO-Thin cell (for calculated discharge profile see Appendix 1, Fig. A1.9). The calculated discharge profile had a capacity of 17.0 mAh, again in close agreement with the experiment. The only parameters that were changed relative to the LTO/LCO-Thin cell calculation was the thickness of each electrode was increased to match their measured values, the discharge current was increased such that both cells were discharged at C/30 on an LCO material mass basis, and the internal cell resistance that was used was the one measured for the appropriate cell. The simulated capacity of the cell matched very well to the experimentally observed value, although the experimental discharge curve had more polarization as was also the case for the thinner cell and was discussed above. The Li^+ concentration profiles in the liquid and solid phase were again extracted from the calculation and summed (see Appendix 1, Fig. A1.10) and the change in total Li^+ concentration was determined relative to the beginning of the discharge. The resulting calculated Li^+ concentration profile through the cell thickness can be found in Fig. 2.6b for the LTO/LCO-Thick cell. Overall, the Li^+ concentration increased in the LCO and decreased in the LTO as the discharge extent/time proceeds. In the LCO electrode, the lithiation was relatively uniform as a function of thickness, though for a couple of the profiles (e.g., “B3” at 409 minutes) there was a slight increase at the two edges of the electrode near the current collector and separator. The increased lithiation near the edges resulted in slightly less lithiation, which would increase the transmission, near the center of the LCO electrode thickness. The extent of the calculated underlithiation was not large enough to account for all of the observed lack of lithiation in the center region of the electrode, but the overall outcome of having relatively low electronic polarization near the current collector and ionic polarization near the separator was likely to play a role. Lithium being selectively deposited at both edge regions (near both the current collector and separator) has been previously reported in the literature for other battery systems, including lithium-air.[39] In the lithium-air case, the sluggish transport of Li^+ on one side and O_2 on the other resulted in peaks in discharge product (and hence Li^+) concentration near the edges. It is suspected that in the observations in the sintered electrode with higher extent of discharge near the edges that it similarly reflected the two sluggish phenomena in the cell at high rates – with one being the transport of Li^+ and the other being the transport of electrons. The calculations and experimental profiles were both consistent with not having a lithiation gradient front that propagated through the LCO cathode, which was in contrast to the LTO anode.

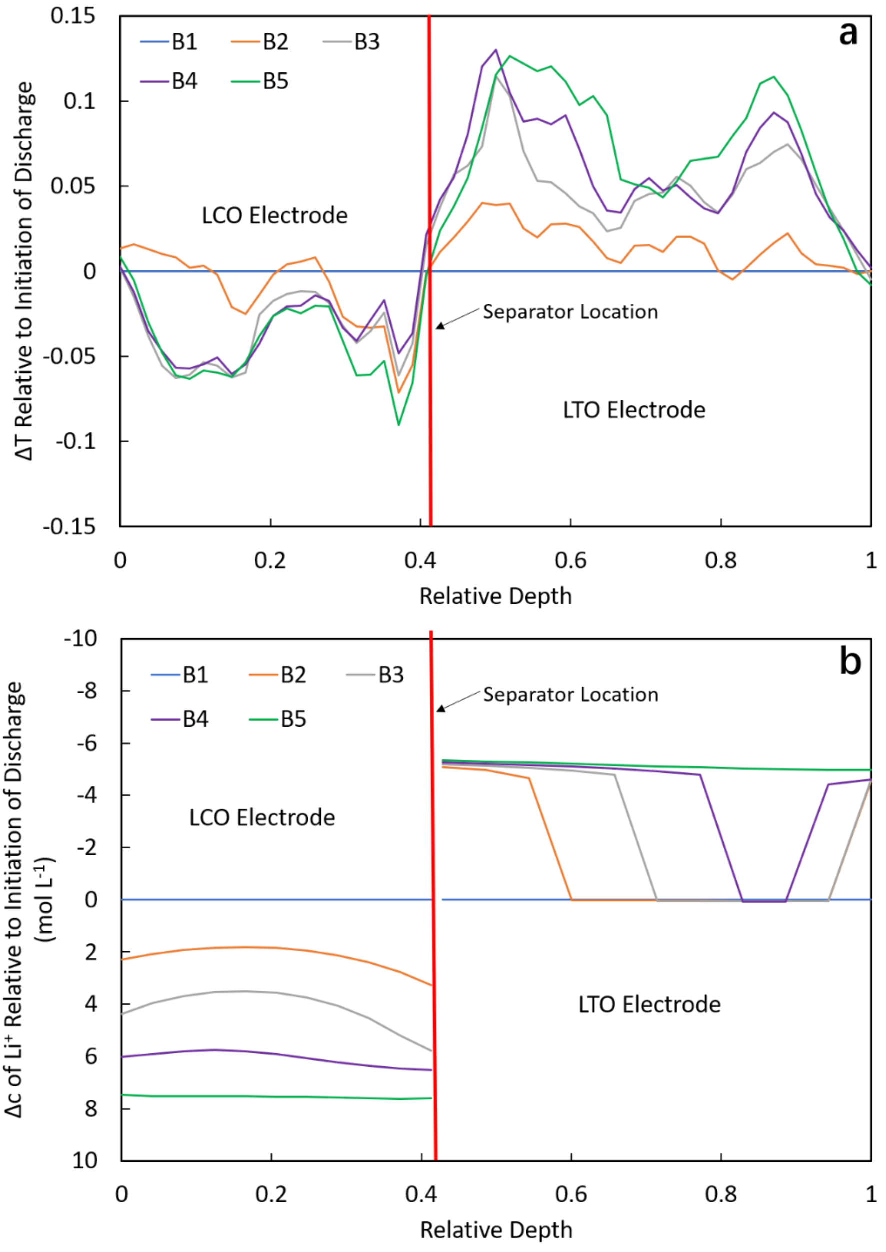

Fig. 2.6. LTO/LCO-Thick cell (a) experimental and (b) model results. The relative depth on the x-axis is the same for (a) and (b), and represents the thickness region normalized between the two electrodes (e.g., 0 is the connection of the LCO electrode to the current collector and 1 is the edge of the LTO

electrode in contact with eh current collector). Change in relative transmission intensity (ΔT) was determined from the neutron images collected during discharge for the B1-B5 timepoints corresponding to Fig. 2.4. Change in transmission intensity was relative to the image taken at the initiation of discharge (B1). Calculated change in Li^+ concentration (Δc) represents the difference between the total Li^+ concentration at that depth compared to the total concentration at the initiation of discharge (B1).

The calculated delithiation of the LTO anode was qualitatively similar to that of the LTO/LCO-Thin cell. Initially a gradient propagated from the separator towards the current collector, where to the left of the front the LTO was completely delithiated and to the right of the front the LTO was all still lithiated, and there was a sharp gradient in Li^+ concentration in the transition region. At a later time (first observed in Fig. 2.6b at "B3" at 409 minutes) a second front of delithiation started which propagated from the current collector toward the separator, and at the end of the calculation almost all of the LTO in the electrode was uniformly delithiated. The transmission profile behavior for the LTO/LCO-Thick cell was very consistent with the calculation. There was a noticeable gradient in the transmission that propagated from the separator towards the current collector, consistent with a delithiation gradient that moved through the electrode, although the experimental delithiation gradient traversed through the electrode thickness more slowly. In addition, the "B3" 409-minute transmission profile had a significant increase in transmission near the current collector, consistent with the calculation results. While it was not as clear in the transmission profiles that the delithiation near the current collector also had a gradient that propagated towards the separator as was observed in the calculation, the relative transmission did increase as a function of discharge time/extent and the peak in transmission shifted slightly towards the separator. At the end of discharge, the calculated relative Li^+ concentration profile was very uniform, while the experimental transmission profile had a significant decrease in transmission in the center region of the electrode, indicating the center of the LTO electrode did not achieve as complete of a delithiation. This suggested the end of the discharge resembled one of the calculated discharge profiles slightly before the end of discharge, where the two gradients had not converged together and there was a substantial region that had not been delithiated between the two. Thus, the difference between experiment and calculation for the delithiation in the center of the LTO electrode may indicate the extent of delithiation of the LTO as a whole was overestimated in the calculation.

The results presented in this manuscript demonstrate that insights into the lithiation/delithiation processes and transport limitations of Li-ion full cells can be obtained via *in situ* neutron imaging experiments using sintered electrodes. It is noted that translation of these results and insights to more commonly used composite Li-ion battery electrodes is not straightforward. While the sintered electrodes have void regions in the pore volume between active material particles which is filled with electrolyte, these same interstitial regions in a composite electrode also contain binder and conductive additives. The additional components result in much better electronic conductivity in the electrode relative to the sintered electrode system, but can significantly restrict the Li^+ transport through the electrode architecture.[40,41] This transport limitation has been accounted for in some reports via correction to the

Bruggeman scaling, but this correction has been very sensitive to the specific electrode composition and processing conditions.[42,43] In addition, the fundamental process which limits the performance of composite electrodes can be very dependent on the details of the active material chemistry and electrode chosen and many other cell factors. For example, Li^+ and/or electron transport within the solid active material phase can limit the rate capability for electrodes with active material particles significantly larger than the ones used in this study.[44] While determining the fundamental processes that limit battery performance is a challenging task, this paper shows how for appropriate systems that neutron imaging can provide significant insights.

2.5 Conclusions

This report described *in situ* neutron imaging experiments to track the lithiation/delithiation of a Li-ion battery full cell, where the electrodes were comprised of sintered active materials. Although the pixel size for neutron imaging is relatively large, the use of thick sintered electrode containing only active material enabled multiple data points through the depth of each electrode to be tracked during the discharge process, when highly attenuating Li^+ was transferred from the anode to the cathode. Comparison was made between the experimentally obtained relative transmission profiles and calculations of the total Li^+ concentration at different depths in the cell. The calculations and experiments showed good qualitative agreement for the two cells investigated, capturing the more uniform lithiation of the LCO electrode during discharge, a delithiation front that propagated from the separator towards the current collector in the LTO electrode, and delithiation that started near the LTO current collector in the thicker LTO/LCO cell. Future efforts to more quantitatively match experiment and calculation will be needed, and such efforts will require improvements in both. For example, higher resolution neutron imaging in the order of 10 μm, coupled with improved alignment, will reduce perceived gradients in regions near the edges of the electrode. The improvements in resolution generally will require a tradeoff with regards to acquisition time and field-of-view.[20] Also, improvements in accuracy of the electronic conductivity of the active material, in particular as a function of different states of lithiation, coupled with estimation of the resistance associated with electron transfer between particle constituents, will greatly improve the accuracy of the matrix electronic conductivity polarization in the model. This study demonstrates the value in using neutron experiments to confirm lithiation/delithiation processes within Li-ion battery cells, which informs rational designs to improve upon the limiting steps in the system.

2.6 Acknowledgements

Funding is acknowledged from the National Science Foundation, grants CMMI-1825338 and CBET-1652488. This research used resources at the High Flux Isotope Reactor and Spallation Neutron Source, a DOE Office of Science User Facility operated by the Oak Ridge National Laboratory.

2.7 References

(1) Tarascon, J. M.; Armand, M. Issues and Challenges Facing Rechargeable Lithium Batteries. *Nature* **2001**, *414*, 359–367.

(2) Passerini, S.; Scrosati, B. Lithium and Lithium-Ion Batteries: Challenges and Prospects. *Electrochem. Soc. Interface* **2016**, *25*, 85–87.

(3) Huang, J. Y.; Zhong, L.; Wang, C. M.; Sullivan, J. P.; Xu, W.; Zhang, L. Q.; Mao, S. X.; Hudak, N. S.; Liu, X. H.; Subramanian, A.; Fan, H.; Qi, L.; Kushima, A.; Li, J. In Situ Observation of the Electrochemical Lithiation of a Single SnO_2 Nanowire Electrode. *Science* **2010**, *330*, 1515–1520.

(4) Reimers, J. N.; Dahn, J. R. Electrochemical and In Situ X-Ray Diffraction Studies of Lithium Intercalation in Li_xCoO_2. *J. Electrochem. Soc.* **1992**, *139*, 2091–2097.

(5) Ebner, M.; Chung, D.-W.; García, R. E.; Wood, V. Tortuosity Anisotropy in Lithium-Ion Battery Electrodes. *Adv. Energy Mater.* **2014**, *4* (5), 1301278.

(6) Gallagher, K. G.; Trask, S. E.; Bauer, C.; Woehrle, T.; Lux, S. F.; Tschech, M.; Lamp, P.; Polzin, B. J.; Ha, S.; Long, B.; Wu, Q.; Lu, W.; Dees, D. W.; Jansen, A. N. Optimizing Areal Capacities through Understanding the Limitations of Lithium-Ion Electrodes. *J. Electrochem. Soc.* **2016**, *163*, A138–A149.

(7) Takamatsu, D.; Yoneyama, A.; Asari, Y.; Hirano, T. Quantitative Visualization of Salt Concentration Distributions in Lithium-Ion Battery Electrolytes during Battery Operation Using X-Ray Phase Imaging. *J. Am. Chem. Soc.* **2018**, 140, 1608–1611.

(8) Wang, J.; Chen-Wiegart, Y.-C. K.; Wang, J. In Situ Three-Dimensional Synchrotron X-Ray Nanotomography of the (de)Lithiation Processes in Tin Anodes. *Angew. Chem. Int. Ed Engl.* **2014**, *53*, 4460–4464.

(9) Zhou, H.; An, K.; Allu, S.; Pannala, S.; Li, J.; Bilheux, H. Z.; Martha, S. K.; Nanda, J. Probing Multiscale Transport and Inhomogeneity in a Lithium-Ion Pouch Cell Using in Situ Neutron Methods. *ACS Energy Lett.* **2016**, *1*, 981–986.

(10) Siegel, J. B.; Lin, X.; Stefanopoulou, A. G.; Hussey, D. S.; Jacobson, D. L.; Gorsich, D. Neutron

Imaging of Lithium Concentration in LFP Pouch Cell Battery. *J. Electrochem. Soc.* **2011**, *158*, A523.

(11) Zhang, Y.; Chandran, K. S. R.; Bilheux, H. Z. Imaging of the Li Spatial Distribution within V_2O_5 Cathode in a Coin Cell by Neutron Computed Tomography. *J. Power Sources* **2018**, *376*, 125–130.

(12) Singh, M.; Kaiser, J.; Hahn, H. Thick Electrodes for High Energy Lithium Ion Batteries. *J. Electrochem. Soc.* **2015**, *162*, A1196–A1201.

(13) Robinson, J. P.; Ruppert, J. J.; Dong, H.; Koenig, G. M., Jr. Sintered Electrode Full Cells for High Energy Density Lithium-Ion Batteries. *J. Appl. Electrochem.* **2018**, *48*, 1297–1304.

(14) Lai, W.; Erdonmez, C. K.; Marinis, T. F.; Bjune, C. K.; Dudney, N. J.; Xu, F.; Wartena, R.; Chiang, Y.-M. Ultrahigh-Energy-Density Microbatteries Enabled by New Electrode Architecture and Micropackaging Design. *Adv. Mater.* **2010**, *22*, E139-44.

(15) Doyle, M.; Fuller, T. F.; Newman, J. Modeling of Galvanostatic Charge and Discharge of the Lithium/Polymer/Insertion Cell. *J. Electrochem. Soc.* **1993**, *140*, 1526–1533.

(16) Fuller, T. F.; Doyle, M.; Newman, J. Simulation and Optimization of the Dual Lithium Ion Insertion Cell. *J. Electrochem. Soc.* **1994**, *141*, 1–10.

(17) Fuller, T. F.; Doyle, M.; Newman, J. Relaxation Phenomena in Lithium-Ion-Insertion Cells. *J. Electrochem. Soc.* **1994**, *141*, 982–990.

(18) Qi, Z.; Koenig, G. M., Jr. High-Performance $LiCoO_2$ Sub-Micrometer Materials from Scalable Microparticle Template Processing. *ChemistrySelect* **2016**, *1*, 3992–3999.

(19) Qi, Z.; Koenig, G. M., Jr. A Carbon-Free Lithium-Ion Solid Dispersion Redox Couple with Low Viscosity for Redox Flow Batteries. *J. Power Sources* **2016**, *323*, 97–106.

(20) Santodonato, L.; Bilheux, H.; Bailey, B.; Bilheux, J.; Nguyen, P.; Tremsin, A.; Selby, D.; Walker, L. The CG-1D Neutron Imaging Beamline at the Oak Ridge National Laboratory High Flux Isotope Reactor. *Phys. Procedia* **2015**, *69*, 104–108.

(21) Versieck, J.; Hoste, J.; Barbier, F.; Steyaert, H.; De Rudder, J.; Michels, H. Determination of Chromium and Cobalt in Human Serum by Neutron Activation Analysis. *Clin. Chem.* **1978**, *24*, 303–308.

(22) Wagner, M.; Vonach, H.; Pavlik, A.; Strohmaier, B.; Tagesen, S.; Martinez Rico, J. Evaluation of Cross Sections for 14 Important Neutron Dosimetry Reactions *Physik Daten (Physics Data)* No.13-5(Fachinformationszentrum, Karlsruhe, Germany, 1990).

(23) Albertus, P.; Newman, J. Introduction to dualfoil 5.0, University of California Berkeley, Berkeley, CA, Tech. Rep. 2007.

(24) Allu, S.; Kalnaus, S.; Elwasif, W.; Simunovic, S.; Turner, J. A.; Pannala, S. A New Open Computational Framework for Highly-Resolved Coupled Three-Dimensional Multiphysics Simulations of Li-Ion Cells. *J. Power Sources* **2014**, *246*, 876–886.

(25) Nitta, N.; Wu, F.; Lee, J. T.; Yushin, G. Li-Ion Battery Materials: Present and Future. *Mater. Today* **2015**, *18*, 252–264.

(26) Du Pasquier, A.; Plitz, I.; Menocal, S.; Amatucci, G. A Comparative Study of Li-Ion Battery, Supercapacitor and Nonaqueous Asymmetric Hybrid Devices for Automotive Applications. *J. Power Sources* **2003**, *115*, 171–178.

(27) Zheng, H.; Li, J.; Song, X.; Liu, G.; Battaglia, V. S. A Comprehensive Understanding of Electrode Thickness Effects on the Electrochemical Performances of Li-Ion Battery Cathodes. *Electrochim. Acta* **2012**, *71*, 258–265.

(28) Moshtev, R.; Johnson, B. State of the Art of Commercial Li Ion Batteries. *J. Power Sources* **2000**, *91*, 86–91.

(29) Rashid, M.; Sahoo, A.; Gupta, A.; Sharma, Y. Numerical Modelling of Transport Limitations in Lithium Titanate Anodes. *Electrochim. Acta* **2018**, *283*, 313–326.

(30) Ménétrier, M.; Saadoune, I.; Levasseur, S.; Delmas, C. The Insulator-Metal Transition upon Lithium Deintercalation from $LiCoO_2$: Electronic Properties and ^{7}Li NMR Study. *J. Mater. Chem.* **1999**, *9*, 1135–1140.

(31) Young, D.; Ransil, A.; Amin, R.; Li, Z.; Chiang, Y.-M. Electronic Conductivity in the $Li_{4/3}Ti_{5/3}O_4$-$Li_{7/3}Ti_{5/3}O_4$ System and Variation with State-of-Charge as a Li Battery Anode. *Adv. Energy Mater.* **2013**, *3*, 1125–1129.

(32) Zaghib, K.; Simoneau, M.; Armand, M.; Gauthier, M. Electrochemical Study of $Li_4Ti_5O_{12}$ as Negative Electrode for Li-Ion Polymer Rechargeable Batteries. *J. Power Sources* **1999**, *81–82*, 300–305.

(33) Geng, L.; Denecke, M. E.; Foley, S. B.; Dong, H.; Qi, Z.; Koenig, G. M., Jr. Electrochemical Characterization of Lithium Cobalt Oxide within Aqueous Flow Suspensions as an Indicator of Rate Capability in Lithium-Ion Battery Electrodes. *Electrochim. Acta* **2018**, *281*, 822–830.

(34) Kataoka, K.; Takahashi, Y.; Kijima, N.; Akimoto, J.; Ohshima, K.-I. Single Crystal Growth and Structure Refinement of $Li_4Ti_5O_{12}$. *J. Phys. Chem. Solids* **2008**, *69*, 1454–1456.

(35) Takahashi, Y.; Kijima, N.; Dokko, K.; Nishizawa, M.; Uchida, I.; Akimoto, J. Structure and Electron Density Analysis of Electrochemically and Chemically Delithiated $LiCoO_2$ Single Crystals. *J. Solid State Chem.* **2007**, *180*, 313–321.

(36) He, Z.; Wang, Z.; Wu, F.; Guo, H.; Li, X.; Xiong, X. Spherical $Li_4Ti_5O_{12}$ Synthesized by Spray Drying from a Different Kind of Solution. *J. Alloys Compd.* **2012**, *540*, 39–45.

(37) Zhang, Q.; Guo, Q.; White, R. E. Semi-Empirical Modeling of Charge and Discharge Profiles for a $LiCoO_2$ Electrode. *J. Power Sources* **2007**, *165*, 427–435.

(38) Park, M.; Zhang, X.; Chung, M.; Less, G. B.; Sastry, A. M. A Review of Conduction Phenomena in Li-Ion Batteries. *J. Power Sources* **2010**, *195*, 7904–7929.

(39) Nanda, J.; Bilheux, H.; Voisin, S.; Veith, G. M.; Archibald, R.; Walker, L.; Allu, S.; Dudney, N. J.; Pannala, S. Anomalous Discharge Product Distribution in Lithium-Air Cathodes. *J. Phys. Chem. C Nanomater. Interfaces* **2012**, *116*, 8401–8408.

(40) Landesfeind, J.; Eldiven, A.; Gasteiger, H. A. Influence of the Binder on Lithium Ion Battery Electrode Tortuosity and Performance. *J. Electrochem. Soc.* **2018**, *165*, A1122–A1128.

(41) Chen, J.; Liu, J.; Qi, Y.; Sun, T.; Li, X. Unveiling the Roles of Binder in the Mechanical Integrity of Electrodes for Lithium-Ion Batteries. *J. Electrochem. Soc.* **2013**, *160*, A1502–A1509.

(42) Cobb, C. L.; Bae, C.-J. Tortuosity of Binder-Free and Carbon-Free High Energy Density LiCoO2 Electrodes for Rechargeable Lithium-Ion Batteries. *ECS Trans.* **2014**, *58*, 13–24.

(43) Thorat, I. V.; Stephenson, D. E.; Zacharias, N. A.; Zaghib, K.; Harb, J. N.; Wheeler, D. R. Quantifying Tortuosity in Porous Li-Ion Battery Materials. *J. Power Sources* **2009**, *188*, 592–600.

(44) Gallagher, K. G.; Nelson, P. A.; Dees, D. W. Simplified Calculation of the Area Specific Impedance for Battery Design. *J. Power Sources* **2011**, *196*, 2289–2297.

Chapter 3

Probing Transport Limitations in Thick Sintered Battery Electrodes with Neutron Imaging

3.1 Abstract

Lithium-ion batteries receive significant research effort due to their advantages in energy and power density, which are important to enabling many devices. One route to further increase energy density is to fabricate thicker electrodes in the battery cell, however, careful consideration must be taken when designing electrodes as to how increasing thickness impacts the multiscale and multiphase molecular transport processes, which can limit the overall battery operating power. Design of these electrodes necessitates probing the molecular processes when the battery cell undergoes electrochemical charge/discharge. One tool to provide *in situ* insights of the cell is neutron imaging, because neutron imaging provides information of where electrochemical processes occur within the electrodes. In this manuscript, neutron imaging is applied to track the lithiation/delithiation processes within electrodes at different current densities for a full cell with thick sintered $Li_4Ti_5O_{12}$ anode and $LiCoO_2$ cathode. The neutron imaging reveals that the molecular distribution of Li^+ during discharge within the electrode is sensitive to the current density, or equivalently discharge rate. An electrochemical model provides additional insights into the limiting processes occurring within the electrodes. In particular, the impact of tortuosity and molecular transport in the liquid phase within the

interstitial regions in the electrode are considered, and the influence of tortuosity will be shown to be highly sensitive to the current density. Qualitatively, the experimental results suggest the electrodes behave consistent with the packed hard sphere approximation of Bruggeman tortuosity scaling, which indicates the electrodes are largely mechanically intact but also that a design that incorporates tunable tortuosity could improve performance of these types of electrodes.

The content of this chapter has been published in the following journal:

Nie, Z.; Ong, S.; Hussey, D. S.; LaManna, J. M.; Jacobson, D. L.; Koenig, G. M. Probing Transport Limitations in Thick Sintered Battery Electrodes with Neutron Imaging. *Mol. Syst. Des. Eng.* **2020**, *5*, 245–256.

3.2 Introduction

Lithium-ion (Li-ion) batteries have received great interest due to their high energy and power density.[1] In researching improved Li-ion batteries, a common area of focus is new materials (e.g., active electrode material or electrolyte chemistry),[2-5] but another route is to increase the energy density through electrode or cell design, for example, by increasing the relative fraction of active electrode in the cell or minimizing inactive additives within the electrode.[6,7] Recently, towards the goal of improving battery energy density, researchers have designed electrodes comprised of only active materials.[8 - 10] Compared to conventional composite electrodes, the sintered electrodes consist of pure active material without conductive carbon additives and polymer binders. In addition, these electrodes can be made much thicker than composite electrodes. The combination of reducing the amount of inactive components in the electrode and making thicker electrodes results in high energy density and areal capacities at the electrode and cell levels.[8-10] When making electrodes comprised of only electroactive material, there is often a sintering step to improve mechanical robustness of the porous thin film; thus we refer to them to as “sintered electrodes”.

While sintered electrodes have very high energy density, the fraction of the electrochemical energy delivered at increasing rates of charge/discharge (or equivalently current densities) decreases quickly relative to many conventional composite electrodes, thus cells with sintered electrodes have low rate capability. This limitation results in the need to better understand the molecular processes limiting the electrochemical performance of the electrodes. Li-ion batteries have a number of different multiscale and multiphase processes which can limit the performance of the cell, including both solid phase, liquid phase, and interphase ion transport with relevant length scales ranging from few nanometers to hundreds of micrometers depending on the specific materials and cell designs employed.[11,12] Two major differences between conventional composite electrodes and sintered electrodes that would be expected to impact rate capability are the electrical conductivity and the Li^+ mass transport through the electrode microstructure. The electrical transport for composite electrodes is primarily facilitated by the carbon black/binder matrix within the interstitial regions between the active material particles, while for the sintered electrodes the electrical conductivity must be provided by the active material particles themselves and their connections. The electrical conductivity for the electrode matrix is orders of magnitude higher for the conventional composite electrode than it is for active materials used in sintered electrodes.[13,14] However, previous reports have suggested that the greater contributor to limitations of rate capability for porous electrodes is the mass transport of Li^+ through the electrode microstructure.[15] Sintered electrodes are much thicker (typically >500 μm) than composite electrodes (often <100 μm),[16,17] and thus the Li^+ must traverse much greater distances through the liquid phase of the tortuous electrode microstructure with sintered electrodes. Increased molecular transport paths result in increased cell polarization and can result in the cell quickly reaching a mass transport limiting current density.[16,17] To better understand the limitations of sintered electrodes and the mass transport through the electrode architecture, an *in situ* technique is needed that provides information on the Li^+ concentration within the cell as a function of time and at different rates/current densities. In this study, neutron imaging will be used to provide *in situ* information on Li^+ concentration in the direction of the molecular Li^+ flux throughout the battery thickness at different discharge rates to provide insights into the transport limitations of sintered electrodes.

Neutron imaging involves passing a low energy neutron beam through a sample and detecting the relative intensity of the beam that passes through the sample via a scintillation detector. Neutrons that do not pass through the sample are either scattered or absorbed, and the combination of these interactions of an element or isotope with the neutrons is the attenuation provided by that species. A highly attenuating isotope is ^6Li (^7Li is nearly transparent), and thus the intensity of individual pixels in a neutron radiograph are highly sensitive to the concentration of Li which the neutrons must pass through before reaching the detector.[18] During charge/discharge of a Li-ion battery, the only species which is expected to substantially change in concentration throughout the cell is Li^+, and the changes of Li^+ at a given depth within the electrode can change in excess of 10 mol L^{-1}.[19] The combination of the sensitivity of neutron imaging to Li concentration, Li being the only elemental or molecular species expected to change in concentration significantly within the cell during operation, and the large changes in Li concentration within the electrode make neutron imaging a promising nondestructive *in situ* tool to probe lithiation/delithiation as a function of electrode depth during electrochemical cycling, improving rational design of the electrode architecture and other battery cell components.[19-21] While neutron imaging has been used previously for conventional composite electrodes, the relatively large pixel size (in some cases >30 μm)[20] limits the number of depth locations that can be mapped for the Li^+ concentration gradient within the cell.[20,21] The relatively large thickness of sintered electrodes makes them ideal for probing the Li^+ concentration gradient throughout the thickness of the cell and subsequently correlating to electrode transport characteristics.

In a previous report,[19] we applied neutron imaging on battery coin cells where both the anode and cathode were thick sintered electrodes and explored how electrode thickness impacted the lithiation/delithiation processes within the cells. Different lithiation processes were observed in each electrode, with the relatively thinner cathode having a relatively uniform lithiation throughout the thickness during discharge and the relatively thicker anode having a front of delithiation that propagated from the separator side of the electrode to the current collector side of the electrode. However, in the previous work only a single and relatively slow rate of discharge was used. In this report, increasing rates of discharge will be investigated and their impact on the lithiation/delithiation processes within the electrodes in a sintered full cell. Electrochemical performance becomes limited at higher current densities, and thus greater insights into the limiting processes within the electrode were expected at higher current densities. Specifically, electrode design elements such as tortuosity in the cell which impacts the molecular mobility in the liquid phase and the possibility of mechanical fracture or cracking of the electrodes will be discussed to interpret combined calculation and experimental results with implication for future design improvements of the cells.

3.3 Materials and methods

3.3.1 Active material powder preparation

The cathode material used in this study was $LiCoO_2$ (LCO). The material was synthesized via $CoC_2O_4 \cdot 2H_2O$ precursor coprecipitation and subsequent calcination with Li_2CO_3 salt in a furnace exposed to an air environment.[10,22] To prepare the $CoC_2O_4 \cdot 2H_2O$ precursor, 1800 mL of 62.8 mM $Co(NO_3)_2 \cdot 6H_2O$ (Fisher Reagent Grade) and 1800 mL of 87.9 mol m^{-3} $(NH_4)_2C_2O_4 \cdot H_2O$ (Fisher Certified ACS) were prepared sepa rately and dissolved in deionized water. After heating to 50 °C, the solutions were mixed together all at once by pouring $Co(NO_3)_2 \cdot 6H_2O$ solution into the $(NH_4)_2C_2O_4 \cdot H_2O$ solution. A Teflon stir bar set at

83.9 rad s^{-1} (800 rpm) was used to maintain solution mixing, and the coprecipitation proceeded at 50 °C for 30 min. Then, the solid precipitate was collected using vacuum filtration and rinsed with 4 L deionized water. The powder was dried in an oven with an air atmosphere at 80 °C for 24 h.

To prepare the LCO active material, the oxalate precursor powder was mixed with Li_2CO_3 (Fisher Chemical) powder with an excess of lithium salt (Li:Co ratio of 1.02:1) by mortar and pestle. The powder mixture was heated to 800 °C at a ramp rate of 1 °C min^{-1} under an air atmosphere in a Carbolite CWF 1300 box furnace. The product was cooled to ambient temperature in the furnace without control over the cooling rate. The LCO material was ground using mortar and pestle. To further reduce the particle size, the LCO was milled in a Fritsch Pulverisette 7 planetary ball mill using 5 mm diameter zirconia beads at 31.4 rad s^{-1} (300 rpm) for 5 hours.

The anode material used in this study $Li_4Ti_5O_{12}$ (LTO) was purchased from a commercial supplier (NANOMYTE BE-10 from NEI Corporation) and used without any additional treatment. The characterization and electrochemical performance of both LCO and LTO material used in this study were reported previously. [10,22-24]

3.3.2 Electrode preparation and battery fabrication

Sintered electrodes which were composed of only active material were used in this study. The same procedure was used to make both cathode and anode pellets. First, active powder was mixed with 1% by weight polyvinyl butyral (Pfaltz& Bauer) dissolved in ethanol (Acros). 2 mL of solution was blended with 1 g of active material within a mortar and pestle and the solvent was allowed to evaporate in air. Next, 0.2 g of the powder and binder mixture was loaded into a 13 mm diameter Carver pellet die and then pressed with about 5443 kg (12,000 lb_f) for 2 minutes in a Carver hydraulic press. After that, the pellets were heated in a Carbolite CWF 1300 box furnace. The furnace heating was carried out in an air atmosphere with a ramping rate of 1 °C min^{-1} from 25 °C to 600 °C. After holding at 600 °C for 1 hour, the pellets were cooled to 25 °C at 1 °C min^{-1}.

The sintered electrodes were assembled into full cells within a CR2032 coin cell. LCO and LTO pellets were pasted onto the bottom plate and the stainless steel spacer of the cell, respectively. A carbon paste of 1:1 weight ratio Super P carbon black (Alfa Aesar) to polyvinylidene difluoride (PVDF, Alfa Aesar) binder dissolved in N-methyl pyrrolidone (NMP, Sigma-Aldrich) was used to attach the pellets to the metal components. Then, the pellets were dried at 80 °C in an oven in air for 12 hours. Next, the pellets were transferred into a glove box (Ar atmosphere, O_2 and H_2O both <1 μL L^{-1}). In the glove box, LTO and LCO electrodes were assembled into a coin cell. The anode and cathode were separated by a Celgard 2325 polymer separator (25 μm thick) and 16 drops of electrolyte (1.2 M $LiPF_6$ in 3:7 ethylene carbonate:ethyl methyl carbonate, BASF) were added into the cell. Other parts of the CR2032 coin cell used in this study include a stainless steel wave spring, a stainless steel top cap, and a Teflon gasket. The LCO pellet used in the study had a thickness of 0.468 mm and the thickness of LTO pellet was 0.691 mm. More information about the structure of the coin cell that contained the sintered electrodes can be found in a previous report.[19] Internal resistance for the coin cells containing sintered electrodes was determined from the high frequency intercept from an electrochemical impedance spectroscopy measurement (amplitude 10 mV).

The LTO/LCO coin cell was cycled galvanostatically at different C rates on a MACCOR battery cycler and Bio-Logic SP-50 potentiostat, with the latter used during the neutron imaging experiments. The C rate was based on the assumed capacity of 150 mAh g^{-1} for LCO mass in the coin cell, where 1C was assumed to correspond to 150 mA g^{-1} LCO. The cut off voltages were set to be 1.0 V-2.8 V (cell voltage, vs. LTO anode) for all cells and C rates evaluated. The cycling capacity data before neutron imaging tests for three cells nominally identical to the one used in this study can be found in Appendix 2, Fig. A2.1.

3.3.3 Neutron imaging

The neutron imaging experiment was carried out at the thermal Neutron Imaging Facility (NIF) beamline BT-2 at the National Institute for Standards and Technology (NIST) Center for Neutron Research.[25] The experimental setup with the coin cell in front of the detector is shown in Fig. 3.1a. The scintillator was Gd_2O_2S:Tb for converting the incident neutrons into visible light. The visible light was then captured with an Andor NEO scientific complementary metal-oxide semiconductor detector coupled with a 105 1:1 Nikon f2.8 lens and PK13 extension tube, which provided a pixel pitch of 6.5 μm. Radiographs were collected every minute from the initiation of the experiment. An example of a raw radiograph is shown in Fig. 3.1b. To reduce non-statistical noise, three radiographs were combined through a median operation. Images were also dark image corrected. The goal of this study was to track changes in Li^+ concentration throughout the thickness of the cell during electrochemical discharge. Therefore, pixel intensities in radiographs at all time points were normalized relative to the image taken before starting cycling (the "no current" image). The change in the pixel intensity relative to the "no current" image (ΔTransmission) will be depicted using a color scale in this manuscript (Fig. 3.1c). The movement of Li^+ results in most of the changes in neutron transmission observed in the radiographs, and thus the differences in transmission were attributed to the net movement of Li^+ in the cell. In the color scale images, blue regions correspond to lower transmission and higher Li^+ concentration than the beginning state of the experiment while red regions correspond to higher transmission and lower Li^+ concentration. The image in Fig. 3.1c was taken at the end of the C/20 discharge to highlight the contrast between anode and cathode regions. In Fig. 3.1c, the dark blue region represents LCO electrode which had higher Li^+ concentration (lower neutron transmission) at the end of discharge and the red region represents LTO electrode which had lower Li^+ concentration (higher neutron transmission).

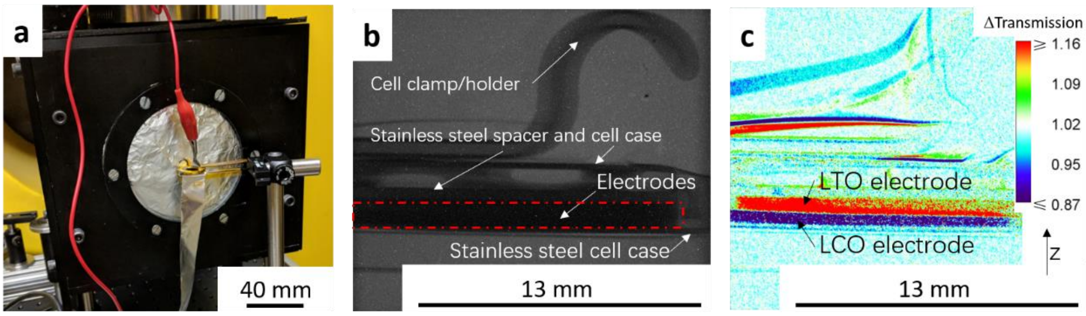

Fig. 3.1. (a) Photograph of experimental setup used for neutron imaging. (b) Example of a raw radiograph image of the coin cell region, (c) example of the change in transmission for a radiograph of the cell after normalizing relative to the "no current" image. A color scale was used to show the relative

change in neutron transmission. The black arrow depicts the z-direction the cell (thickness/depth dimension). Note that the brightest red regions have $\Delta T \geq 1.16$ and deepest blue regions have $\Delta T \leq 0.87$ and do not reflect the absolute maximum or minimum ΔT values and the same color scale was used for all neutron images displayed in this work.

To obtain quantitative information of the Li^+ movement, a 1000-pixel wide line scan was used across the electrode area from bottom to the top (z-direction in Fig. 3.1c). An example showing the line scan region in this study can be found in Appendix 2, Fig. A2.2. The LTO/LCO cell used in the neutron imaging was charged to 2.8 V at a rate of C/20 before travelling to NIST. At NIST, after the cell was set up for experiment (Fig. 3.1a), the cell was charged again at a rate of C/20 to 2.8 V to compensate for any capacity potentially lost during the shipment.

3.3.4 Model analysis

To aid in interpretation of the experimental results, an electrochemical mathematical model developed by Newman *et al.*[26] was used to calculate the discharge curves and Li^+ concentration in both the solid and electrolyte phases within the cell as a function of depth within the cell and time. These results were compared in relation with the experimentally measured discharge curve and change in neutron transmission in the neutron radiographs. Details of the model can be found in previous publications.[27-29]

3.4 Results and discussion

3.4.1 Neutron radiographs before and after discharge at different rates

After being charged to 2.8 V, the cell was cycled at different rates. The procedure and capacity for each charge/discharge step are listed in Table 3.1. The charge rates for each cycle were the same (C/20, corresponding to 1.46 mA and 1.10 mA cm^{-2}), while the discharge rate varied for each cycle. Since discharge processes were the focus of this study, D^i is used to represent the i^{th} discharge in the experiment. The discharge rate for D^1 was the same as the charge rate (C/20). The discharge rates for D^2, D^3 and D^4 were C/10 (corresponding to 2.92 mA and 2.20 mA cm^{-2}), C/5 (corresponding to 5.85 mA and 4.40 mA cm^{-2}) and C/2.5 (corresponding to 11.70 mA and 8.80 mA cm^{-2}), respectively. Between each cycle, there was a 10 min rest to allow the voltage to stabilize. Inspection of Table 3.1 reveals that each charge capacity after the first discharge (D^1) matched well with the capacity of the preceding discharge process, indicating that each discharge process initiated from a similar state of charge for the cell. The capacities in Table 3.1 were also consistent with experimental results for nominally equivalent sintered LTO/LCO coin cells not used in neutron imaging experiments (Fig. A2.1).

Table 3.1. Cycling rates and capacities for the LTO/LCO sintered coin cell during neutron imaging

Charge/Discharge	C Rate	Capacity (mAh g^{-1} LCO)
Charge	C/20	7.5[a]
Discharge (D^1)[b]	C/20	104.0
Charge	C/20	101.8
Discharge (D^2)[b]	C/10	92.5
Charge	C/20	92.1
Discharge (D^3)[b]	C/5	69.0
Charge	C/20	69.6
Discharge (D^4)[b]	C/2.5	34.0

[a] Capacity charged at NIST before the first discharge. The charge capacity before travel to NIST was 100.0 mAh g^{-1} LCO

[b] Label D^i is used to represent the i^{th} discharge in the test

The voltage profiles for the four discharges conducted during the neutron imaging experiment are displayed in Fig. 3.2a. Higher discharge rate resulted in lower final capacity and more significant polarization in the discharge profile. Although these outcomes are generally observed with Li-ion batteries, the capacity fade was relatively large for the sintered electrode cell. To gain further insights into how the Li^+ distributed within the cell at the different rates of discharge, the neutron images with changes in neutron intensity were analyzed for the 4 beginning of discharge points and 4 end of discharge points shown in Fig. 3.2a. These points are labeled as D^i_x, which indicates the neutron image at the x^{th} minute of the i^{th} discharge. The corresponding neutron imaging radiographs are displayed in Fig. 3.2b. The first important result in Fig. 3.2b is that all images taken at the beginning of discharge (the D^i_0 images) were very similar, suggesting that each discharge process started with a similar Li^+ distribution in both electrodes. However, neutron images at the end of discharge revealed redistribution of Li^+ in the electrode that was highly dependent on the rate. For all rates, the bottom electrode (LCO) had regions which were blue due to higher Li^+ concentration (and lower relative neutron transmission) after discharging and the top electrode (LTO) had regions which were red due to lower Li^+ concentration (and higher relative neutron transmission). This overall result was consistent with the expected flux of Li^+ from the anode to the cathode during discharge. In addition, with the color scale, the darker the blue the higher Li^+ concentration in LCO electrode and the brighter the red the lower the Li^+ concentration for LTO electrode. Comparing the end state of different discharge process, D_{832}^{1} showed the darkest blue and the brightest red in cathode and anode area, respectively. This implies that greater amounts of Li^+ were transferred from LTO to LCO while discharging at a rate of C/20, consistent with D^1 having the highest discharge capacity (Table 3.1). With increasing rates of discharge, the blue regions are both not as dark and do not go as deep into the cathode and the red regions are not as bright and also do not go as deep into the anode, consistent with the lower capacities and lower amounts of net Li^+ exchanged at increasing rates (Table 3.1). Qualitatively, The C/20 discharge (D_{832}^{1}) and C/10 discharge (D_{371}^{2}) appear to have lithiation/delithiation of the entire electrode regions but the capacity difference primarily appeared to result in changes in color intensity, or equivalently differences in extents of lithiation, within the electrodes. However, at the highest rates of C/5 (D_{138}^{3}) and C/2.5 (D_{34}^{4}), the lithiation/delithiation becomes more localized to near the separator region as a function of increasing rate/current density. This outcome indicated much lower utilization of the electrode thickness at increasing rate and the Li^+ redistribution being highly localized to near the separator region within the cell. This observation suggested limitations in the availability and transport of Li$^+$ in the cell, which will be discussed in detail in Section 3.4.3.

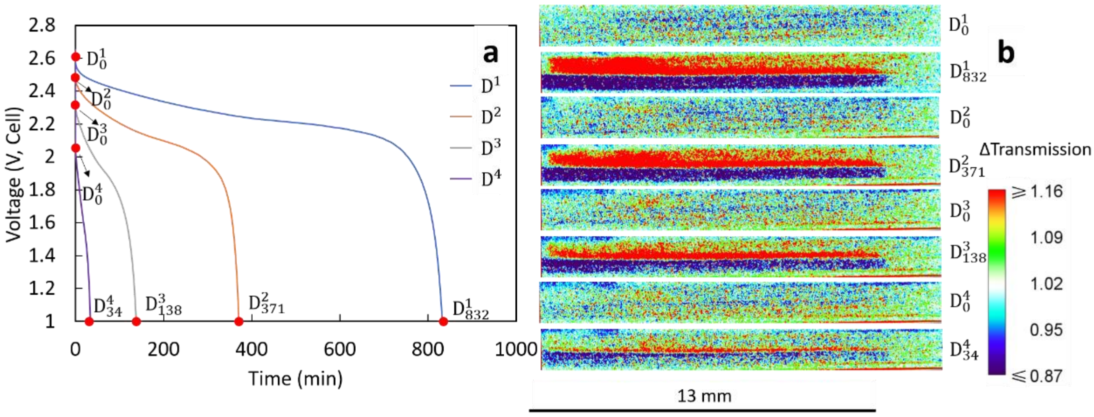

Fig. 3.2. (a) Discharge profiles at C/20 (blue), C/10 (orange), C/5 (grey), and C/2.5 (purple). The points labeled D_x^i represent the xth minute in the ith discharge process. (b) The neutron imaging radiographs corresponding to the points noted in (a).

3.4.2 Numerical calculation of discharge profiles with different Bruggeman exponent

To gain insight into the discharge process at different rates, a 1-D porous electrode model was used to calculate the discharge curves and Li$^+$ compositional profile in the sintered electrode full cell. The model was developed by Newman *et al.* and has been adopted in a number of previous reports.[27-31] The parameters used in this study are listed in Table 3.2. These values were either from experimental measurement, reported in literature, [3,13,22,23, 32 - 38] provided by the commercial material supplier or assumed using approximations previously developed for the model, as indicated in the table.

Table 3.2. Battery parameters used in discharge calculations.

Parameters	Value	Source
Thickness of negative electrode/LTO (m)	6.91×10^{-4}	Measured
Thickness of separator (m)	2.5×10^{-5}	Manufacturer
Thickness of positive electrode/LCO (m)	4.68×10^{-4}	Measured
Bulk $LiPF_6$ concentration (mol m^{-3})	1200	Manufacturer
Initial stoichiometric parameter, y for anode (y in $Li_{(4/3+y)}Ti_{(5/3)}O_4$)	0.64	Estimate from experimental capacities
Initial stoichiometric parameter, x for cathode (x in Li_xCoO_2)	0.57	Estimate from experimental capacities
Solid-state Li^+ diffusion coef. in anode (m^2 s^{-1})	1×10^{-12}	Experimental data and Ref. Zaghib *et al.*[32]
Solid-state Li^+ diffusion coef. in cathode (m^2 s^{-1})	5×10^{-19}	Ref. Geng *et al.*[33]
Radius of anode active particles (m)	1.0×10^{-7}	Ref. Qi *et al.*[23]
Radius of cathode active particles (m)	1.5×10^{-7}	Ref. Qi *et al.*[22]
Volume fraction of electrolyte in negative electrode	0.42	Based on measured porosity using pellet dimensions and material density
Volume fraction of electrolyte in separator	0.39	Manufacturer
Volume fraction of electrolyte in positive electrode	0.38	Based on measured porosity using pellet dimensions and material density
Conductivity of negative matrix (S m^{-1})	2	Ref. Young *et al.*[34]
Conductivity of positive matrix (S m^{-1})	0.3	Ref. Ménétrier *et al.*[13]
Coulombic gravimetric capacity of negative material (mAh g^{-1})	175	Ref. Nitta *et al.*[3]
Coulombic gravimetric capacity of positive material (mAh g^{-1})	274	Ref. Nitta *et al.*[3]
Density of negative insertion material (kg m^{-3})	3485	Theoretical crystal density, Ref. Kataoka *et al.*[35]
Density of positive insertion material (kg m^{-3})	5010	Theoretical crystal density, Ref. Takahashi *et al.*[36]
Rate constant for negative reaction	8.7×10^{-6}	Calculated based on Ref. He *et al.*[37]
Rate constant for positive reaction	4.3×10^{-7}	Ref. Zhang *et al.*[38]
Internal resistance ($\Omega\cdot m^2$)	5.8×10^{-3}	Experimental data

In this study, tortuosity (τ) was investigated in greater detail to better understand the contributions of molecular transport in the liquid phase through the interconnected electrode pores on the sintered electrode battery performance. For the calculations using the electrochemical model, the tortuosity was accounted for using a Bruggeman exponent (α), where by using the measured porosity of the electrode, ε, the tortuosity of the electrode was determined by $\tau=\varepsilon^{1-\alpha}$.[39] Typically, the value assumed for α in porous electrode calculations is 1.5, a value which would be consistent with close packing of uniform hard spheres.[39] Though the particles used in the sintered electrodes were not monodisperse, experimentally it was determined that $\alpha \approx 1.5$ was a reasonable approximation for the sintered electrodes. The experimental determination of the tortuosity of the sintered electrodes was done by measuring the effective ionic conductivity in symmetric Li/Li coin cells.[27,39] Details of the tortuosity measurements can be found in the Appendix 2 and include Fig. A2.3 and A2.4 and Table A2.1, and the method was adapted from ref. 39. Also included in this section are further details on electrolyte properties used in calculations.[26,40,41]

It is noted that for the tortuosity measurements performed that an assumption was that the LTO electronic conductivity could be neglected. While pristine LTO has been reported to have electronic conductivity of ~10^{-5} mS cm^{-1} which could safely be neglected for the tortuosity determination,[34] the lithiation profiles and polarization during discharge (presented later in the manuscript) suggested that the electronic conductivity of LTO was likely much greater. The contributions from the electronic conductivity of the LTO would result in the measured resistance in the experiments being lower than that provided by just the ion transport through the electrode microstructure, which means that the measured values of tortuosity described below should be considered as lower bounds for the actual tortuosity and Bruggeman exponent for the electrodes.

While assembling the pellets into a coin cell, some cracking may occur during the crimping process. These cracks would create vertical channels though the electrode. Assuming the channels were perfectly aligned, within the channel region the tortuosity would be 1, corresponding to the Bruggeman exponent α being 1.0. Taking the whole pellet into consideration, the cracks would result in a tortuosity between the packed hard sphere Bruggeman tortuosity ($\alpha=1.5$) and no tortuosity ($\alpha=1$). Therefore, in this work, the behavior of both $\alpha=1.5$ and $\alpha=1$ were calculated and compared with the experimental results. Note that for the $\alpha=1.5$ case that $\tau=1.62$ for the LCO electrode and $\tau=1.54$ for the LTO electrode, which was relatively low compared to values of >3 reported for composite electrodes.[42] Note that the composite electrodes have higher tortuosity due to additional restrictions to ion transport by the binder and carbon black additives in the interstitial regions between active material particles. Consideration of these two extremes of α also was expected to provide insights to the potential value of designing cells with template structures to improve tortuosity and/or improved molecular transport through the electrode pores. Note that the α values were applied to both electrodes in the calculations. The value of α used for the separator in calculations was 2.2 (and thus a τ of 3.10), which was determined experimentally from tortuosity measurements using a symmetric cell with only separators.

Fig. 3.3. contains the experimental discharge profiles for the coin cell at the four different rates and the calculated discharge profiles using Bruggeman exponent values of α=1.0 and α=1.5. As can be seen in Fig. 3.3a and 3.3b, at low discharge rate (C/20 (D^1) and C/10 (D^2)), the calculated profiles for the two different tortuosity exponents were almost the same, suggesting that limitations to Li^+ transport through the electrode were not significantly impacted by the tortuosity of the microstructure. The experimental agreement with the calculated profiles was also very good at the two lowest discharge rates, although the C/10 discharge ended slightly before the calculated profiles. For D^1 (Fig. 3.3a) the capacity for both calculated discharge profiles were 105 mAh g^{-1} LCO, which was a <1% difference compared to the experimental value (104 mAh g^{-1} LCO, Table 3.1). In Fig. 3.3b, the calculated capacities were 99 mAh g^{-1} LCO, which was a ~7% difference from the experimental value (92.5 mAh g^{-1} LCO, Table 3.1). At the two higher rates of discharge, the two calculated profiles had significant differences in final discharge capacity and time. In Fig. 3.3c, the calculated capacity for D^3 with α=1.0 was 86 mAh g^{-1} LCO while the calculated capacity for α=1.5 was 72 mAh g^{-1} LCO. Compared with the experimental result which had a capacity of 69 mAh g^{-1} LCO, the result of α=1.5 showed better agreement, although all profiles had similar polarization at early times of the discharge. For D^4 in Fig. 3.3d, the calculated final capacities for α=1.0 and α=1.5 were significantly different, with values of 39 mAh g^{-1} LCO and 24 mAh g^{-1} LCO, respectively. The experimental capacity was 34 mAh g^{-1} LCO, which was between the two calculated values. The increasing differences in total delivered capacity for the two values of α reflects the increasing limitations to Li^+ transport through the electrode microstructure dictating the

performance of the battery, consistent with previous studies of the impacts of tortuosity on Li-ion battery capacity at high discharge rates.[43] There were only slight difference in the two extremes of tortuosity at the lower rates of D^1 and D^2 because the necessary flux of Li^+ to maintain those rates was low enough that the differences in tortuosity did not impact the Li^+ transport significantly. At higher rates, the impact of tortuosity started to limit Li^+ transport at the higher flux necessary to accommodate the increased current density and resulted in significant differences in the calculated total capacity that could be delivered. At C/5 (D^3), compared to the no tortuosity condition, the pellet with α=1.5 lost 16 % capacity (14 mAh g^{-1} LCO), while at C/2.5 nearly 40 % capacity (16 mAh g^{-1} LCO) was lost.

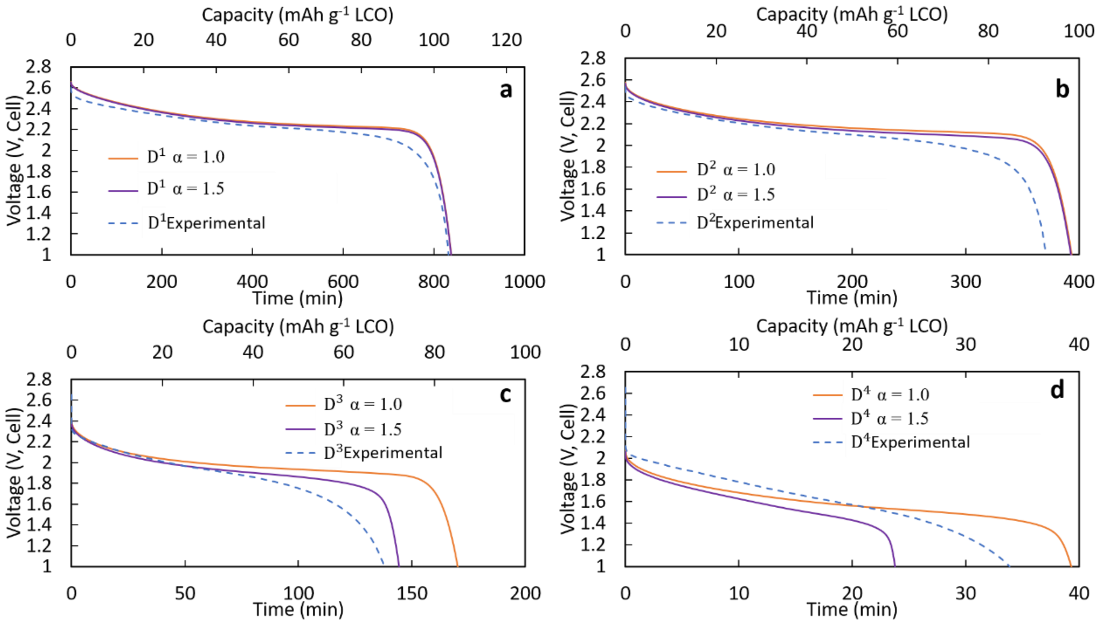

Fig. 3.3. Discharge profiles experimentally measured (blue dashed) and calculated using a Bruggeman exponent of 1.0 (orange) or 1.5 (purple) for discharge (a) D^1 at C/20, (b) D^2 at C/10, (c) D^3 at C/5, and (d) D^4 at C/2.5.

3.4.3 Comparison of experimental and calculated Li^+ composition profiles

To gain further insights into the Li^+ transport behavior and lithiation/delithiation processes within the cell, calculated Li^+ concentration profiles within the cell, based on the model, were compared to the neutron images collected during discharge. Note that both the liquid and solid phase Li^+ concentrations were calculated, but that in most cases when Li^+ concentration is discussed that it is the volume weighted sum of these two concentrations (or the net change of this concentration) because the neutrons will be attenuated by all the Li^+ in the region they pass through. For this analysis, 5 time points were analyzed: the beginning of discharge, the end of discharge, and 25 %, 50 %, and 75 % of the discharge time. Due to the different total discharge times, the specific time points were at different values for each rate. The selected time points on the discharge profile and the corresponding neutron images can be found in Appendix 2, Fig. A2.5-A2.8. To obtain a more quantitative comparison between the neutron images and calculated Li^+ concentration profiles, a 1000-pixel line scan was applied for each image analyzed. The direction of the scan is from bottom to top (z-direction as noted in Fig.3.1). The scan was done from a position slightly below the LCO electrode to a position slightly above the LTO electrode to ensure all electrode regions were included (example of the scan region can be found in Appendix 2, Fig. A2.2). All neutron radiographs were originally normalized by the no current image; thus, the line scan results were change in transmission relative to initiation of the experiment (these profiles for all discharge rates can be found in the Appendix 2, Fig. A2.9a, A2.10a, A2.11a, A2.12a). As the focus of the work is to observe the net Li^+ movement for each discharge process, all the transmission profiles were normalized again by subtracting the transmission profiles at the initiation of each cycle. The resulting profiles were ΔTransmission relative to initiation of each discharge process and thus every D_0^x profile (x=1,2,3,4) became a horizontal line with a value of 0 (these profiles can be found in Appendix 2, Fig. A2.9b, A2.10b, A2.11b, A2.12b). In addition, to facilitate more direct comparison with the calculated Li^+ concentration profiles, the electrode region in the neutron images was defined (this region is labeled in Fig. A2.9b, A2.10b, A2.11b, A2.12b in the Appendix 2). Details and discussion about selection of electrode region can be found in Appendix 2, including Fig. A2.13. The total depth of the selected region was 1.248 mm, which was 5 % greater than the 1.184 mm total measured thickness of the combined electrodes and separator. The cause of this difference was likely due to image magnification and a slight misalignment of the sample relative to the neutron beam. The final resulting profiles of ΔTransmission relative to the beginning of discharge and with the normalized electrode depth for the 4 different rates of discharge can be found in Fig. 3.4a and Fig. 3.5a (for D^1 and D^3) and in the Appendix 2, Fig. A2.14a and Fig. A2.15a (for D^2 and D^4).

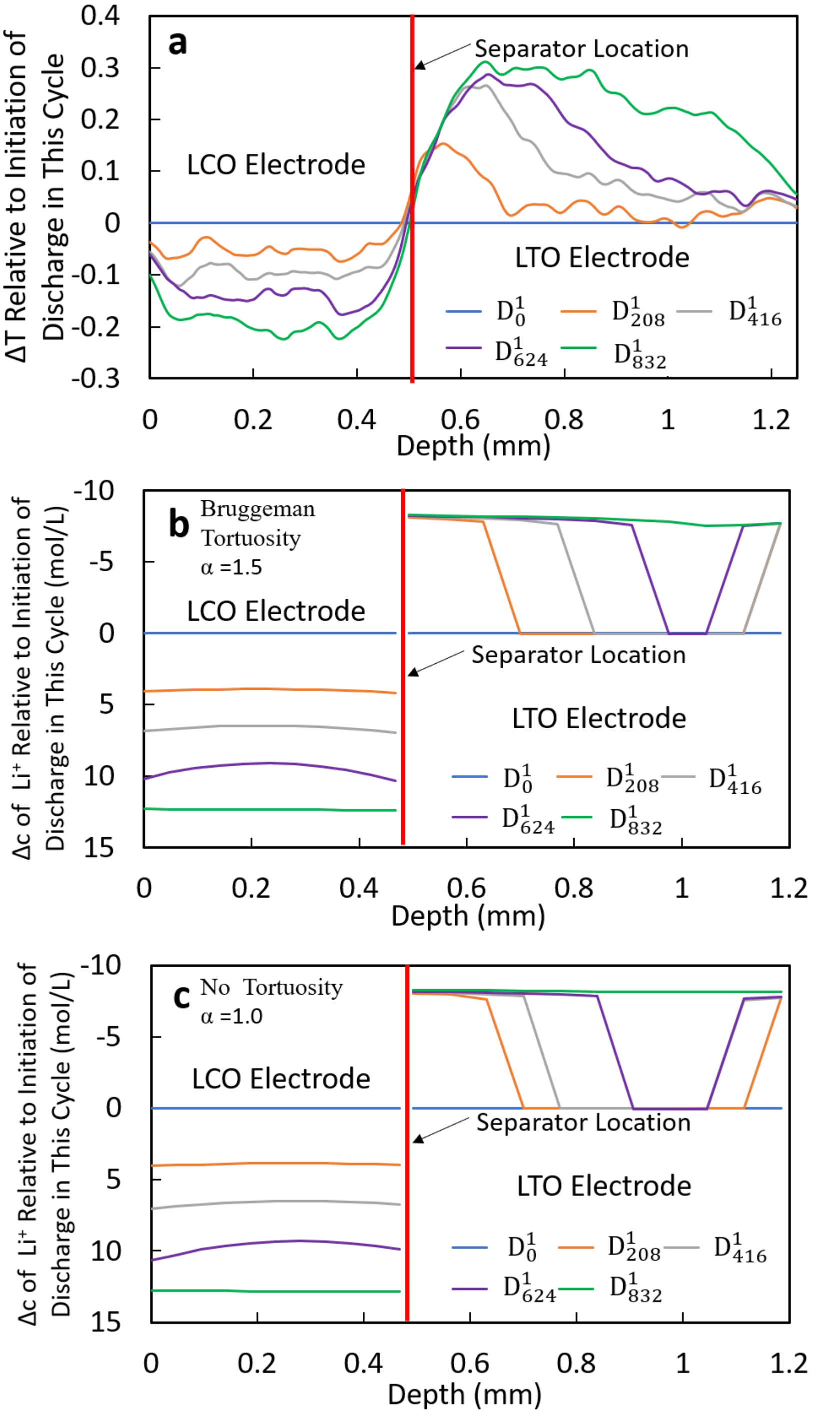

Fig. 3.4. Experimental and calculated results of D^1 discharge process. (a) ΔTransmission at different time relative to initiation of discharge in this cycle from neutron radiographs. (b) Calculated change in Li^+ concentration at different times relative to initiation of discharge in this cycle for α=1.5. (c) Calculated change in Li^+ concentration at different times relative to initiation of discharge in this cycle for α=1.0.

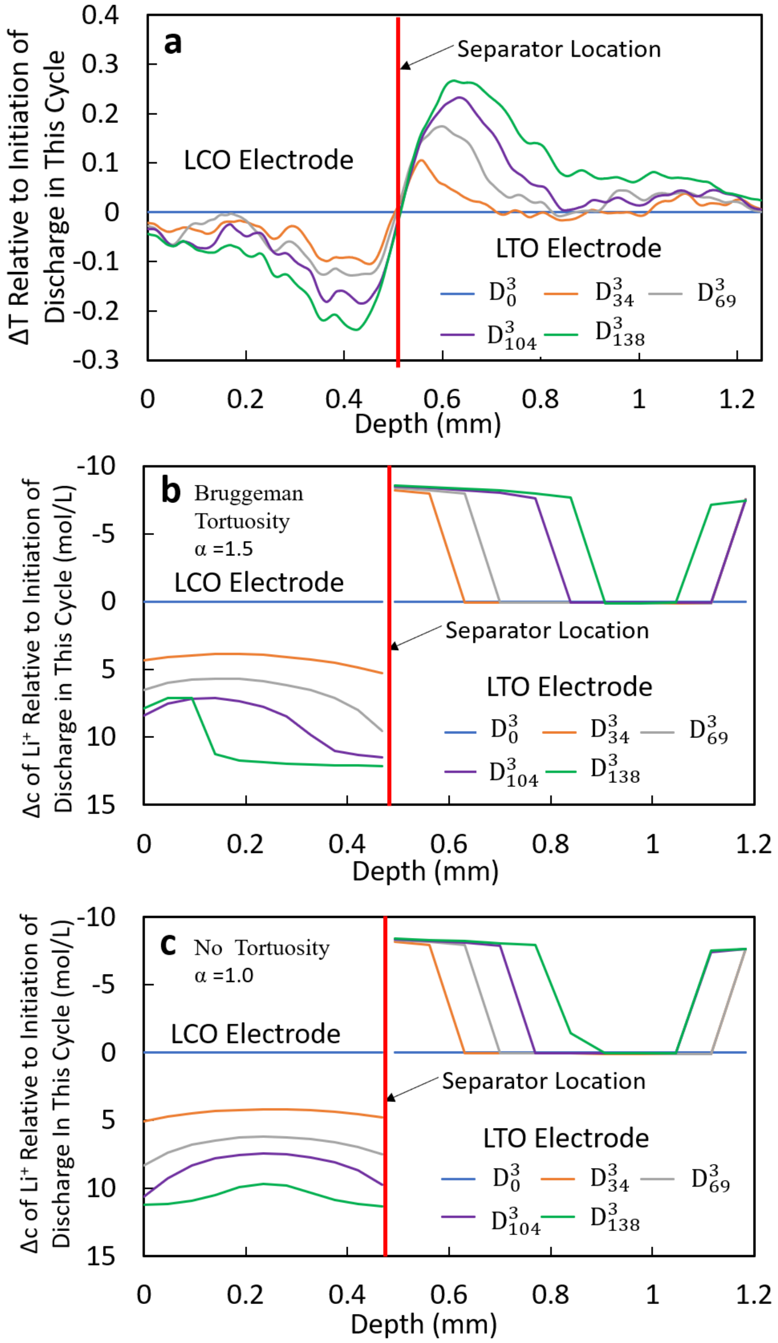

Fig. 3.5. Experimental and calculated results of D3 discharge process. (a) ΔTransmission at different time relative to initiation of discharge in this cycle from neutron radiographs. (b) Calculated change in Li+ concentration at different times relative to initiation of discharge in this cycle for α=1.5. (c) Calculated change in Li+ concentration at different times relative to initiation of discharge in this cycle for α=1.0.

The calculated Li^+ concentration profiles of the same time points chosen for each discharge process were also extracted. The concentration profiles included the sum of the Li^+ concentration in both the electrolyte and solid phases and accounted for their relative volume fraction in the electrode. The changes in Li^+ concentration were dominated by changes due to lithiation/delithiation of the solid phase. To maintain charge neutrality the PF_6^- anion would also be expected to have a corresponding gradient that matched the Li^+ liquid phase gradient, however, for discussion of consequences to neutron transmission the PF_6^- was not taken into account. Due to the relatively low attenuation of P and F compared to Li, as well as the primary influence to neutron attenuation being changes in solid phase composition, neglecting the PF_6^- gradient was not expected to impact interpretation of results. The detailed individual Li^+ concentration profiles for the individual solid and electrolyte phases using both $\alpha=1.0$ and $\alpha=1.5$ for the Bruggeman exponent can be found in Appendix 2, Fig. A2.16-A2.23. For comparison with the ΔTransmission profiles from neutron imaging experiments, the concentration profiles were also normalized by subtracting the initial concentration profile for each discharge process (D_0^x profiles (x=1,2,3,4)). In neutron imaging experiments, lower transmission corresponded to higher Li^+ concentration. Thus, for calculated results, the y-axis of concentration was reversed for easier comparison (e.g., increasing concentration is down instead of up on the y-axis). The final results of concentration profiles for each discharge process with different tortuosity are displayed in Fig. 3.4b, 3.4c, 3.5b, 3.5c, and in the Appendix 2 in Fig. A2.14b, A2.14c, A2.15b, A2.15c.

The ΔTransmission (ΔT) and Δconcentration (Δc) profiles for D^1 and D^2 processes were similar, thus only D^1 will be discussed in detail (Fig. 3.4). The corresponding information for D^2 can be found in Appendix 2, Fig. A2.14. From the transmission profiles, it can be clearly seen that the lithiation of LCO was uniform during the discharge process, i.e. the extent of lithiation increased gradually for all LCO material throughout the thickness of the electrode. The less negative ΔT towards the edges of the electrode near the separator and current collector/stainless steel was interpreted as being due to those regions having contributions from both the LCO material and stainless steel (near the current collector electrode edge) or separator/LTO (near the separator electrode edge). In contrast, the LTO electrode did not have as uniform of a delithiation throughout the anode thickness. At 208 min (D^1_{208}), it can be clearly observed that the delithiation first occurred at the position near the separator, and there was a region within the LTO where there was a sharp transition from completely delithiated to almost completely lithiated – although not obvious in the figure there was slight delithiation in all regions of the electrode. Then, the location of this delithiation front propagated towards the LTO current collector as the discharge proceeded. At the end of discharge, a nearly uniform distribution of Li^+ was achieved. This qualitative behavior was consistent for both the neutron imaging and calculation results using both Bruggeman exponents. The similarity between the two calculations (Fig. 3.4b, 3.4c) suggested that at low rates (C/20 and C/10 for this cell) tortuosity would not be expected to influence the Li^+ distribution, at least within the range of 1.0-1.5 considered. One noticeable difference between both calculated results and the neutron ΔT profile was that in the calculations there was a second delithiation front which initiated from the current collector and there was no evidence for this second front in the ΔT profile. There does appear to be some delithiation that occurs near the current collector even as early as at D^1_{208}, however, there was not a delithiation front that proceeded towards the separator. It was suspected that the difference between calculation and experiment with regards to the second delithiation front may have been due to assumption of a single value for the electronic conductivity for the matrix conductivity of the electrode, although LTO and LCO both have electronic conductivity which is dependent on the extent of lithiation.[13,34] It is expected that this simplification of the electronic conductivity of using a single value for each electrode as opposed to a lithiation-dependent value was also a major contributor to differences in the experimental and calculated discharge potentials as a function of time (Fig. 3.3). The electrodes will have differences in extent of lithiation not just as a function of time/discharge extent but also as a function of depth within the electrode, thus the electronic conductivity varies with both time and electrode depth. The calculated potential during discharge and the presence and propagation of the second delithiation front is highly sensitive to the electronic conductivity, and a future research direction will include incorporating an electronic conductivity in calculations which is a function of state of lithiation and measuring this conductivity for the materials used in the cells.

At higher rates, both the experimental and the calculated results showed a different lithiation/delithiation trend. The ΔT and Δc profiles for D^3 and D^4 processes can be found in Fig. 3.5 and Fig. A2.15, respectively. Both discharge rates resulted in significant limitations in the extent and propagation of lithiation/delithiation in the electrodes, and only one of these (D^3)

will be discussed in greater detail here. Inspection of the ΔT profiles for the LCO electrode during D^3 (Fig. 3.5a) revealed the lithiated region was primarily between 0.3 mm and 0.5 mm while the delithiated region for LTO was primarily between 0.5 mm and 0.9 mm. Beyond these regions, relatively low lithiation/delithiation was observed for both electrodes. However, in the lithiated region of LCO, the profiles still followed the same trend as observed for lower discharge rate (D^1 process in Fig. 3.4a), where the lithiation distribution as a function of depth in the electrode was relatively uniform within the region of the electrode undergoing lithiation. For LTO, the delithiation front was still observed, but in contrast to the lower discharge rate the delithiation did not propagate as deep into the electrode and the peak in ΔT grew larger during discharge, indicating the regions closer to the separator were more gradually lithiated during discharge relative to lower discharge rates. At higher rates of discharge (D^3 at C/5 and D^4 at C/2.5), the calculated concentration profiles for α=1.0 and α=1.5 had significant differences (Fig. 3.5b, 3.5c, A2.15b, A2.15c). In the LTO region in Fig. 3.5b and 3.5c, the concentration profiles were qualitatively similar and in both cases a delithiation front can be observed. The difference was the extent and depth of delithiation, which would be expected because the calculated capacity was different for these two cases as shown in Fig. 3.3c. In the LCO region for α=1.5 a relatively uniform distribution of Li^+ could still be observed at 34 minutes, but a gradient of lithiation started to build up in the electrode. At later times the gradient of Li^+ concentration within the LCO was clearly observed with higher Li^+ concentration in the regions near the separator and lower concentration in regions near the current collector. Inspection of the last two time points (D_{104}^{3} and D_{138}^{3}) revealed the Li^+

concentration still went up near the separator while there was no further lithiation near the current collector. This outcome was consistent with the higher discharge rate resulting in a higher concentration gradient in electrolyte phase in which there was much greater Li^+ in electrolyte within the LTO electrode and less Li^+ in LCO electrolyte regions (Fig. A2.20a). Near the end of discharge, Li^+ was driven to zero in LCO regions near the current collector, and this lack of Li^+ transport to the regions of the cathode still with lithium capacity resulted in the end of the discharge process. For α=1.0, the distribution of Li^+ showed a different pattern. The overall trend for LCO was similar to the calculated results for lower discharge rates where lithiation occurred across all depths of the LCO electrode, although at 69 min (D_{69}^{3}), 104 min (D_{104}^{3}) and 138 min (D_{138}^{3}) the Li^+ concentration was higher at both the regions near separator and near current collector with the middle region having a slightly lower concentration. The more uniform LCO electrode lithiation was due to the lack of tortuosity in the calculation, resulting in a smaller Li^+ concentration gradient in the electrolyte. There was not a large limitation of Li^+ availability in the electrolyte phase even at the highest discharge rate (Fig. A2.21a). The electrode then was lithiated both on the current collector and separator ends, due to favorable electronic polarization near the current collector and ionic polarization near the separator.[19,44]

Comparing the experimental and calculated results, the tortuosity condition with α=1.5 (Bruggeman hard sphere packing) had better agreement with the transmission profiles, particularly with regards to both demonstrating a confined lithiation/delithiation in both electrodes at high rates of discharge. The lithiation/delithiation profiles and discharge polarization curves (Fig. 3.3c) suggest the transport in the liquid phase through the pore volume in the sintered electrodes was consistent with a thin film of close packed spheres, and that any cracks that may have formed during cell processing did not significantly impact the average transport experienced by liquid molecular species within the cell. Comparisons to calculations with the no tortuosity scaling (α=1.0) revealed that at low rates of discharge the tortuosity did not significantly impact electrochemical performance or the ability of Li^+ to redistribute within the cell. At high rates, however, lithiation/delithiation profiles were qualitatively different, with no tortuosity enabling more uniform lithiation of the LCO, greater penetration of the Li^+ front into the LTO electrode towards the current collector, and enabling the liquid phase Li^+ concentration to not drop to values which resulted in the discharge process stopping earlier in the cell. This outcome suggests that improvements to tortuosity could result in gains in electrochemical performance with thick electrodes at high current densities.

It is noted that at the highest rate of discharge investigated in this study (Fig. 3.3d), that for the best case with regards to tortuosity ($\alpha = 1.0$) that only ~40% of the available discharge capacity could be accessed. The limitation with regards to extracting that additional ~60% of the capacity still remaining in the cell was still attributed to limited ionic transport in the electrolyte phase. This result suggested that modifying tortuosity can play a role in improving the electrochemical performance of thick electrodes (extracting up to ~40% compared to ~23% for the simulation example in Fig. 3.3d), but that there are limits where the intrinsic transport properties of the electrolyte itself must be modified to further increase the electrode capacity.

The tortuosity in the electrodes represented a combination of many processes occurring which limited the transport of molecules in the liquid phase relative to their transport in the bulk electrolyte. Several strategies may be employed to reduce the tortuosity and/or the transport limitations of Li^+ in the electrolyte phase to improve the electrochemical performance of the cells. First, it is important to note that the use of sintered electrodes without inactive materials already improved the transport relative to composite electrodes. While for the electrodes in this study the tortuosity scaling was consistent with α=1.5, in studies with conventional composite electrodes reported values have ranged from 1.9 to 3.2.[45] This increased tortuosity was due to the pore volume not just being filled with electrolyte, but also with carbon and polymeric binders which further restrict the transport of molecules through the liquid phase which fills the pores. Second, reductions in tortuosity could be achieved by controlling the electrodes architecture to direct the pore alignment in the direction of Li^+ flux. A few strategies have been reported in the literature, including using magnetic fields to align the pores and/or the particles themselves.[46,47] Third, molecular approaches could be developed to modify the interactions between the liquid phase within the pores and the solid active material. Many of the pores would have regions of high confinement, which may provide an opportunity for modifying the particle interface or the solvent molecules to design the solvent-solid interactions to facilitate enhanced transport. Finally, increasing the Li^+ concentration and/or the conductivity of the electrolyte itself will improve overcoming the transport limitations without modifying the tortuosity. Changes to the electrolyte are not trivial due to the many metastable interfaces in within Li-ion batteries, however, such improvements would improve the prospects for utilizing more of the capacity of thick battery electrodes at high rates of charge/discharge.

3.5 Conclusions

In this manuscript, neutron imaging was used to probe the Li^+ transport in LTO/LCO battery full cells with sintered electrodes at different discharge rates. More Li^+ was transferred from LTO to LCO at lower rates, resulting in higher discharge capacity. At higher rates, neutron imaging provided confirmation that the lithiation/delithiation only occurred in the region near the separator, limiting the delivered discharge capacity. This outcome was consistent with the discharge process being limited by the transport of Li^+ through the porous electrode architecture. A numerical model was also used to calculate the discharge profiles and Li^+ concentration profile during the different discharge conditions. Tortuosity scaling considering either hard sphere packing or the absence of tortuosity was used for the calculations. The calculations indicated that within the limits considered the tortuosity had only a slight impact on discharge performance and expected Li^+ compositional profiles within the cell at lower discharge rates. However, at higher discharge rate, the discharge capacities and Li^+ compositional profiles were significantly different depending on the tortuosity scaling used. Compared with the experimental results, all calculations had good agreement at low discharge rate regardless of the tortuosity scaling. However, at higher discharge rate, the tortuosity scaling for hard spheres had much closer agreement with the experimental results, indicating that assuming the pellets as packed hard spheres was an appropriate assumption for electrolyte transport processes even though the particles were polydisperse and there were likely some cracks within the electrode pellets. The calculations also revealed that at higher discharge rate the limited region for lithiation/delithiation and subsequently much lower delivered electrochemical capacity was due to the limited access of Li^+ from the electrolyte phase. These results thus provide insights into the significant quantitative impact that could result from improving transport within the porous electrode architecture. For example, molecular designs to improve the performance of these electrodes could be achieved through either templating the electrode pores to decrease tortuosity or by modifying the electrolyte properties to increase the conductivity of Li^+ in the liquid phase within these cells.

3.6 Acknowledgements

Research funding support provided by the National Science Foundation grant CMMI-1825216. We acknowledge the use of the neutron research facilities of the National Institute of Standards and Technology in providing the neutron imaging used in this work. NIST authors acknowledge the efforts of Mr. Elias Baltic in the conduct of the measurements and support from the U.S. Department of Commerce, the NIST Radiation Physics Division, the Director's office of NIST, and the NIST Center for Neutron Research.

3.7 References

(1) Etacheri, V.; Marom, R.; Elazari, R.; Salitra, G.; Aurbach, D. Challenges in the Development of Advanced Li-Ion Batteries: A Review. *Energy Environ. Sci.* **2011**, *4*, 3243.

(2) Goodenough, J. B.; Park, K.-S. The Li-Ion Rechargeable Battery: A Perspective. *J. Am. Chem. Soc.* **2013**, *135*, 1167–1176.

(3) Nitta, N.; Wu, F.; Lee, J. T.; Yushin, G. Li-Ion Battery Materials: Present and Future. *Mater. Today* **2015**, *18*, 252–264.

(4) Pan, H.; Zhang, S.; Chen, J.; Gao, M.; Liu, Y.; Zhu, T.; Jiang, Y. Li- and Mn-Rich Layered Oxide Cathode Materials for Lithium-Ion Batteries: A Review from Fundamentals to Research Progress and Applications. *Mol. Syst. Des. Eng.* **2018**, *3*, 748–803.

(5) Weng, W.; Lin, J.; Du, Y.; Ge, X.; Zhou, X.; Bao, J. Template-Free Synthesis of Metal Oxide Hollow Micro-/Nanospheres via Ostwald Ripening for Lithium-Ion Batteries. *J. Mater. Chem. A Mater. Energy Sustain.* **2018**, *6*, 10168–10175.

(6) Zheng, H.; Li, J.; Song, X.; Liu, G.; Battaglia, V. S. A Comprehensive Understanding of Electrode Thickness Effects on the Electrochemical Performances of Li-Ion Battery Cathodes. *Electrochim. Acta* **2012**, *71*, 258–265.

(7) Chen, Z.; Dahn, J. R. Reducing Carbon in $LiFePO_4$/C Composite Electrodes to Maximize Specific Energy, Volumetric Energy, and Tap Density. *J. Electrochem. Soc.* **2002**, *149*, A1184.

(8) Bae, C.-J.; Erdonmez, C. K.; Halloran, J. W.; Chiang, Y.-M. Design of Battery Electrodes with Dual-Scale Porosity to Minimize Tortuosity and Maximize Performance. *Adv. Mater.* **2013**, *25*, 1254–1258.

(9) Lu, L.-L.; Lu, Y.-Y.; Xiao, Z.-J.; Zhang, T.-W.; Zhou, F.; Ma, T.; Ni, Y.; Yao, H.-B.; Yu, S.-H.; Cui, Y. Wood-Inspired High-Performance Ultrathick Bulk Battery Electrodes. *Adv. Mater.* **2018**, *30*, e1706745.

(10) Robinson, J. P.; Ruppert, J. J.; Dong, H.; Koenig, G. M., Jr. Sintered Electrode Full Cells for High Energy Density Lithium-Ion Batteries. *J. Appl. Electrochem.* **2018**, *48*, 1297–1304.

(11) Sheu, S. P.; Yao, C. Y.; Chen, J. M.; Chiou, Y. C. Influence of the $LiCoO_2$ Particle Size on the Performance of Lithium-Ion Batteries. *J. Power Sources* **1997**, *68*, 533–535.

(12) Pikul, J. H.; Gang Zhang, H.; Cho, J.; Braun, P. V.; King, W. P. High-Power Lithium Ion Microbatteries from Interdigitated Three-Dimensional Bicontinuous Nanoporous Electrodes. *Nat. Commun.* **2013**, *4*, 1732.

(13) Ménétrier, M.; Saadoune, I.; Levasseur, S.; Delmas, C. The Insulator-Metal Transition upon Lithium Deintercalation from $LiCoO_2$: Electronic Properties and ^{7}Li NMR Study. *J. Mater. Chem.* **1999**, *9*, 1135–1140.

(14) Ji, H.; Zhang, L.; Pettes, M. T.; Li, H.; Chen, S.; Shi, L.; Piner, R.; Ruoff, R. S. Ultrathin Graphite Foam: A Three-Dimensional Conductive Network for Battery Electrodes. *Nano Lett.* **2012**, *12*, 2446–2451.

(15) Wang, K.-X.; Li, X.-H.; Chen, J.-S. Surface and Interface Engineering of Electrode Materials for Lithium-Ion Batteries. *Adv. Mater.* **2015**, *27*, 527–545.

(16) Singh, M.; Kaiser, J.; Hahn, H. Thick Electrodes for High Energy Lithium Ion Batteries. *J. Electrochem. Soc.* **2015**, *162*, A1196–A1201.

(17) Yang, G.-F.; Song, K.-Y.; Joo, S.-K. Ultra-Thick Li-Ion Battery Electrodes Using Different Cell Size of Metal Foam Current Collectors. *RSC Adv.* **2015**, *5*, 16702–16706.

(18) Kardjilov, N.; Manke, I.; Hilger, A.; Strobl, M.; Banhart, J. Neutron Imaging in Materials Science. *Mater. Today* **2011**, *14*, 248–256.

(19) Nie, Z.; McCormack, P.; Bilheux, H. Z.; Bilheux, J. C.; Robinson, J. P.; Nanda, J.; Koenig, G. M., Jr. Probing Lithiation and Delithiation of Thick Sintered Lithium-Ion Battery Electrodes with Neutron Imaging. *J. Power Sources* **2019**, *419*, 127–136.

(20) Zhou, H.; An, K.; Allu, S.; Pannala, S.; Li, J.; Bilheux, H. Z.; Martha, S. K.; Nanda, J. Probing Multiscale Transport and Inhomogeneity in a Lithium-Ion Pouch Cell Using in Situ Neutron Methods. *ACS Energy Lett.* **2016**, *1*, 981–986.

(21) Siegel, J. B.; Lin, X.; Stefanopoulou, A. G.; Hussey, D. S.; Jacobson, D. L.; Gorsich, D. Neutron Imaging of Lithium Concentration in LFP Pouch Cell Battery. *J. Electrochem. Soc.* **2011**, *158*, A523.

(22) Qi, Z.; Koenig, G. M., Jr. High-Performance $LiCoO_2$ Sub-Micrometer Materials from Scalable Microparticle Template Processing. *ChemistrySelect* **2016**, *1*, 3992–3999.

(23) Qi, Z.; Koenig, G. M., Jr. A Carbon-Free Lithium-Ion Solid Dispersion Redox Couple with Low Viscosity for Redox Flow Batteries. *J. Power Sources* **2016**, *323*, 97–106.

(24) Qi, Z.; Liu, A. L.; Koenig, G. M., Jr. Carbon-Free Solid Dispersion $LiCoO_2$ Redox Couple Characterization and Electrochemical Evaluation for All Solid Dispersion Redox Flow Batteries. *Electrochim. Acta* **2017**, *228*, 91–99.

(25) Hussey, D. S.; Jacobson, D. L.; Arif, M.; Coakley, K. J.; Vecchia, D. F. In Situ Fuel Cell Water Metrology at the NIST Neutron Imaging Facility. *J. Fuel Cell Sci. Technol.* **2010**, *7*, 021024.

(26) Albertus, P.; Newman, J. Introduction to dualfoil 5.0, University of California Berkeley, Berkeley, CA, Tech. Rep. 2007.

(27) Doyle, M.; Fuller, T. F.; Newman, J. Modeling of Galvanostatic Charge and Discharge of the Lithium/Polymer/Insertion Cell. *J. Electrochem. Soc.* **1993**, *140*, 1526–1533.

(28) Fuller, T. F.; Doyle, M.; Newman, J. Simulation and Optimization of the Dual Lithium Ion Insertion Cell. *J. Electrochem. Soc.* **1994**, *141*, 1–10.

(29) Fuller, T. F.; Doyle, M.; Newman, J. Relaxation Phenomena in Lithium-Ion-Insertion Cells. *J. Electrochem. Soc.* **1994**, *141*, 982–990.

(30) Rashid, M.; Sahoo, A.; Gupta, A.; Sharma, Y. Numerical Modelling of Transport Limitations in Lithium Titanate Anodes. *Electrochim. Acta* **2018**, *283*, 313–326.

(31) Allu, S.; Kalnaus, S.; Elwasif, W.; Simunovic, S.; Turner, J. A.; Pannala, S. A New Open Computational Framework for Highly-Resolved Coupled Three-Dimensional Multiphysics Simulations of Li-Ion Cells. *J. Power Sources* **2014**, *246*, 876–886.

(32) Zaghib, K.; Simoneau, M.; Armand, M.; Gauthier, M. Electrochemical Study of $Li_4Ti_5O_{12}$ as Negative Electrode for Li-Ion Polymer Rechargeable Batteries. *J. Power Sources* **1999**, *81–82*, 300–305.

(33) Geng, L.; Denecke, M. E.; Foley, S. B.; Dong, H.; Qi, Z.; Koenig, G. M., Jr. Electrochemical Characterization of Lithium Cobalt Oxide within Aqueous Flow Suspensions as an Indicator of Rate Capability in Lithium-Ion Battery Electrodes. *Electrochim. Acta* **2018**, *281*, 822–830.

(34) Young, D.; Ransil, A.; Amin, R.; Li, Z.; Chiang, Y.-M. Electronic Conductivity in the $Li_{4/3}Ti_{5/3}O_4$-$Li_{7/3}Ti_{5/3}O_4$ System and Variation with State-of-Charge as a Li Battery Anode. *Adv. Energy Mater.* **2013**, *3*, 1125–1129.

(35) Kataoka, K.; Takahashi, Y.; Kijima, N.; Akimoto, J.; Ohshima, K.-I. Single Crystal Growth and Structure Refinement of $Li_4Ti_5O_{12}$. *J. Phys. Chem. Solids* **2008**, *69*, 1454–1456.

(36) Takahashi, Y.; Kijima, N.; Dokko, K.; Nishizawa, M.; Uchida, I.; Akimoto, J. Structure and Electron Density Analysis of Electrochemically and Chemically Delithiated $LiCoO_2$ Single Crystals. *J. Solid State Chem.* **2007**, *180*, 313–321.

(37) He, Z.; Wang, Z.; Wu, F.; Guo, H.; Li, X.; Xiong, X. Spherical $Li_4Ti_5O_{12}$ Synthesized by Spray Drying from a Different Kind of Solution. *J. Alloys Compd.* **2012**, *540*, 39–45.

(38) Zhang, Q.; Guo, Q.; White, R. E. Semi-Empirical Modeling of Charge and Discharge Profiles for a $LiCoO_2$ Electrode. *J. Power Sources* **2007**, *165*, 427–435.

(39) Thorat, I. V.; Stephenson, D. E.; Zacharias, N. A.; Zaghib, K.; Harb, J. N.; Wheeler, D. R. Quantifying Tortuosity in Porous Li-Ion Battery Materials. *J. Power Sources* **2009**, *188*, 592–600.

(40) Capiglia, C.; Saito, Y.; Kageyama, H.; Mustarelli, P.; Iwamoto, T.; Tabuchi, T.; Tukamoto, H. ^{7}Li and ^{19}F Diffusion Coefficients and Thermal Properties of Non-Aqueous Electrolyte Solutions for Rechargeable Lithium Batteries. *J. Power Sources* **1999**, *81–82*, 859–862.

(41) Doyle, C. M. PhD Thesis, Lawrence Berkeley Laboratory, 1995.

(42) Landesfeind, J.; Ebner, M.; Eldiven, A.; Wood, V.; Gasteiger, H. A. Tortuosity of Battery Electrodes: Validation of Impedance-Derived Values and Critical Comparison with 3D Tomography. *J. Electrochem. Soc.* **2018**, *165*, A469–A476.

(43) Ebner, M.; Chung, D.-W.; García, R. E.; Wood, V. Tortuosity Anisotropy in Lithium-Ion Battery Electrodes. *Adv. Energy Mater.* **2014**, *4*, 1301278.

(44) Nanda, J.; Bilheux, H.; Voisin, S.; Veith, G. M.; Archibald, R.; Walker, L.; Allu, S.; Dudney, N. J.; Pannala, S. Anomalous Discharge Product Distribution in Lithium-Air Cathodes. *J. Phys. Chem. C Nanomater. Interfaces* **2012**, *116*, 8401–8408.

(45) Kehrwald, D.; Shearing, P. R.; Brandon, N. P.; Sinha, P. K.; Harris, S. J. Local Tortuosity Inhomogeneities in a Lithium Battery Composite Electrode. *J. Electrochem. Soc.* **2011**, *158*, A1393.

(46) Li, L.; Erb, R. M.; Wang, J.; Wang, J.; Chiang, Y.-M. Fabrication of Low-tortuosity Ultrahigh-area-capacity Battery Electrodes through Magnetic Alignment of Emulsion-based Slurries. *Adv. Energy Mater.* **2019**, *9*, 1802472.

(47) Billaud, J.; Bouville, F.; Magrini, T.; Villevieille, C.; Studart, A. R. Magnetically Aligned Graphite Electrodes for High-Rate Performance Li-Ion Batteries. *Nat. Energy* **2016**, *1*, 16097.

Chapter 4

Pore Microstructure Impacts on Lithium Ion Transport and Rate Capability of Thick Sintered Electrodes

4.1 Abstract

Increasing electrode thickness is one route to improve the energy density of lithium-ion battery cells. However, restricted Li^+ transport in the electrolyte phase through the porous microstructure of thick electrodes limits the ability to achieve high current densities and rates of charge/discharge with these high energy cells. In this work, processing routes to mitigate transport restrictions were pursued. The electrodes used were comprised of only active material sintered together into a porous pellet. For one of the electrodes, comparisons were done between using ice-templating to provide directional porosity and using sacrificial particles during processing to match the geometric density without pore alignment. The ice-templated electrodes retained much greater discharge capacity at higher rates of cycling, which was attributed to improved transport properties provided by the processing. The electrodes were further characterized using an electrochemical model of the cells evaluated and neutron imaging of a cell containing the ice-templated pellet. The results indicate that significant improvements can be made to electrochemical cell properties via templating the electrode microstructure for situations where the rate limiting step includes ion transport limitations in the cell.

The content of this chapter has been published in the following journal:

Nie, Z.; Parai, R.; Cai, C.; Michaelis, C.; LaManna, J. M.; Hussey, D. S.; Jacobson, D. L.; Ghosh, D.; Koenig, G. M., Jr. Pore Microstructure Impacts on Lithium Ion Transport and Rate Capability of Thick Sintered Electrodes. *J. Electrochem. Soc.* **2021**, *168*, 060550.

4.2 Introduction

Lithium-ion (Li-ion) batteries have achieved significant commercial success and found widespread use in numerous applications, particularly for powering small devices including consumer electronics. However, to meet the ever-increasing power and energy demands for these devices, further improvements in Li-ion batteries are needed, which is of significant fundamental interest.[1,2] To develop more powerful Li-ion batteries, one of the most important areas of research focus is to discover and characterize new electrode and electrolyte materials.[3,4] However, another route to improve energy and power density is through electrode or cell engineering. There are several options to modify the electrode or cell design and structure; however, the two most relevant components to the study herein are to increase the relative fraction of active material in the cell and modify the electrode microstructure for improvement of transport properties.[5-7]

For conventional composite Li-ion battery electrodes, carbon additives and polymer binders are blended with active material powders to provide the desired mechanical properties and electronic conductivity for the electrode. During electrode fabrication, a slurry containing active material and inert additives is coated onto a metal current collector to form a thin electrode.[6] The thickness of the electrode and relative fraction of the active material are two factors which determine the overall energy density within the final battery cell.[5,6,8] Thus, developing thicker electrodes as well as reducing inert additives would both increase the energy density of the cell. However, increasing the volume fraction of active electrode material and electrode thickness must be balanced with other competing factors such as limitations in ion transport for thicker electrodes and electrode mechanical properties.[8,9] Recently, methods have been reported to fabricate very thick electrodes containing only active materials by sintering pure active materials into porous thin films via hydraulic compression and thermal treatment.[6,10,11] These "sintered electrodes" do not contain any conductive or binder additives and are generally much thicker than composite electrodes.

Compared to composite electrodes, reports have shown that thick sintered electrodes can have much higher energy density and areal capacity at the cell level, but sintered electrodes also exhibit lower mass-based capacity utilization at higher charge/discharge rate.[6,9,12] This is due to the increased polarization for the sintered electrodes due to electron and ion transport through the electrode matrix and microstructure, respectively. Matrix electronic conductivity of the composite electrodes is primarily facilitated by the conductive additives (e.g., carbon black), which is several orders of magnitude higher than pure active material particles that must conduct electrons throughout the sintered electrodes.[13,14] It is noted, however, that for some electrode materials such as $LiCoO_2$ (LCO) and $Li_4Ti_5O_{12}$ (LTO), that slight changes in the extent of lithiation due to electrochemical charge/discharge result in dramatic increase in the electronic conductivity relative to the initial pristine material.[13, 15] The improvement in electronic conductivity with a change in the extent of lithiation is expected to help compensate for the overall lower electronic conductivity in sintered electrodes. Another cause for increased polarization and limited rate capability in sintered electrodes is the increased resistance to ion transport through the thick electrode microstructure. This limitation is generally attributed to the relatively large thickness of the electrodes, though the lack of inactive composite components in the interstitial regions between the particles likely improves ion transport relative to a composite electrode with equivalent active material volume fraction and total electrode thickness. Previous reports have suggested the ion transport limitations were the greatest contributor to rate capability limitations for thick sintered electrodes.[16,17] Thus, to mitigate this ion transport challenge and improve the rate capability of thick sintered electrodes, improvements will be needed in the microstructure of the electrodes, the electrolyte transport properties, or both. This paper will focus on an effort to control and improve the ion transport properties of the sintered electrodes through modification of the electrode microstructure. One route to improve transport through the electrode microstructure is to provide alignment of the pores in the direction of the net ion flux during charge/discharge, and recently different techniques have been applied to fabricate thick electrodes with aligned pores to achieve this goal.[7, 18 - 20] Among these techniques, ice-templating (also known as freeze casting) is a promising method that is particularly well-suited to fabricate sintered electrodes with aligned pores, i.e., directional porosity. Ice templating involves preferentially growing ice crystals within a particulate suspension in the direction of an applied unidirectional temperature gradient, sublimation of the water phase, and then thermal treatment to sinter the templated structure that retains aligned pore architecture and provides strength to the porous electrode.[7, 21, 22] Compared to electrodes fabricated without ice-templating, ice-templated electrodes have lower pore tortuosity, which improves the effective ionic conductivity within the liquid phase-laden pore microstructure, and the enhanced ionic conductivity improves the rate capability of the electrodes.[7,23-26] However, a detailed comparison of the electrochemical properties between the ice-templated sintered electrodes and pressed sintered electrodes with nominally equivalent geometric density would provide further support to the benefits of employing the ice-templating technique toward developing sintered electrodes for Li-ion batteries.

In this work, we prepared sintered LTO anodes via both the ice-templating technique and regular hydraulic pressing technique – where the hydraulic pressed sample had a geometric density and thickness targeted to match the ice-templated sample. After being paired with pressed sintered LCO electrodes, the electrochemical properties of the LTO-LCO full cells were evaluated. The impact of electrode tortuosity on Li^+ transport will be discussed in the context of the electrochemical outcomes and calculations based on an electrochemical model, though it is noted that other effects such as electrolyte accessibility would also lead to alleviating the transport restrictions in the electrode microstructure. To further support the electrochemical and modelling outcomes, *in operando* neutron imaging was conducted to support the redistribution of the Li^+ during discharge.[17, 27 - 29] The combination of the experimental and computational efforts provides insights into the net impacts of aligning the pore microstructure within sintered electrode Li-ion batteries.

4.3 Materials and methods

4.3.1 Particle material preparation

4.3.1.1 Active material particles

$LiCoO_2$ (LCO) was used as the cathode material. LCO was prepared from a $CoC_2O_4 \cdot 2H_2O$ precursor synthesized via coprecipitation.[30] First, 1800 mL of 62.8 mM $Co(NO_3)_2 \cdot 6H_2O$ (Fisher Reagent Grade) solution and 1800 mL of 87.9 mM $(NH_4)_2C_2O_4 \cdot H_2O$ (Fisher Certified ACS) solution were prepared separately in deionized water. Both solutions were heated to 50 °C, and the $Co(NO_3)_2 \cdot 6H_2O$ solution was then poured into the $(NH_4)_2C_2O_4 \cdot H_2O$ solution all at once. A polytetrafluoroethylene (PTFE) stir bar was used to maintain solution mixing at a stir rate of 800 rpm. After coprecipitation at 50 °C for 30 minutes, the solid precipitate was collected using vacuum filtration and rinsed with 4 L deionized water. The powder was then dried in an oven which was set at 80 °C in air atmosphere for 24 h.

Then, to prepare the LCO active material, the oxalate precursor powder was mixed with Li_2CO_3 (Fisher Chemical) powder using mortar and pestle. The molar ratio of the two powders was targeted to be 1.02:1 for Li:Co. The powder mixture was placed in a Carbolite CWF 1300 box furnace and heated to 800 °C at a ramp rate of 1 °C min^{-1} under an air atmosphere. After reaching 800 °C, the heat was turned off and the product was cooled to room temperature in the furnace without controlling the cooling rate. Then the product LCO material was ground with mortar and pestle by hand and was further milled in a Fritsch Pulverisette 7 planetary ball mill using 5 mm diameter zirconia beads at 300 rpm for 5 hours.

$Li_4Ti_5O_{12}$ (LTO) was used as anode material and was purchased from a commercial supplier (NANOMYTE BE-10 from NEI Corporation). No additional treatment was applied before processing this material powder into a sintered electrode. The characterization and electrochemical performance of both LCO and LTO material used in this study can be found in previous publications.[22,31]

4.3.1.2 Polystyrene particles

Colloidal polystyrene particles (diameters 300 nm to 500 nm) were synthesized using procedures adapted from literature.[32] Styrene (Sigma-Aldrich, ReagentPlus, with 4-tert-butylcatechol as stabilizer, ≥ 99.0%) was pretreated using a prepacked column (Sigma-Aldrich, Inhibitor, prepacked column for removing tert-butylcatechol) to remove the polymerization inhibitor. In a typical synthesis, a three-neck 500 mL round bottom flask was filled with 290 mL DI water and 8.86 g styrene and heated to 70 ˚C in an oil bath and allowed to thermally equilibrate for 30 minutes. Next, 0.204 g potassium persulfate (Sigma-Aldrich) was added to catalyze the styrene polymerization reaction. The head space was purged with nitrogen and flowed at 1 mL s^{-1} for the duration of the experiment. The two-phase system was stirred for 8.5 h with a magnetic stir bar, resulting in a final milky white suspension. To obtain the polystyrene powder, ~5 mL of the suspension was placed in a glass container and was dried in the air until all water was evaporated. Then the polystyrene powder was collected.

4.3.2 Electrode preparation and characterization

4.3.2.1 Sintered LCO pellet preparation

Sintered LCO electrodes were used as cathodes in this study. To prepare the sintered LCO pellet, the LCO active material powder was first mixed with 1 wt.% polyvinyl butyral (Pfaltz & Bauer) solution dissolved in ethanol (Acros). 1 g LCO powder was blended with 2 mL polymer binder solution with a mortar and pestle by hand to mix the materials. The mixture was collected after all the solvent was evaporated in air. Then, 0.2 g of the powder was loaded into a 13 mm diameter Carver pellet die and pressed with 12,000 lb_f for 2 minutes in a Carver hydraulic press. Next, the pellets were heated in a Carbolite CWF 1300 box furnace in an air atmosphere with a ramping rate of 1 °C min^{-1} from 25 °C to 600 °C and the pellets were cooled to 25 °C at 1 °C min^{-1} after holding at 600 °C for 1 hour.

4.3.2.2 Ice-templated LTO pellet preparation

Ice-templated LTO materials were fabricated from aqueous suspensions containing 30 % by volume LTO particles. To prepare an aqueous suspension, as received LTO powder was mixed with deionized (DI) water and yttria stabilized zirconia (ZrO_2) spheres (5 mm diameter, Inframat Advanced Materials LLC) in a Nalgene bottle, with ceramic powder to milling media mass ratio of 1:4. Then, cetyl trimethyl ammonium bromide (CTAB) cationic dispersant, at a concentration of with 0.02 g cm^{-3} of distilled water, was added to the aqueous LTO suspension. The addition of CTAB caused slight foaming in the suspension. To avoid foaming, an antifoaming agent Surfynol 104PG50 (0.003 g g^{-1} of LTO powder) was added to LTO suspension. Then, the LTO suspension was milled for 24 h at 30 RPM. Next, a binder solution was prepared by dissolving poly(2-ethyl-2-oxazoline) in distilled water, and the binder solution was added to the LTO suspension such that the binder amount was 4% of the LTO powder mass. LTO suspension was further ball milled for another hour at 10 RPM to ensure proper mixing of binder solution and LTO suspension and then the ZrO_2 spheres were separated from suspension.

In this work a custom-made ice-templating device was employed to fabricate LTO electrodes with aligned pores,[33] and the resulting LTO pellets were referred to as LTO_{ICE} in the following discussion. This setup contains an assembly of a PTFE tube (mold) placed on a thin copper plate (referred to here as “cold-finger”), which is filled with an aqueous ceramic suspension. Next, to freeze the suspension under the influence of unidirectional temperature gradient, the mold assembly containing ceramic suspension is inserted inside a liquid nitrogen Dewar, where the cold-finger is placed above the liquid nitrogen. The distance between cold-finger and liquid N_2 determines the unidirectional temperature gradient, and hence the growth velocity of the freezing front. In this work, a 1 mm gap between the cold-finger and liquid nitrogen was used to achieve a relatively high freezing front velocity (FFV) of about 28 $\mu m\ s^{-1}$. As the temperature of the cold-finger reaches below 0 °C, ice crystals nucleate at the bottom of the suspension in contact with the cold-finger and grow upward under the influence of the applied thermal gradient.

Unidirectionally solidified samples were freeze dried in a freeze-dryer (2.5 L, Labconco, Kansas City, MI) for 96 h at a pressure of 0.014 mbar and temperature of -50 °C. Freeze dried LTO pellets were sintered using a tube furnace (NBD, T-1700-60IT). Samples were first heated to 450 °C at a rate of 5 °C min^{-1} and held for 4 hours for binder burnout. Next, samples were heated to 950 °C at a rate of 2 °C min^{-1} and sintered for 2 h. Finally, samples were cooled down to room temperature using a cooling rate of 5 °C min^{-1}. Dimensions of sintered LTO samples were approximately 13 mm in diameter and 10 mm in height. From each sintered LTO sample, a LTO$_{ICE}$ electrode disk of 1 mm thickness was extracted from a 2 mm height above the bottom of the sample.

Microstructure of LTO$_{ICE}$ materials was characterized using a desktop scanning electron microscope (SEM, Phenom Pure), and SEM images were obtained from cross-sectional planes perpendicular to the growth direction of ice crystals. Microstructure of the sintered materials were also characterized using X-ray computed tomography (XCT). A sintered LTO sample was first infiltrated with epoxy to achieve better contrast during XCT imaging. Next from the infiltrated sample, a small specimen of dimensions 1.5 mm × 1.5 mm × 3 mm was extracted and used for XCT. The extracted specimen was scanned using a 3D X-ray microscope (XRM, Zeiss Xradia 510 Versa available at Analytical Instrumentation Facility, North Carolina State University, Raleigh, NC) with 110 kV X-ray source, 90 µA target current, and 15 s exposure time. The obtained 983 X-ray 2D radiographs were used to reconstruct a 3D image using XMR Reconstructor software with image resolution of 1008 × 976 pixels with a pixel size of 0.8 µm. The obtained reconstructed data sets were imported to Dragonfly 2020.1 (Object Research Systems, Montreal) for 3D volume rendering.

4.3.2.3 Porosity-controlled LTO pellet preparation

The porosity-controlled LTO electrodes were prepared using a similar method for sintered LCO electrodes. The sintered LCO electrodes have a porosity of 36 %, and if processed identical to the LCO an LTO sintered electrode generally has a porosity of 40 %.

The LTO_{ICE} electrodes, however, had a porosity of 57 %. Porosity was determined by determining the volume of a processed electrode using dimensions measured with a digital micrometer and combining with the weight to determine the pellet density, where porosity accounted for the difference between the electrode density and the true density of the active material. Active material densities can be found in the Appendix 3, Table A3.1 and for LTO were also provided on the specification sheet from the supplier. To have a more direct comparison of the impact of the pore alignment on the electrochemical and ion transport properties of the sintered electrodes, it was desired to fabricate hydraulically pressed electrodes with random pore microstructure which had porosity that matched the LTO_{ICE} electrodes. To increase the porosity of the hydraulically pressed LTO electrodes, sacrificial spherical particles were added to the LTO powder before the hydraulic pressing step with the goal of providing added porosity to the electrode after their subsequent removal. To achieve this higher porosity, first, the LTO powder was mixed with polystyrene powder in a mortar and pestle with a mass ratio of 5:1 for LTO:polystyrene. Then, the powder mixture was blended with 1 wt.% polyvinyl butyral solution. 2 mL solution was used for 1 g LTO powder in the mixture. After the solvent was evaporated, 0.24 g of the mixture powder was loaded in the 13 mm diameter pellet die and pressed with 12,000 lb_f for 2 minutes. The polystyrene was removed via decomposition at a lower temperature condition by firing the LTO/polystyrene pellets in a Lindberg/Blue M tube furnace from room temperature to 400 °C at a ramp rate of 1 °C min^{-1} under N_2 atmosphere. After holding at 400 °C for 1 h, the furnace was cooled to room temperature at a rate of 1 °C min^{-1}. This thermal treatment decomposed the polystyrene particles leaving increased porosity in the volume regions where the particles previously were.[34] No changes were observed in the LTO pellet diameter or thickness after the polystyrene removal step. Next, the pellets were transferred to a Carbolite CWF 1300 box furnace in air atmosphere and sintered at 600 °C for 1 h with both the heating and cooling rate of 1 °C min^{-1}. The resulting LTO pellets with the increased porosity due to the sacrificial polystyrene particles are referred to as LTO$_{POR}$, and their final porosity was 57 %. The surface morphology of the LTO$_{POR}$ pellets was imaged using a SEM (FEI Quanta 650). The extra heat treatment at 600 °C in air was expected to oxidize and remove any residual polystyrene on the LTO surfaces in the pellet.[35] The LTO pellet after processing appeared white, suggesting there were no carbon deposits. The pellet was also weighed, and the mass was consistent with the initial amount of LTO in the sample suggesting the polymer materials were no longer present.

4.3.2.4 Thermogravimetric Analysis

Thermogravimetric analysis (TGA, TA Instruments Q50) was conducted using pieces of both LTO$_{ICE}$ and LTO$_{POR}$ electrodes, and the results can be found in Appendix 3, Fig. A3.1. Both pellets showed very small weight loss (~0.2 wt.%) at 200 C~300 ºC and no further weight out to at least 800 ºC. These results were consistent with the lack of a carbon coating or deposits on the electrodes being retained after processing. The TGA was conducted by heating to 100 ºC and holding at 100 ºC for 1 hour to remove any adsorbed water. Then, the temperature was increased to 1000 ºC at a rate of at 10 ºC min^{-1}. TGA samples were each ~35 mg, and the sample atmosphere was air.

4.3.2.5 X-Ray Diffraction

The X-ray diffraction (XRD, Empyrean) patterns were collected for the as-received LTO powder, the LTO powder after firing at 950 °C for 1 hour, and for both LTO_{POR} and LTO_{ICE} pellets. The patterns can be found in Appendix 3, Fig. A3.2. The XRD patterns were all consistent with spinel phase LTO, with no impurity peaks observed.

4.3.2.6 Electrode Surface Area

N_2 adsorption-desorption experiments were used to measure the surface area for both LTO_{ICE} and LTO_{POR} pellets. The experiments were carried out with a NOVA 2200e analyzer. Both sample pellets were degassed for 90 min at 150 °C before adsorption-desorption and multipoint Brunauer-Emmett-Teller (BET) method was used to calculate the surface area. The LTO_{POR} materials had a BET surface area of 5.4 $m^2\ g^{-1}$, which for the approximate 340 nm length scale of the primary particles suggests there was not much porosity beyond the surfaces of the particles themselves. The BET surface area of the LTO_{ICE} was measured to be <1 $m^2\ g^{-1}$, however, the total adsorbed volume was below the threshold that is recommended for the instrument and thus the value was not reliable (it is noted that even the LTO_{POR} sample was right at the lower limit), and the total amount of ice templated samples available to dedicate for BET analysis was limited.

4.3.2.7 Electrode Electronic Conductivity

Direct current conductivity was used to measure the electronic conductivity of LTO_{ICE} and LTO_{POR} electrodes using stainless steel current collectors. The values were measured to be

0.9×10^{-9} S cm^{-1} and 1.0×10^{-9} S cm^{-1}, respectively, for the as prepared electrodes. These values are within the range of previous reports for pristine LTO electronic conductivity.[15]

4.3.3 Electrochemical cell fabrication

CR2032 coin cells were used for electrochemical evaluation of full cells containing sintered LTO anodes paired with sintered LCO cathodes. To fabricate the cell, the LCO pellets were pasted onto the bottom plate and LTO pellets (either an LTO_{ICE} or LTO_{POR} pellet) were pasted on a stainless steel spacer used in the cell. The paste for attaching the sintered electrode to the metal bottom plate/spacer was composed of 1:1 weight ratio Super P carbon black (Alfa Aesar) to polyvinylidene difluoride (PVDF, Alfa Aesar) binder dissolved in N-methyl pyrrolidone (NMP, Sigma-Aldrich). After the pellets were dried in air at 80 ˚C for 12 hours, they were transferred into an Ar atmosphere glove box with both O_2 and H_2O content <1 ppm. Then, LTO and LCO electrodes were assembled into a coin cell with two layers of Celgard 2325 polymer separator (25 μm thick for each layer) between the anode and cathode. In a coin cell, 16 total drops of electrolyte (1.2 M $LiPF_6$ in 3:7 ethylene carbonate:ethyl methyl carbonate, BASF) were added. Other parts of the CR2032 coin cell used in this study include a stainless steel wave spring, a stainless steel top cap, and a polypropylene or PTFE gasket (where PTFE was used only for cells assembled for neutron imaging experiments).[28]

The rate capability of LTO/LCO sintered electrode coin cells was determined by galvanostatically cycling at different C rates using a MACCOR battery cycler. For the neutron imaging experiment, the cell was cycled using a Bio-Logic SP-50 potentiostat. The C rate was based on an assumed capacity of 150 mAh g^{-1} for LCO mass in the coin cell, where 1C was assumed to correspond to 150 mA g^{-1} LCO. The voltage range used for all LTO/LCO cells was 1.0 V to 2.7 V (cell voltage, relative to LTO anode).

4.3.4 Model analysis

An electrochemical numerical model developed by Newman *et al*.[36-38] was used to calculate the discharge voltage profiles. In addition, the simulation provides outputs of the Li^+ concentration in both the solid and electrolyte phases at different time points during discharge and as a function of the depth dimension within the cells for the region between the current collectors (e.g. for the depth region comprised of the anode, separator, and cathode). More details about the model can be found in previous publications, and a summary of the model equations can be found in the Appendix 3.[36-38] A specific recent addition to the model which was applied in this work as well was the incorporation of a matrix conductivity which was a function of the extent of lithiation of the active material at each depth within the cell, and also the gradient in Li^+ resulting from the charging process was accounted for when determining the discharge profile. Details of the updated model used in this work can be found in a previous publication.[39]

4.3.5 Neutron imaging

Neutron imaging was carried out at the thermal neutron imaging beamline at the National Institute for Standards and Technology (NIST) Center for Neutron Research.[40] Details of the neutron imaging experiment set up and data analysis can be found in Appendix 3 (including Fig. A3.3) and previous publications.[17,28] The results of neutron imaging were a series of radiographs collected at different times *in operando* during the discharge process. The changes in neutron intensity at different depths within the cell extracted from the neutron radiographs were most sensitive to the changes in Li^+ concentration at those locations.[17,28,39] Thus, changes in pixel intensity correlated with changes in Li^+ concentration (mostly in the solid phase of the active material) at the different cell locations and were analyzed as a function of time during discharge. The neutron imaging provided information on the relative redistribution of Li^+ in the electrodes during discharge as a function of time and cell depth.

4.4 Results and discussion

4.4.1 Morphology characterization for LTO_{ICE} and LTO_{POR} pellets

Top view SEM images with different magnification of sintered ice templated LTO_{ICE} and porosity controlled LTO_{POR} pellets are displayed in Fig. 4.1. In the LTO_{ICE} pellet, lamellar pore morphology was developed and retained after sintering (Fig. 4.1a), consistent with previous results.[9] XCT results (Fig. A3.4) confirmed that LTO_{ICE} contained aligned pores which extended significant distances through the thickness (e.g., along the growth direction of ice crystals, which is also the direction of net ion flux when electrochemically cycled within coin cells) of the pellet. From the higher magnification SEM image (Fig. 4.1b), it was observed that the lamella wall region was composed of densely packed LTO particles with average wall thickness of ~10 μm. For LTO_{POR} pellet, the surface was much flatter with small pores present (Fig. 4.1c). None of these pores in LTO_{POR} formed deep channels through the pellet as the bottom of these pores was often noticeable just below the surface. In Fig. 4.1d, at higher magnification, it can be seen that the surface of the LTO_{POR} pellet was composed of loosely packed LTO particles. Compared with the lamella wall region of LTO_{ICE} pellet, the density of the LTO_{POR} pellet appeared slightly lower. This may have been due to the lower sintering temperature used during fabrication for LTO_{POR} pellet (600 ˚C) compared to that for LTO_{ICE} pellet (950 ˚C). However, both LTO pellets had similar total geometric density, with combined pore/void volume of ~57 %. From the morphology characterization of sintered LTO pellets, it was confirmed that the ice-templating technique resulted in much larger and directionally oriented pores, which would be expected to result in lower tortuosity and thus improved ion transport in the direction of the freezing front propagation.

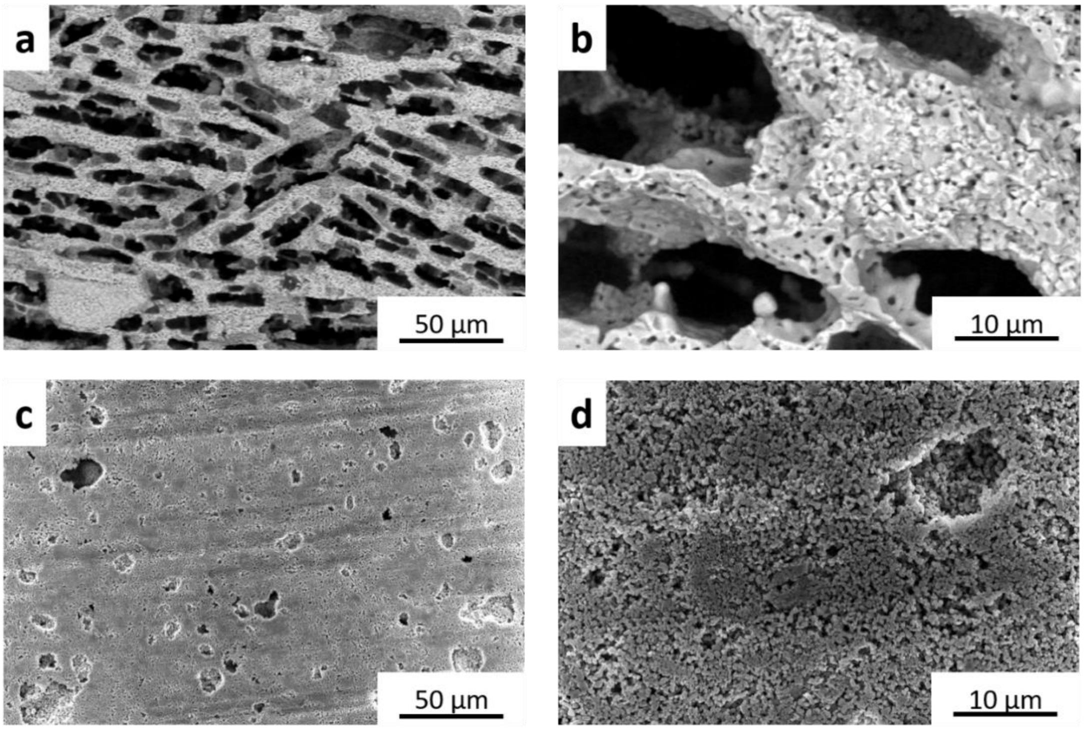

Fig. 4.1. SEM images of the surfaces of (a, b) LTO_{ICE} and (c, d) LTO_{POR} pellets at low (a,c) and high (b,d) magnification.

4.4.2 Electrochemical evaluation of LTO_{ICE}/LCO and LTO_{POR}/LCO cells

To study the electrochemical properties of sintered electrode full cells fabricated using LTO pellets with different pore microstructures, the LTO_{ICE} and LTO_{POR} pellets were paired with nominally identically sintered LCO pellets and were fabricated into LTO/LCO CR2032 coin cells. The discharge capacity for LTO_{ICE}/LCO and LTO_{POR}/LCO cells at different C rates is displayed in Fig. 4.2. The data points provided are the average discharge capacity per mass of LCO from rate capability test of 3 nominally identical cells of each for both LTO_{ICE}/LCO and LTO_{POR}/LCO. In all cases the charge cycle was at a current of C/20, with C rate determined by the mass of LCO in the cell. Note that the range in LCO mass, and thus the range in currents and current densities during charge and discharge, varied by 0.002 g, which was ~1 % of the mean LCO mass for all cathode pellets used. The full rate capability test of representative LTO_{ICE}/LCO and LTO_{POR}/LCO cells can be found in Appendix 3, Fig. A3.5. As can be seen in Fig. 4.2 and Fig A3.5, the discharge capacities for both cells were similar at relatively low rates (e.g., C/50 and C/20). At C/20, the discharge capacity of the LTO_{ICE}/LCO cells was (94.6 ± 3.4) mAh g^{-1} LCO and LTO_{POR}/LCO was (90.6 ± 8.1) mAh g^{-1} LCO (uncertainty is the standard deviation computed from several discharge capacities measured for 3 different cells). The higher capacity for the cell containing LTO_{ICE} may have resulted from higher charging capacity due to improved transport during that process,[39] however, the difference was still relatively small at the lowest rates. When the discharge rate was increased, LTO_{POR}/LCO cells lost more capacity compared with LTO_{ICE}/LCO cells, both on an absolute and percentage basis. At C/5 discharge rate, the LTO_{POR}/LCO cells only obtained (36.1 ± 10.9) mAh g^{-1} LCO, which was 39.8 % of the discharge capacity at C/20. In contrast, LTO_{ICE}/LCO cells had

(74.0 ± 3.4) mAh g^{-1} LCO capacity at C/5 discharge, which was 78.2 % of the discharge capacity at C/20. In Fig. 4.2, the "C/20*" reflects the discharge capacity achieved in the cells at a C rate of C/20 after completion of the full rate capability cycling. The discharge capacity after the rate capability was completed was comparable to the capacity obtained at C/20 during the initial cycles. This outcome indicated the difference in capacity was due to rate capability limitations, and not due to capacity fade. It was concluded that LTO_{ICE}/LCO cells had improved rate capability relative to LTO_{POR}/LCO cells. The most substantial difference between the two cell types was the pore microstructure for the LTO pellets used. All LTO_{ICE} and LTO_{POR} had similar thickness and total porosity and used the same electrolyte and equivalent cathode material and processing. These results provided support to the conclusion that the introduction of the ice-templated pore microstructure for thick sintered electrode improves active material utilization at high rates of charge and discharge. One explanation for this observation would be improved Li^+ transport in the electrolyte phase through the porous microstructure of the LTO_{ICE} pellet facilitated by the directional porosity, although other effects in addition to alignment such as pore size, pore interconnectivity, and electrolyte accessibility could also improve the Li^+ transport through the microstructure.

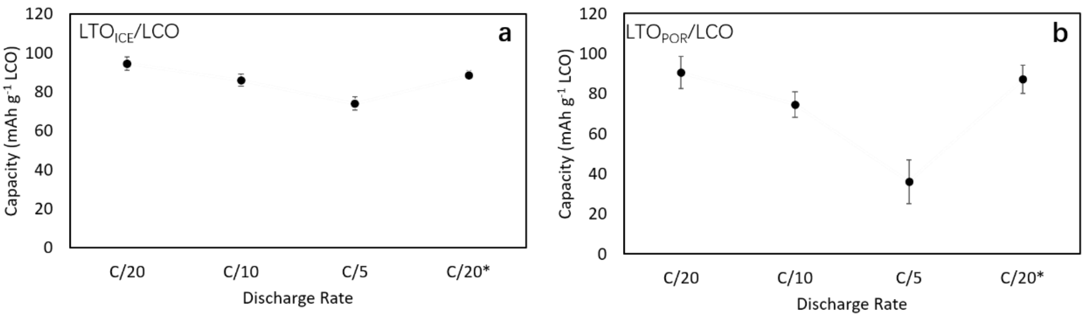

Fig. 4.2. Discharge capacity of (a) LTO$_{\text{ICE}}$/LCO and (b) LTO$_{\text{POR}}$/LCO cells. All charge cycles were conducted at a rate of C/20, while discharge was at the rate indicated on the x-axis. The "C/20*" represents the C/20 discharge cycles conducted after conclusion of the rate capability test at increasing rates. Note that the average total capacity at C/20 for a) was 94.6 mAh and for b) was 90.6 mAh. The currents used were based on the mass of LCO in each cell used which was similar for all cases and on average was 1.4 mA (1.1 mA cm^{-2}) at C/20, 2.8 mA (2.1 mA cm^{-2}) at C/10, and 5.7 mA (4.3 mA cm^{-2}) at C/5.

4.4.3 Numerical calculations of discharge process for LTO$_{ICE}$/LCO and LTO$_{POR}$/LCO cells

Numerical calculations of the discharge process were applied to further understand the impact of material processing and pore microstructure on electrochemical properties and the Li^{+} distribution during discharge for the sintered electrode cells. Details of the model can be found in previous publications. [36-39] The discharge simulations include the voltage profile as a function of time during constant current discharge, and representative experimental discharge curves were selected for comparison from different discharge rates (C/20, C/10 and C/5). The experimental discharge profiles, including their previous C/20 charge profiles, for

LTO_{ICE}/LCO and LTO_{POR}/LCO cells can be found in Appendix 3, Fig. A3.6. For the calculations, a subset of key parameters is listed in Table 4.1, and a more detailed list of all parameters used in the calculations can be found in Appendix 3, Table A3.1. These parameters were either from experimental measurements, supplier/manufacturer data sheets, or published reports[3,13,15,30,31 ,41-50]. In the calculations, the Bruggeman exponent α was used to account for differences in electrode tortuosity and can be modified to incorporate pore alignment effects.[36,37] The relation between tortuosity τ and α are defined by the following equation: $\tau = \epsilon^{1-\alpha}$, where ϵ is the porosity of the electrode.[51] For perfectly aligned pores, the α value is 1.0 and for randomly packed spheres the α value is 1.5.[52] It is noted here that while alignment is one interpretation of changing tortuosity and α values, tortuosity is really an adjustment for the effective conductivity/diffusivity in the electrolyte through the microstructure. Thus, while one context discussed here is the pore alignment impact introduced from the ice templating, other effects such as pore interconnectivity and pore size can also be the phenomena that results in changes in tortuosity. Electrolyte accessibility might also contribute to tortuosity, although if there were inaccessible pores these would additionally result in a decreased porosity in the model – and inaccessible pores were not in the model because these values were not experimentally assessed. The output of the calculations includes not only discharge profiles but also the concentration of Li^+ in both liquid and solid phases as a function of time and electrode depth. Fig. A3.7 and Fig. A3.8 in the Appendix 3 show the comparison of the experimental and calculated discharge profile for LTO_{ICE}/LCO and LTO_{POR}/LCO cells, respectively, at C rates of C/20, C/10, and C/5. Overall, the calculated discharge profiles have a good fit to the experimental data at low rates of discharge. At increasing discharge rates, the initial polarization in the cell matched well between the calculations and experiments, however, the final discharge capacity was predicted to be higher in the calculations compared to the experimental outcomes. An exception was the C/5 discharge process for LTO_{POR}/LCO cell, in which case the calculated capacity was much higher than the experiment results. The detailed origins of the relatively large discrepancy for this particular case are still being investigated and will be discussed in later in this manuscript.

Table 4.1. Parameters of cells used for calculation

Parameters	LTO_{ICE}/LCO	LTO_{POR}/LCO	Source
Thickness of negative electrode/LTO (m)	9.10×10^{-4}	8.95×10^{-4}	Measured
Thickness of positive electrode/LCO (m)	4.57×10^{-4}	4.64×10^{-4}	Measured
Volume fraction of electrolyte in negative electrode	0.57	0.56	Based on measured porosity.
Volume fraction of electrolyte in positive electrode	0.36	0.36	Based on measured porosity.
Bruggeman exponent α for cathode	1.5	1.5	Value for randomly packed spheres
Bruggeman exponent α for anode	1.0	1.5	Value for perfectly aligned pores (1.0) and randomly packed spheres (1.5)

To provide insight into the impact of pore tortuosity during the discharge process, the net change in Li^+ in the cell within the electrode and separator regions relative to the initiation of discharge was extracted from the discharge simulations. Fig. 4.3 and Fig. 4.4 display the total change in Li^+ concentration at different percentages of the discharge capacity delivered for LTO_{ICE}/LCO and LTO_{POR}/LCO cells at different discharge rates. Note that the Li^+ concentration in Fig. 4.3 and Fig. 4.4 is the total concentration including both the solid and electrolyte phase weighted by their volume fractions, with the change in the solid phase generally providing the majority of the change in Li^+.[17,28] In the profiles, the x-axis represents the depth across the electrode region, where 0 mm is the location of cathode (LCO) current collector and the maximum x-axis value corresponds to the location of anode (LTO) current collector. The location of separator is also noted in the figures. The concentration profiles have been normalized by subtracting the concentration profiles at the initiation of the discharge process in that cycle, and thus at 0 % discharge capacity the profile is a horizontal line at a concentration change of zero. The detailed absolute concentration profiles in the electrolyte phase for each relevant condition in Fig. 4.3 and Fig. 4.4 can be found in Appendix 3 Fig. A3.9 and Fig. A3.10 for LTO_{ICE}/LCO and LTO_{POR}/LCO cells, respectively. Relative concentration profiles in solid phase can be also be found in Appendix 3, Fig. A3.11 and Fig. A3.12 for LTO_{ICE}/LCO and LTO_{POR}/LCO cells, respectively.

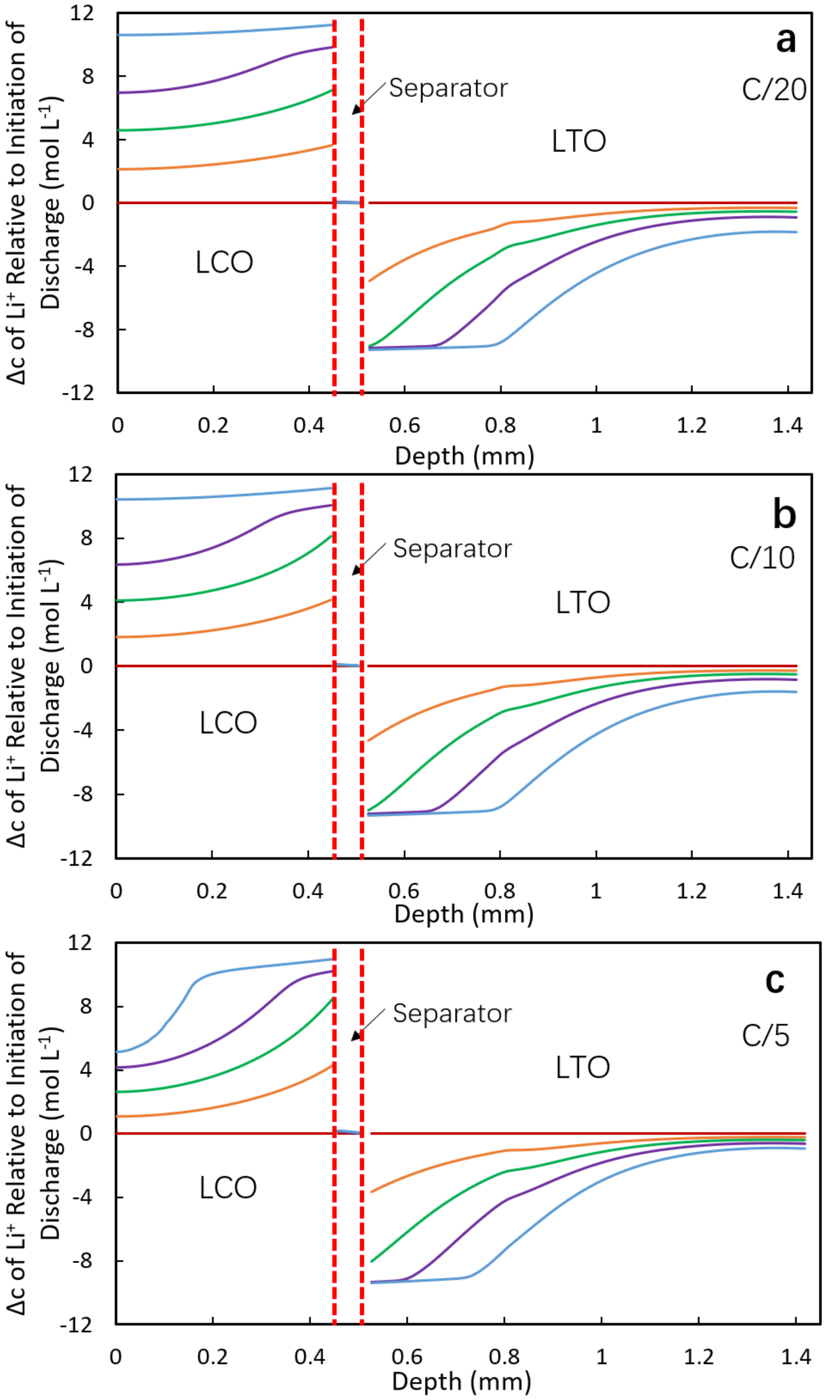

Fig. 4.3. Calculated change in total Li^+ concentration profiles for LTO_{ICE}/LCO cell at (a) C/20, (b) C/10 and (c) C/5 discharge process. The different curves correspond to the different extents of discharge capacity delivered, with the concentrations being shown for 0 % (magenta), 25 % (orange), 50 % (green), 75 % (purple), and 100 % (blue).

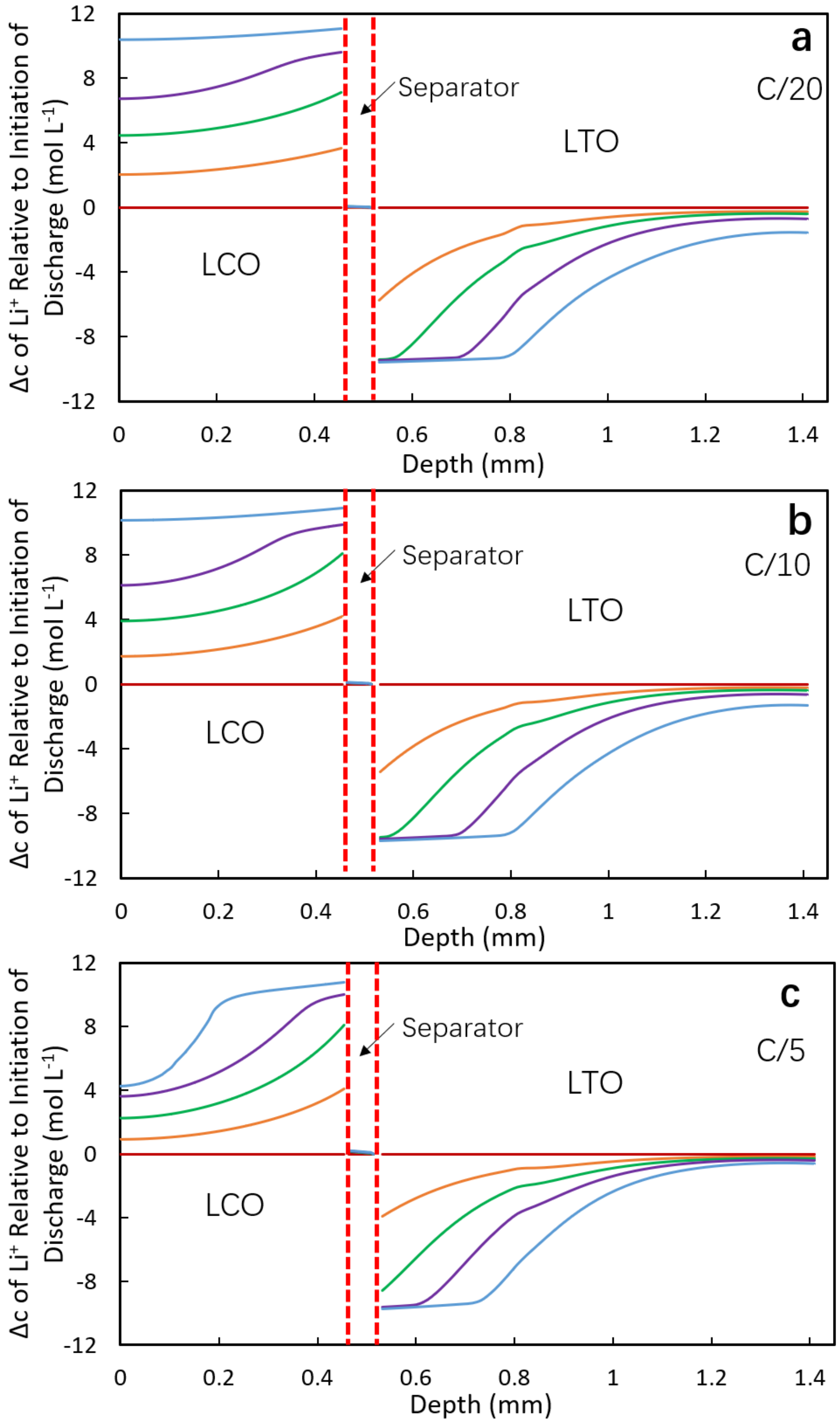

Fig. 4.4. Calculated change in total Li$^+$ concentration profiles for LTO$_{POR}$/LCO cell at (a) C/20, (b) C/10 and (c) C/5 discharge process. The different curves correspond to the different extents of discharge capacity delivered, with the concentrations being shown for 0 % (magenta), 25 % (orange), 50 % (green), 75 % (purple), and 100 % (blue).

In reviewing the calculated profiles for change in Li^+, a few outcomes are highlighted. First, at relatively low rates such as C/20 and C/10, for both LTO_{ICE}/LCO and LTO_{POR}/LCO cells, the Li^+ concentration change in the LCO or cathode regions were similar, with a relatively uniform lithiation during discharge (Fig. 4.3a, 4.3b, 4.4a and 4.4b). A small gradient was noted and more pronounced at certain extents of discharge (e.g., 50 % and 75 % delivered capacity). However, the profiles corresponding to the delithiation process in LTO or anode differed between the two LTO cell types. For LTO_{ICE} anode (Fig. 4.3a and 4.3b), the delithiation initially (e.g. at 25 % delivered capacity) primarily occurred near the separator region, with a gradual decrease in the change in Li^+ concentration towards the LTO current collector side. As the discharge continued for the LTO_{ICE} anode, the region closest to the separator reached its maximum delithiation by 50 % discharge capacity, and a gradient in Li^+ concentration propagated towards the current collector as the discharge capacity reached greater extents. The Li^+ concentration in the region closest to the current collector slowly decreased as the discharge proceeded. For LTO_{POR} pellet (Fig. 4.4a and 4.4b), the delithiation also first occurred at the separator side, but unlike LTO_{ICE}/LCO cell, the delithiation front which propagated toward the current collector had a sharper concentration gradient (Fig. 4.4a and 4.4b). A direct comparison between the profiles shown in Fig. 4.3 and Fig. 4.4 that highlights the gradient change between these two cells can be found in Appendix 3 Fig. A3.13. These observations were consistent with the higher tortuosity of the LTO_{POR} electrode resulting in greater transport restrictions for the Li^+ though the electrolyte phase in the electrode microstructure. These observations for the LTO_{POR} electrode were consistent with previous reports using hydraulically pressed LTO sintered electrodes with more restricted transport of Li^+ in liquid phase relative to having lower tortuosity.[17]

At the higher discharge rate of C/5, the LCO pellets for both cells formed a gradient in Li^+ concentration. The gradient formed during discharge and none of the LCO was fully lithiated at the end of discharge (Fig. 4.3c and 4.4c). This was because at the high discharge rate, the concentration gradient in electrolyte phase increased. At the end of discharge, the Li^+ concentration in electrolyte phase was approximately 0 within regions corresponding to the first 0.1 mm from the current collector into the LCO electrode (Fig. A3.9c and A3.10c). At the end of discharge, the region with minimal lithiation in the LCO pellet for the LTO_{POR}/LCO cell was larger than the region for LTO_{ICE}/LCO cell. This was consistent with the observed higher discharge capacity for the LTO_{ICE}/LCO cell (Fig. 4.2). The lower discharge capacity for the cell with a LTO_{POR} anodes had a greater “trapped” region of inaccessible capacity/Li^+ due to the more restricted mass transport resulting from the higher tortuosity in LTO_{POR} pellets. At C/5, the delithiation process in the LTO region for LTO_{ICE}/LCO cell was similar to the trends observed at lower discharge rates (Fig. 4.3), although less Li^+ moved from LTO to LCO electrode and thus the delithiation gradient did not propagate as far towards the current collector and there was less total discharge capacity delivered relative to lower rates. For LTO_{POR}/LCO cell, the delithiation in LTO_{POR} pellet also showed a sharper gradient. However, the delithiation propagation was limited to closer to the separator region, and there was very little delithiation near the current collector relative to the lower discharge rates. Comparing the concentration profiles in cells with LTO_{ICE} and LTO_{POR} electrodes, the delithiation in LTO_{ICE} was more uniform with a less steep gradient than LTO_{POR} pellet at all discharge rates, which was consistent with reduced tortuosity in the sintered anode will facilitating the Li^+ transport and resulting in higher discharge capacity, particularly at higher rates. The simulated increased discharge capacity at higher rates was consistent with the experimental observations of improved rate capability for cells with LTO_{ICE} electrodes relative to those with LTO_{POR} electrodes (Fig. 4.2).

As stated above, the calculated capacity matched well with the experimental capacity for LTO_{ICE}/LCO cell and for slow rates (C/20 and C/10) for LTO_{POR}/LCO cell. But for the highest rate (C/5), the calculated capacity for the LTO_{POR}/LCO cell was much higher than the experimental data. Some potential causes of this discrepancy are briefly discussed here. In our previous report, the sintered LTO and LCO pellet were directly pressed and fired after being mixed with polyvinyl butyral binder.[17,28] In this work, in order to control the porosity of LTO pellet, sacrificial polystyrene particles were added. After firing, the voids/pores resulting from decomposing polystyrene may be different from those that result from the interstitial particle void regions. This nonuniform and multimodal porosity could result in increased tortuosity in LTO_{POR} pellets.[53,54] To confirm the potential effect of increased LTO_{POR} tortuosity relative to the assumed α=1.5 Bruggeman exponent on LTO_{POR}/LCO electrochemical cell properties, calculations were conducted using higher Bruggeman α exponents for the anode with the intention to match the discharge capacity at C/5. The results are displayed in Fig. A3.14 and showed that when α was set to be 4.0, which was much higher than the value for randomly packed spheres (α=1.5), the calculated capacity was close to the experimental capacity. However, the calculated discharge profile did not match the experimental profile as well, even at slow rates and at the first stages of delivered capacity. Concentration profiles were also calculated for α(LTO_{POR})=4.0 and can be found in Appendix 3 Fig. A3.15. Compared to Fig. 4.4 where α(LTO_{POR})=1.5, the delithiation within LTO_{POR} pellet was more confined to the region near the separator and there was almost no delithiation of the LTO near the current collector, which was caused by higher transport resistance for the increased tortuosity.

While increased tortuosity for the multimodal pore size LTO electrode may account for some of the differences between the experimental and calculated polarization curves and profiles, other factors not accounted for in the simulations likely also contributed to the mismatch. For example, while multimodal pore size may have specifically had an impact on the LTO_{POR} electrode, LTO_{POR} and LTO_{ICE} had very different pore size distributions and connectivity, consistent with the reductions in BET surface area measured with LTO_{ICE} relative to LTO_{POR}. While the sacrificial polystyrene particles were used to match the overall geometric pellet density, matching the detailed pore size distribution and connectivity with and without alignment would be very challenging. Compensating for these other factors would provide further evidence of the impact of pore alignment on transport properties in the electrodes. It is noted that in some ways the electrochemical model accounts for these other factors by accounting for all net transport impacts through modifying effective diffusion/conductivity, however, the relative role of the pore size distribution, pore connectivity, and pore directionality individually were not separated. Also, electrolyte accessibility, which could impact both tortuosity and the total pore volume, was not experimentally assessed. Another possible factor for the deviation between calculation and experiment was the separator deformation due to internal pressure applied by the wave spring in the cell. When increasing the total electrode thickness within the coin cell, the pressure provided by the wave spring on the polymer separator will be higher and the impacts to ion transport resulting from compression of the separator may no longer be negligible. Separator deformation due to compressive loading can result in decreased thickness, lower porosity and higher tortuosity, and the latter two will contribute to increased ion transport restrictions.[55,56] Further research to quantify the pellet tortuosity and to study the behavior of compressed separator are beyond the topic of this work and will be directions for future work. Note that the separator compression is expected to be particularly complex to account for because the ice-templated electrodes are noticeably rougher than the porosity-controlled electrodes, and hydraulically pressed electrodes without porosity control are between these two, which would be expected to result in heterogeneous pinch points on the separator. Despite these limitations, both experiments and calculations supported that applying ice-templating techniques to process sintered electrodes improved the ion transport through the electrode microstructure which significantly improved the rate capability of electrochemical cells using these electrodes.

4.4.4 Neutron imaging radiographs before and after discharge at different rates for LTO_{ICE2}/LCO cell

To provide further comparison between the simulations of sintered electrode cell discharge behavior and experimental cells, neutron imaging was applied to provide experimental support to changes in Li^+ concentration as a function of cell depth *in operando* during discharge. Neutron imaging is a non-destructive technique which passes a low energy neutron beam through a sample and then detects the relative transmitted intensity with a scintillation detector. As ^6Li is a highly attenuating isotope for neutrons, neutron imaging is an ideal technique to track changes in the concentration of Li^+ during charge/discharge processes in Li-ion cells.[29, 57] Details about the set up and data analysis of the neutron imaging experiments in this work can be found in Appendix 3 and previous publications.[17,28] As the LTO electrode used for neutron imaging experiment was slightly different in thickness from the representative cell discussed in previous sessions (Table A3.1), it was denoted as LTO_{ICE2}/LCO cell (LTO_{ICE} thickness: 0.91 mm vs. LTO_{ICE2} thickness: 0.86 mm). Before delivery to NIST, the cell was cycled 8 times to ensure it was functioning properly and then was charged at C/20 to a cell voltage of 2.7 V. At the beginning of the neutron imaging test, the cell was charged again at C/20 to compensate for any capacity lost due to self-discharge between the end of the charge cycle and initiating the neutron experiment (total time that elapsed between the final charge and setting up at NIST was ~24 hours). Then, following this C/20 charge, the cell was discharged at C/10, charged again at C/20 and then discharged at C/5. Unfortunately, a cell containing an LTO_{POR} anode did not have suitable imaging quality for analysis, however, we have previously reported neutron imaging for sintered LTO/LCO cells where the LTO did not have aligned pores.[17,28]

Fig. 4.5a displays the two experimental discharge profiles collected *in operando* during the neutron imaging experiment. The capacities obtained for C/10 and C/5 discharge were 90.5 mAh g^{-1} LCO and 79.0 mAh g^{-1} LCO, respectively, which was consistent with the rate capability achieved with equivalently processed cells described earlier (Fig. 4.2a). Four points at the start and the end of each discharge process are noted in Fig. 4.5a. The neutron images of these points are displayed in Fig. 4.5b. The images were normalized by the ones taken before the short C/20 charge process after the cell was set up. Therefore, the change in the electrode region was highlighted. Since ^{6}Li is a highly attenuating isotope and is expected to be moving during the discharge process, the change in transmission can be related to the change of Li concentration in the electrode. During discharge, the Li^+ will move from LTO electrode to LCO electrode, which will result in a lower Li^+ concentration in LTO electrode than the initial state and vice versa for LCO electrode. Lower Li^+ concentration relative to the initial state will increase the neutron transmission and was represented using red color in the color scale radiograph, while higher Li^+ concentration will decrease the neutron transmission relative to the initial state and was represented by the blue color.

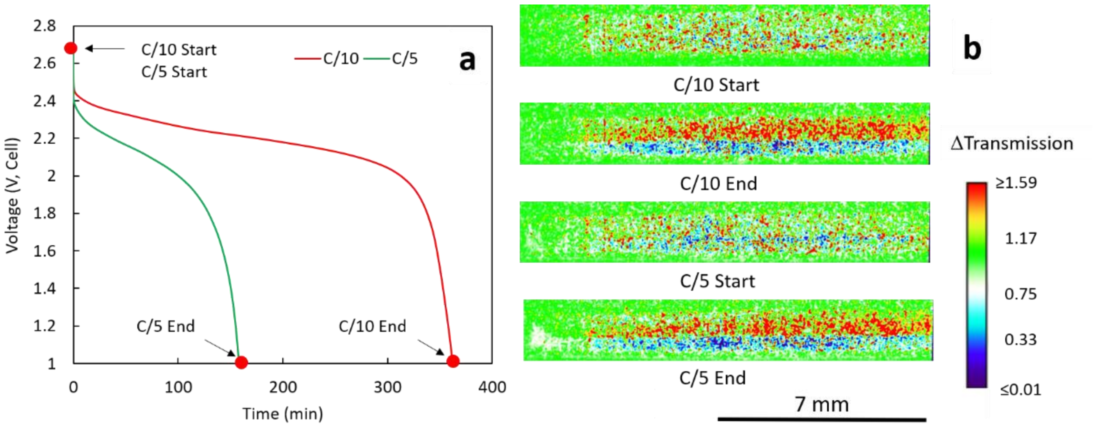

Fig. 4.5. (a) Discharge profiles at C/10 (red) and C/5 (green). (b) Neutron imaging radiographs corresponding to the points noted in (a). A color scale was used to show the relative change in neutron transmission (ΔT). The brightest red regions have ΔT ≥ 1.59 and deepest blue regions have ΔT ≤ 0.01 and do not reflect the absolute maximum or minimum ΔT values.

At the beginning of discharge, the changes in neutron transmission were relatively small (C/10 Start in Fig. 4.5b), although it is noted that these are changes relative to initially setting up the cell and the only net change in Li^+ concentration would be from the 5.1 mAh g^{-1} LCO from the short charge cycle initiated to compensate for any cell self-discharge. After the C/10 discharge, it can be observed that the LTO region became red and LCO region became blue (C/10 End in Fig. 4.5b), indicating the movement of Li^+ from LTO to LCO electrode. Then, after another C/20 charge, the Li^+ moved back and the image of C/5 Start was very similar to C/10 Start. As the charge capacity of the second C/20 charge was 88.6 mAh g^{-1} LCO, almost the same as the previous C/10 discharge capacity (90.5 mAh g^{-1} LCO), it was assumed that the two discharge processes started at the similar lithiation/delithiation condition. Finally, after the C/5 discharge, the net redistribution of Li^+ from the anode to the cathode was again observed. However, while comparing the image of C/5 End to the image of C/10 End, both the red region and the blue region were smaller, which was attributed to the reduction in discharge capacity obtained, i.e., less Li^+ was transferred from anode to cathode.

4.4.5 Comparison of calculated and experimental results for LTO_{ICE2}/LCO cell

To study the Li^+ transport process during discharge in greater detail, three additional extents of discharge (25 %, 50 %, and 75 %) were included in analysis of the neutron imaging profiles. The relevant neutron imaging radiographs of the electrode regions in the cell can be found in Fig. A3.16 and Fig. A3.17 in Appendix 3 for C/10 and C/5 discharge processes, respectively. For quantitative analysis, a 1000-pixel line scan was applied across the electrode region for all selected radiographs, and the average of these 1000 pixels was used to calculate the transmission or change in transmission at each depth location within the cell. To be consistent with the analysis done for calculated concentration profiles and highlight the change of transmission (ΔT) during discharging, all line scan profiles were normalized by the initial transmission profile of the cycle, which resulted in all 0 % discharge capacity profiles becoming horizontal lines. Fig. 4.6a and 4.6b display line scan profiles for the different extents of discharge. In the profiles, the y-axis was reversed for easier comparison to calculated profiles for the total change in Li$^+$ because negative ΔT indicates higher Li$^+$ concentration in LCO region and vice versa for LTO region.

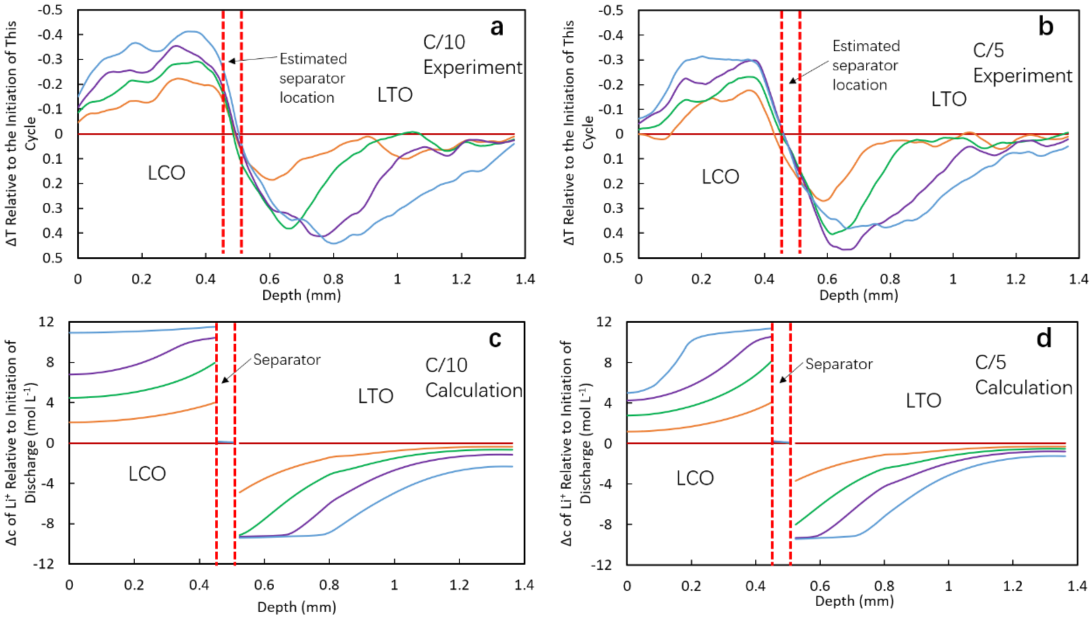

Fig. 4.6. Normalized transmission profiles for LTO$_{ICE2}$/LCO cell at discharge rates of (a) C/10 and (b) C/5, and comparative calculated profiles of the changes in relative Li$^+$ concentration for LTO$_{ICE2}$/LCO cell at (c) C/10 and (d) C/5. The different curves correspond to the different extents of discharge capacity delivered, with the concentrations being shown for 0 % (magenta), 25 % (orange), 50 % (green), 75 % (purple), and 100 % (blue).

The discharge process of LTO$_{ICE2}$/LCO cell was calculated for comparison with experimental neutron imaging results. The parameters used for calculation and the comparison of discharge profiles can be found in Table A3.1 and Fig. A3.18 in Appendix 3. The calculation results were very similar to the representative LTO_{ICE}/LCO cell discussed in previous sessions because the only difference between these two cells was a slight change in the LTO electrode thickness (Table A3.1). The calculated concentration profiles are displayed in Fig. 4.6c and Fig. 4.6d. Compared with the experimental transmission profiles, the calculated results show good agreement. In the LCO region, at both C/10 and C/5, the lithiation was relatively uniform with a gradient slowly formed during discharge. For both experimental and calculated results, the lithiation near the current collector of the LCO at C/5 did not reach completion, which was caused by the Li^+ transport limitations at the increased rate. For the LTO region, results at both rates showed a consistent gradient forming during discharge which propagated towards the current collector. Therefore, the neutron imaging results confirmed that the calculation reflected the Li^+ transport and redistribution processes occurring during discharge for the C rates investigated.

4.5 Conclusions

In this work, the electrochemical and transport properties of sintered electrodes were compared between ice-templated electrodes with aligned pore structures and hydraulically pressed electrodes which had random interconnected pores but had the geometric pellet density matched to the ice-templated electrodes using sacrificial additive particles. Electrochemical charge/discharge at increasing rates confirmed that coin cells containing electrodes processed using the ice-templating technique had significantly better retention of capacity at higher discharge rates. This outcome was explained in the context of the improved ion transport through the electrode microstructure due to the reduced tortuosity, with on possibility being that the tortuosity reduction was the result of aligned pore microstructures. The impact of the improved ion transport was further supported by numerical simulations of the discharge process, which for many cases matched the experimental outcomes well. In addition, neutron imaging on a cell containing an ice-templated electrode provided evidence for the concentration profile associated with Li^+ redistribution during discharge, which also was matched with Li^+ concentration changes calculated from simulations. Overall, this study provides support for the significant improvements in mitigating ion transport limitations in thick electrodes that can be made by ice-templated microstructures.

4.6 Acknowledgement

This research was supported by the National Science Foundation, via grants CBET-1652488 and CMMI-1825216. NIST authors acknowledge supported from the U.S. Department of Commerce, the NIST Radiation Physics Division, the Director's office of NIST, and the NIST Center for Neutron Research, and thank Mr. Eli Baltic for assistance with experimental setup. The authors thank Patrick McCormack for running the TGA measurements and Prof. Geoff Geise for use of their TGA instrument.

4.7 References

(1) Etacheri, V.; Marom, R.; Elazari, R.; Salitra, G.; Aurbach, D. Challenges in the Development of Advanced Li-Ion Batteries: A Review. *Energy Environ. Sci.* **2011**, *4*, 3243.

(2) Abraham, K. M. Prospects and Limits of Energy Storage in Batteries. *J. Phys. Chem. Lett.* **2015**, *6*, 830–844.

(3) Goodenough, J. B.; Park, K.-S. The Li-Ion Rechargeable Battery: A Perspective. *J. Am. Chem. Soc.* **2013**, *135*, 1167–1176.

(4) Nitta, N.; Wu, F.; Lee, J. T.; Yushin, G. Li-Ion Battery Materials: Present and Future. *Mater. Today* **2015**, *18*, 252–264.

(5) Chen, Z.; Dahn, J. R. Reducing Carbon in $LiFePO_4$/C Composite Electrodes to Maximize Specific Energy, Volumetric Energy, and Tap Density. *J. Electrochem. Soc.* **2002**, *149*, A1184.

(6) Robinson, J. P.; Ruppert, J. J.; Dong, H.; Koenig, G. M., Jr. Sintered Electrode Full Cells for High Energy Density Lithium-Ion Batteries. *J. Appl. Electrochem.* **2018**, *48*, 1297–1304.

(7) Zhang, X.; Ju, Z.; Housel, L. M.; Wang, L.; Zhu, Y.; Singh, G.; Sadique, N.; Takeuchi, K. J.; Takeuchi, E. S.; Marschilok, A. C.; Yu, G. Promoting Transport Kinetics in Li-Ion Battery with Aligned Porous Electrode Architectures. *Nano Lett.* **2019**, *19*, 8255–8261.

(8) Zheng, H.; Li, J.; Song, X.; Liu, G.; Battaglia, V. S. A Comprehensive Understanding of Electrode Thickness Effects on the Electrochemical Performances of Li-Ion Battery Cathodes. *Electrochim. Acta* **2012**, *71*, 258–265.

(9) Parai, R.; Walters, T.; Marin, J.; Pagola, S.; Koenig, G. M., Jr; Ghosh, D. Strength Enhancement in Ice-Templated Lithium Titanate Li4Ti5O12 Materials Using Sucrose. *Materialia* **2020**, *14*, 100901.

(10) Bae, C.-J.; Erdonmez, C. K.; Halloran, J. W.; Chiang, Y.-M. Design of Battery Electrodes with Dual-Scale Porosity to Minimize Tortuosity and Maximize Performance. *Adv. Mater.* **2013**, *25*, 1254–1258.

(11) Wu, X.; Xia, S.; Huang, Y.; Hu, X.; Yuan, B.; Chen, S.; Yu, Y.; Liu, W. High-performance, Low-

cost, and Dense-structure Electrodes with High Mass Loading for Lithium-ion Batteries. *Adv. Funct. Mater.* **2019**, *29*, 1903961.

(12) Sotomayor, M. E.; Torre-Gamarra, C. de la; Levenfeld, B.; Sanchez, J.-Y.; Varez, A.; Kim, G.-T.; Varzi, A.; Passerini, S. Ultra-Thick Battery Electrodes for High Gravimetric and Volumetric Energy Density Li-Ion Batteries. *J. Power Sources* **2019**, *437*, 226923.

(13) Ménétrier, M.; Saadoune, I.; Levasseur, S.; Delmas, C. The Insulator-Metal Transition upon Lithium Deintercalation from $LiCoO_2$: Electronic Properties and ^{7}Li NMR Study. *J. Mater. Chem.* **1999**, *9*, 1135–1140.

(14) Colclasure, A. M.; Tanim, T. R.; Jansen, A. N.; Trask, S. E.; Dunlop, A. R.; Polzin, B. J.; Bloom, I.; Robertson, D.; Flores, L.; Evans, M.; Dufek, E. J.; Smith, K. Electrode Scale and Electrolyte Transport Effects on Extreme Fast Charging of Lithium-Ion Cells. *Electrochim. Acta* **2020**, *337*, 135854.

(15) Young, D.; Ransil, A.; Amin, R.; Li, Z.; Chiang, Y.-M. Electronic Conductivity in the $Li_{4/3}Ti_{5/3}O_4$-$Li_{7/3}Ti_{5/3}O_4$ System and Variation with State-of-Charge as a Li Battery Anode. *Adv. Energy Mater.* **2013**, *3*, 1125–1129.

(16) Wang, K.-X.; Li, X.-H.; Chen, J.-S. Surface and Interface Engineering of Electrode Materials for Lithium-Ion Batteries. *Adv. Mater.* **2015**, *27*, 527–545.

(17) Nie, Z.; Ong, S.; Hussey, D. S.; LaManna, J. M.; Jacobson, D. L.; Koenig, G. M. Probing Transport Limitations in Thick Sintered Battery Electrodes with Neutron Imaging. *Mol. Syst. Des. Eng.* **2020**, *5*, 245–256.

(18) Lu, L.-L.; Lu, Y.-Y.; Xiao, Z.-J.; Zhang, T.-W.; Zhou, F.; Ma, T.; Ni, Y.; Yao, H.-B.; Yu, S.-H.; Cui, Y. Wood-Inspired High-Performance Ultrathick Bulk Battery Electrodes. *Adv. Mater.* **2018**, *30*, e1706745.

(19) Billaud, J.; Bouville, F.; Magrini, T.; Villevieille, C.; Studart, A. R. Magnetically Aligned Graphite Electrodes for High-Rate Performance Li-Ion Batteries. *Nat. Energy* **2016**, *1*, 16097.

(20) Jeong, H.; Lim, S.-J.; Chakravarthy, S.; Kim, K. H.; Lee, J.; Heo, J. S.; Park, H. Three-Dimensional Cathode with Periodically Aligned Microchannels for Improving Volumetric Energy Density of Lithium-Ion Batteries. *J. Power Sources* **2020**, *451*, 227764.

(21) Deville, S. Ice-Templating, Freeze Casting: Beyond Materials Processing. *J. Mater. Res.* **2013**, *28*, 2202–2219.

(22) Banda, M.; Ghosh, D. Effects of Temperature and Platelets on Lamella Wall Microstructure, Structural Stability, and Compressive Strength in Ice-Templated Ceramics. *Materialia* **2020**, *9*, 100537.

(23) Ju, Z.; Zhu, Y.; Zhang, X.; Lutz, D. M.; Fang, Z.; Takeuchi, K. J.; Takeuchi, E. S.; Marschilok, A. C.; Yu, G. Understanding Thickness-Dependent Transport Kinetics in Nanosheet-Based Battery Electrodes. *Chem. Mater.* **2020**, *32*, 1684–1692.

(24) Delattre, B.; Amin, R.; Sander, J.; De Coninck, J.; Tomsia, A. P.; Chiang, Y.-M. Impact of Pore Tortuosity on Electrode Kinetics in Lithium Battery Electrodes: Study in Directionally Freeze-Cast $LiNi_{0.8}Co_{0.15}Al_{0.05}O_2$(NCA). *J. Electrochem. Soc.* **2018**, *165*, A388–A395.

(25) Azami-Ghadkolai, M.; Yousefi, M.; Allu, S.; Creager, S.; Bordia, R. Effect of Isotropic and Anisotropic Porous Microstructure on Electrochemical Performance of Li Ion Battery Cathodes: An Experimental and Computational Study. *J. Power Sources* **2020**, *474*, 228490.

(26) Huang, C.; Grant, P. S. Coral-like Directional Porosity Lithium Ion Battery Cathodes by Ice Templating. *J. Mater. Chem. A Mater. Energy Sustain.* **2018**, *6*, 14689–14699.

(27) Kardjilov, N.; Manke, I.; Hilger, A.; Strobl, M.; Banhart, J. Neutron Imaging in Materials Science. *Mater. Today* **2011**, *14*, 248–256.

(28) Nie, Z.; McCormack, P.; Bilheux, H. Z.; Bilheux, J. C.; Robinson, J. P.; Nanda, J.; Koenig, G. M., Jr. Probing Lithiation and Delithiation of Thick Sintered Lithium-Ion Battery Electrodes with Neutron Imaging. *J. Power Sources* **2019**, *419*, 127–136.

(29) Siegel, J. B.; Lin, X.; Stefanopoulou, A. G.; Hussey, D. S.; Jacobson, D. L.; Gorsich, D. Neutron Imaging of Lithium Concentration in LFP Pouch Cell Battery. *J. Electrochem. Soc.* **2011**, *158*, A523.

(30) Qi, Z.; Koenig, G. M., Jr. High-Performance $LiCoO_2$ Sub-Micrometer Materials from Scalable Microparticle Template Processing. *ChemistrySelect* **2016**, *1*, 3992–3999.

(31) Qi, Z.; Koenig, G. M., Jr. A Carbon-Free Lithium-Ion Solid Dispersion Redox Couple with Low Viscosity for Redox Flow Batteries. *J. Power Sources* **2016**, *323*, 97–106.

(32) Tuin, G.; Peters, A. C. I.; van Diemen, A. J. G.; Stein, H. N. Preparation of Large Monodisperse Polystyrene Particles by a One Step Surfactant-Free Emulsion Polymerization. *J. Colloid Interface Sci.* **1993**, *158*, 508–510.

(33) Ghosh, D.; Dhavale, N.; Banda, M.; Kang, H. A Comparison of Microstructure and Uniaxial Compressive Response of Ice-Templated Alumina Scaffolds Fabricated from Two Different Particle Sizes. *Ceram. Int.* **2016**, *42* (14), 16138–16147.

(34) Cao, Y.; Wang, Y.; Zhu, Y.; Chen, H.; Li, Z.; Ding, J.; Chi, Y. Fabrication of Anatase Titania Inverse Opal Films Using Polystyrene Templates. *Superlattices Microstruct.* **2006**, *40* (3), 155–160.

(35) Malhotra, S. Thermal Decomposition of Polystyrene. *Polymer* **1975**, *16*, 81–93.

(36) Doyle, M.; Fuller, T. F.; Newman, J. Modeling of Galvanostatic Charge and Discharge of the Lithium/Polymer/Insertion Cell. *J. Electrochem. Soc.* **1993**, *140*, 1526–1533.

(37) Fuller, T. F.; Doyle, M.; Newman, J. Simulation and Optimization of the Dual Lithium Ion Insertion Cell. *J. Electrochem. Soc.* **1994**, *141*, 1–10.

(38) Fuller, T. F.; Doyle, M.; Newman, J. Relaxation Phenomena in Lithium-Ion-Insertion Cells. *J. Electrochem. Soc.* **1994**, *141*, 982–990.

(39) Cai, C.; Nie, Z.; Robinson, J. P.; Hussey, D. S.; LaManna, J. M.; Jacobson, D. L.; Koenig, G. M., Jr. Thick Sintered Electrode Lithium-Ion Battery Discharge Simulations: Incorporating Lithiation-Dependent Electronic Conductivity and Lithiation Gradient Due to Charge Cycle. *J. Electrochem. Soc.* **2020**, *167*, 140542.

(40) Hussey, D. S.; Jacobson, D. L.; Arif, M.; Coakley, K. J.; Vecchia, D. F. In Situ Fuel Cell Water Metrology at the NIST Neutron Imaging Facility. *J. Fuel Cell Sci. Technol.* **2010**, *7*, 021024.

(41) Zaghib, K.; Simoneau, M.; Armand, M.; Gauthier, M. Electrochemical Study of $Li_4Ti_5O_{12}$ as Negative Electrode for Li-Ion Polymer Rechargeable Batteries. *J. Power Sources* **1999**, *81–82*, 300–305.

(42) Xie, J.; Imanishi, N.; Matsumura, T.; Hirano, A.; Takeda, Y.; Yamamoto, O. Orientation Dependence of Li–Ion Diffusion Kinetics in LiCoO2 Thin Films Prepared by RF Magnetron Sputtering. *Solid State Ion.* **2008**, *179*, 362–370.

(43) Levasseur, S. Evidence for Structural Defects in Non-Stoichiometric HT-$LiCoO_2$: Electrochemical, Electronic Properties and ^{7}Li NMR Studies. *Solid State Ion.* **2000**, *128*, 11–24.

(44) Kataoka, K.; Takahashi, Y.; Kijima, N.; Akimoto, J.; Ohshima, K.-I. Single Crystal Growth and Structure Refinement of $Li_4Ti_5O_{12}$. *J. Phys. Chem. Solids* **2008**, *69*, 1454–1456.

(45) Mao, J.; Tiedemann, W.; Newman, J. Simulation of Li-Ion Cells by Dualfoil Model under Constant-Resistance Load. *ECS Trans.* **2014**, *58*, 71–81.

(46) Habte, B. T.; Jiang, F. Microstructure Reconstruction and Impedance Spectroscopy Study of $LiCoO_2$, $LiMn_2O_4$ and $LiFePO_4$ Li-Ion Battery Cathodes. *Microporous Mesoporous Mater.* **2018**, *268*, 69–76.

(47) Chen, J.; Yang, L.; Fang, S.; Hirano, S.-I.; Tachibana, K. Synthesis of Hierarchical Mesoporous Nest-like $Li_4Ti_5O_{12}$ for High-Rate Lithium Ion Batteries. *J. Power Sources* **2012**, *200*, 59–66.

(48) Landesfeind, J.; Hattendorff, J.; Ehrl, A.; Wall, W. A.; Gasteiger, H. A. Tortuosity Determination of Battery Electrodes and Separators by Impedance Spectroscopy. *J. Electrochem. Soc.* **2016**, *163*, A1373–A1387.

(49) Capiglia, C.; Saito, Y.; Kageyama, H.; Mustarelli, P.; Iwamoto, T.; Tabuchi, T.; Tukamoto, H. ^{7}Li and ^{19}F Diffusion Coefficients and Thermal Properties of Non-Aqueous Electrolyte Solutions for Rechargeable Lithium Batteries. *J. Power Sources* **1999**, *81–82*, 859–862.

(50) Nyman, A.; Behm, M.; Lindbergh, G. Electrochemical Characterisation and Modelling of the Mass Transport Phenomena in $LiPF_6$–EC–EMC Electrolyte. *Electrochim. Acta* **2008**, *53*, 6356–6365.

(51) Thorat, I. V.; Stephenson, D. E.; Zacharias, N. A.; Zaghib, K.; Harb, J. N.; Wheeler, D. R. Quantifying Tortuosity in Porous Li-Ion Battery Materials. *J. Power Sources* **2009**, *188*, 592–600.

(52) Robert, E.; Tobias, C. W. On the Conductivity of Dispersions. *J. Electrochem. Soc.* **1959**, *106*, 827.

(53) Fang, R.; Ge, H.; Wang, Z.; Li, Z.; Zhang, J. A Two-Dimensional Heterogeneous Model of Lithium-Ion Battery and Application on Designing Electrode with Non-Uniform Porosity. *J. Electrochem. Soc.* **2020**, *167*, 130513.

(54) Prachayawarakorn, S.; Mann, R. Effects of Pore Assembly Architecture on Catalyst Particle Tortuosity and Reaction Effectiveness. *Catal. Today* **2007**, *128*, 88–99.

(55) Lagadec, M. F.; Zahn, R.; Wood, V. Designing Polyolefin Separators to Minimize the Impact of Local Compressive Stresses on Lithium Ion Battery Performance. *J. Electrochem. Soc.* **2018**, *165*, A1829–A1836.

(56) Yan, S.; Huang, X.; Xiao, X. Measurement of the through Thickness Compression of a Battery Separator. *J. Power Sources* **2018**, *382*, 13–21.

(57) Zhou, H.; An, K.; Allu, S.; Pannala, S.; Li, J.; Bilheux, H. Z.; Martha, S. K.; Nanda, J. Probing Multiscale Transport and Inhomogeneity in a Lithium-Ion Pouch Cell Using in Situ Neutron Methods. *ACS Energy Lett.* **2016**, *1*, 981–986.

Chapter 5

Improving High Rate Cycling Limitations of Thick Sintered Battery Electrodes by Mitigating Molecular Transport Limitations through Modifying Electrode Microstructure and Electrolyte Conductivity

5.1 Abstract

For batteries, thicker electrodes increase energy density, however, molecular transport limits the rate of charge/discharge for extracting large fractions of available energy. Mitigating transport limitations by increasing electrolyte conductivity and aligning the pores in the electrode microstructure will be described.

The content of this chapter has been published in the following journal:

Nie, Z.; Parai, R.; Cai, C.; Ghosh, D.; Koenig, G. M. Improving High Rate Cycling Limitations of Thick Sintered Battery Electrodes by Mitigating Molecular Transport Limitations through Modifying Electrode Microstructure and Electrolyte Conductivity. *Mol. Syst. Des. Eng.* **2021**, *6* (9), 708–712.

5.2 Introduction

Lithium-ion (Li-ion) batteries have received great research interest due to their relatively high energy and power density.[1,2] Although Li-ion batteries have been successfully commercialized and used in many applications, further improvements are still necessary as energy storage demands are ever increasing.[3,4] Often gains are made in energy and power density though new electrode materials or cell chemistry.[5-9] However, improvements in desired cell properties can also be achieved by engineering the electrode structure and/or using electrolytes with different transport characteristics.[10-12] Commercial Li-ion batteries use composite electrodes. These thin film (typically <100 μm)[13] composites are coated on metal current collectors and consist of active material that undergoes electrochemical reactions, conductive additives to improve electronic conductivity and polymer binders to maintain the electrode integrity.[14,15] Therefore, at the cell level, increasing electrode thickness and reducing inactive additives are routes to increase energy density. However, the inactive components in composite electrode pores greatly increase tortuosity and restrict ion transport at increased thicknesses.[16] One alternative electrode architecture recently explored includes only electroactive material free of additives, which undergoes a heat treatment to improve the mechanical strength of the porous pellet. These will be referred to as “sintered” electrodes, and such processing has been used to fabricate relatively thick electrodes, in some cases exceeding 1,500 μm.[17-19]

While sintered electrodes do not have inactive components in the interstitial regions between electroactive particles, the electrodes are still very thick and thus previous reports have suggested the long molecular transport path length for Li^+ through the microstructure limits the ability to achieve high active material utilization (e.g., capacity) and high rates of charge/discharge.[20,21] To mitigate this liquid phase ion transport limitation while maintaining thick and high energy density electrodes, there are two main routes to pursue: engineer the electrode microstructure to facilitate improved molecular transport,[22 - 24] or modify the molecular composition of the electrolyte to use an electrolyte with higher ionic conductivity (and/or Li^+ transference number).[25,26] From an electrode microstructure standpoint, typically the goal is to process electrodes such that the pores are aligned in the direction of net Li^+ flux during charge/discharge, such that the tortuosity is reduced and mass transport limitations are alleviated. To achieve such engineered microstructures (both for sintered and composite electrodes), techniques have included templating pores/voids using ice,[22] magnetic fields[23] and wood.[24] Higher electrolyte conductivity, and in some cases concentration, can also mitigate Li^+ transport limitations through the electrode microstructure and facilitate faster charge/discharge for battery electrodes in general.[27] In previous publications, hydraulically pressed and sintered $LiCoO_2$ (LCO) cathodes and $Li_4Ti_5O_{12}$ (LTO) anodes were cycled in battery cells and transport processes were inferred using electrochemical and neutron imaging measurements combined with simulations.[20, 28] Recently, the advantages of ice-templated sintered electrodes with regards to rate capability (and speculated to result from improved transport through the electrode microstructure) were reported.[22] In this work, the impact of higher ionic conductivity electrolytes, in isolation and in combination with ice-templating to facilitate aligning the pores/voids in the electrode microstructure, on the retention of capacity at increasing rates of charge/discharge for sintered electrode LTO/LCO full cells will be reported. As the thick sintered electrodes have been reported to be limited by the process of ion transport through the electrode microstructure, both the microstructure templating and change in electrolyte were expected to improve the rate capability of the cells, and the effects of these changes in isolation and combination will be reported and were found to be substantive.

5.3 Results and discussion

As mentioned earlier, the capacity retention for thick sintered electrodes at increasing charge/discharge rates and current densities (i.e., rate capability) has for many cases been reported to be limited by Li^+ transport through the electrolyte-laden porous electrode microstructure. One way to improve on Li^+ transport limitations is to change the electrolyte used in the cell to increase the ionic conductivity. For this study, the electrolyte investigated contained lithium bis(fluorosulfonyl)imide (LiFSI) as the primary salt dissolved in dimethyl carbonate (DMC). LiFSI was chosen as it has previously been investigated as an electrolyte for high rate battery applications,[29,30] and DMC was chosen as it has relatively low viscosity.[25,26] Factors such as electrolyte viscosity and its interactions with the electrode components (e.g., wetting and contact angle) have previously been demonstrated as important for electrolyte transport properties.[26,29,31] $LiPF_6$ at 0.5 mol L^{-1} was also added to all LiFSI electrolytes, to mitigate any potential corrosion of the current collector. A $LiPF_6$-based commercial electrolyte (denoted in this work as GEN2, which was 1.2 mol L^{-1} $LiPF_6$ in 3:7 (w/w) ethylene carbonate (EC)/ethyl methyl carbonate (EMC)) was also used as a baseline comparison, and its conductivity as a function of $LiPF_6$ molarity can be found in Supporting Information, Fig. A4.1.[32] The LiFSI-based electrolyte compositions used in this study can be found in Table 5.1.

The ionic conductivity as a function of concentration for the three different LiFSI:LiPF$_6$ ratios used can be found in Fig. 5.1. The blue dots in Fig. 5.1 correspond to the locations for the total Li$^+$ concentrations and measured ionic conductivities for the three electrolytes. The electrolytes are referred to as HIGH (the highest concentration of the three, 2.5 mol L^{-1} Li$^+$ and 6:1 LiFSI:LiPF$_6$), LOW (the lowest concentration of the three, 1.3 mol L^{-1} Li$^+$ and 2:1 LiFSI:LiPF$_6$), and PEAK (located near the peak in ionic conductivity, with 2.0 mol L^{-1} Li$^+$ and 4:1 LiFSI:LiPF$_6$). Additional experimental details on electrolyte preparation can be found in Supporting Information (including ref. 33, 34). The measured conductivity as a function of Li$^+$ concentration was similar for the 3 different FSI$^-$:PF$_6^-$ ratios, although the electrolyte with the higher relative PF$_6^-$ concentration was slightly lower at a given Li$^+$ molarity. Overall, the conductivities were similar to previous reports for pure LiFSI in DMC solution.[29]

Table 5.1. Composition of LiFSI-based electrolytes used

Electrolyte	Li$^+$ concentration (mol L^{-1})	LiFSI:LiPF$_6$ (mol:mol)
HIGH	2.5	6:1
PEAK	2.0	4:1
LOW	1.3	2:1

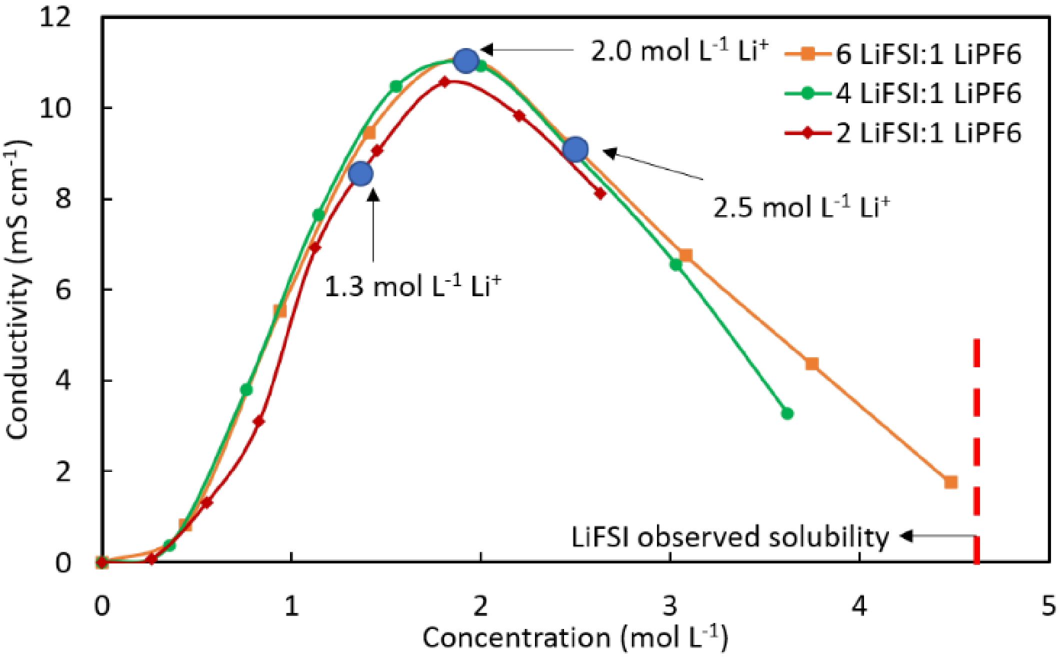

Fig. 5.1. Ionic conductivity as a function of total Li^+ concentration for molar ratios of $LiFSI:LiPF_6$ salt added of 6:1 (orange squares), 4:1 (green circles), and 2:1 (red diamonds). Lines added to guide the eye. The three LiFSI-based electrolytes used in this study are indicated at the blue circle locations. The observed solubility for LiFSI is noted at the concentration where there is a vertical red dashed line.

To evaluate impact of the different electrolytes on rate capability of sintered electrode full cells, coin cells were fabricated where the only difference was the electrolyte used (PEAK, LOW, HIGH, or GEN2). Details of the electrode material and electrode fabrication can be found in Supporting and in previous publications.[20,22,28, 35 - 38] The LTO anodes were approximately 0.19 g, 900 µm thick, and had a geometric porosity/void volume fraction of 55 %; The LCO cathodes were approximately 0.19 g, 450 mm thick and had a geometric porosity/void volume fraction of 40 %. It is noted that lower pore volume fractions would be desirable to increase electrode and cell energy density, especially for the LTO; however, the LTO porosity was near the limit of what was achievable for the slurry conditions used for the freeze-casting process to direct the microstructure. The geometric area of the all electrodes was ~1.33 cm^2, and the reversible low rate (C/50 charge and discharge, or 0.43 mA cm^{-2}) capacity for all cells was similar (ranging 123 to 129 mAh g^{-1} LCO, or 23.5 to 24.6 mAh). For all cells, after initial slow cycling at C/50 charge/discharge, rate capability was performed by charging at C/20 and discharging at the indicated rate with the discharge capacity retention noted in Fig. 5.2a for the indicated electrolytes (discharge capacity on a total and LCO gravimetric bases can be found in Supporting Information, Fig. A4.2). Each cycling data point was averaged from outcomes of 5 cycles at each rate for at least two nominally identical cells for each electrode-electrolyte combination.

For Fig. 5.2a, the discharge capacity retention was relative to the capacity delivered at C/20 discharge. As is generally the case, the discharge capacity was reduced as the rate of discharge increased, and C/20 cycling after the rate capability testing ("C/20* in Fig. 5.2a) indicated capacity losses were not due to capacity fade but were consistent with other processes within the cell limiting achievable capacity at increasing rate/current density. Further evidence supporting cycling stability was through cycle life testing of sintered LTO/LCO cells with GEN2 and PEAK electrolyte (Supporting Information, Fig. A4.3). After the rate capability testing, the capacity retention for an additional 100 cycles for both GEN2 and PEAK cells was above 90%. The discharge capacities for the different electrolytes started to separate even at C/10, and at C/5 and C/2.5 it became clear that the order of rate capability for the cells was PEAK>HIGH>GEN2>LOW from the best to the worst. With regards to the three LiFSI-based electrolytes, the rate capability outcomes were consistent with ion conduction through the electrolyte being the rate limiting process. The PEAK electrolyte had the highest initial conductivity, consistent with the highest rate capability if Li^+ transport was the limiting process. In addition, during discharge Li^+ deintercalated from the LTO solid phase, traversed to the cathode via the liquid electrolyte, and intercalated into the LCO solid phase. This resulted in a concentration gradient in the electrolyte where there was a relatively high concentration of Li^+ in regions where reactions were occurring in the LTO anode and a relatively low concentration of Li^+ in regions where reactions were occurring in the LCO cathode.[20,28] Thus, there were gradients in concentration (and conductivity) throughout the cell depth and areas of extreme depletion would result in polarization that results in reaching the cut off voltage and ending the discharge. From the initial conductivity/concentration point for PEAK, there was a significant buffer in either direction of Li^+ concentration of relatively high conductivity, which would help with retaining rate capability for a large concentration gradient due to high Li^+ flux at high rate. The influence of the likely effect of concentration gradient that develops during discharge was more pronounced for LOW and HIGH, where the as-prepared ionic conductivities were similar, but where in regions of Li^+ depletion during discharge the LOW conductivity will drop much faster than the HIGH conductivity drops for regions where the Li^+ concentration was increasing (and much bigger Li^+ concentration swings would be needed for effects from high Li^+ concentration in LOW or low Li^+ concentration in HIGH). GEN2 was provided as a baseline because this has been the electrolyte in previous sintered electrode full cell reports.[17,20] Note that relative to GEN2, PEAK had much higher capacity retention at increasing rates: 62 vs. 83 % at C/5 (4.3 mA cm^{-2}) and 38 vs. 58 % at C/2.5 (8.6 mA cm^{-2}), consistent with significant benefits of improving electrolyte conductivity for mitigating transport limitations in thick sintered electrodes.

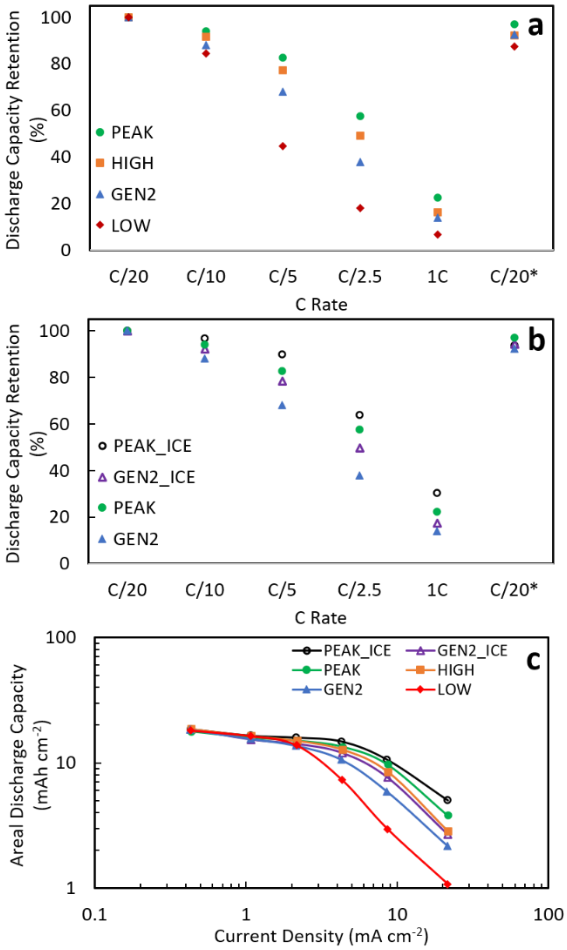

Fig. 5.2. (a) Discharge capacity retention at the indicated different discharge rates for LTO/LCO sintered cells containing the electrolytes described in the text and Table 5.1: Peak (green circles), HIGH (orange squares), LOW (red diamonds), and GEN2 (blue triangles). (b) Discharge capacity retention at the indicated different discharge rates for LTO/LCO sintered cells containing the electrolytes PEAK and GEN2, where the cases where the LTO was ice-templated and paired with the PEAK (black border circle) and GEN2 (purple border triangle) have been added. (c) Areal discharge capacity delivered as a function of current density for all cells in this report, where the symbols correspond to the same cells as described in (a) and (b). For (a) and (b), all charge cycles were at C/20, and the * represents C/20 discharge cycles after the rate capability test was completed. For (c), lines have been added to guide the eye.

As described earlier, another route to improve transport through the electrode microstructure is the provide directional porosity in the direction of the net flux of Li^+ transport during charge/discharge.[22-24] Towards this end, the pores in the electrode microstructure for the thicker LTO electrode were aligned via ice-templating, also known as freeze-casting, and two of the electrolyte formulations had rate capability evaluation paired with ice-templated LTO electrodes (LCO electrodes for all cells used in this study were processed using the same methods/processes). Details on the ice-templating process can be found in the Supporting Information and previous reports.[39-41] In previous studies, ice-templated LTO was found to improve the rate capability of sintered electrodes, consistent with mitigating the rate limiting Li^+ mass transport processes.[22] In that previous report, GEN2 was used as the electrolyte, and thus GEN2 electrolyte with an ice-templated electrolyte was evaluated (noted as GEN2_ICE). The other electrolyte evaluated with an ice-templated LTO anode was the one with the highest rate capability from earlier (PEAK, Fig. 5.2a), and this combination was referred to as PEAK_ICE. As shown in Fig. 5.2b, for both electrolytes the retention of capacity at increasing rates was greater for the ice-templated electrodes relative to those that did not have templated directional porosity (e.g., GEN2_ICE>GEN2 and PEAK_ICE>PEAK). This was consistent with previous results that ice-templated microstructures with aligned pores facilitated improved rate capability, which was interpreted in the context of improved ion transport through the electrode microstructure mitigating the limiting process in the electrochemical cell.[22]

To further demonstrate the improvements of higher conductivity electrolytes and ice-templated microstructures for thick sintered electrode batteries, a Ragone plot of areal capacity dependence on areal current density during discharge for all cells used in this report is shown in Fig. 5.2c. This is the same cycling data as Fig. A4.2 with the rate and capacity on areal basis and mA/mAh outputs. The advantages of mitigated Li^+ transport limitations through both ice-templating and a higher conductivity electrolyte (PEAK_ICE) relative to the baseline electrolyte with both electrodes processed via hydraulic pressing (GEN2) is apparent at increasing rates. For example, at 8.6 mA cm^{-2} the discharge capacity of GEN2 was 5.9 mAh cm^{-2}, while the capacity of PEAK_ICE was 10.5 mAh cm^{-2}. Relative to other published results for high electrode loadings,[18,19,24,42-46] the cells in this report were relatively high in areal capacity especially for current densities exceeding 5 mA cm^{-2} (Fig. 5.3). While these results are encouraging, further efforts are ongoing to better understand the transport properties of the electrolyte with multiple salts and the impacts of pore size and connectivity in addition to alignment in the microstructure.

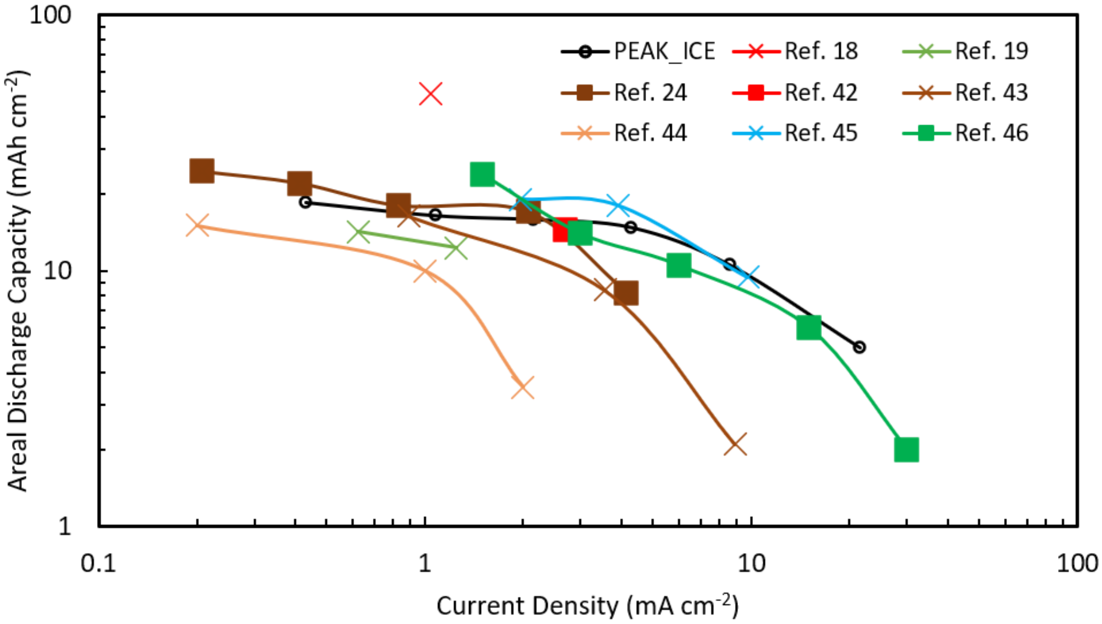

Fig. 5.3. Areal discharge capacity delivered as a function of current density for PEAK_ICE cell compared to other published results.

5.4 Conclusions

In this work, batteries where both electrodes were thick sintered electrodes comprised of all electroactive materials were evaluated with regards to retention of capacity at increasing rate. Under the assumption that rate capability limitations were due to molecular transport limitations in the electrode microstructure, two design routes were pursued in isolation and combination: a higher conductivity electrolyte formulation and templated electrode microstructure with directional pore alignment. Both the higher conductivity electrolyte and the templated microstructure were found to improve rate capability, and the combination of both of these design improvements had the highest rate capability of the evaluated cells. This work demonstrated promising results in design strategies to enable higher rate capability for thick sintered electrode batteries, which is a key limitation that must be overcome for this high energy density strategy to have potential in applications that require even moderate rates relative to composite electrode Li-ion battery technology.

5.5 Acknowledgement

Funding is acknowledged from the National Science Foundation, grant CMMI-1825338. Nippon Shokubai Co., Ltd. is acknowledged for providing the LiFSI used in the electrolytes.

5.6 References

(1) Etacheri, V.; Marom, R.; Elazari, R.; Salitra, G.; Aurbach, D. Challenges in the Development

of Advanced Li-Ion Batteries: A Review. *Energy Environ. Sci.* **2011**, *4*, 3243.

(2) Thackeray, M. M.; Wolverton, C.; Isaacs, E. D. Electrical Energy Storage for Transportation—Approaching the Limits of, and Going beyond, Lithium-Ion Batteries. *Energy Environ. Sci.* **2012**, *5*, 7854.

(3) Ge, X.; Liu, S.; Qiao, M.; Du, Y.; Li, Y.; Bao, J.; Zhou, X. Enabling Superior Electrochemical Properties for Highly Efficient Potassium Storage by Impregnating Ultrafine Sb Nanocrystals within Nanochannel-containing Carbon Nanofibers. *Angew. Chem. Weinheim Bergstr. Ger.* **2019**, *131*, 14720–14725.

(4) Liao, J.; Han, Y.; Zhang, Z.; Xu, J.; Li, J.; Zhou, X. Recent Progress and Prospects of Layered Cathode Materials for Potassium-ion Batteries. *Energy Environ. Mater.* **2021**, *4*, 178–200.

(5) Goodenough, J. B.; Park, K.-S. The Li-Ion Rechargeable Battery: A Perspective. *J. Am. Chem. Soc.* **2013**, *135*, 1167–1176.

(6) Nitta, N.; Wu, F.; Lee, J. T.; Yushin, G. Li-Ion Battery Materials: Present and Future. *Mater. Today* **2015**, *18*, 252–264.

(7) Pan, H.; Zhang, S.; Chen, J.; Gao, M.; Liu, Y.; Zhu, T.; Jiang, Y. Li- and Mn-Rich Layered Oxide Cathode Materials for Lithium-Ion Batteries: A Review from Fundamentals to Research Progress and Applications. *Mol. Syst. Des. Eng.* **2018**, *3*, 748–803.

(8) Zhou, X.; Wan, L.-J.; Guo, Y.-G. Binding SnO_2 Nanocrystals in Nitrogen-Doped Graphene Sheets as Anode Materials for Lithium-Ion Batteries. *Adv. Mater.* **2013**, *25*, 2152–2157.

(9) Liu, K.; Liu, Y.; Zhu, H.; Dong, X.; Wang,Y.; Wang, C.; Xia, Y. $NaTiSi_2O_6$/C Composite as a Novel Anode Material for Lithium-Ion Batteries. *Acta Physico-Chimica Sinica* **2020**, *36*, 1912030.

(10) Braun, P. V.; Cook, J. B. Deterministic Design of Chemistry and Mesostructure in Li-Ion Battery Electrodes. *ACS Nano* **2018**, *12*, 3060–3064.

(11) Yamada, Y.; Wang, J.; Ko, S.; Watanabe, E.; Yamada, A. Advances and Issues in Developing Salt-Concentrated Battery Electrolytes. *Nat. Energy* **2019**, *4*, 269–280.

(12) Diederichsen, K. M.; McCloskey, B. D. Electrolyte Additives to Enable Nonaqueous Polyelectrolyte Solutions for Lithium Ion Batteries. *Mol. Syst. Des. Eng.* **2020**, *5*, 91–96.

(13) Zheng, H.; Li, J.; Song, X.; Liu, G.; Battaglia, V. S. A Comprehensive Understanding of Electrode Thickness Effects on the Electrochemical Performances of Li-Ion Battery Cathodes. *Electrochim. Acta* **2012**, *71*, 258–265.

(14) Murray, V.; Hall, D. S.; Dahn, J. R. A Guide to Full Coin Cell Making for Academic Researchers. *J. Electrochem. Soc.* **2019**, *166*, A329–A333.

(15) Marks, T.; Trussler, S.; Smith, A. J.; Xiong, D.; Dahn, J. R. A Guide to Li-Ion Coin-Cell Electrode Making for Academic Researchers. *J. Electrochem. Soc.* **2011**, *158*, A51.

(16) Kehrwald, D.; Shearing, P. R.; Brandon, N. P.; Sinha, P. K.; Harris, S. J. Local Tortuosity Inhomogeneities in a Lithium Battery Composite Electrode. *J. Electrochem. Soc.* **2011**, *158*, A1393.

(17) Robinson, J. P.; Ruppert, J. J.; Dong, H.; Koenig, G. M., Jr. Sintered Electrode Full Cells for High Energy Density Lithium-Ion Batteries. *J. Appl. Electrochem.* **2018**, *48*, 1297–1304.

(18) Lai, W.; Erdonmez, C. K.; Marinis, T. F.; Bjune, C. K.; Dudney, N. J.; Xu, F.; Wartena, R.; Chiang, Y.-M. Ultrahigh-Energy-Density Microbatteries Enabled by New Electrode Architecture and Micropackaging Design. *Adv. Mater.* **2010**, *22*, E139-44.

(19) Sotomayor, M. E.; Torre-Gamarra, C. de la; Levenfeld, B.; Sanchez, J.-Y.; Varez, A.; Kim, G.-T.; Varzi, A.; Passerini, S. Ultra-Thick Battery Electrodes for High Gravimetric and Volumetric Energy Density Li-Ion Batteries. *J. Power Sources* **2019**, *437*, 226923.

(20) Nie, Z.; Ong, S.; Hussey, D. S.; LaManna, J. M.; Jacobson, D. L.; Koenig, G. M. Probing Transport Limitations in Thick Sintered Battery Electrodes with Neutron Imaging. *Mol. Syst. Des. Eng.* **2020**, *5*, 245–256.

(21) Wang, K.-X.; Li, X.-H.; Chen, J.-S. Surface and Interface Engineering of Electrode Materials for Lithium-Ion Batteries. *Adv. Mater.* **2015**, *27*, 527–545.

(22) Nie, Z.; Parai, R.; Cai, C.; Michaelis, C.; LaManna, J. M.; Hussey, D. S.; Jacobson, D. L.; Ghosh, D.; Koenig, G. M., Jr. Pore Microstructure Impacts on Lithium Ion Transport and Rate Capability of Thick Sintered Electrodes. *J. Electrochem. Soc.* **2021**, *168*, 060550.

(23) Li, L.; Erb, R. M.; Wang, J.; Wang, J.; Chiang, Y.-M. Fabrication of Low-tortuosity Ultrahigh-area-capacity Battery Electrodes through Magnetic Alignment of Emulsion-based Slurries. *Adv. Energy Mater.* **2019**, *9*, 1802472.

(24) Lu, L.-L.; Lu, Y.-Y.; Xiao, Z.-J.; Zhang, T.-W.; Zhou, F.; Ma, T.; Ni, Y.; Yao, H.-B.; Yu, S.-H.; Cui, Y. Wood-Inspired High-Performance Ultrathick Bulk Battery Electrodes. *Adv. Mater.* **2018**, *30*, e1706745.

(25) Logan, E. R.; Hall, D. S.; Cormier, M. M. E.; Taskovic, T.; Bauer, M.; Hamam, I.; Hebecker, H.; Molino, L.; Dahn, J. R. Ester-Based Electrolytes for Fast Charging of Energy Dense Lithium-Ion Batteries. *J. Phys. Chem. C Nanomater. Interfaces* **2020**, *124*, 12269–12280.

(26) Logan, E. R.; Tonita, E. M.; Gering, K. L.; Li, J.; Ma, X.; Beaulieu, L. Y.; Dahn, J. R. A Study of the Physical Properties of Li-Ion Battery Electrolytes Containing Esters. *J. Electrochem. Soc.* **2018**, *165*, A21–A30.

(27) Logan, E. R.; Dahn, J. R. Electrolyte Design for Fast-Charging Li-Ion Batteries. *Trends in Chemistry* **2020**, *2* (4), 354–366.

(28) Nie, Z.; McCormack, P.; Bilheux, H. Z.; Bilheux, J. C.; Robinson, J. P.; Nanda, J.; Koenig, G. M., Jr. Probing Lithiation and Delithiation of Thick Sintered Lithium-Ion Battery Electrodes with Neutron Imaging. *J. Power Sources* **2019**, *419*, 127–136.

(29) Neuhaus, J.; von Harbou, E.; Hasse, H. Physico-Chemical Properties of Solutions of Lithium Bis(Fluorosulfonyl)Imide (LiFSI) in Dimethyl Carbonate, Ethylene Carbonate, and Propylene Carbonate. *J. Power Sources* **2018**, *394*, 148–159.

(30) Berhaut, C. L.; Lemordant, D.; Porion, P.; Timperman, L.; Schmidt, G.; Anouti, M. Ionic Association Analysis of LiTDI, LiFSI and $LiPF_6$ in EC/DMC for Better Li-Ion Battery Performances. *RSC Adv.* **2019**, *9*, 4599–4608.

(31) Zhang, Z.; Du, Y.; Wang, Q.-C.; Xu, J.; Zhou, Y.-N.; Bao, J.; Shen, J.; Zhou, X. A Yolk-Shell-Structured $FePO_4$ Cathode for High-Rate and Long-Cycling Sodium-Ion Batteries. *Angew. Chem. Int. Ed Engl.* **2020**, *59*, 17504–17510.

(32) Nyman, A.; Behm, M.; Lindbergh, G. Electrochemical Characterisation and Modelling of the Mass Transport Phenomena in $LiPF_6$–EC–EMC Electrolyte. *Electrochim. Acta* **2008**, *53*,

6356–6365.

(33) Kim, H. J.; Voronina, N.; Yashiro, H.; Myung, S.-T. High-Voltage Stability in KFSI Nonaqueous Carbonate Solutions for Potassium-Ion Batteries: Current Collectors and Coin-Cell Components. *ACS Appl. Mater. Interfaces* **2020**, *12*, 42723–42733.

(34) Han, H.-B.; Zhou, S.-S.; Zhang, D.-J.; Feng, S.-W.; Li, L.-F.; Liu, K.; Feng, W.-F.; Nie, J.; Li, H.; Huang, X.-J. Lithium Bis(Fluorosulfonyl)Imide (LiFSI) as Conducting Salt for Nonaqueous Liquid Electrolytes for Lithium-Ion Batteries: Physicochemical and Electrochemical Properties. *J. Power Sources* **2011**, *196*, 3623–3632.

(35) Qi, Z.; Koenig, G. M., Jr. High-Performance $LiCoO_2$ Sub-Micrometer Materials from Scalable Microparticle Template Processing. *ChemistrySelect* **2016**, *1*, 3992–3999.

(36) Qi, Z.; Koenig, G. M., Jr. A Carbon-Free Lithium-Ion Solid Dispersion Redox Couple with Low Viscosity for Redox Flow Batteries. *J. Power Sources* **2016**, *323*, 97–106.

(37) Tuin, G.; Peters, A. C. I.; van Diemen, A. J. G.; Stein, H. N. Preparation of Large Monodisperse Polystyrene Particles by a One Step Surfactant-Free Emulsion Polymerization. *J. Colloid Interface Sci.* **1993**, *158*, 508–510.

(38) Ghosh, D.; Dhavale, N.; Banda, M.; Kang, H. A Comparison of Microstructure and Uniaxial Compressive Response of Ice-Templated Alumina Scaffolds Fabricated from Two Different Particle Sizes. *Ceram. Int.* **2016**, *42*, 16138–16147.

(39) Zhang, X.; Ju, Z.; Housel, L. M.; Wang, L.; Zhu, Y.; Singh, G.; Sadique, N.; Takeuchi, K. J.; Takeuchi, E. S.; Marschilok, A. C.; Yu, G. Promoting Transport Kinetics in Li-Ion Battery with Aligned Porous Electrode Architectures. *Nano Lett.* **2019**, *19*, 8255–8261.

(40) Deville, S. Ice-Templating, Freeze Casting: Beyond Materials Processing. *J. Mater. Res.* **2013**, *28*, 2202–2219.

(41) Parai, R.; Walters, T.; Marin, J.; Pagola, S.; Koenig, G. M., Jr; Ghosh, D. Strength Enhancement in Ice-Templated Lithium Titanate Li4Ti5O12 Materials Using Sucrose. *Materialia* **2020**, *14*, 100901.

(42) Wu, X.; Xia, S.; Huang, Y.; Hu, X.; Yuan, B.; Chen, S.; Yu, Y.; Liu, W. High-performance, Low-cost, and Dense-structure Electrodes with High Mass Loading for Lithium-ion Batteries. *Adv. Funct. Mater.* **2019**, *29*, 1903961.

(43) Qin, X.; Wang, X.; Xie, J.; Wen, L. Hierarchically Porous and Conductive LiFePO4 Bulk Electrode: Binder-Free and Ultrahigh Volumetric Capacity Li-Ion Cathode. *J. Mater. Chem.* **2011**, *21*, 12444.

(44) Sander, J. S.; Erb, R. M.; Li, L.; Gurijala, A.; Chiang, Y.-M. High-Performance Battery Electrodes via Magnetic Templating. *Nat. Energy* **2016**, *1*, 16099.

(45) de la Torre-Gamarra, C.; Sotomayor, M. E.; Sanchez, J.-Y.; Levenfeld, B.; Várez, A.; Laïk, B.; Pereira-Ramos, J.-P. High Mass Loading Additive-Free $LiFePO_4$ Cathodes with 500 Mm Thickness for High Areal Capacity Li-Ion Batteries. *J. Power Sources* **2020**, *458*, 228033.

(46) Elango, R.; Nadeina, A.; Cadiou, F.; De Andrade, V.; Demortière, A.; Morcrette, M.; Seznec, V. Impact of Electrode Porosity Architecture on Electrochemical Performances of 1 Mm-Thick LiFePO4 Binder-Free Li-Ion Electrodes Fabricated by Spark Plasma Sintering. *J. Power Sources* **2021**, *488*, 229402.

Chapter 6

Sintered Electrode Full Cells Incorporating $TiNb_2O_7$ Anode Materials

6.1 Abstract

The energy density of lithium-ion batteries at a cell level can be improved via increasing thickness and reducing inactive material content of electrodes. One system which achieves both attributes is sintered electrodes comprised of porous thin films of only electroactive material. $Li_4Ti_5O_{12}$ has often been the used as a sintered anode, however, higher energy density anodes could significantly improve cell energy density. In this work, $TiNb_2O_7$ (TNO) was synthesized and evaluated as a sintered anode material. Sintered TNO had stable cycling and relatively high volumetric energy density, suggesting TNO has promise as a sintered anode.

The content of this chapter has been submitted in the following journal:

Nie, Z.; Koenig, G. M. Improving High Rate Sintered Electrode Full Cells Incorporating $TiNb_2O_7$ Anode Materials. *J. Am. Ceram. Soc*

6.2 Introduction

Lithium-ion (Li-ion) batteries are an indispensable technology which have been applied in many applications.[1,2] Compared to other rechargeable batteries, Li-ion cells have high energy and power density.[1,3] However, the performance demands for energy storage are still increasing and necessitate further research. Conventional Li-ion battery electrodes are composites consisting of electroactive material, conductive additive, and polymer binders.[1,4,5] Recently, electrodes composed of porous thin films containing only electroactive material which has undergone a thermal treatment ("sintered electrodes") have been studied.[6,7] Sintered electrodes can be made much thicker than composite electrodes, and thus the energy density at the cell level can be increased.

Reversible electrochemical cycling of sintered electrodes was previously reported with $LiCoO_2$ (LCO) cathodes and $Li_4Ti_5O_{12}$ (LTO) anodes.[6,8,9] These very thick electrodes resulted in ion transport resistances which limited the ability to charge/discharge at high rates. Routes to mitigate the transport restrictions have included processing electrodes with reduced tortuosity and incorporating electrolytes with increased ion concentration/conductivity.[10,11] Cell improvements (especially energy density) can also be achieved by changing the active material components. Alternative materials evaluated for sintered cathodes include $LiMn_2O_4$ (LMO) and $LiFePO_4$ (LFP).[12,13] LMO and LFP have environmental and cost advantages, though not necessarily higher energy density, than LCO but have electronic conductivity limitations.[12]. LTO is a popular anode option due to minimal strain during Li^+ insertion/extraction and an operating voltage within the stability window of carbonate electrolyes.[1,14] However, the gravimetric capacity of LTO (175 mAh g^{-1}) is relatively low compared to other Li-ion anode materials.[1,15,16] An alternative anode with electrochemical capacity within the stability window of carbonate electrolytes is $TiNb_2O_7$ (TNO).[17,18] TNO has higher theoretical gravimetric capacity (388 mAh g^{-1}) and density (4.3 g cm^{-3} TNO vs. 3.5 g cm^{-3} LTO) than LTO, suggesting significant opportunity to increase volumetric capacity as a sintered electrode anode.[17,19]

In this work, TNO was synthesized via sol-gel method. TNO was then processed into both composite and sintered electrodes and evaluated electrochemically when paired in half and full cell configurations. The outcomes indicted that TNO is a suitable material as a sintered anode, providing stable and reversible electrochemical cycling.

6.3 Results and Discussion

Experimental procedures regarding material synthesis and cell fabrication can be found in Supporting Information and in previous reports.[6,20-22] The charge and discharge capacity of a Li/TNO cell with a composite TNO cathode at different rates of charge/discharge can be found Fig. 6.1a. The charge/discharge rate was the same for each cycle and is noted on the figure. Also, the first discharge-charge cycles (Li/TNO cell starts with discharge) at C/10 are shown in Fig. 6.1b. The voltage window was 1.2-3.0 V (vs. Li/Li^+), and the average voltage at C/10 rate was ~1.6~1.7 V vs. Li/Li^+, slightly above the voltage plateau for LTO (~1.5 V vs. Li/Li^+). A flat voltage plateau was not observed for TNO, consistent with previous reports.[17,20] The first cycle columbic efficiency was 95 %, possibly due to some slight electrolyte decomposition and interphase formation on cell components (Li foil, Al current collector and TNO).[23] After the first cycle, the columbic efficiency approached 100 % and the capacity was stable at each cycling rate, indicating good reversibility of electrochemical capacity. The capacity at a relatively low rate (C/10) was ~230 mAh g^{-1} TNO; and at a high rate of 5C, 78 mAh g^{-1} TNO capacity was delivered. Compared to a prior report, the gravimetric capacity of TNO was lower, but this was in part due to a slightly different voltage window.[17] More capacity can be obtained at a lower voltage cut off (i.e., 0.8 V vs. Li/Li$^+$), but at the expense of increased capacity fade with cycling (see Supporting Information, Fig. A5.2). In this work, stable cycling of the sintered TNO electrode was desired, thus the voltage range was restricted to avoid excessive capacity fade.

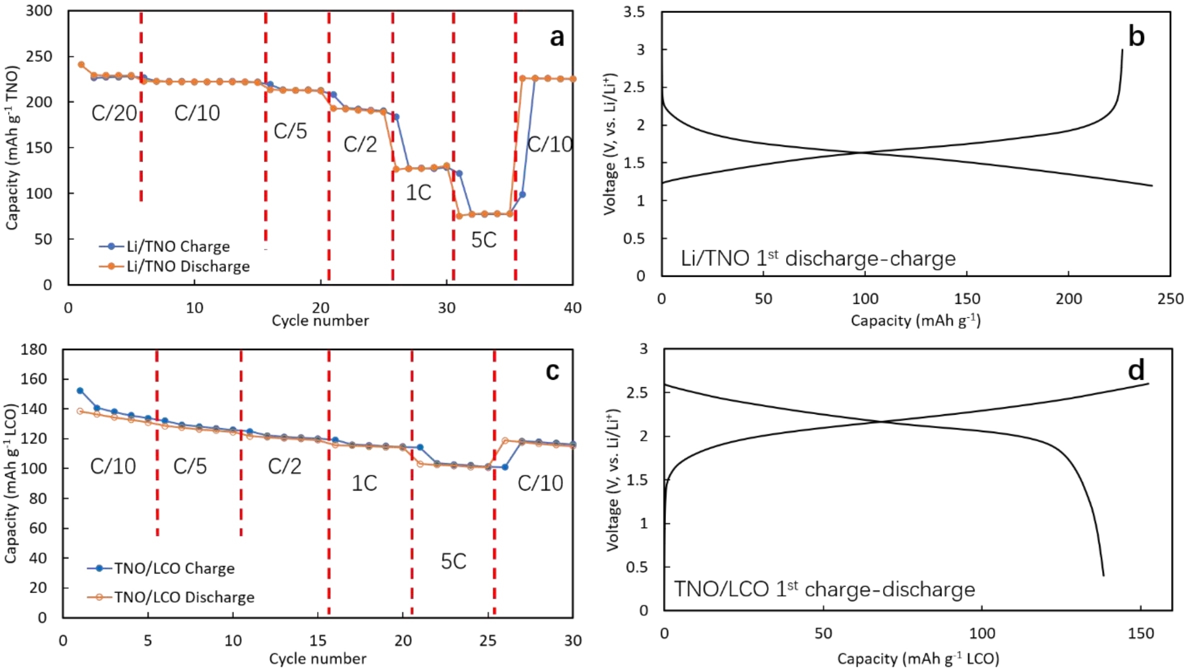

Fig. 6.1. TNO composite electrodes electrochemically cycled in (a,b) half cells paired with Li metal anodes and (c,d) full cells paired with LCO cathodes. The charge and discharge capacities at different rates are shown in (a,c). The initial charge/discharge cycle at relatively low rate is shown in (b,d). The charge/discharges rates for the Li/TNO cell and the discharge rates for the TNO/LCO cell are indicated in the figure, while the charge rate for the TNO/LCO cell was C/10 for all cycles.

Composite full cell electrochemical capacity (on a LCO cathode basis) for full cells of TNO composite anodes paired with LCO composite cathodes can be found in Fig. 6.1c. The charge rate was set at C/10 for all cycles and the discharge rate is noted in the figure. The charge/discharge voltage profile for the first cycle of the TNO/LCO composite electrode cell can be seen in Fig. 6.1d. Both TNO and LCO have sloped voltage profiles as a function of extent of lithiation,[16,17] and thus the full cell also had a gradual slope (e.g., no clear plateau regions). The capacity of the TNO/LCO cell was fairly stable with cycling, and a low (C/10) rate capacity of ~134 mAh g^{-1} LCO was delivered. The irreversible first cycle capacity of 9 % for the TNO/LCO cell likely had significant contribution from the presence of the TNO (with 6 % first cycle irreversible capacity, Fig. 6.1b); however, slight capacity fade in later cycles may have been due to LCO capacity losses.[21] At higher discharge rate such as 5C, ~101 mAh g^{-1} LCO capacity was still delivered, indicating good retention of capacity at increasing rates (i.e., 75 % at 5C relative to C/10) with thin composite electrodes. Cycling at increasing rates for TNO composite anodes paired two other composite cathode materials can be found in Supporting information, Fig. A5.3, with corresponding cell parameters in Table S1. The TNO material was overall stable for multiple cycles at a variety of rates when processed into composite electrodes.

Stability of TNO in composite electrodes led to further assessment of its suitability as a sintered electrode active material. Sintered electrodes do not have conductive carbon and polymer binder as additives. The electrodes consist of only active materials and were much thicker than the composite electrodes (for TNO ~70 μm for composite and ~400 μm for sintered electrodes). TNO sintered anodes were paired with LCO sintered cathodes. Two cell variations will be described: one was a cathode limited condition, where the LCO was 191 mg and TNO was 177 mg (~38.9 mAh anode and ~28.6 mAh cathode based on composite electrode capacities). The second condition was anode limited where 147 mg TNO was paired with 250 mg LCO (~32.3 mAh anode and ~37.5 mAh cathode based on composite electrode capacities). The gravimetric capacities on both TNO and LCO bases at increasing rates can be found in Fig. 6.2. For each condition, 3 nominally identical cells were tested and the data shown in Fig. 6.2 was one representative cell chosen for each condition.

The capacity was relatively stable for each cell at each rate (Fig. 6.2), though an overall slight fade in capacity was observed with cycling. The retention of capacity at increasing rate was not as high as the composite TNO/LCO cell (Fig. 6.1c). This was attributed to the increased ion transport resistance from the thicker electrodes. It is noted that the electronic conductivity especially of the sintered TNO was lower than the composite electrode due to lack of conductive additives. However, the much greater thickness of the sintered electrodes results in capacity increases on an areal and cell level, where for the composite electrodes the low rate cell capacity was 1.2 mAh and for the sintered electrodes the low rate cell capacity was 25 mAh. Detailed discussion on limitations and improvements of cells with sintered electrodes can be found in previous publications.[8,9]

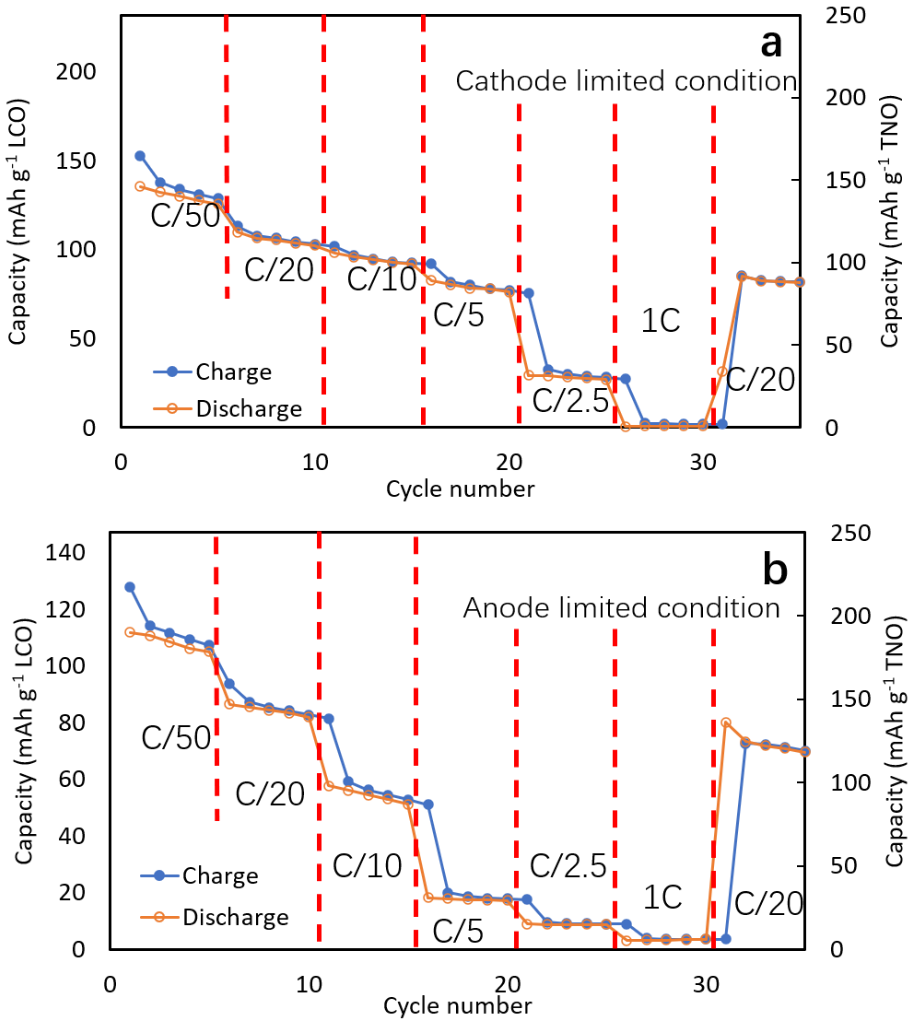

Fig. 6.2. Discharge capacity at different rates on gravimetric basis for both the TNO and LCO sintered electrodes in full cells for (a) cathode limited and (b) anode limited conditions.

The rate capability results in Fig. 6.2 revealed that the cathode limited cell condition resulted in higher capacity retention at increasing rate. This outcome was attributed to differences in the transport restrictions for the two conditions. For the two cells showed in Fig. 6.2, the total active material loading was not equivalent. Loading differences changed estimates of cell capacity (28.6 mAh for cathode limited vs. 32.3 mAh for anode limited); thus with the C rate being adjusted by the cell capacity an equivalent C rate for the anode limited condition had higher total current and current density. Increased current resulted in higher electronic and ionic transport polarization in the cell. Electrode thicknesses were also note equivalent. For the cathode limited condition, the anode thickness was 0.51 mm and the cathode thickness was 0.44 mm. For anode limited condition, the anode thickness was 0.44 mm and the cathode was 0.59 mm. The LCO electrodes had lower porosity (~35 %) than TNO electrodes (~40 %), and thicker LCO would result in higher ion transport polarization and reduced rate capability.

Another difference between the cells was capacity fade with cycling. Although for the cycles within each rate the capacity was stable, comparison of the series of cycles at C/20 (e.g., cycles 6-10 compared with cycles 31-35) revealed different capacity fade. The underlying cause of capacity fade will be the subject of future reports; however, several factors may have contributed to the fade. One factor was that the volume change of TNO material during lithiation/delithiation process has been reported as 7.22 %,[24] which was much larger than the volume change of LTO (0.2 %) used in previous studies,[14] and also higher than the LCO material (1.9 %) used as cathode in this work.[7] This volume change could result in internal stress and impact particle contacts necessary for electronic conductivity through the electrode matrix and access to electrode capacity. Another contributor may have been the different extents and progression of lithiation/delithiation during the cycling. Although the overall cell voltage window was carefully controlled, TNO does not have a flat voltage plateau and thus it is challenging to be confident the overpotential experienced by the active material particles was the same both conditions. There may have been regions within the sintered electrodes where the local potential could have resulted in extra irreversible capacity loss due to exceeding electrolyte stability limits or reversible lithiation extents of the TNO.[9] Overall, sintered TNO/LCO cells showed promising cycling performance.

The use of TNO can improve the energy density at a cell level and ion transport polarization relative to using LTO. For example, a 0.5 mm thick, 35 % porosity LCO pellet has a capacity of 32.2 mAh. And thus, a balanced LTO (40 % porosity) anode requires a thickness of 0.66 mm. However, a balanced TNO anode needs a thickness of only 0.43 mm, which is a 35 % reduction in anode thickness and a 20 % reduction in total cell electrode thickness. Assuming a constant cathode, a thinner sintered anode will reduce ion transport resistance and increase volumetric energy density – increasing both the power and energy of the cell.

6.4 Conclusions

In this work, TNO was synthesized via sol-gel method and processed into composite and sintered electrodes. Composite TNO electrodes showed good cycling stability both in half cells paired with Li metal anodes and full cells paired with composite LCO cathodes. TNO/LCO sintered electrode full cells also had promising reversible electrochemical capacity, although some fade was observed which warrants further investigation. TNO has a relatively high gravimetric and volumetric capacity, and this work demonstrated the cycling of TNO anodes in sintered full cells, which shows promise for providing high cell level energy density when coupling the electrochemical properties of TNO materials with the large thicknesses achievable with sintered electrode processing.

6.5 Acknowledgement

This work was funded by the National Science Foundation, grant CMMI-1825216. The authors acknowledge CAMP facility for providing composite NCA electrodes used in this work.

6.6 References

(1) Armand, M.; Axmann, P.; Bresser, D.; Copley, M.; Edström, K.; Ekberg, C.; Guyomard, D.; Lestriez, B.; Novák, P.; Petranikova, M.; Porcher, W.; Trabesinger, S.; Wohlfahrt-Mehrens, M.; Zhang, H. Lithium-Ion Batteries – Current State of the Art and Anticipated Developments. *J. Power Sources* **2020**, *479*, 228708..

(2) Goodenough, J. B.; Park, K.-S. The Li-Ion Rechargeable Battery: A Perspective. *J. Am. Chem. Soc.* **2013**, *135*, 1167–1176.

(3) Etacheri, V.; Marom, R.; Elazari, R.; Salitra, G.; Aurbach, D. Challenges in the Development of Advanced Li-Ion Batteries: A Review. *Energy Environ. Sci.* **2011**, *4* , 3243.

(4) Wang, Y.; Fu, X.; Zheng, M.; Zhong, W.-H.; Cao, G. Strategies for Building Robust Traffic Networks in Advanced Energy Storage Devices: A Focus on Composite Electrodes. *Adv. Mater.* **2019**, *31*, e1804204.

(5) Marks, T.; Trussler, S.; Smith, A. J.; Xiong, D.; Dahn, J. R. A Guide to Li-Ion Coin-Cell Electrode Making for Academic Researchers. *J. Electrochem. Soc.* **2011**, *158*, A51.

(6) Robinson, J. P.; Ruppert, J. J.; Dong, H.; Koenig, G. M., Jr. Sintered Electrode Full Cells for High Energy Density Lithium-Ion Batteries. *J. Appl. Electrochem.* **2018**, *48*, 1297–1304.

(7) Lai, W.; Erdonmez, C. K.; Marinis, T. F.; Bjune, C. K.; Dudney, N. J.; Xu, F.; Wartena, R.; Chiang, Y.-M. Ultrahigh-Energy-Density Microbatteries Enabled by New Electrode Architecture and Micropackaging Design. *Adv. Mater.* **2010**, *22*, E139-44.

(8) Nie, Z.; McCormack, P.; Bilheux, H. Z.; Bilheux, J. C.; Robinson, J. P.; Nanda, J.; Koenig, G. M., Jr. Probing Lithiation and Delithiation of Thick Sintered Lithium-Ion Battery Electrodes with Neutron Imaging. *J. Power Sources* **2019**, *419*, 127–136.

(9) Nie, Z.; Ong, S.; Hussey, D. S.; LaManna, J. M.; Jacobson, D. L.; Koenig, G. M., Jr. Probing Transport Limitations in Thick Sintered Battery Electrodes with Neutron Imaging. *Mol. Syst. Des. Eng.* **2020**, *5*, 245–256.

(10) Nie, Z.; Parai, R.; Cai, C.; Michaelis, C.; LaManna, J. M.; Hussey, D. S.; Jacobson, D. L.; Ghosh, D.; Koenig, G. M., Jr. Pore Microstructure Impacts on Lithium Ion Transport and Rate Capability of Thick Sintered Electrodes. *J. Electrochem. Soc.* **2021**, *168*, 060550.

(11) Nie, Z.; Parai, R.; Cai, C.; Ghosh, D.; Koenig, G. M. Improving High Rate Cycling Limitations of Thick Sintered Battery Electrodes by Mitigating Molecular Transport Limitations through Modifying Electrode Microstructure and Electrolyte Conductivity. *Mol. Syst. Des. Eng.* **2021**, *6*, 708–712.

(12) Cai, C.; Koenig, G. M., Jr. Investigating Dopants to Improve Sintered $LiMn_2O_4$ Spinel Electrode Electrochemical Cycling Limitations. *Electrochim. Acta* **2022**, *401*, 139484.

(13) Elango, R.; Nadeina, A.; Cadiou, F.; De Andrade, V.; Demortière, A.; Morcrette, M.; Seznec, V. Impact of Electrode Porosity Architecture on Electrochemical Performances of 1 Mm-Thick $LiFePO_4$ Binder-Free Li-Ion Electrodes Fabricated by Spark Plasma Sintering. *J. Power Sources* **2021**, *488*, 229402.

(14) Sun, X.; Radovanovic, P. V.; Cui, B. Advances in Spinel $Li_4Ti_5O_{12}$ Anode Materials for Lithium-Ion Batteries. *New J Chem.* **2015**, *39*, 38–63.

(15) Goriparti, S.; Miele, E.; De Angelis, F.; Di Fabrizio, E.; Proietti Zaccaria, R.; Capiglia, C. Review on Recent Progress of Nanostructured Anode Materials for Li-Ion Batteries. *J. Power Sources* **2014**, *257*, 421–443.

(16) Nitta, N.; Wu, F.; Lee, J. T.; Yushin, G. Li-Ion Battery Materials: Present and Future. *Mater. Today* **2015**, *18*, 252–264.

(17) Han, J.-T.; Huang, Y.-H.; Goodenough, J. B. New Anode Framework for Rechargeable Lithium Batteries. *Chem. Mater.* **2011**, *23*, 2027–2029.

(18) Lou, S.; Cheng, X.; Zhao, Y.; Lushington, A.; Gao, J.; Li, Q.; Zuo, P.; Wang, B.; Gao, Y.; Ma, Y.; Du, C.; Yin, G.; Sun, X. Superior Performance of Ordered Macroporous $TiNb_2O_7$ Anodes for Lithium Ion Batteries: Understanding from the Structural and Pseudocapacitive Insights on Achieving High Rate Capability. *Nano Energy* **2017**, *34*, 15–25.

(19) Gasperin, M. Affinement de la structure de $TiNb_2O_7$ et répartition des cations. *J. Solid State Chem.* **1984**, *53*, 144–147.

(20) Lin, C.; Hu, L.; Cheng, C.; Sun, K.; Guo, X.; Shao, Q.; Li, J.; Wang, N.; Guo, Z. Nano-$TiNb_2O_7$/Carbon Nanotubes Composite Anode for Enhanced Lithium-Ion Storage. *Electrochim. Acta* **2018**, *260*, 65–72.

(21) Qi, Z.; Koenig, G. M., Jr. High-Performance LiCoO2Sub-Micrometer Materials from Scalable Microparticle Template Processing. *ChemistrySelect* **2016**, *1*, 3992–3999.

(22) Qi, Z.; Dong, H.; Koenig, G. M., Jr. Electrochemical Characterization of Lithium-Ion Battery Cathode Materials with Aqueous Flowing Dispersions. *Electrochim. Acta* **2017**, *253*, 163–170.

(23) Wang, A.; Kadam, S.; Li, H.; Shi, S.; Qi, Y. Review on Modeling of the Anode Solid Electrolyte Interphase (SEI) for Lithium-Ion Batteries. *Npj Comput. Mater.* **2018**, *4*.

(24) Guo, B.; Yu, X.; Sun, X.-G.; Chi, M.; Qiao, Z.-A.; Liu, J.; Hu, Y.-S.; Yang, X.-Q.; Goodenough, J. B.; Dai, S. A Long-Life Lithium-Ion Battery with a Highly Porous $TiNb_2O_7$ Anode for Large-Scale Electrical Energy Storage. *Energy Environ. Sci.* **2014**, *7*, 2220–2226.

Chapter 7

Conclusions and Future Directions

Lithium-ion battery is an important energy storage technique and still needs further improvement in both energy and power density. Conventional lithium-ion battery electrodes are composite thin films coated on metal current collectors. The composite consists of active material, conductive carbon and polymer binder. To further improve the energy density at the cell level, sintered electrodes can be an alternative for cell manufacturing. Sintered electrodes are fabricated via thermal treatment of pure active material pellets so the electrodes do not have any inert additives and can be made much thicker than composite electrodes. However, the greater thickness and carbon free network posed challenges on both ionic transport and electronic conduction during the cell cycling. Thus, this thesis focused on investigating the ionic transport properties of sintered electrode system and exploring ways to improve the energy and power density.

First, to study the ion transport of the sintered electrode system, LTO/LCO cells with sintered electrodes were cycled and characterized by *operando* neutron imaging technique to track the Li^+ movement during the test. Numerical calculation was also used to interpret the result from the neutron imaging experiment. The cell tested had different electrode thickness and were discharged at different discharge rate. This was the first report to use neutron imaging to map out lithium distribution in detail in thick electrode batteries. And the numerical calculation provides additional information on limitation factors.

The study found that the ion transport was the rate limiting factors in thick sintered electrode system. Especially, when the electrodes were thicker and the charge/discharge rate was higher, depletion of Li^+ in electrolyte phase on one electrode during charge/discharge was the main reason for limited capability delivered. Another finding was the lithiation of LCO cathode and delithiation of LTO anode during discharge showed different patterns. For LCO, the lithiation process was more homogeneous across the whole thickness of the pellet, while for LTO, the delithation formed a front propagated from separator side to the current collector side. This was caused by the greater thickness of LTO electrode and also the flatter voltage plateau of LTO material than LCO material.

Based on the transport properties, several approaches have been applied to improve the power output/rate capability of the cell. One approach was to use ice-templated technique to fabricate sintered electrodes with aligned pores. These pellets with lower tortuosity showed improvement on the rate capability than electrodes with random packed particles. Another approach was to use high concentration, high conductivity electrolyte in the system, which can mitigate the Li^+ depletion during fast discharge process. Both methods work very well and a combination of them showed even further improvement. The cell with high concentration/conductivity electrolyte and ice templated electrodes showed 69 % improvement in discharge capacity retention compared to the cell with commercial electrolyte and non-templated electrodes.

The approaches mentioned above are focused on engineering on the system. To further improve the energy density and environmental economy, different materials should be explored. In this thesis, we also tried new anode material TNO as sintered electrode. Compared to LTO, TNO has higher gravimetric and volumetric capacity, and its operating voltage range can be adjusted within the safe rage of the electrolyte. The cycling results of the cells with sintered electrodes was promising with some fading observed. From the results, the benefits of incorporation TNO as anode worth further study.

With what has been found in this thesis, some future directions can be proposed. From the electrode morphology perspective, although ice-templated LTO have been successfully fabricated and cycled, the ice-templated cathode hasn’t been fabricated. Thus, it is worth to try a cathode material with the ice templated technique and this needs collaboration with colleagues at Old Dominion University. From the electrolyte perspective, the high concentration/conductivity electrolyte explored in Chapter 5 showed good results, but it is also worth to explore electrolyte system with even higher conductivity or concentration. This requires some trouble shooting work due to the stability and corrosion issue with the new system. On the material side, studying the fading mechanism of sintered TNO electrode should be one of the future directions as mentioned in Chapter 6 and in previous paragraph. Besides, exploration of new cathode materials for sintered electrodes could also be a direction for future research.

In conclusion, this work studied the limitation and improved the energy and power density of the lithium-ion cells with sintered electrodes. More investigations are still needed for further improvement of the sintered electrode system.

Appendix

Appendix 1. Supporting material for chapter 2

Conservation equations used in calculation.

The equations we used were developed by Newman *et al.*[1,2,3] and have been widely used for Li-ion battery simulation.[4,5] Four conservation equations were used in the calculation, which are listed below:

(1) Conservation of Li ion in electrolyte.

$$\varepsilon\frac{\partial c_e}{\partial t}-\varepsilon\frac{\partial}{\partial z}\left(D_e^{eff}\frac{\partial c_e}{\partial z}\right)=aj_n(1-t_+^0)$$

Boundary conditions:

$$\frac{\partial c_e}{\partial z}=0\ at\ x=0,\ x=L$$

(2) Conservation of Li in solid electrode.

$$\frac{\partial c_s}{\partial t}-\frac{1}{r^2}\frac{\partial}{\partial r}\left(D_s^{eff}r^2\frac{\partial c_s}{\partial z}\right)=0$$

Boundary conditions:

$$\frac{\partial c_s}{\partial z}=0\ at\ r=0 \qquad j_n=-D_s^{eff}\frac{\partial c_s}{\partial z}\ \text{at r}=R_s$$

(3) Conservation of charge in electrolyte

$$\frac{\partial \phi_e}{\partial z}+\frac{RT}{F}(t_+^0-1)\left(1+\frac{\partial lnf_A}{\partial lnc_e}\right)\frac{\partial lnc_e}{\partial z}+\frac{i_e}{\kappa^{eff}}=0$$

Boundary conditions:

$$\frac{\partial \phi_e}{\partial z}=0\ at\ x=0,\ x=L$$

(4) Conservation of charge in active material.

$$\frac{\partial \phi_s}{\partial z}+\frac{i_s}{\sigma}=0$$

Boundary conditions:

$$\frac{\partial \phi_s}{\partial z} = -\frac{I}{\sigma}\ at\ x = 0,\ x = L$$

In the equations above, j_n is decided by the Butler-Volmer equation:

$$j_n = k c_e^{\alpha_a} (c_t - c_s)^{\alpha_a} c_s^{\alpha_c} \left[\exp\left(\frac{\alpha_a F}{RT} \eta \right) - \exp\left(\frac{\alpha_c F}{RT} \eta \right) \right]$$

And the over potential η is calculated by

$$\eta = \phi_s - \phi_e - U_{OCP}$$

By solving the conservation equations together with a set of boundary conditions, the electrochemical behavior of battery discharge, including the discharge polarization curve and the Li$^+$ concentration in both the solid and liquid phases throughout the depth of the cell, was calculated. Resulting were discharge profiles and concentration distributions at different time point for this study can be found below in Fig. A1.5, Fig. A1.6, Fig. A1.9, and Fig. A1.10. To compare the results with the neutron imaging results (Fig. 2.5a, Fig. 2.6a), both concentrations and dimensions were normalized (Fig. 2.5b, Fig. 2.6b)

List of symbols:

a	specific interracial area
c_e	Li concentration in electrolyte,
c_s	Li concentration in solid electrode
c_t	total concentration of sites available for Li$^+$ in solid phase
D_e^{eff}	effective diffusivity of Li ion in electrolyte
D_s^{eff}	effective diffusivity of Li in electrode
f_A	activity coefficient of Li salt
F	Faraday constant

i_e	current density in electrolyte
i_s	current density in solid electrodes
j_n	flux of Li ion across the interface between the electrolyte and electrode
k	reaction rate constant
r	radial length in active material length
R	universal gas constant
t	time
t_+^0	cation transference number
T	temperature
U_{OCP}	open circuit potential of the electrode as a function of Li concentration in solid phase
z	transversal direction from anode to cathode within the cell sandwich
α_a	anodic transfer coefficients
α_c	cathodic transfer coefficients
ε	volume fraction of electrolyte,
η	over potential
κ^{eff}	effective ionic conductivity of the electrolyte
σ	electronic conductivity of solid material.
ϕ_e	electrolyte potential
ϕ_s	solid electrode potential

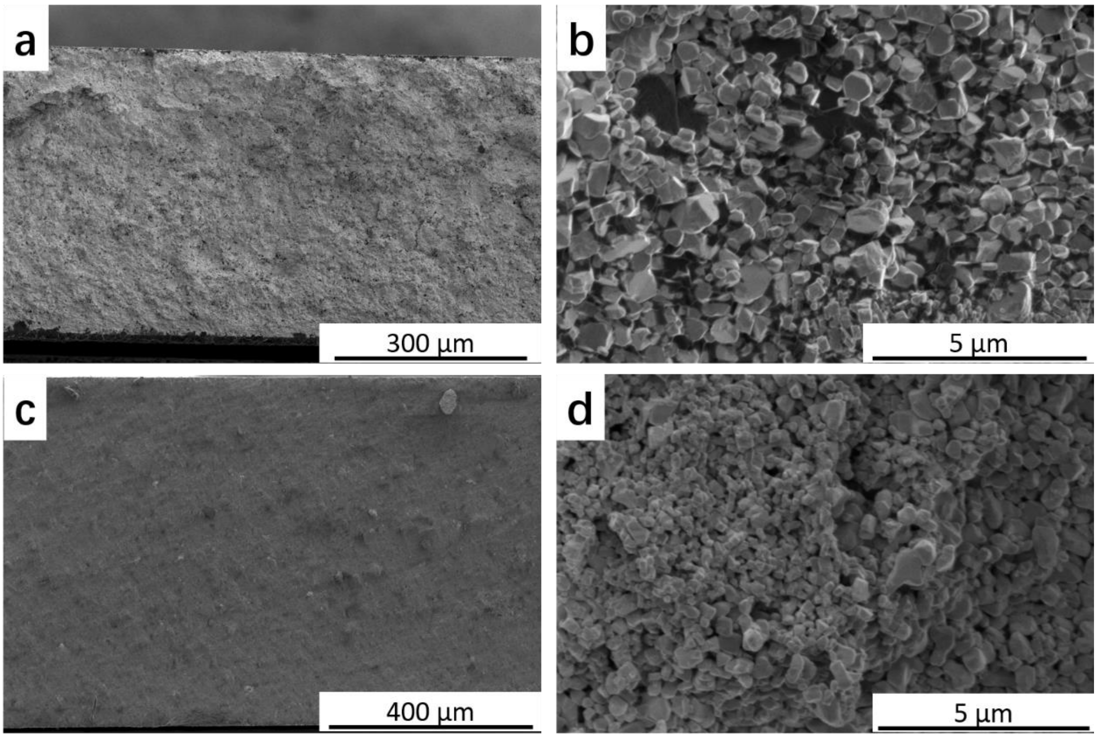

Fig. A1.1. Cross-sectional SEM images for (a), (b) sintered LCO pellet and (c), (d) sintered LTO pellet at relatively low (a,c) and high (b,d) magnifications.

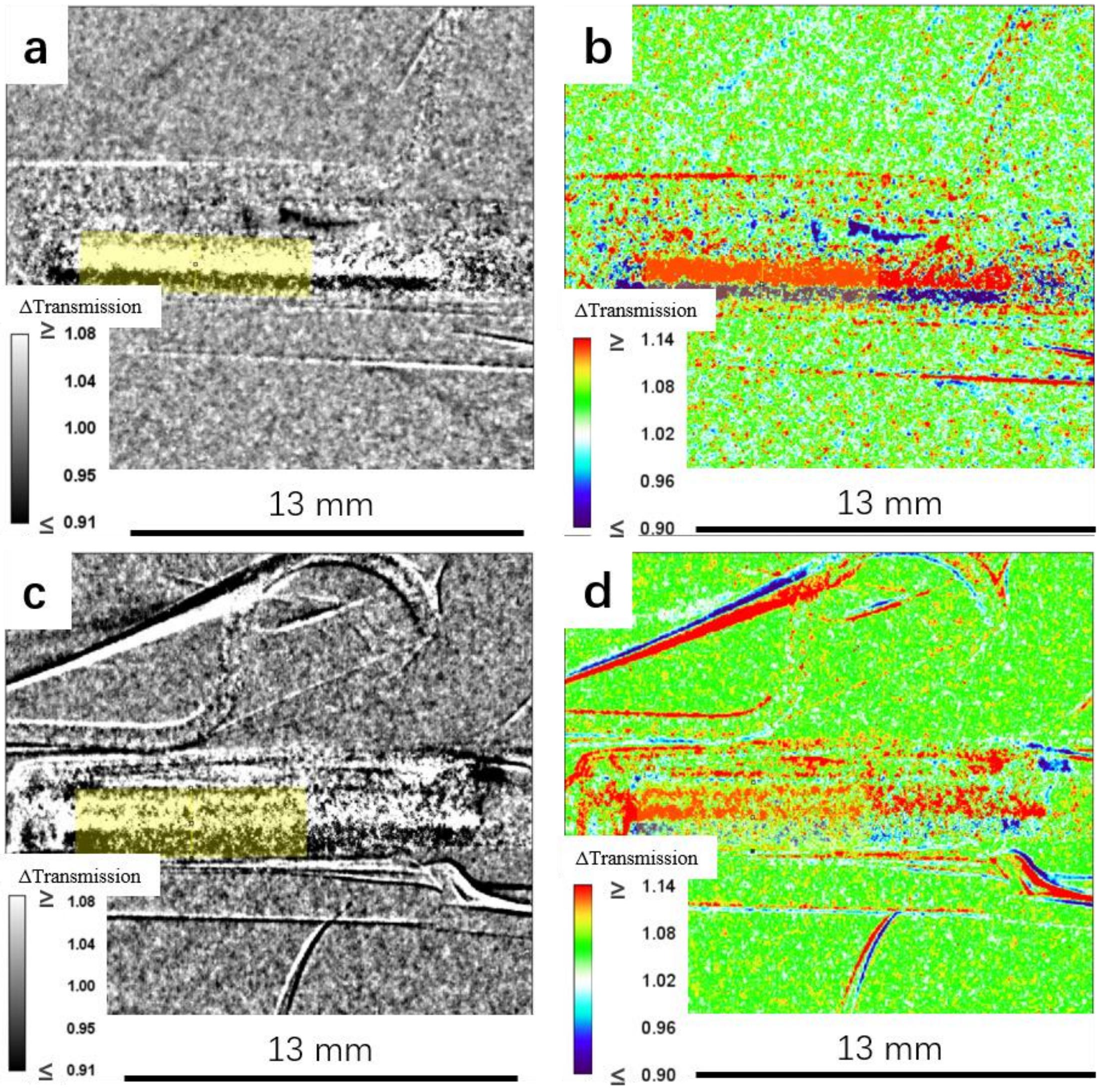

Fig. A1.2. (a, b) LTO/LCO-Thin cell and (c, d) LTO/LCO-Thick cell neutron images, where each pixel represents the change in transmitted neutron intensity relative to the initiation of discharge. Neutron images were collected after 1357 minutes of discharge for the LTO/LCO-Thin cell and 819 minutes of discharge for the LTO/LCO-Thick cell. Grayscale (a, c) and color scale (b, d) plots corresponding to the change in transmitted intensity are both shown. Yellow shading has been added to (a) and (c) to highlight the regions used for obtaining the average change in transmitted intensity as a function of depth within the electrodes. Insets depict the gray scale bar and color scale bar with the numerical value corresponding to the changes in relative neutron transmission at each pixel relative to the initiation of discharge. Note that for (b, d) the brightest red regions have ΔT ≥ 1.14 and deepest blue regions have

ΔT ≤ 0.90 and do not reflect the absolute maximum or minimum ΔT values. The color scale was truncated to best highlight the net change in the pixels throughout the electrode. The numerical grayscale in (a, c) also reflects thresholds for white/black and not the absolute scale limits.

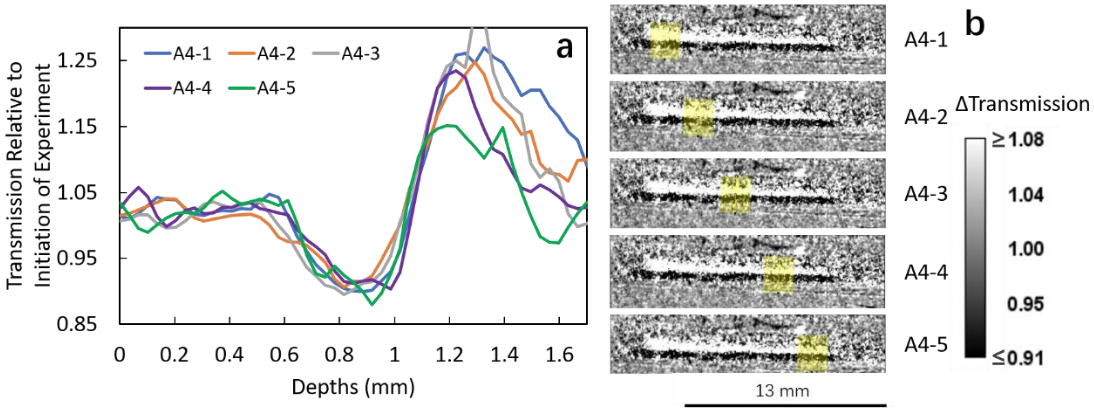

Fig. A1.3. (a) Transmission relative to initiation of experiment as a function of the depth in the electrode, where the depth is the vertical dimension in the yellow shaded region in (b). (b) Neutron images at discharge time point A4 (refer to Fig. 2.3) for the LTO/LCO-Thin cell. Each relative transmission data point in (a) corresponds to an average over all of the horizontal pixels at a given location in the corresponding shaded region in (b). Inset in (b) depicts the gray scale bar with the numerical value corresponding to the changes in relative neutron transmission at each pixel relative to the initiation of the experiment. Note that for (b) the brightest regions have ΔT ≥ 1.08 and darkest regions have ΔT ≤ 0.91 and do not reflect the absolute maximum or minimum ΔT values. The grayscale was truncated to best highlight the net change in the pixels throughout the electrode.

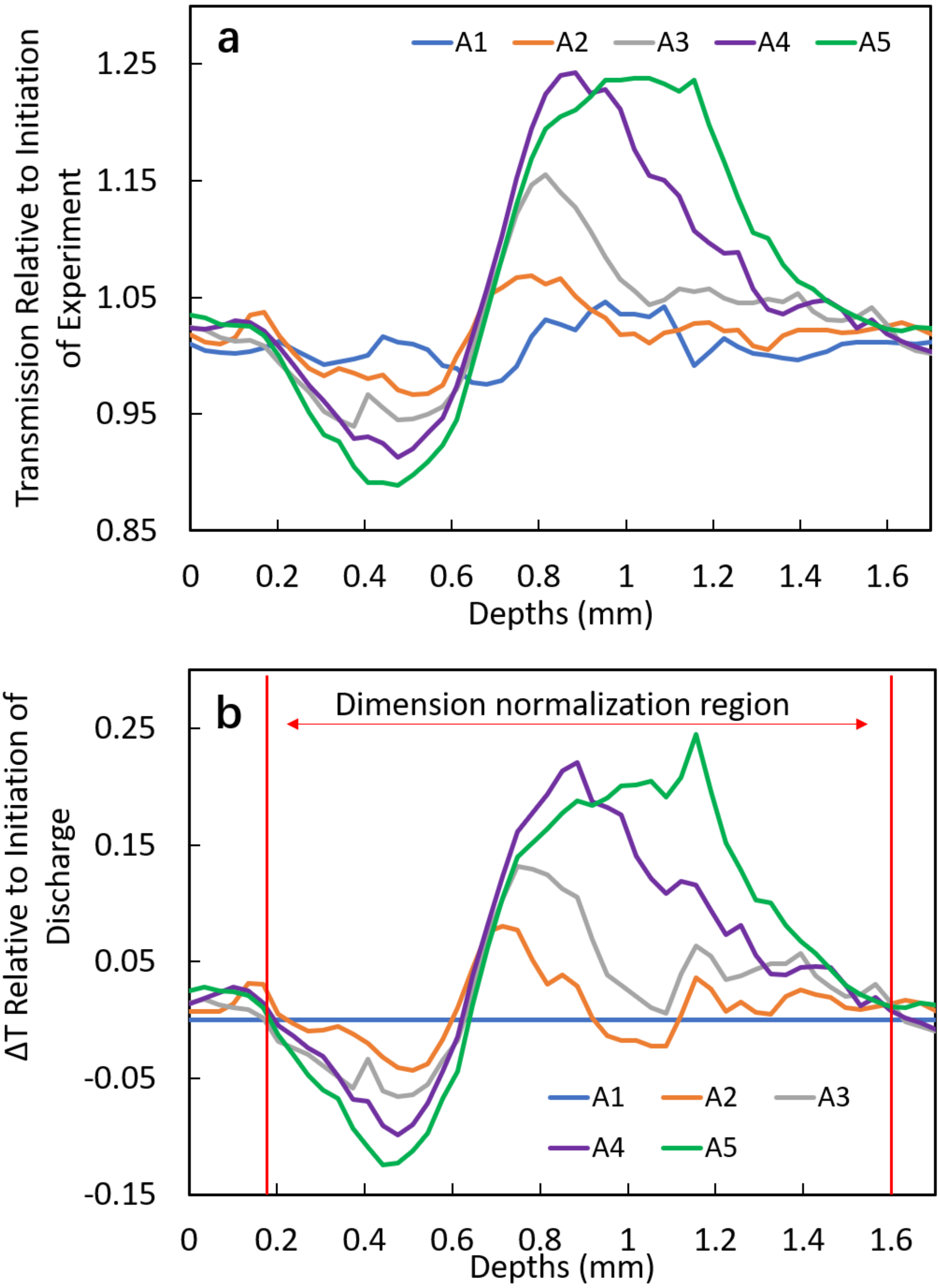

Fig. A1.4. (a) Relative transmission profiles of LTO/LCO-Thin cell, where the transmission was relative to the initiation of the experiment. The depth of 0 corresponds to an arbitrary position slightly below LCO pellet in the stainless steel. (b) The same data as in (a) after subtracting the relative transmission observed at time A1, which was the initiation of discharge. Red vertical lines highlight the normalization region used to normalize the x-axis on a 0 to 1 scale for Fig. 2.5 in the main text.

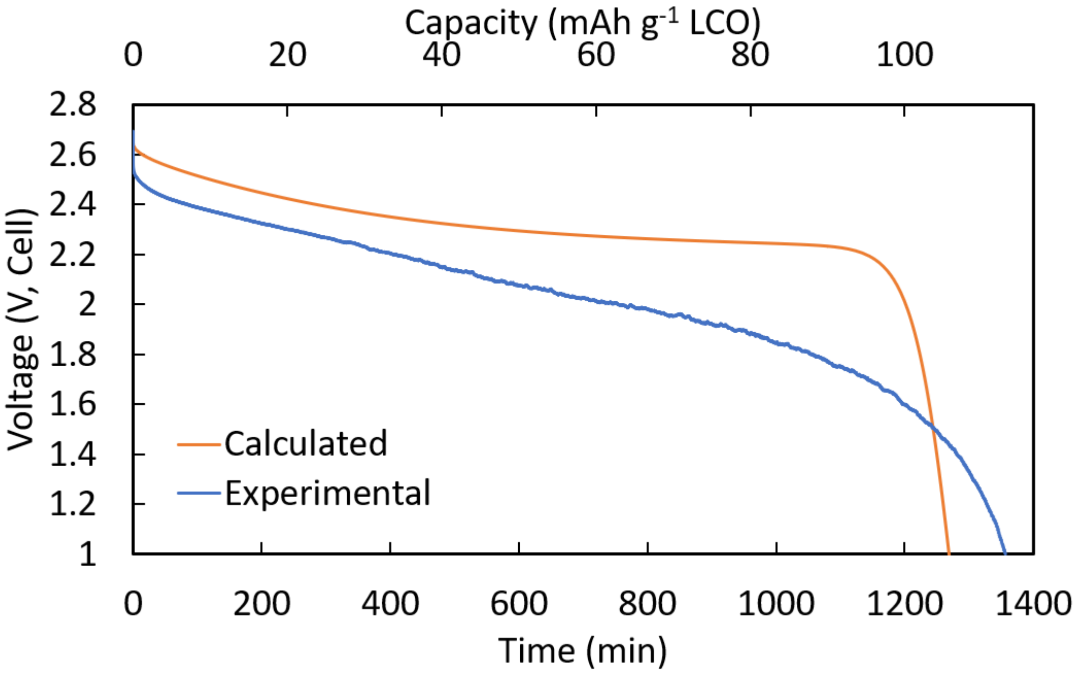

Fig. A1.5. Calculated (orange) and experimentally measured (blue) discharge profiles for the LTO/LCO-Thin cell.

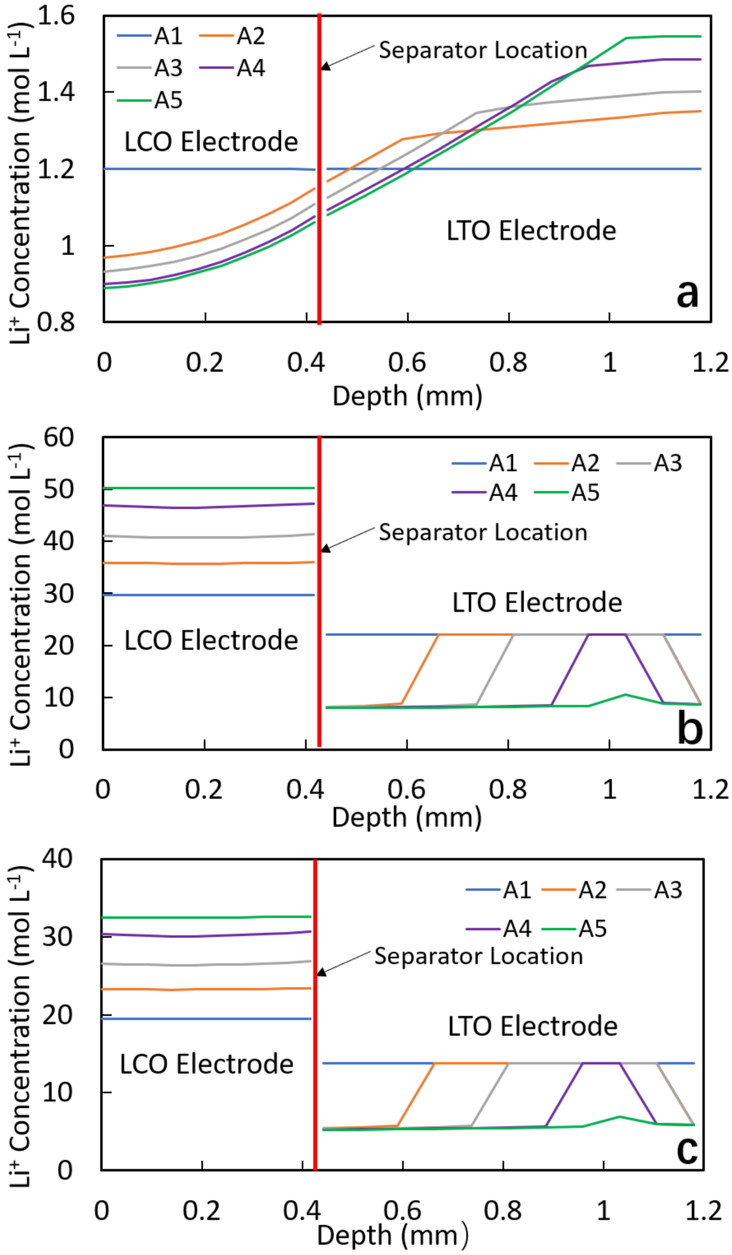

Fig. A1.6. Li^+ concentrations at different locations within both electrodes calculated using the model for the LTO/LCO-Thin cell on a molar basis. Concentrations are shown for the (a) liquid electrolyte phase, (b) solid active material phase, (c) and the sum of the total concentration. The A1-A5 corresponds to the time points chosen in the discharge profile (refer to Fig. 2.3). Total concentration was calculated using the equation: $c_t=c_e\times\varepsilon+c_s\times(1-\varepsilon)$, where c_t is the total concentration, c_e is the concentration in electrolyte, c_s is the concentration in solid phase, ε is the porosity of the electrode.

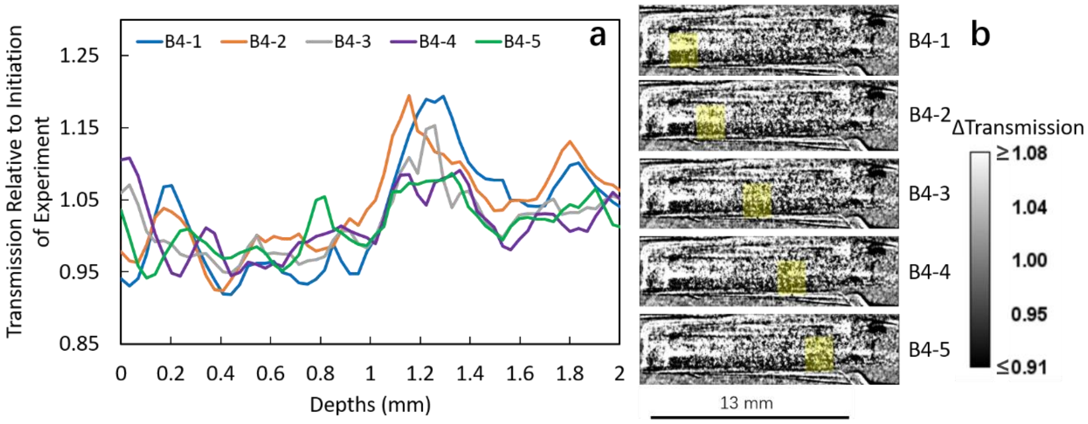

Fig. A1.7. (a) Transmission relative to initiation of experiment as a function of the depth in the electrode, where the depth is the vertical dimension in the yellow shaded region in (b). (b) Neutron images at discharge time point B4 (refer to Fig. 2.4) for the LTO/LCO-Thick cell. Each relative transmission data point in (a) corresponds to an average over all of the horizontal pixels at a given location in the corresponding shaded region in (b). Inset in (b) depicts the gray scale bar with the numerical value corresponding to the changes in relative neutron transmission at each pixel relative to the initiation of the experiment. Note that for (b) the brightest regions have ΔT ≥ 1.08 and darkest regions have ΔT ≤ 0.91 and do not reflect the absolute maximum or minimum ΔT values. The grayscale was truncated to best highlight the net change in the pixels throughout the electrode.

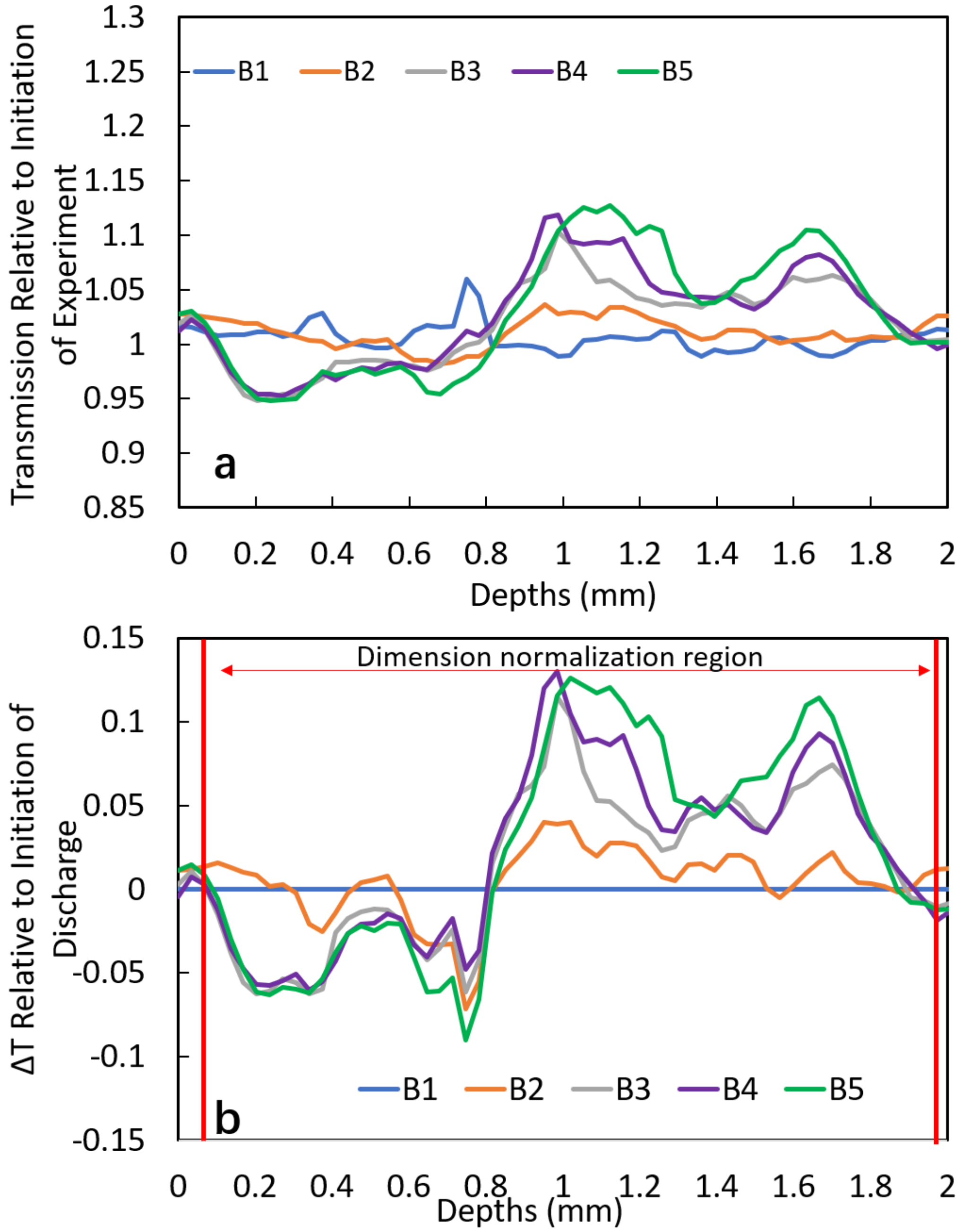

Fig. A1.8. (a) Relative transmission profiles of LTO/LCO-Thick cell, where the transmission was relative to the initiation of the experiment. The depth of 0 corresponds to an arbitrary position slightly below LCO pellet in the stainless steel. (b) The same data as in (a) after subtracting the relative transmission observed at time A1, which was the initiation of discharge. Red vertical lines highlight the normalization region used to normalize the x-axis on a 0 to 1 scale for Fig. 2.6 in the main text.

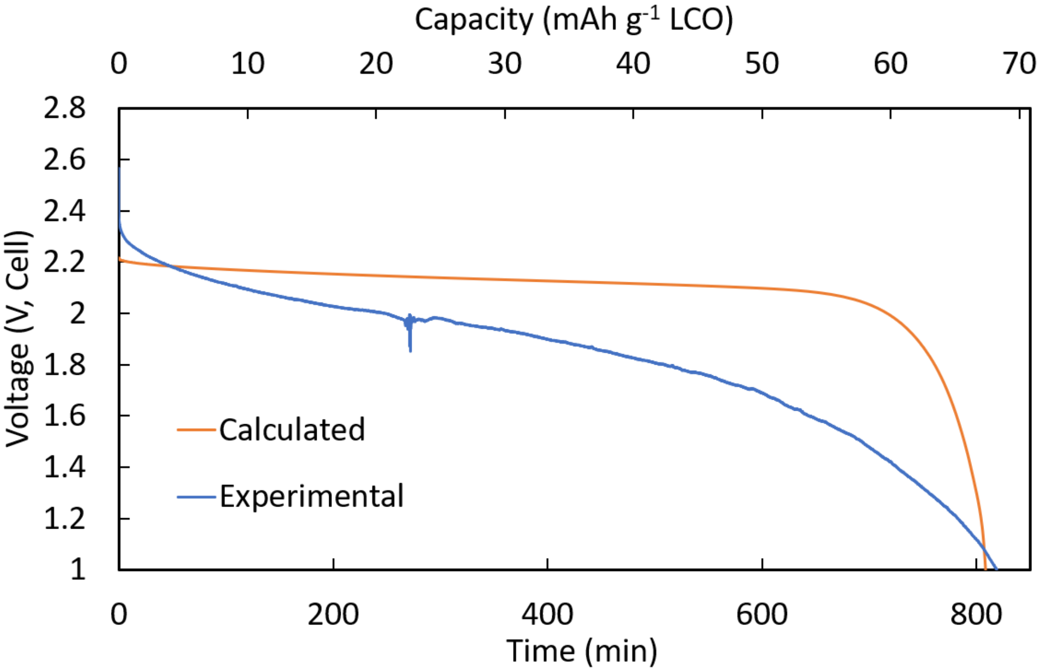

Fig. A1.9. Calculated (orange) and experimentally measured (blue) discharge profiles for the LTO/LCO-Thin cell.

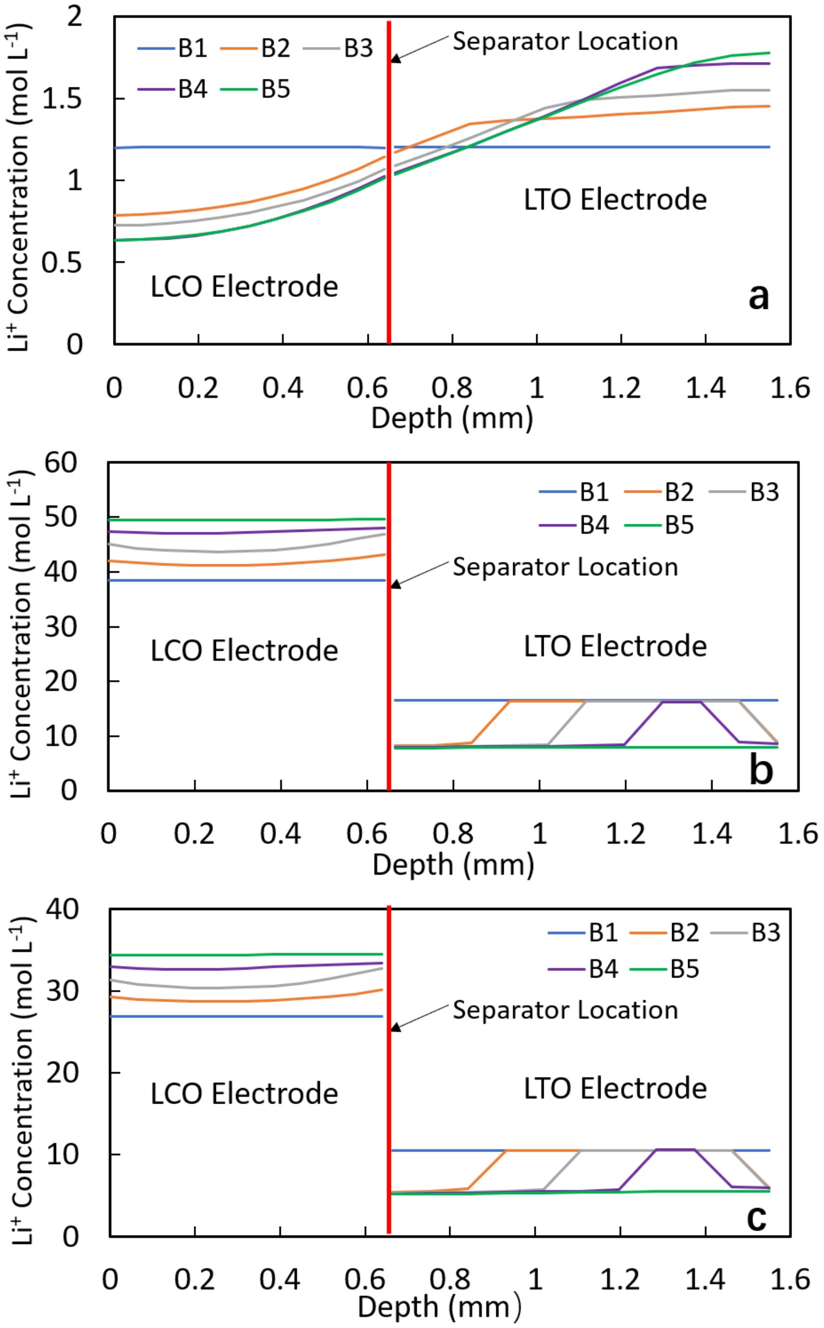

Fig. A1.10. Li^+ concentrations at different locations within both electrodes calculated using the model for the LTO/LCO-Thin cell on a molar basis. Concentrations are shown for the (a) liquid electrolyte phase, (b) solid active material phase, (c) and the sum of the total concentration. The B1-B5 corresponds to the time points chosen in the discharge profile (refer to Fig. 2.6). Total concentration was calculated using the equation: $c_t=c_e\times\varepsilon+c_s\times(1-\varepsilon)$, where c_t is the total concentration, c_e is the concentration in electrolyte, c_s is the concentration in solid phase, ε is the porosity of the electrode.

References

(1) Doyle, M.; Fuller, T. F.; Newman, J. Modeling of Galvanostatic Charge and Discharge of the Lithium/Polymer/Insertion Cell. *J. Electrochem. Soc.* **1993**, *140*, 1526–1533.

(2) Fuller, T. F.; Doyle, M.; Newman, J. Simulation and Optimization of the Dual Lithium Ion Insertion Cell. *J. Electrochem. Soc.* **1994**, *141*, 1–10.

(3) Fuller, T. F.; Doyle, M.; Newman, J. Relaxation Phenomena in Lithium-Ion-Insertion Cells. *J. Electrochem. Soc.* **1994**, *141*, 982–990.

(4) Allu, S.; Kalnaus, S.; Elwasif, W.; Simunovic, S.; Turner, J. A.; Pannala, S. A New Open Computational Framework for Highly-Resolved Coupled Three-Dimensional Multiphysics Simulations of Li-Ion Cells. *J. Power Sources* **2014**, *246*, 876–886.

(5) Zhou, H.; An, K.; Allu, S.; Pannala, S.; Li, J.; Bilheux, H. Z.; Martha, S. K.; Nanda, J. Probing Multiscale Transport and Inhomogeneity in a Lithium-Ion Pouch Cell Using in Situ Neutron Methods. *ACS Energy Lett.* **2016**, *1*, 981–986.

Appendix 2. Supporting material for chapter 3

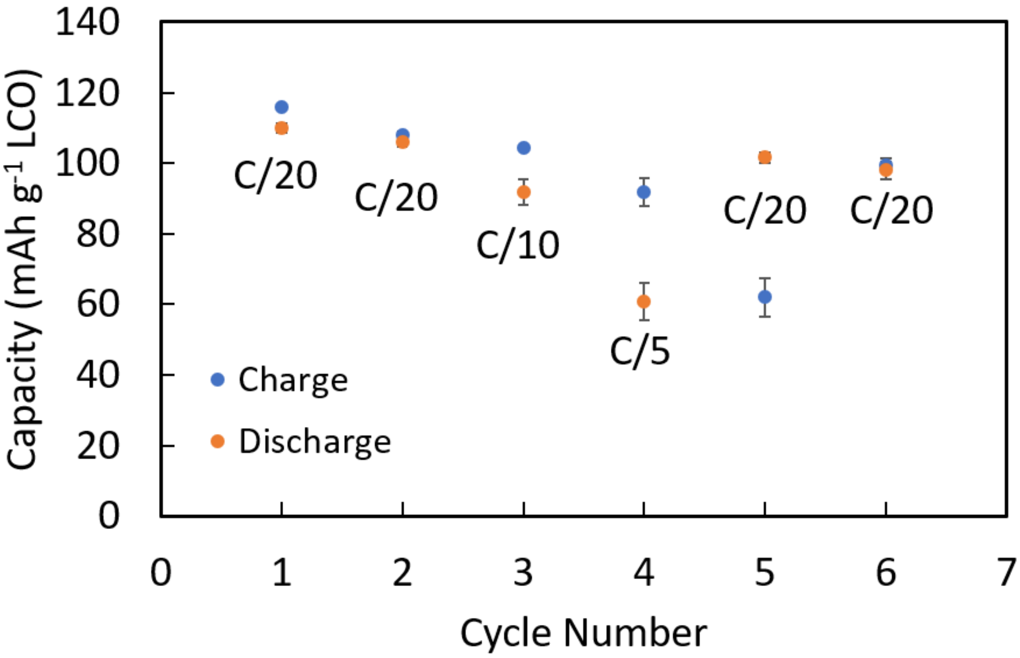

Fig. A2.1. Average electrochemical charge (blue circles) and discharge (orange circles) capacities for three nominally identical sintered LTO/LCO coin cells which were processed the same as the cell used in the neutron imaging experiment. Error bars represent the standard deviations for the three cells, and where error bars are not apparent they were smaller than the data markers. The charge rate for all cycles was C/20 (7.5 mA g^{-1} LCO) while the discharge rates were C/20 (cycles 1, 2, 5, and 6), C/10 (cycle 3, 15.0 mA g^{-1} LCO), and C/5 (cycle 4, 30 mA g^{-1} LCO), with the discharge rate labelled on the figure.

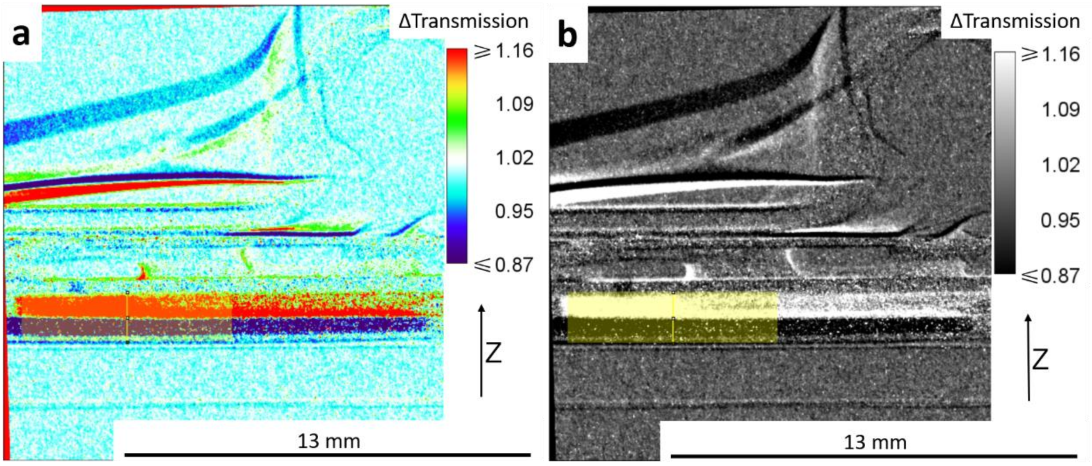

Fig. A2.2. Example color scale (a) and grey scale (b) of the same neutron images from the end of the first discharge (images are from D^{1}_{832} in Fig. 3.2 in the main text). The yellow shaded region in the images represent the area chosen for line scans to obtain the average transmission profiles as a function of depth in the cell (z-direction as shown in (a) and (b)). The grey scale image is given here to more clearly show the yellow line scan region.

Tortuosity measurement of sintered electrode

The tortuosity measurement was based on the publication of Thorat *et al.*[1] For tortuosity analysis, only LTO pellets were evaluated. The electronic conductivity of the LCO is much greater than the LTO and results in incorrectly low measured resistance in the cell, consistent with other reports in the literature.[2,3] As described in the main text, although LTO electronic conductivity has been reported to be much lower than LCO, the neutron radiographs and polarization curves presented in this study suggested that the LTO electronic conductivity was likely greater than expected. Thus, measured values of tortuosity described below should be considered as lower bounds for the actual tortuosity and Bruggeman exponent for the electrodes. However, the electrodes were prepared identically and thus the relative comparison between coin cell and split cell measurements described below should still be appropriate. The LTO and LCO have similar particle sizes and particle size distributions which should result in similar tortuosity in the resulting pellets. A Li/Li symmetric cell was constructed as illustrated in Fig A2.3. This structure was assembled both by crimping within a CR2032 coin cell as well by fastening together a split cell (MTI corporation). Previous experience in assembling coin cells has sometimes resulted in cracking in the porous thin films, while in the split cell the compression is much more gradual. All pellets used in the split cell were extracted after electrochemical evaluation and confirmed not to have cracks. The LTO within coin cells required excessive physical force to harvest the electrodes and thus it could not be assessed if cracking was due to the initial crimping or the pellet extraction process.

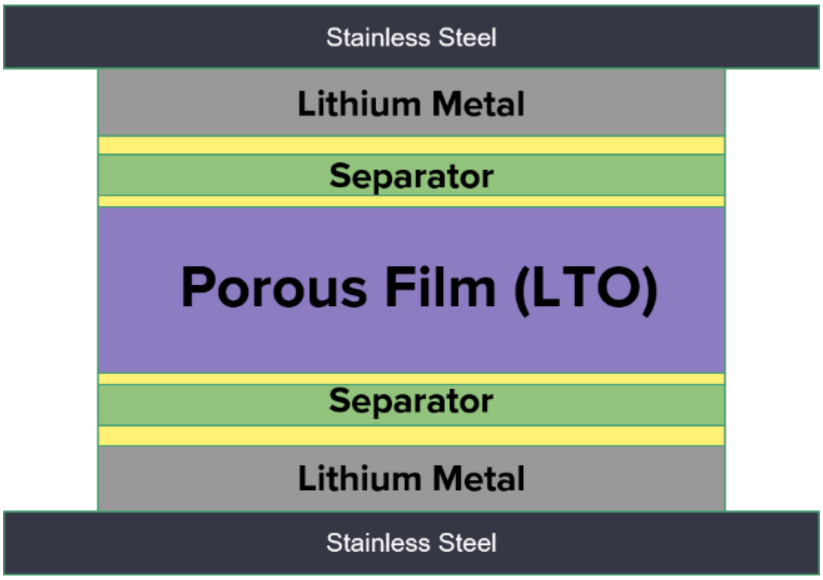

Fig. A2.3. Illustration of a cross-sectional view of the Li/Li symmetric cell used for tortuosity measurements.

Both the coin cell and the split cell were evaluated using potentiostatic electrochemical impedance spectroscopy (EIS). From the EIS results, the high frequency intercept (R_∞) was extracted (Fig. A2.4). The tortuosity (τ) and Bruggeman exponent (α) were calculated using the following equations:

$$k_{eff} = \frac{L}{A \times R_\infty}$$

$$\tau = \frac{k_{real} \times \epsilon}{k_{eff}}$$

$$\tau = \epsilon^{1-\alpha}$$

where L is the thickness of the porous film; A is its cross-sectional area; k_{eff} is the effective ionic conductivity of the electrolyte; ϵ is the porosity; k_{real} is the intrinsic conductivity of the electrolyte with a value of 5.41 mS/cm (measured using a conductivity probe).

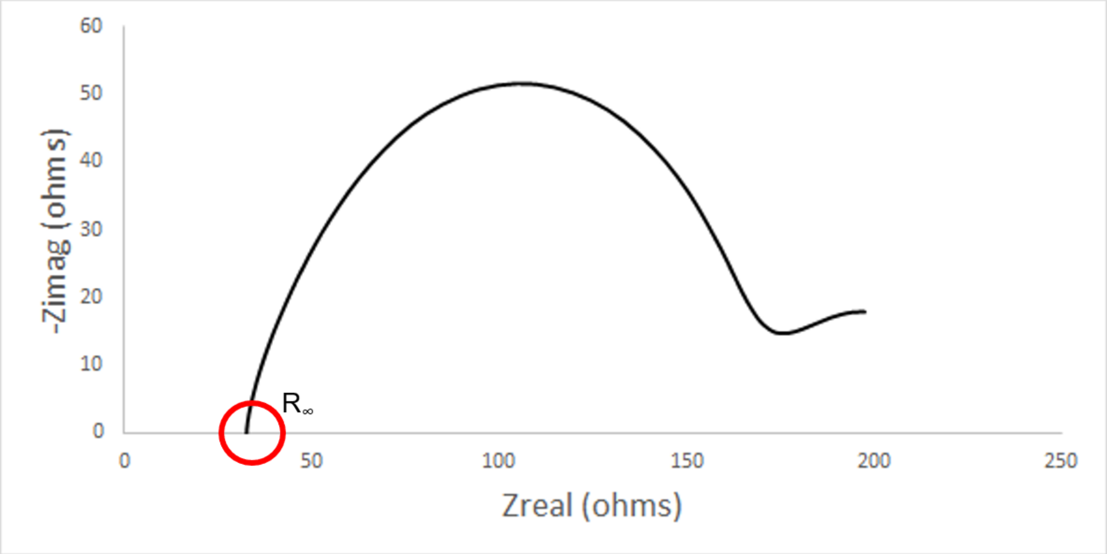

Fig. A2.4. Example of EIS results form a Li/Li symmetric cell as shown in Fig. A2.3 and R_∞

The results of multiple samples with different cell structures are shown in Table A2.1. From the average results, the split cell with an uncracked pellet showed good agreement with the commonly assumed empirical Bruggeman exponent value (α=1.5). The coin cell samples all showed a value less than 1.5, which indicated some cracking likely occurred during the crimping process.

Table A2.1. Bruggeman exponent for different Li/Li symmetric cell

	Bruggeman Exponent	
Sample No.	Coin Cell	Split Cell
1	1.28	1.49
2	1.38	1.58
3	1.18	1.39
4	1.10	1.49
5		1.43
Average	1.23	1.48

Additional Details on Electrolyte Properties

As mentioned above the measured ionic conductivity of the bulk electrolyte as prepared was of 5.41 mS/cm, however, for the detailed calculations done in this study additional electrolyte properties were required beyond this single conductivity value and the bulk salt concentration of 1.2 mol/L $LiPF_6$.

The electrolyte properties as a function of concentration used in calculations were originally from Newman's Dualfoil code.[4] These properties, acknowledged in the code, were measured by Capiglia *et al*[5] and Doyle[6] and are listed below:

Diffusion coefficient:

$$\mathrm{D} = 5.34 \times 10^{-10} \times \varepsilon^{\alpha} e^{6.5\times10^{-4} c}$$

Transference number:

$$t^{+} = 0.4$$

Conductivity:

$$\kappa = \varepsilon^{\alpha}(0.0911 + 1.9101 \times 10^{-3}c - 1.052 \times 10^{-6}c^2 + 1.554 \times 10^{-10}c^3)$$

List of symbols:

c	Concentration of electrolyte (mol/m^3)
D	Diffusion coefficient (m^2/s)
t^+	Transference number
α	Bruggeman exponent
ε	Porosity
κ	Conductivity of electrolyte (S/m)

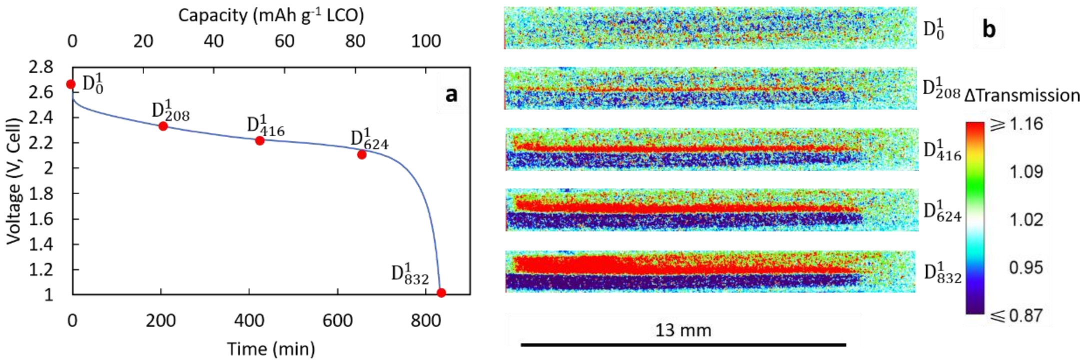

Fig. A2.5. (a) Discharge profiles of D^1 at C/20. (b) Neutron images corresponding to the time points noted in (a).

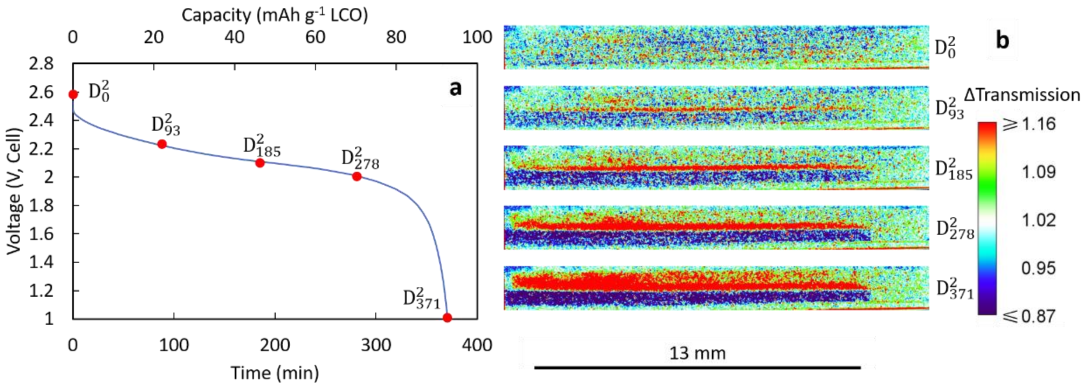

Fig. A2.6. (a) Discharge profiles of D^2 at C/10. (b) Neutron images corresponding to the time points noted in (a).

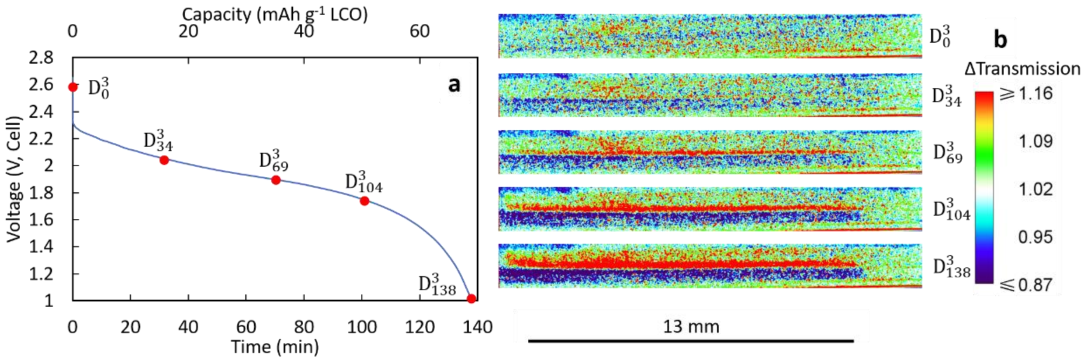

Fig. A2.7. (a) Discharge profiles of D^3 at C/5. (b) Neutron images corresponding to the time points noted in (a).

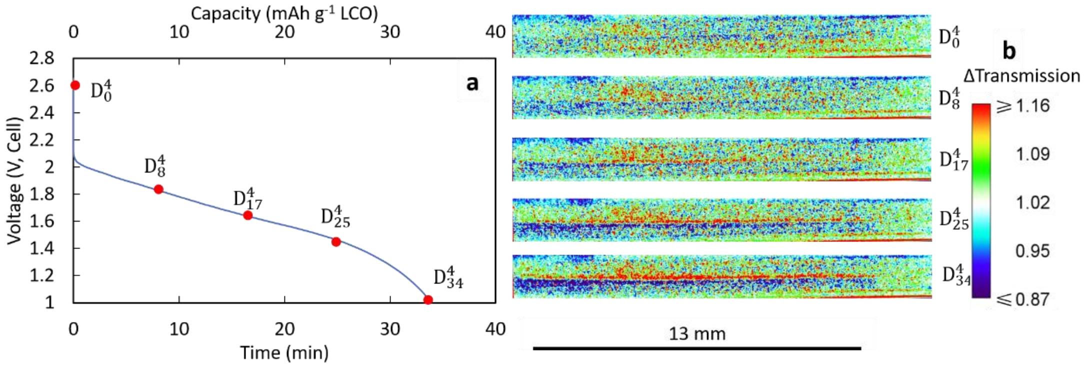

Fig. A2.8. (a) Discharge profiles of D^4 at C/2.5. (b) Neutron images corresponding to the time points noted in (a).

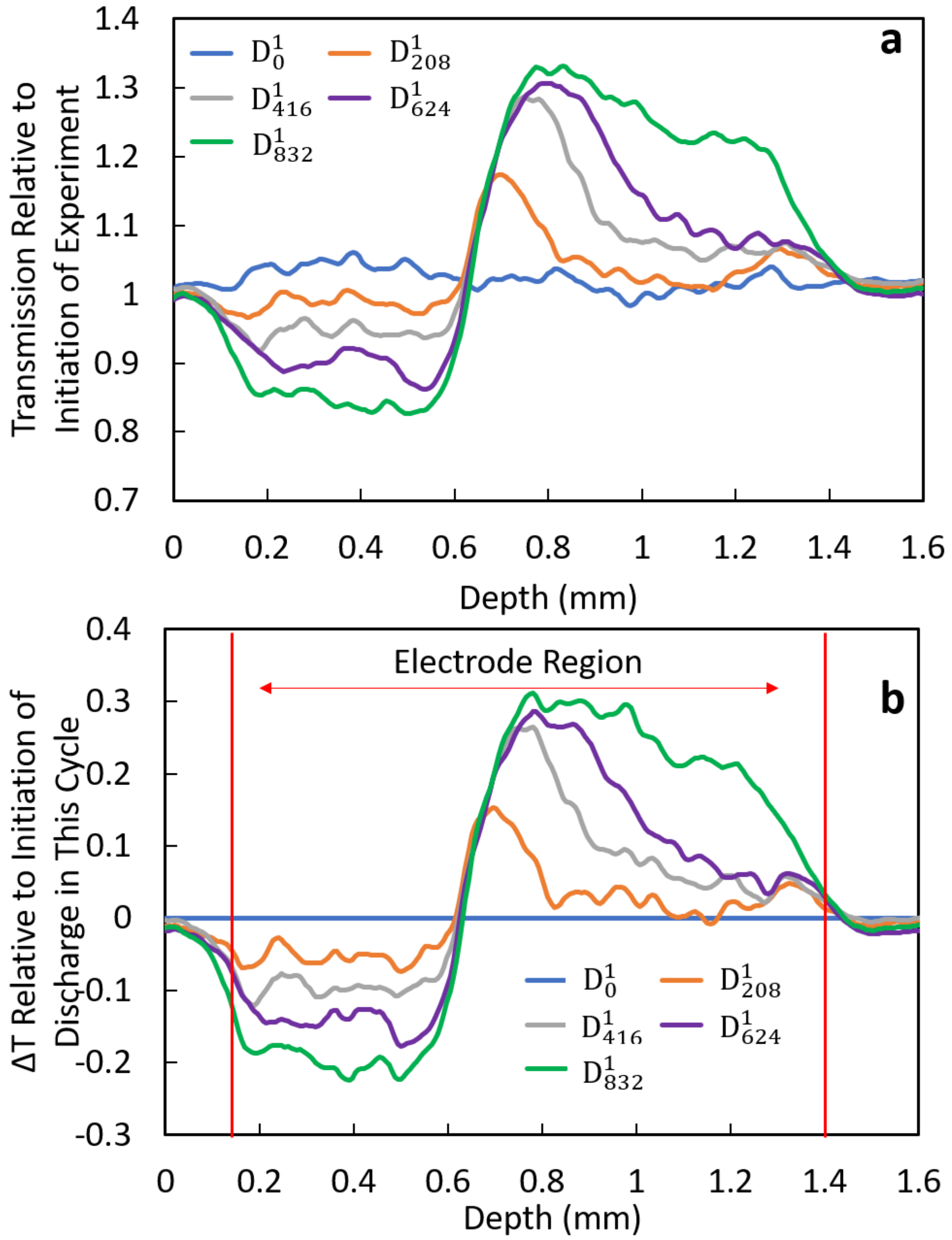

Fig. A2.9. (a) Relative transmission profiles of D^1 discharge process, where the transmission was relative to the initiation of the experiment. The depth of 0 corresponds to an arbitrary position slightly below LCO pellet in the stainless steel. (b) The same data as in (a) after subtracting the relative transmission observed at time D^1_0, which was the initiation of discharge in this cycle. Red vertical lines highlight the region of electrodes selected based on the method described above, and this region was rescaled from 0 mm for the final results shown in the main text in Fig. 3.4.

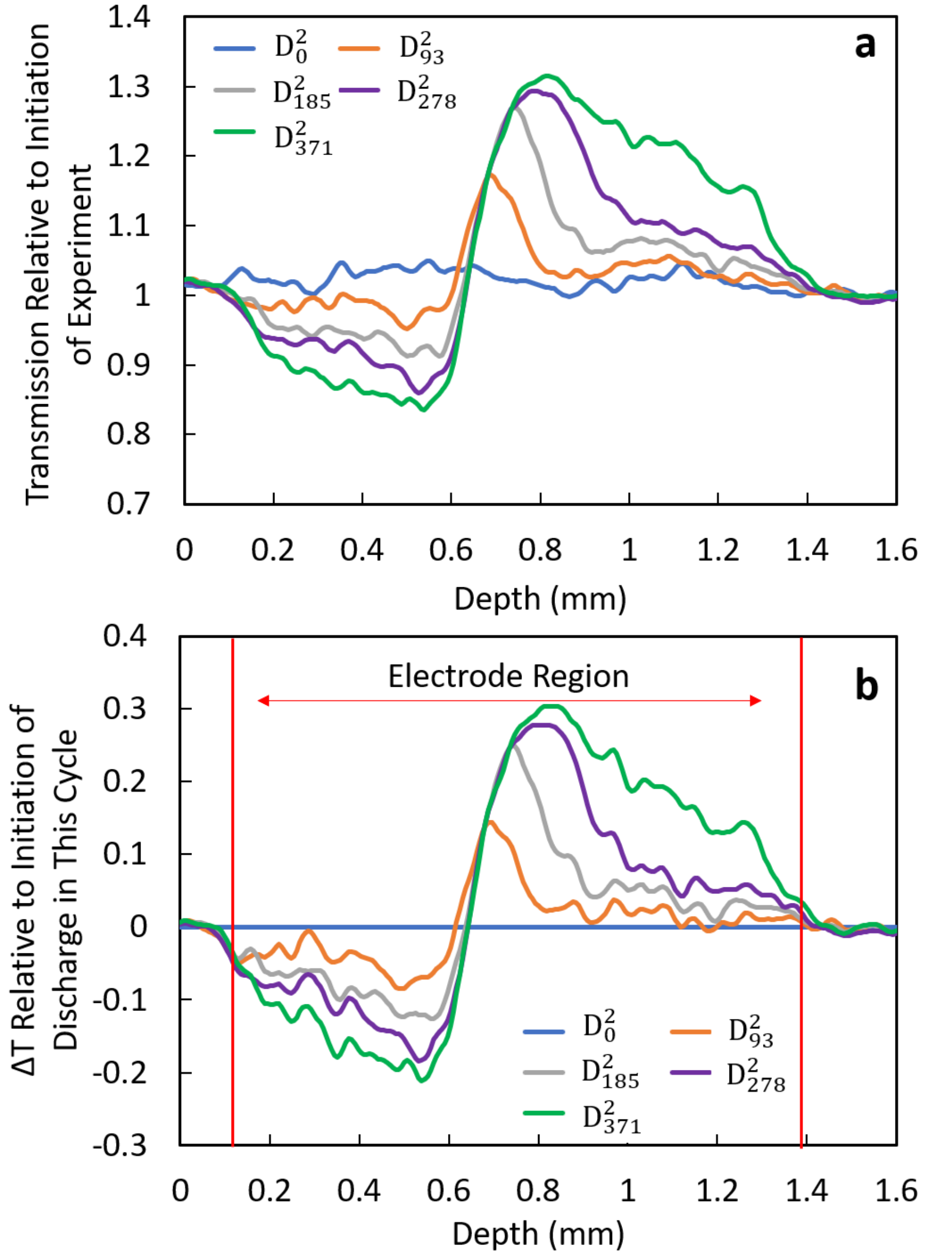

Fig. A2.10. (a) Relative transmission profiles of D^2 discharge process, where the transmission was relative to the initiation of the experiment. The depth of 0 corresponds to an arbitrary position slightly below LCO pellet in the stainless steel. (b) The same data as in (a) after subtracting the relative transmission observed at time D^2_0, which was the initiation of discharge in this cycle. Red vertical lines highlight the region of electrodes selected based on the method described above, and this region was rescaled from 0 mm for the final results shown in Fig. A2.14.

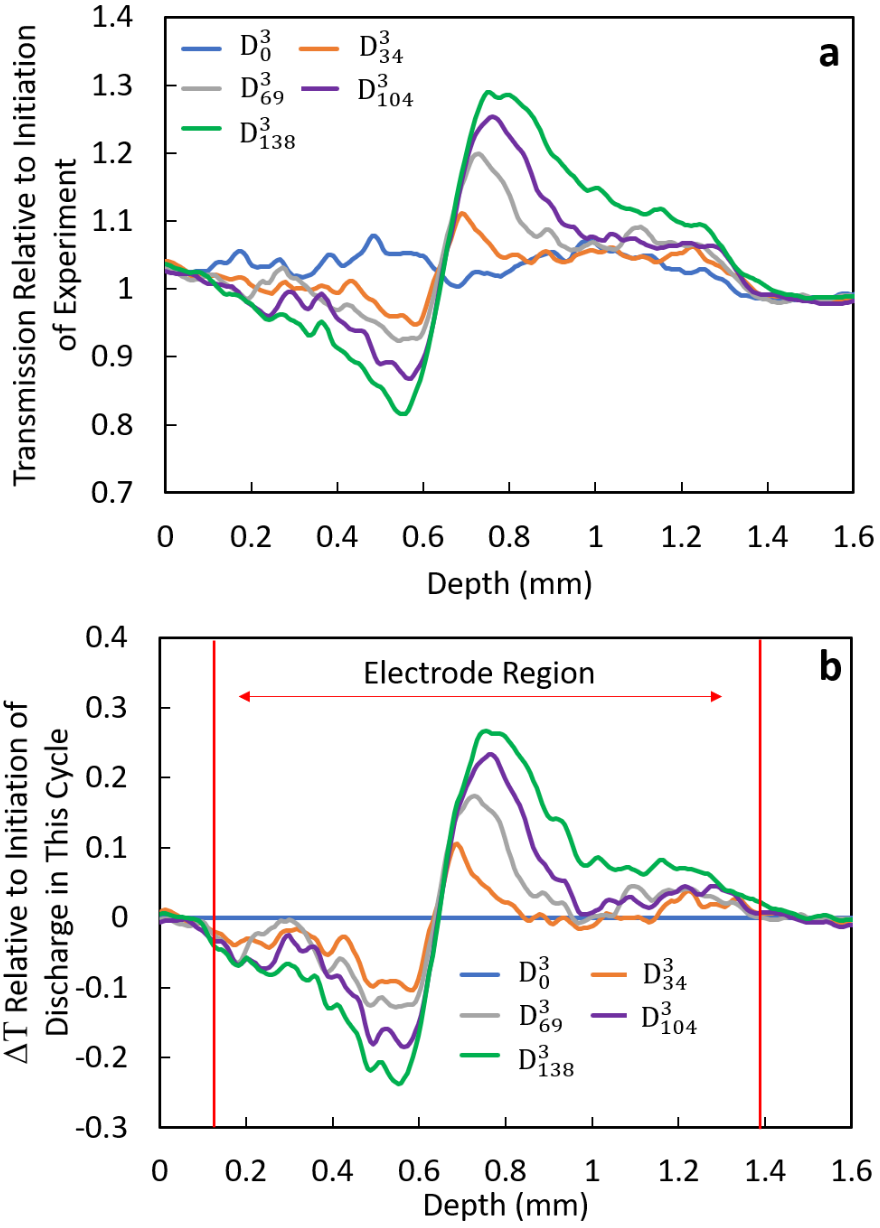

Fig. A2.11. (a) Relative transmission profiles of D^3 discharge process, where the transmission was relative to the initiation of the experiment. The depth of 0 corresponds to an arbitrary position slightly below LCO pellet in the stainless steel. (b) The same data as in (a) after subtracting the relative transmission observed at time D^3_0, which was the initiation of discharge in this cycle. Red vertical lines highlight the region of electrodes selected based on the method described above, and this region was rescaled from 0 mm for the final results shown in the main text in Fig. 3.5.

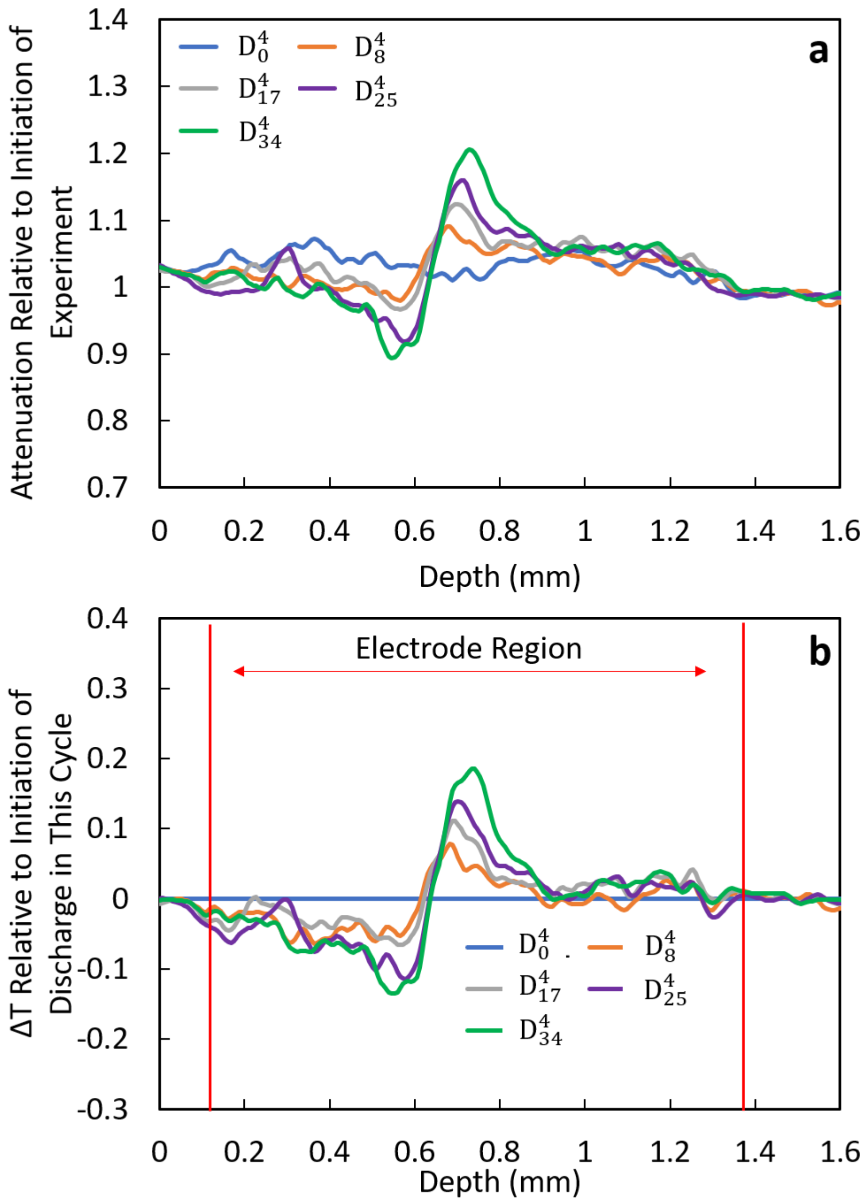

Fig. A2.12. (a) Relative transmission profiles of D^4 discharge process, where the transmission was relative to the initiation of the experiment. The depth of 0 corresponds to an arbitrary position slightly below LCO pellet in the stainless steel. (b) The same data as in (a) after subtracting the relative transmission observed at time D_0^4, which was the initiation of discharge in this cycle. Red vertical lines highlight the region of electrodes selected based on the method described above, and this region was rescaled from 0 mm for the final results shown in Fig. A2.15.

Selection of electrode region.

The line scan region was from a selected position below the LCO electrode to a selected position above the LTO electrode. Thus, the line scan profiles showed a depth longer than the total thickness of the real electrode region (Fig. A2.9, A2.10, A2.11, A2.12). To select the electrode region, the position of the bottom of the LCO, top of the LTO, and the separator must be located. To do this, a line scan was applied to the raw neutron imaging radiograph. The line scan region is shown in Fig. A2.13a. The image of Fig. A2.13a is the same one displayed in the main text Fig. 3.1b, but the contrast was adjusted to better display the inner structure of the coin cell. From Fig. A2.13a, the electrode region was clearly identified because the electrodes contain high concentrations of highly attenuating Li, and thus those regions were much darker than other regions in the coin cell. The transmission intensity profile is displayed in Fig. A2.13b. At the interface regions for different materials (e.g. stainless steel vs. LCO, LCO vs. LTO and LTO vs. stainless steel), there exists gradient regions. In this study, the midpoints of these gradient regions were chosen as the interface location. The bottom of LCO and the top of LTO pellet were thus located (Fig. A2.13b). The total thickness of the electrode region is 1.248 mm, which was 5 % greater than the experimentally measured combined thickness of the electrodes and separator, and this difference was attributed to image magnification and imperfect alignment of the cell. For the separator location, because the separator (25 μm) was much thinner than LCO (468 μm) and LTO (691 μm) pellets, a single line is shown in Fig. A2.13b instead of two lines representing the bottom and top of the separator. To confirm the selected locations for the electrode regions were consistent with the measured electrode dimension, comparison was made to the proportions of LCO and LTO electrodes. The physical measurements would result in LCO occupying 40.5 % of the total thickness and LTO occupying 59.5 % (assuming half the separator with each electrode). From the selected location in neutron imaging test, the LCO and LTO occupied 41.1 % and 58.9 % of total thickness, respectively, which was close to the physical measurements. Based on the three locations selected, the electrode region of the ΔTransmission profiles were chosen for each discharge process (Fig. A2.9b, A2.10b, A2.11b, A2.12b). The depth for the selected region with was rescaled to get the final ΔTransmission profiles showed in Fig. 3.4a, 3.5a, A2.14a, A2.15a.

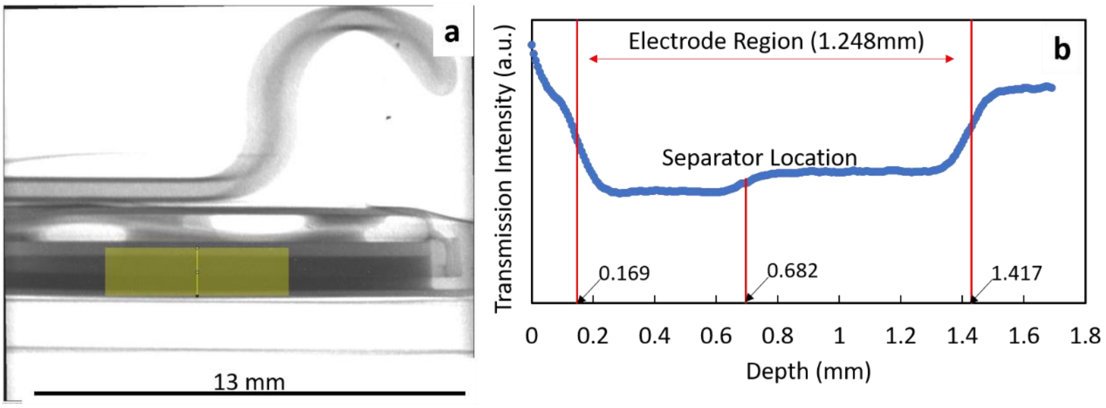

Fig. A2.13. (a) Neutron imaging radiograph. Image is the same as in main text Fig. 3.1b with contrast adjusted. (b) Line scan profiles of the yellow shaded region in (a), the scan direction was from bottom to top. Selected locations of LCO edge, LTO edge and separator are noted with red lines.

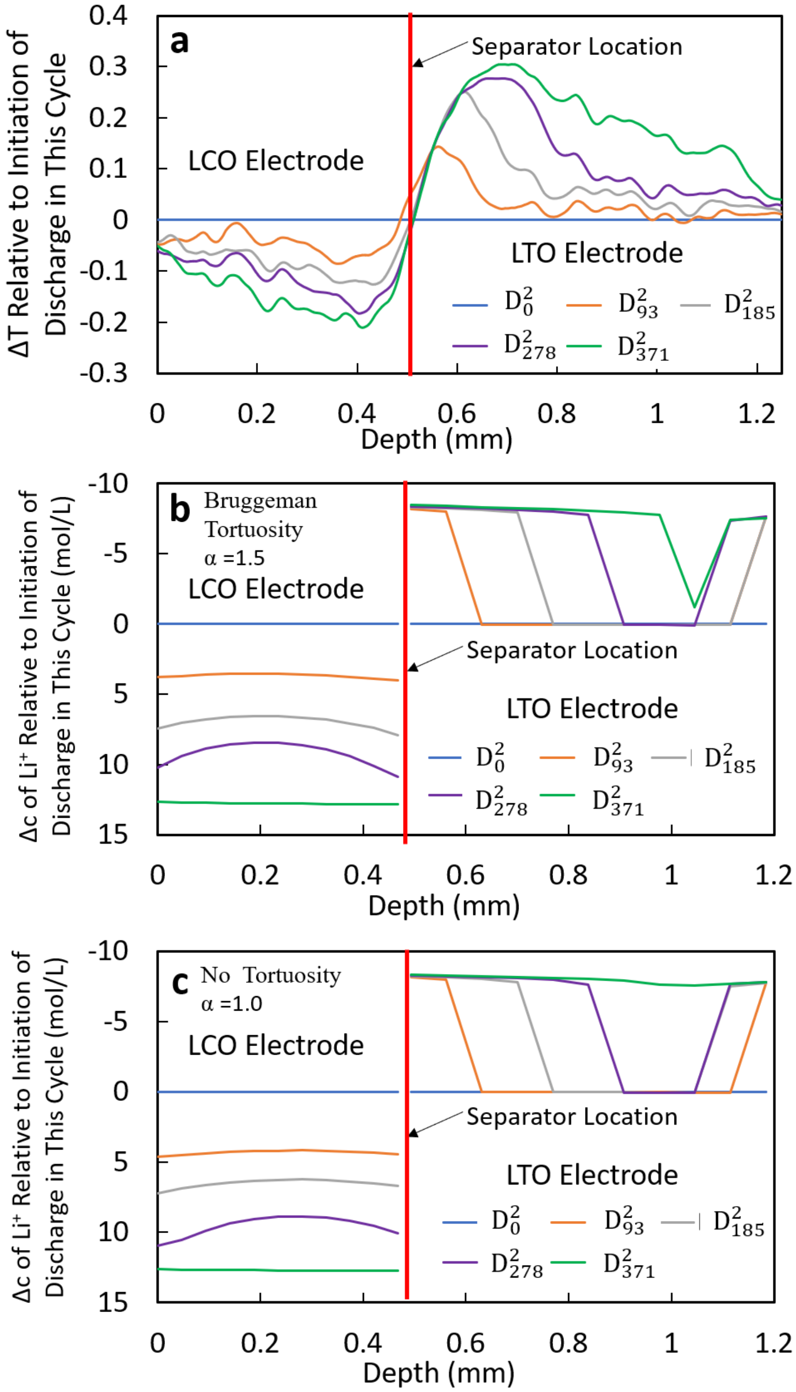

Fig. A2.14. Experimental and calculated results of D^2 discharge process. (a) ΔTransmission at different time relative to initiation of discharge in this cycle from neutron radiographs. (b) Calculated change in Li^+ concentration at different times relative to initiation of discharge in this cycle for α=1.5. (c) Calculated change in Li^+ concentration at different times relative to initiation of discharge in this cycle for α=1.0.

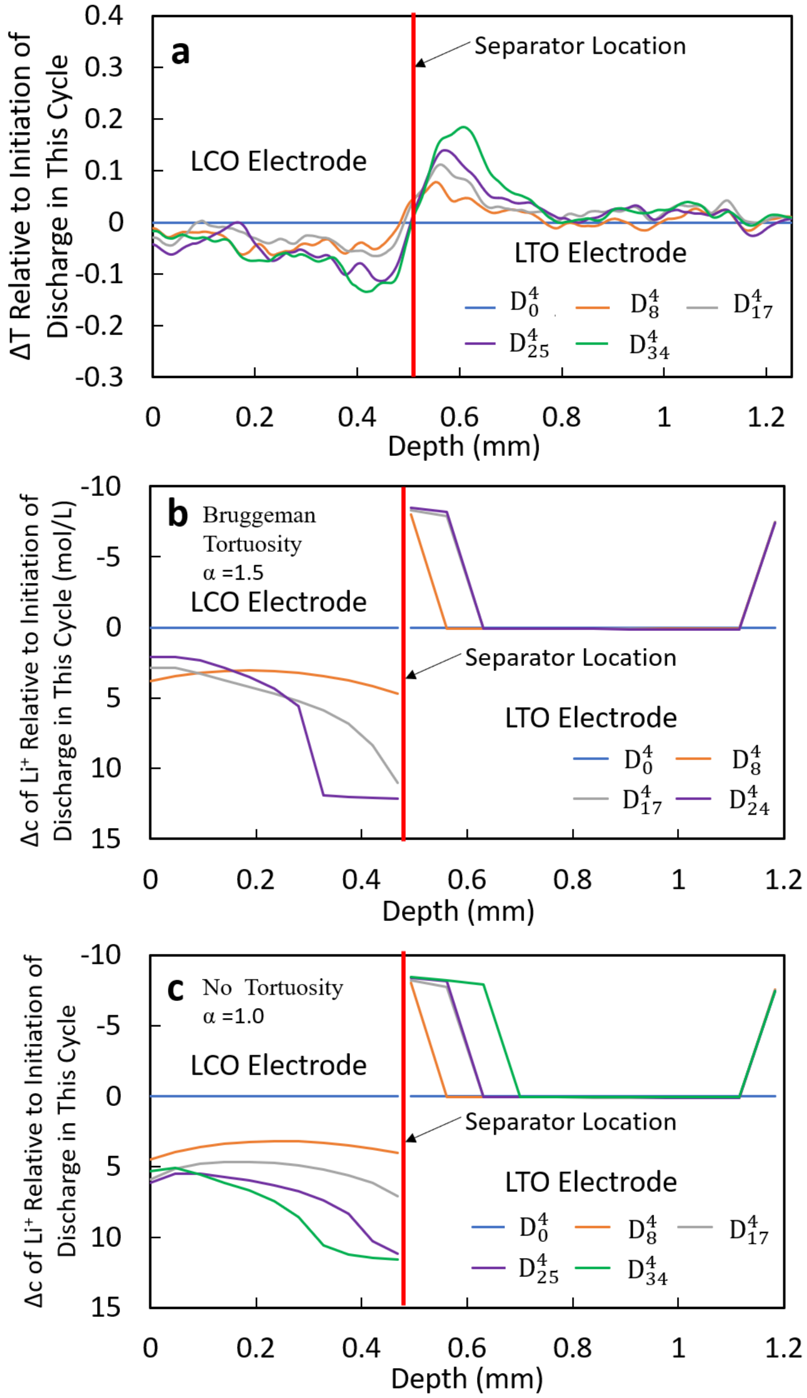

Fig. A2.15. Experimental and calculated results of D^4 discharge process. (a) ΔTransmission at different time relative to initiation of discharge in this cycle from neutron radiographs. (b) Calculated change in Li^+ concentration at different times relative to initiation of discharge in this cycle for α=1.5. (c) Calculated change in Li^+ concentration at different times relative to initiation of discharge in this cycle for α=1.0.

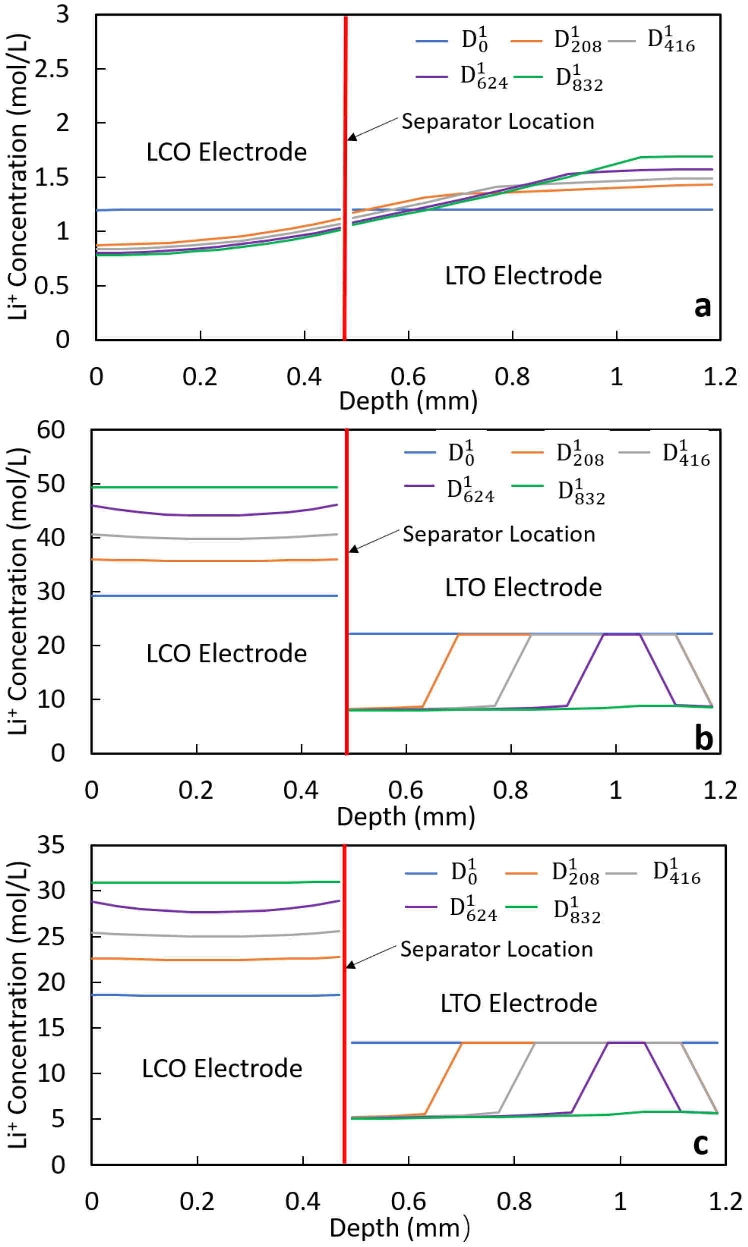

Fig. A2.16. Calculated Li$^+$ concentrations at different locations within both electrodes on a molar basis for D^1 process with Bruggeman tortuosity exponent $\alpha=1.5$. Concentrations are shown for the (a) liquid electrolyte phase, (b) solid active material phase, (c) and the sum of the total concentration. The subscript for each "D" corresponds to the time points in the discharge profile. Total concentration was calculated using the equation: $c_t=c_e\times\varepsilon+c_s\times(1-\varepsilon)$, where c_t is the total concentration, c_e is the concentration in electrolyte, c_s is the concentration in solid phase, ε is the electrode porosity.

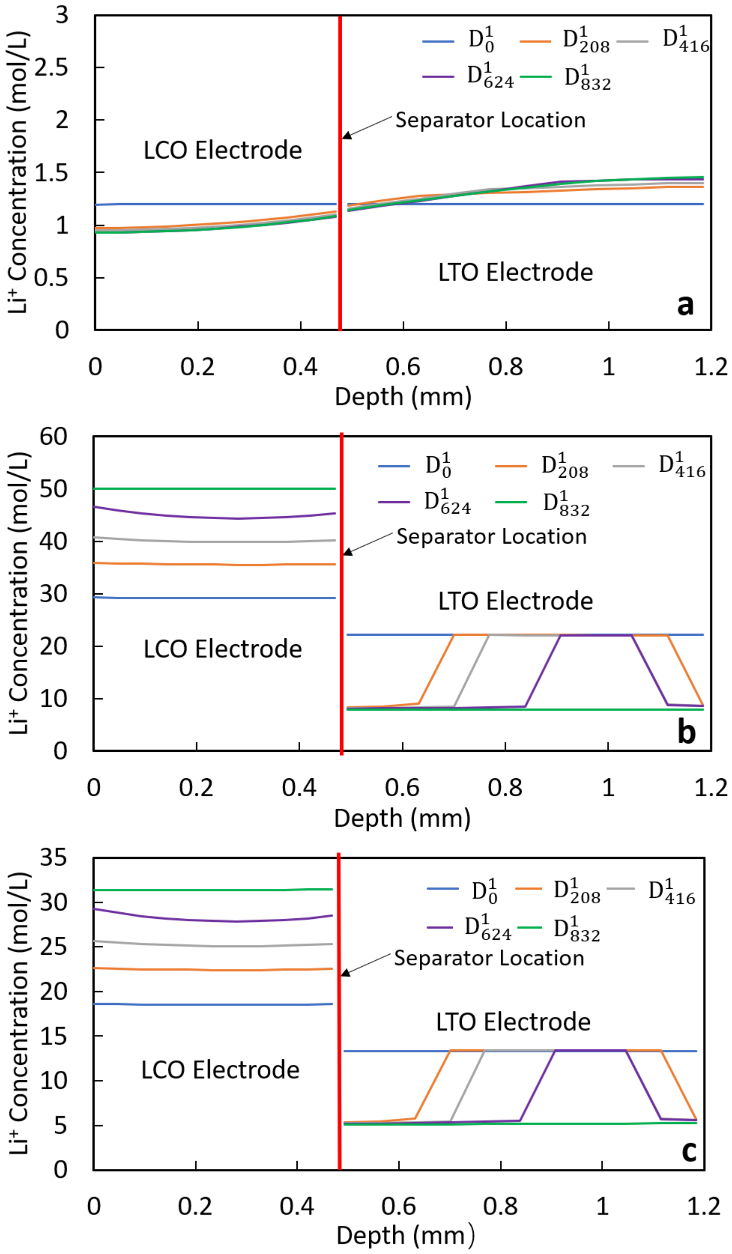

Fig. A2.17. Calculated Li^+ concentrations at different locations within both electrodes on a molar basis for D^1 process with no tortuosity (α=1.0). Concentrations are shown for the (a) liquid electrolyte phase, (b) solid active material phase, (c) and the sum of the total concentration. The subscript for each "D" corresponds to the time points in the discharge profile. Total concentration was calculated using the equation: $c_t=c_e\times\varepsilon+c_s\times(1-\varepsilon)$, where c_t is the total concentration, c_e is the concentration in electrolyte, c_s is the concentration in solid phase, ε is the porosity of the electrode.

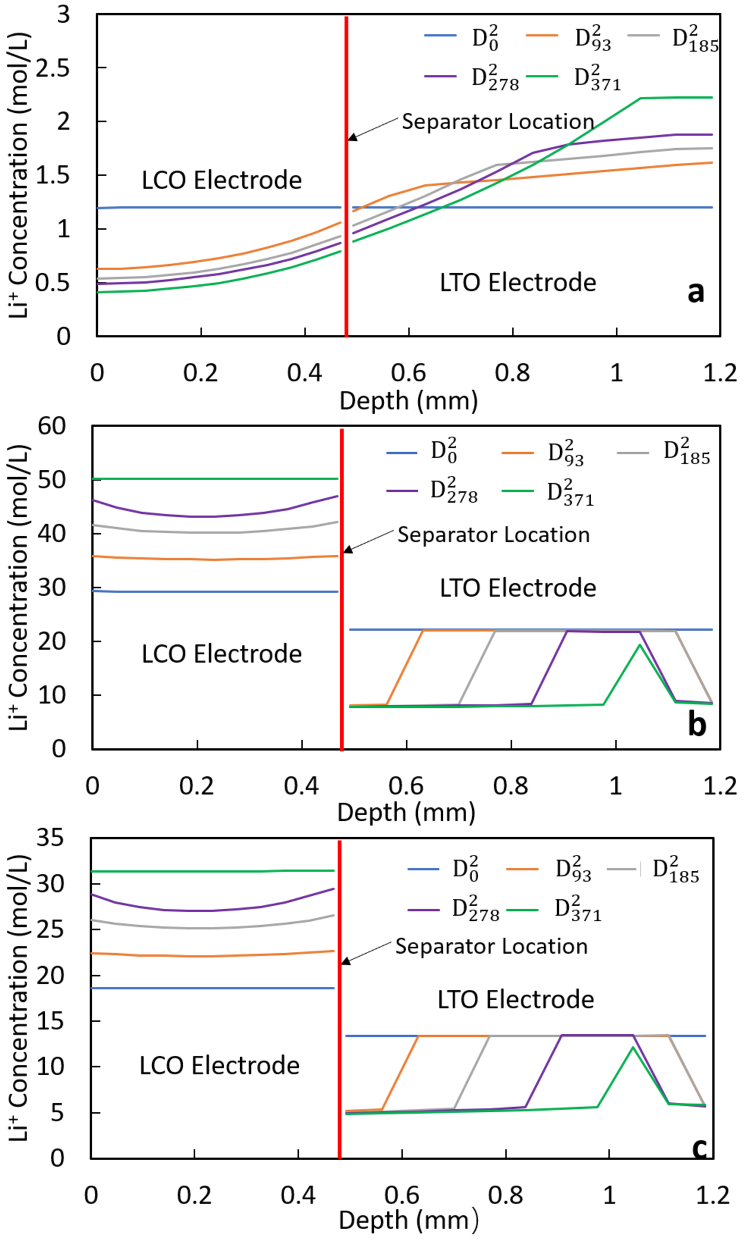

Fig. A2.18. Calculated Li$^+$ concentrations at different locations within both electrodes on a molar basis for D^2 process with Bruggeman tortuosity exponent α=1.5. Concentrations are shown for the (a) liquid electrolyte phase, (b) solid active material phase, (c) and the sum of the total concentration. The subscript for each "D" corresponds to the time points in the discharge profile. Total concentration was calculated using the equation: $c_t=c_e\times\varepsilon+c_s\times(1-\varepsilon)$, where c_t is the total concentration, c_e is the concentration in electrolyte, c_s is the concentration in solid phase, ε is the electrode porosity.

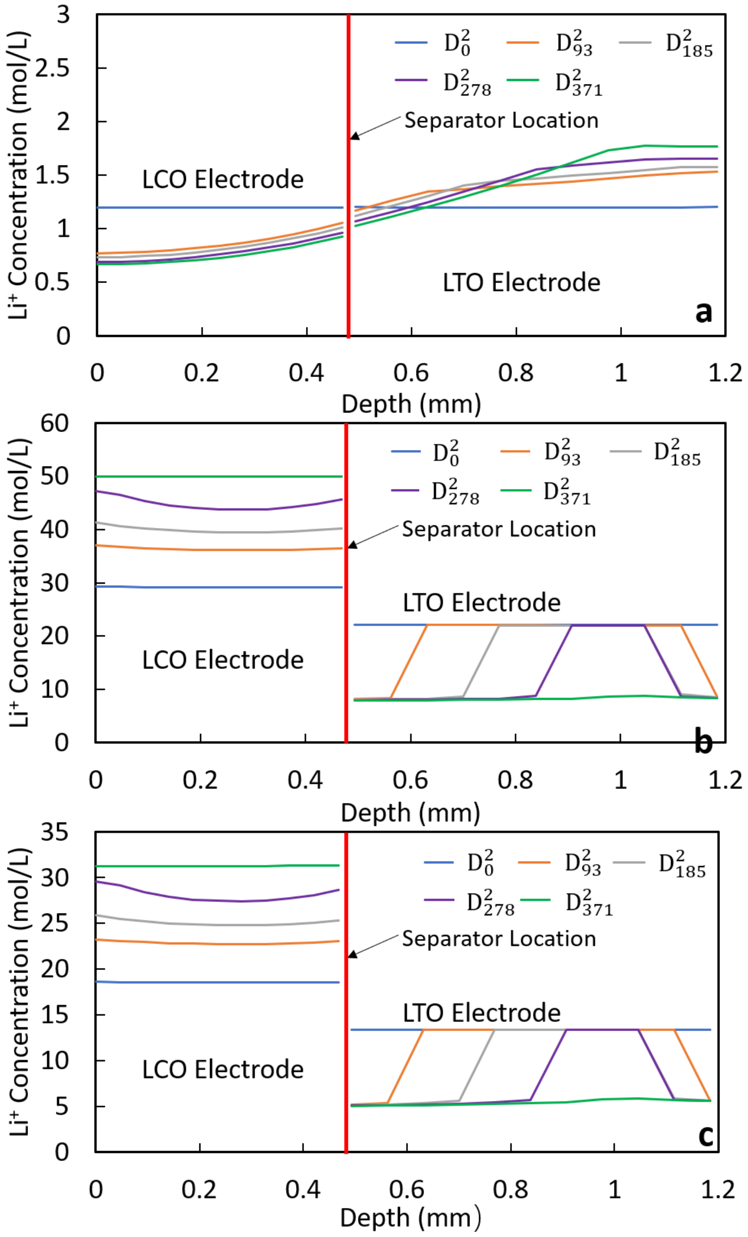

Fig. A2.19. Calculated Li^+ concentrations at different locations within both electrodes on a molar basis for D^2 process with no tortuosity (α=1.0). Concentrations are shown for the (a) liquid electrolyte phase, (b) solid active material phase, (c) and the sum of the total concentration. The subscript for each "D" corresponds to the time points in the discharge profile. Total concentration was calculated using the equation: $c_t=c_e\times\varepsilon+c_s\times(1-\varepsilon)$, where c_t is the total concentration, c_e is the concentration in electrolyte, c_s is the concentration in solid phase, ε is the porosity of the electrode.

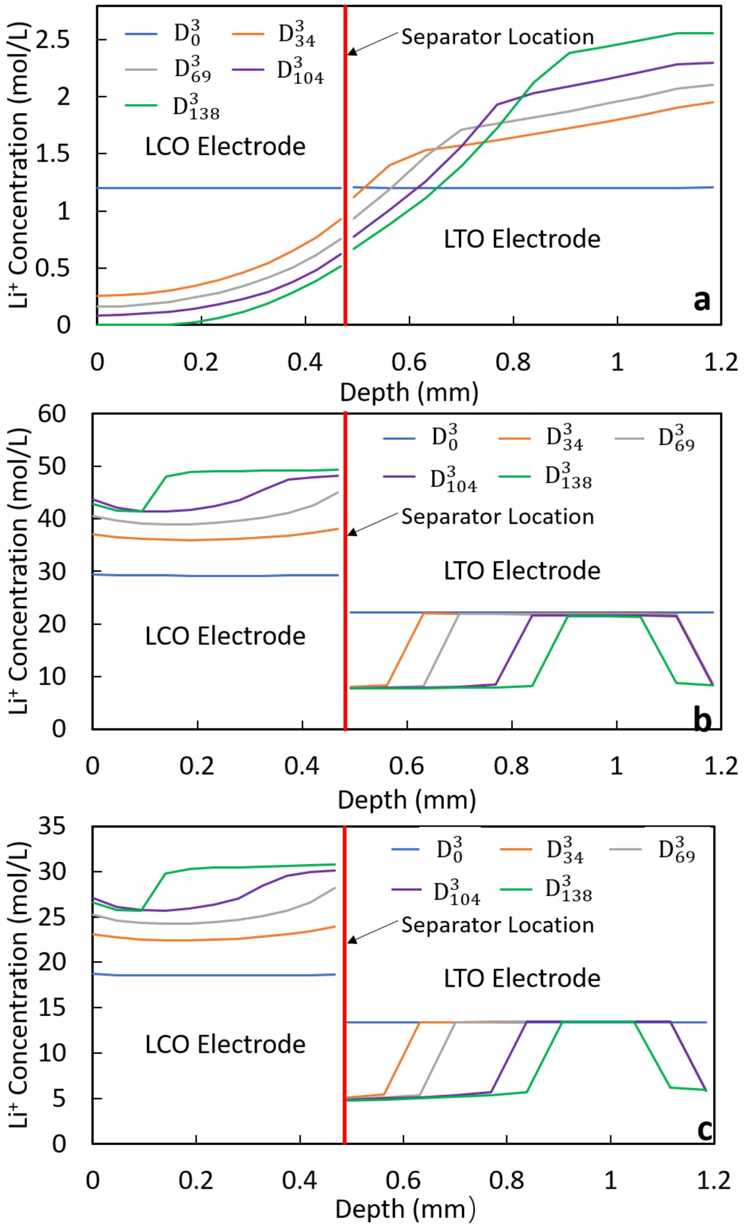

Fig. A2.20. Calculated Li^+ concentrations at different locations within both electrodes on a molar basis for D^3 process with Bruggeman tortuosity exponent α=1.5. Concentrations are shown for the (a) liquid electrolyte phase, (b) solid active material phase, (c) and the sum of the total concentration. The subscript for each "D" corresponds to the time points in the discharge profile. Total concentration was calculated using the equation: $c_t=c_e\times\varepsilon+c_s\times(1-\varepsilon)$, where c_t is the total concentration, c_e is the concentration in electrolyte, c_s is the concentration in solid phase, ε is the electrode porosity.

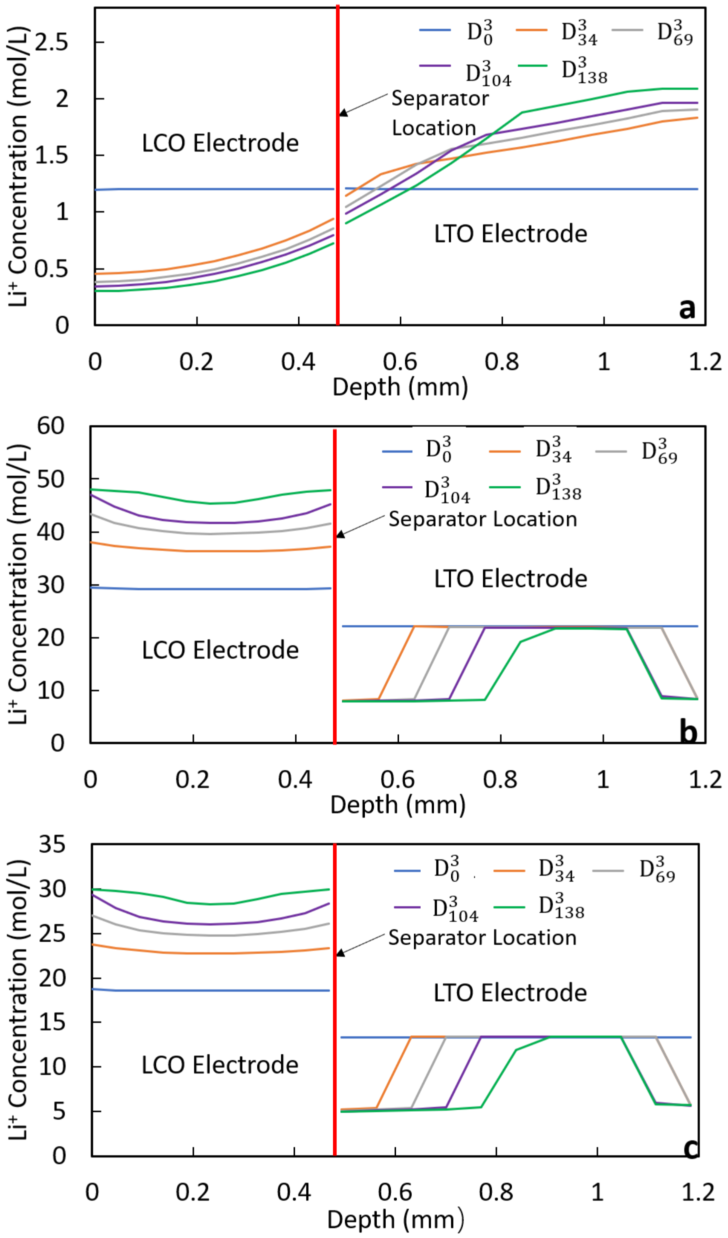

Fig. A2.21. Calculated Li$^+$ concentrations at different locations within both electrodes on a molar basis for D^3 process with no tortuosity (α=1.0). Concentrations are shown for the (a) liquid electrolyte phase, (b) solid active material phase, (c) and the sum of the total concentration. The subscript for each "D" corresponds to the time points in the discharge profile. Total concentration was calculated using the equation: $c_t=c_e\times\varepsilon+c_s\times(1-\varepsilon)$, where c_t is the total concentration, c_e is the concentration in electrolyte, c_s is the concentration in solid phase, ε is the porosity of the electrode.

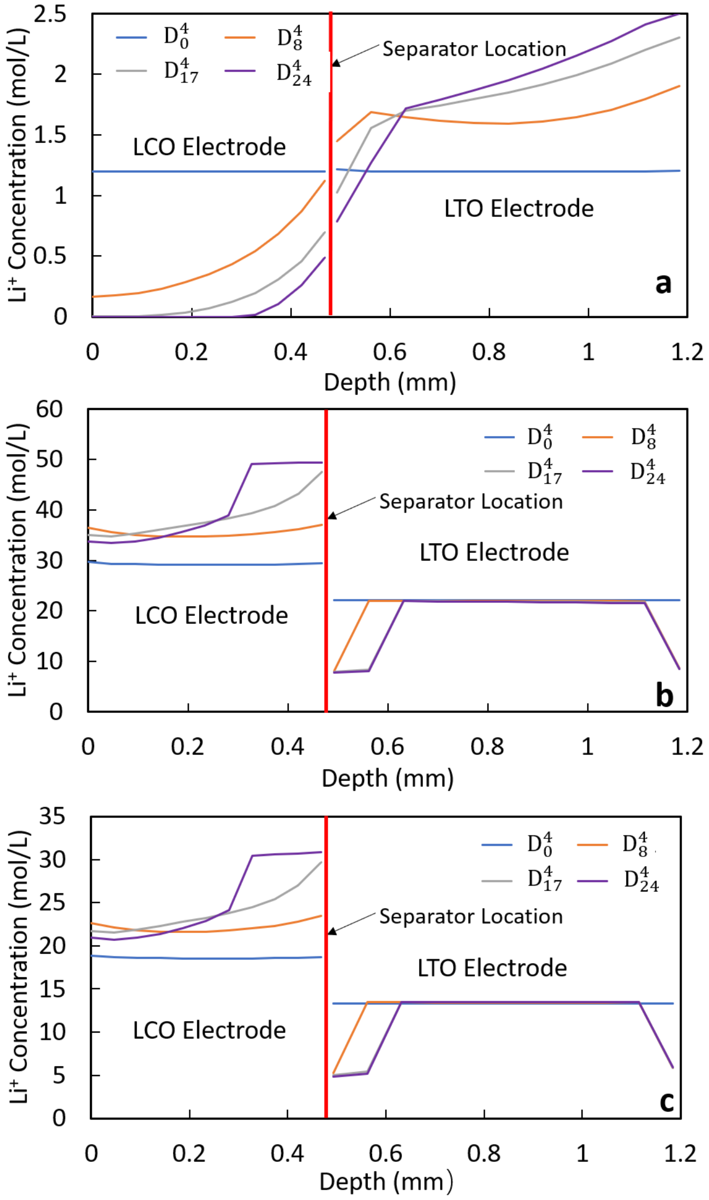

Fig. A2.22. Calculated Li^+ concentrations at different locations within both electrodes on a molar basis for D^4 process with Bruggeman tortuosity exponent α=1.5. Concentrations are shown for the (a) liquid electrolyte phase, (b) solid active material phase, (c) and the sum of the total concentration. The subscript for each "D" corresponds to the time points in the discharge profile. Total concentration was calculated using the equation: $c_t=c_e\times\varepsilon+c_s\times(1-\varepsilon)$, where c_t is the total concentration, c_e is the concentration in electrolyte, c_s is the concentration in solid phase, ε is the electrode porosity.

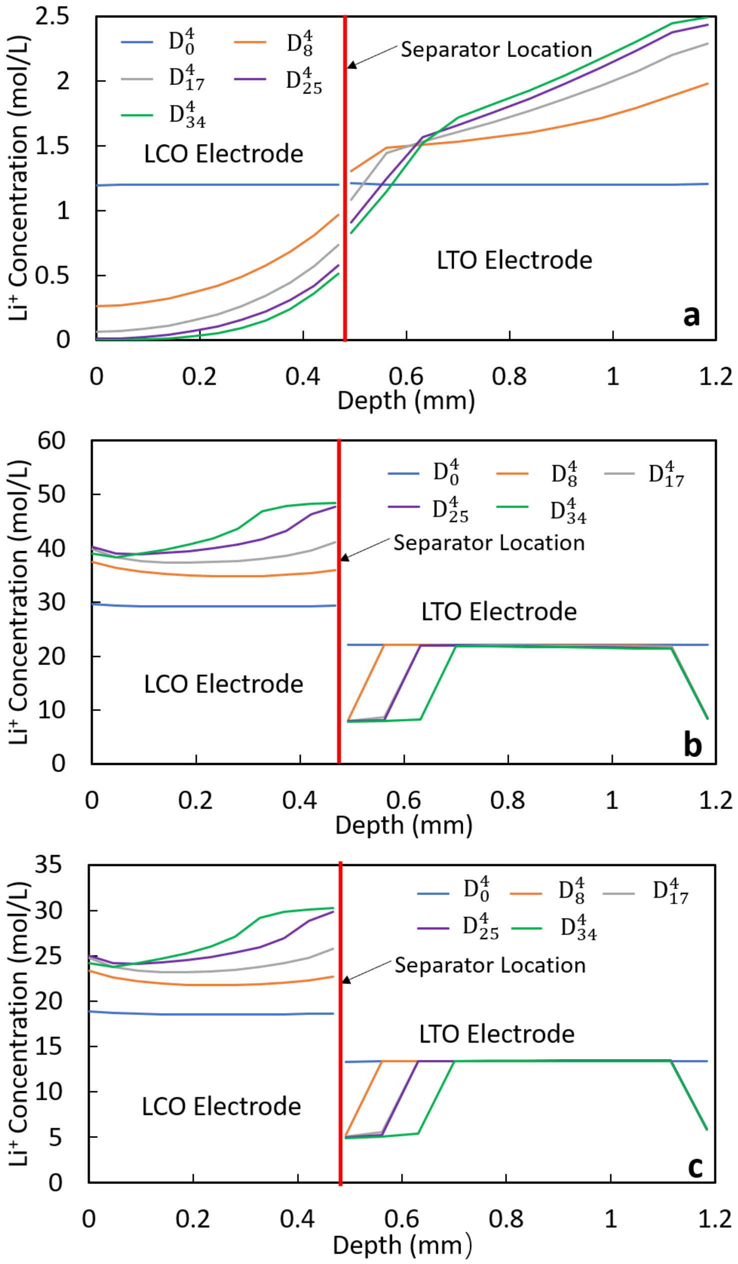

Fig. A2.23. Calculated Li$^+$ concentrations at different locations within both electrodes on a molar basis for D^4 process with no tortuosity (α=1.0). Concentrations are shown for the (a) liquid electrolyte phase, (b) solid active material phase, (c) and the sum of the total concentration. The subscript for each “D” corresponds to the time points in the discharge profile. Total concentration was calculated using the equation: $c_t=c_e\times\varepsilon+c_s\times(1-\varepsilon)$, where c_t is the total concentration, c_e is the concentration in electrolyte, c_s is the concentration in solid phase, ε is the porosity of the electrode.

References

(1) Thorat, I. V.; Stephenson, D. E.; Zacharias, N. A.; Zaghib, K.; Harb, J. N.; Wheeler, D. R. Quantifying Tortuosity in Porous Li-Ion Battery Materials. *J. Power Sources* **2009**, *188*, 592–600.

(2) Ménétrier, M.; Saadoune, I.; Levasseur, S.; Delmas, C. The Insulator-Metal Transition upon Lithium Deintercalation from $LiCoO_2$: Electronic Properties and ^7Li NMR Study. *J. Mater. Chem.* **1999**, *9*, 1135–1140.

(3) Young, D.; Ransil, A.; Amin, R.; Li, Z.; Chiang, Y.-M. Electronic Conductivity in the $Li_{4/3}Ti_{5/3}O_4$-$Li_{7/3}Ti_{5/3}O_4$ System and Variation with State-of-Charge as a Li Battery Anode. *Adv. Energy Mater.* **2013**, *3*, 1125–1129.

(4) Albertus, P.; Newman, J. Introduction to dualfoil 5.0, University of California Berkeley, Berkeley, CA, Tech. Rep. 2007.

(5) Capiglia, C.; Saito, Y.; Kageyama, H.; Mustarelli, P.; Iwamoto, T.; Tabuchi, T.; Tukamoto, H. ^7Li and ^{19}F Diffusion Coefficients and Thermal Properties of Non-Aqueous Electrolyte Solutions for Rechargeable Lithium Batteries. *J. Power Sources* **1999**, *81–82*, 859–862.

(6) Doyle, C. M. PhD Thesis, Lawrence Berkeley Laboratory, 1995.

Appendix 3. Supporting material for chapter 4

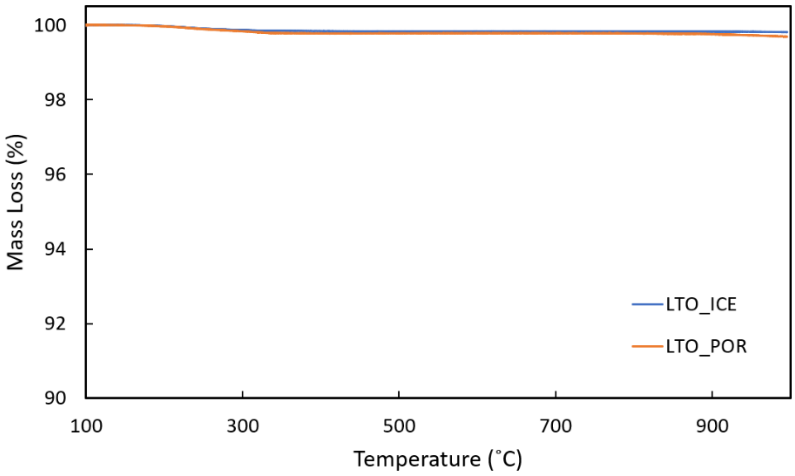

Fig. A3.1. Thermalgravimetric analysis results for $\mathrm{LTO_{ICE}}$ (blue) and $\mathrm{LTO_{POR}}$ (orange) pellets.

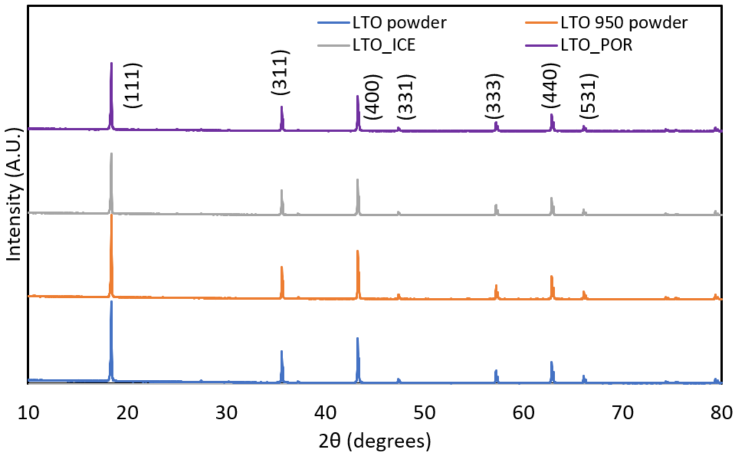

Fig. A3.2. X-ray diffraction patterns for as-received LTO powder (blue), LTO powder after firing at 950 ˚C for 1 hour (orange, "LTO 950 powder"), an $\mathrm{LTO_{ICE}}$ electrode pellet and an $\mathrm{LTO_{POR}}$ electrode pellet. After Rietveld refinement, the *a* lattice parameter for all samples was 0.836 nm. The pattern was indexed using reference pattern PDF 00-049-0207.[1]

Conservation equations used in calculations.

The equations used were a 1-D version of the electrochemical model developed by Newman *et al.*[2-4] and have been previously used for Li-ion battery simulations. The main equations are listed below:

Electrolyte Concentration:

$$\epsilon \frac{\partial c}{\partial t} = \frac{\partial}{\partial x}\left(D_{eff}(c)\frac{\partial c}{\partial x}\right) + Aj(1 - t_+^0)$$

Electrode Potential:

$$\frac{\partial \phi_1}{\partial x} = \frac{-i_1}{\sigma(c_s)}$$

Electrolyte Potential:

$$\frac{\partial \phi_2}{\partial x} = -\frac{i_2}{\kappa_{eff}(c)} + \frac{2RT}{F}\left(1 + \frac{\partial \, ln\, f_\pm(c)}{\partial \, ln\, c}\right)(1 - t_+^0)\frac{\partial \, ln\, c}{\partial x}$$

Lithium Flux Kinetics:

$$j = -2kc^{0.5}\left(c_s^{surface}\right)^{0.5}(c_s^{surface} - \, c_{s,max}^{surface})^{0.5} Sinh\left(\frac{F}{RT}(\phi_1 - \phi_2 - U)\right)$$

Lithium Flux across Electrode & Electrolyte Interface:

$$j = -D_s \frac{\partial c_s^{surface}}{\partial r}$$

Electrolyte Current:

$$Aj = -\frac{1}{F}\frac{\partial i_2}{\partial x}$$

Conservation of Current:

$$I = i_1 + i_2$$

Volumetric Surface Area:

$$A = \frac{3}{r_0}(1 - \, \epsilon)$$

Electrode Particle Concentration:

$$\frac{\partial c_s}{\partial t} = D_s \left(\frac{1}{r^2} \frac{\partial}{\partial r} \left(r^2 \frac{\partial c_s}{\partial r} \right) \right)$$

Effective Ionic Conductivity and Diffusivity:

$$\frac{\kappa_{eff}(c)}{\kappa(c)} = \frac{D_{eff}(c)}{D(c)} = \epsilon^{\alpha}$$

The α is the Bruggeman exponent which reflects the impact of electrode tortuosity τ. These two parameters can be related using the following equation:

$$\tau = \epsilon^{1-\alpha}$$

List of Symbols	
Volumetric Solid Particle Surface Area	A
Liquid Li$^+$ Concentration	c
Solid Li$^+$ Concentration	c_s
Electrolyte Diffusivity	D
Solid State Diffusivity	D_s
Faraday Constant	F
Current Density	I
Solid Phase Current Density	i_1
Liquid Phase Current Density	i_2
Lithium Flux across Electrode & Electrolyte Interface	j
Gas Constant	R
Solid Particle Radius	r_0
Temperature	T
Transference number	t_+^0
Open Circuit Potential	U
Bruggeman Exponent	α
Porosity/Electrolyte Volume Fraction	ϵ
Tortuosity	η
Ionic Conductivity	κ
Electronic Conductivity	σ
Solid Potential	ϕ_1
Liquid Potential	ϕ_2

Neutron imaging experiment set up and data analysis.

Neutron imaging experiments were carried out at the thermal neutron imaging beamline at the National Institute for Standards and Technology (NIST) Center for Neutron Research.[5] The experimental setup is shown in Fig. A3.3a. The cell was held with a clip in front of the detector and two stainless steel foils were used as leads connecting the positive and negative electrode of the cell. The detector was an Andor Neo sCMOS camera with a 1:1 macro lens that gives a pixel pitch of 6.5 micrometer. A 20-micrometer thick gadolinium oxysulfide scintillator was used. After starting the experiment, radiographs were collected every minute. An example of a raw radiograph collected is shown in Fig. A3.3b. While analyzing the data, three radiographs were averaged for each time point and combined in order to reduce signal noise. To compare neutron imaging results to simulated Li^+ concentration throughout the thickness of the cell during discharge, radiographs of all time points were normalized relative to the image that combined several radiographs taken before cycling (the “no current” image) and a dark field correction was carried out at the same time. The change in the transmission intensity of each pixel relative to the “no current” image (Transmission) were shown using a color scale in this manuscript (Fig. A3.3c). Since ^6Li had the largest neutron cross section than other species (except ^1H) in the system and the concentration of Li was higher (and had the greatest change in concentration) than other elements in the cell regions between the current collectors, changes in Li^+ (in particular in the solid phase within the electrode regions) should result in most of the observed changes in neutron transmission.[6] In the normalized color scale images (Fig. A3.3c), the regions of lower transmission (higher Li^+ concentration) relative to the initial state are shown in blue and the regions of relatively higher transmission (lower Li^+

concentration) compared to the initial state are shown in red. To highlight the contrast between anode and cathode, the image displayed Fig. A3.3c was taken at the end of the C/10 discharge of the LTO_{ICE}/LCO cell. In Fig. A3.3c, the blue region represents LCO electrode which had higher Li^+ concentration than the initial state at the end of discharge and the red region represents LTO electrode which had lower Li^+ concentration at the end of discharge relative to the initial state.

To quantitatively analyze the transmission radiographs, a 1000-pixel wide line scan was used across the electrode area from bottom to the top (z-direction in Fig. A3.3c). Before being transported to NIST, the cells used in the neutron imaging were charged to 2.7 V at a rate of C/20. Then, after the cells were aligned for experiments at NIST (Fig. A3.3a), they were charged again at a rate of C/20 to 2.7 V to compensate for any capacity lost between their previous charge cycle and arriving at NIST.

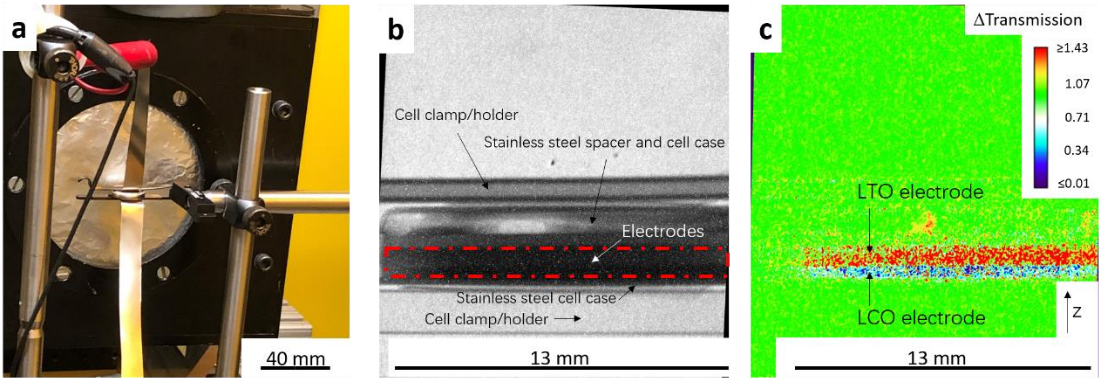

Fig. A3.3 (a) Photograph of experimental setup used for neutron imaging. (b) Example of a raw radiograph image of the coin cell region. (c) Example of the change in transmission for a radiograph of the cell after normalizing relative to the "no current" image. A color scale was used to show the relative change in neutron transmission. The black arrow to the bottom right of the image depicts the z-direction used for line scan analysis of the cell (thickness/depth dimension). Note that the brightest red regions have $\Delta T \geq 1.43$ and deepest blue regions have $\Delta T \leq 0.01$ and do not reflect the absolute maximum or minimum ΔT values and the same color scale was used for all neutron images displayed in this work.

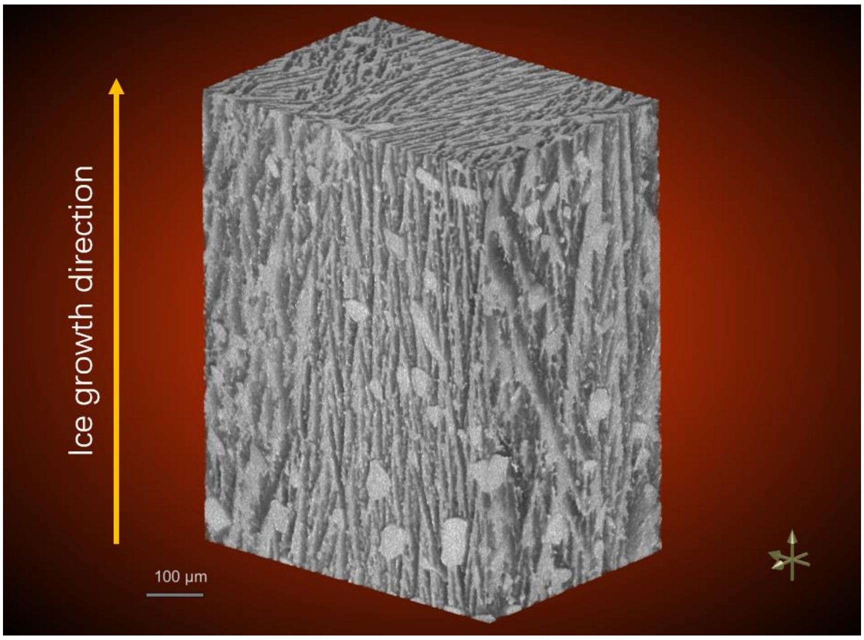

Fig. A3.4 X-CT image of a sample region for a LTO_{ICE} pellet.

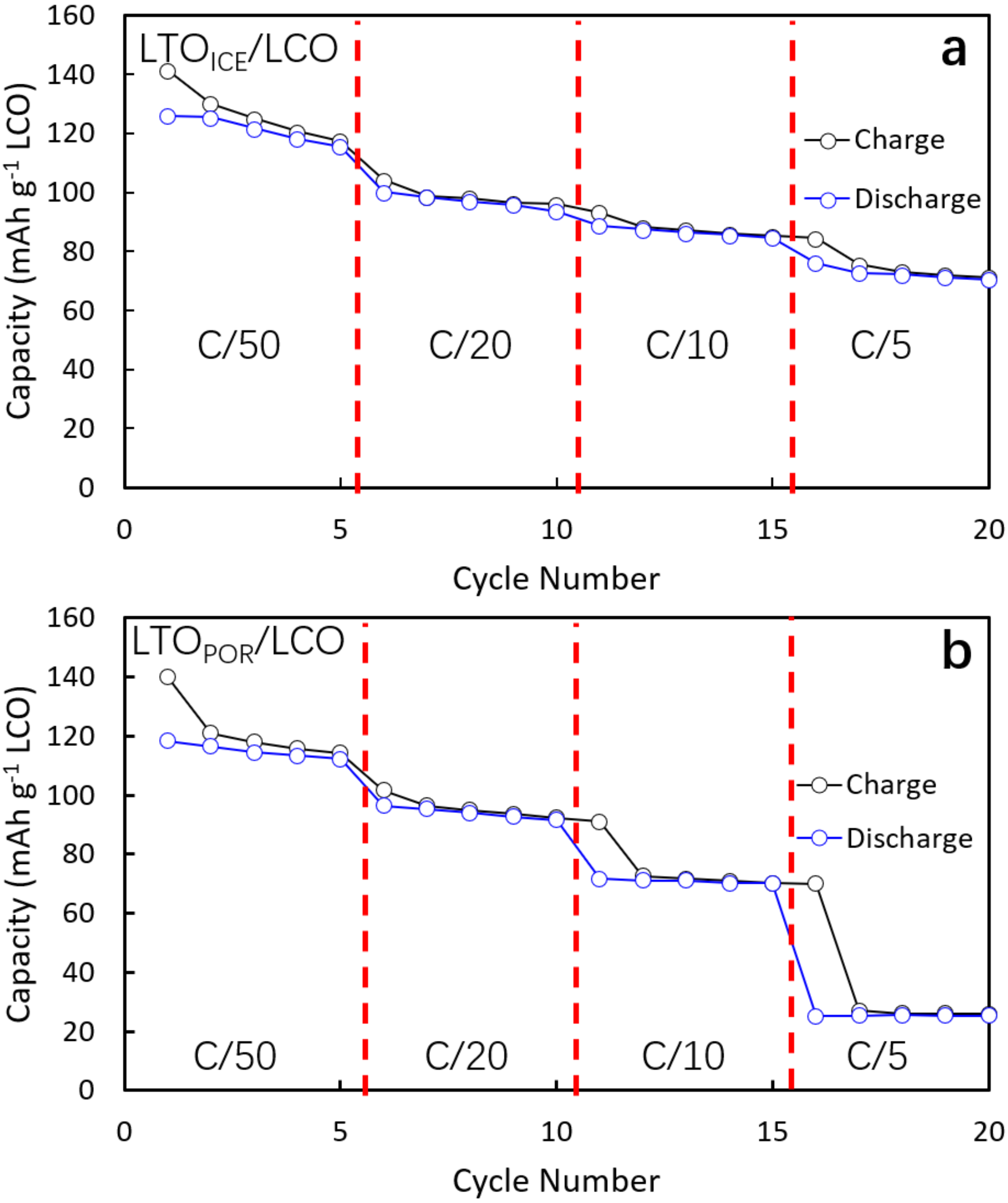

Fig. A3.5 Rate capability test of a representative (a) LTO$_{\text{ICE}}$/LCO and (b) LTO$_{\text{POR}}$/LCO cell. The discharge rate for each cycle is noted in the figure. For both cells, the charge rate for the first 5 cycles (C/50 discharge) was C/50. The charge rate for all following cycles was C/20.

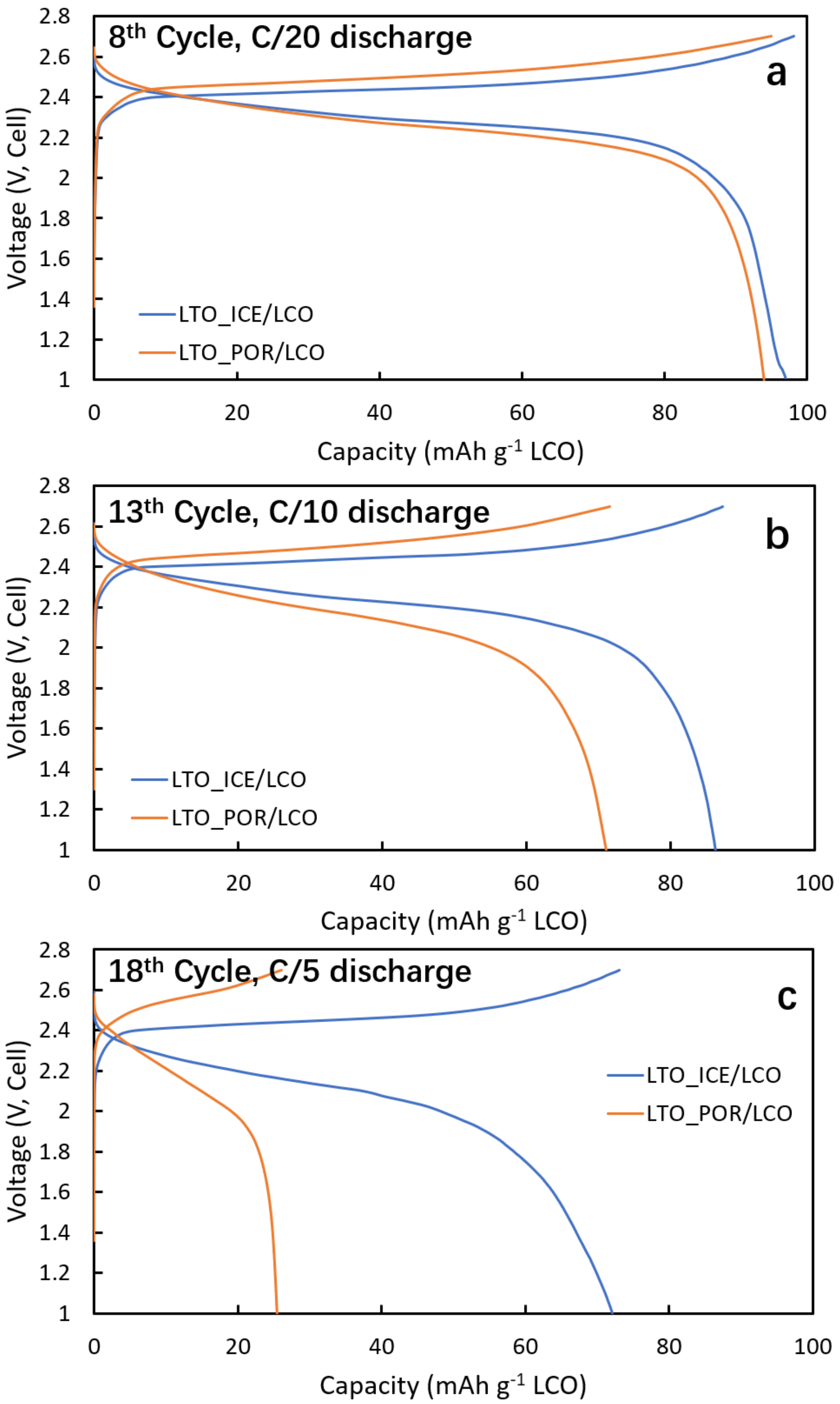

Fig. A3.6 Charge/discharge profiles corresponding to the (a) 8th cycle, (b) 13th cycle, and (c) 18th cycle from Fig. A3.5. The profiles correspond to the $\mathrm{LTO_{ICE}}$/LCO (blue) and $\mathrm{LTO_{POR}}$/LCO (orange) cells. For all cases, the charge was at C/20. The discharge was conducted at (a) C/20, (b) C/10, and (c) C/5.

Table A3.1. Detailed parameters used in calculations

Parameters	$\mathrm{LTO_{ICE}}$/LCO	$\mathrm{LTO_{POR}}$/LCO	$\mathrm{LTO_{ICE2}}$/LCO	Source
Thickness of negative electrode/LTO (m)	9.10×10^{-4}	8.95×10^{-4}	8.56×10^{-4}	Measured
Thickness of separator (m)	5.0×10^{-5}			Manufacturer
Thickness of positive electrode/LCO (m)	4.57×10^{-4}	4.64×10^{-4}	4.57×10^{-4}	Measured
Bulk $LiPF_6$ concentration (mol m^{-3})	1200			Manufacturer
Solid-state Li^+ diffusion coef. In anode (m^2 s^{-1})	2×10^{-12}			Ref. 7
Solid-state Li^+ diffusion coef. In cathode (m^2 s^{-1})	3.5×10^{-13}			Ref. 8
Radius of anode active particles (m)	1.7×10^{-7}			Ref. 1
Radius of cathode active particles (m)	2.0×10^{-7}			Ref. 9
Volume fraction of electrolyte in negative electrode	0.57	0.56	0.57	Based on measured porosity.
Volume fraction of electrolyte in separator	0.39			Manufacturer
Volume fraction of electrolyte in positive electrode	0.36	0.36	0.37	Based on measured porosity.
Conductivity of negative matrix (S m^{-1})	$7000(1 – x)^2 + 5 (1 – x) + 0.054$, $0.5\leqslant x\leqslant 1.0$ in Li_xCoO_2			Ref. 10,11
Conductivity of positive matrix (S m^{-1})	$300(y+10^{-6})^{0.38}\cdot 5^{(y-1)}/\exp(4.37(y-1)^{200})$, $0\leqslant y\leqslant 1.0$ in $Li_{4+3y}Ti_5O_{12}$			Ref. 12
Coulombic gravimetric capacity of negative material (mAh g^{-1})	175			Ref. 13
Coulombic gravimetric capacity of positive material (mAh g^{-1})	274			Ref. 13
Density of negative insertion material (kg m^{-3})	3480			Theoretical crystal density, Ref 14
Density of positive insertion material (kg m^{-3})	5010			Theoretical crystal density. Ref. 15
Rate constant for negative reaction ($m^{2.5}$ $mol^{-0.5}$ s^{-1})	3.10×10^{-13}			Ref. 16
Rate constant for positive reaction ($m^{2.5}$ $mol^{-0.5}$ s^{-1})	3.90×10^{-13}			Ref. 17
0000				
Bruggeman exponent α for cathode	1.5			Value for randomly packed spheres
Bruggeman exponent α for anode	1.0	1.5	1.0	Value for perfectly aligned pores (1.0) and randomly packed spheres (1.5)
Separator Bruggeman Exponent	2.5			Ref. 18

Open circuit voltage for anode (V)	0.21Exp(-116.96y) + 0.45Exp(-5000y) + 0.27706 Exp(-1010.1y) + 1.54, $0 \leq y \leq 1.0$ in $Li_{4+3y}Ti_5O_{12}$	Fitted from experimental data
Open circuit voltage for cathode (V)	0.076tanh(64.13 –51.30x) + 1.50tanh(50.85× 51.71x) + tanh(9.09– 21.09x) + 0.21tanh(3.47 – 5.83x) + 0.25tanh(8.10x + 4.29) – 0.022tanh(1.06x – 0.52) + 2.61, $0.5 \leq x \leq 1.0$ in Li_xCoO_2	Ref. 15
Electrolyte transference number	0.415	Ref. 19
Thermodynamic Factor, $(1 + \frac{\partial ln f_{\pm}}{\partial ln c})(1 - t_{+}^{0})$	$0.28687\ c^2 + 0.74678\ c + 0.44103$	Ref. 20
Electrolyte conductivity (S m^{-1})	$0.1297c^3 + 2.51c^{1.5} + 3.329c$	Ref. 20
Electrolyte diffusivity ($m^2\ s^{-1}$)	$(-6.9444c^2 + 7.3611c + 2.65) \times 10^{-10}$, $c < 0.8$, $6.4753 \times Exp(-0.573c) \times 10^{-10}$, $c \geq 0.8$	Ref. 20
Temperature (K)	298.15	Room temperature
Internal resistance ($\Omega\ m^2$)	0.0034	Estimated from experimental data

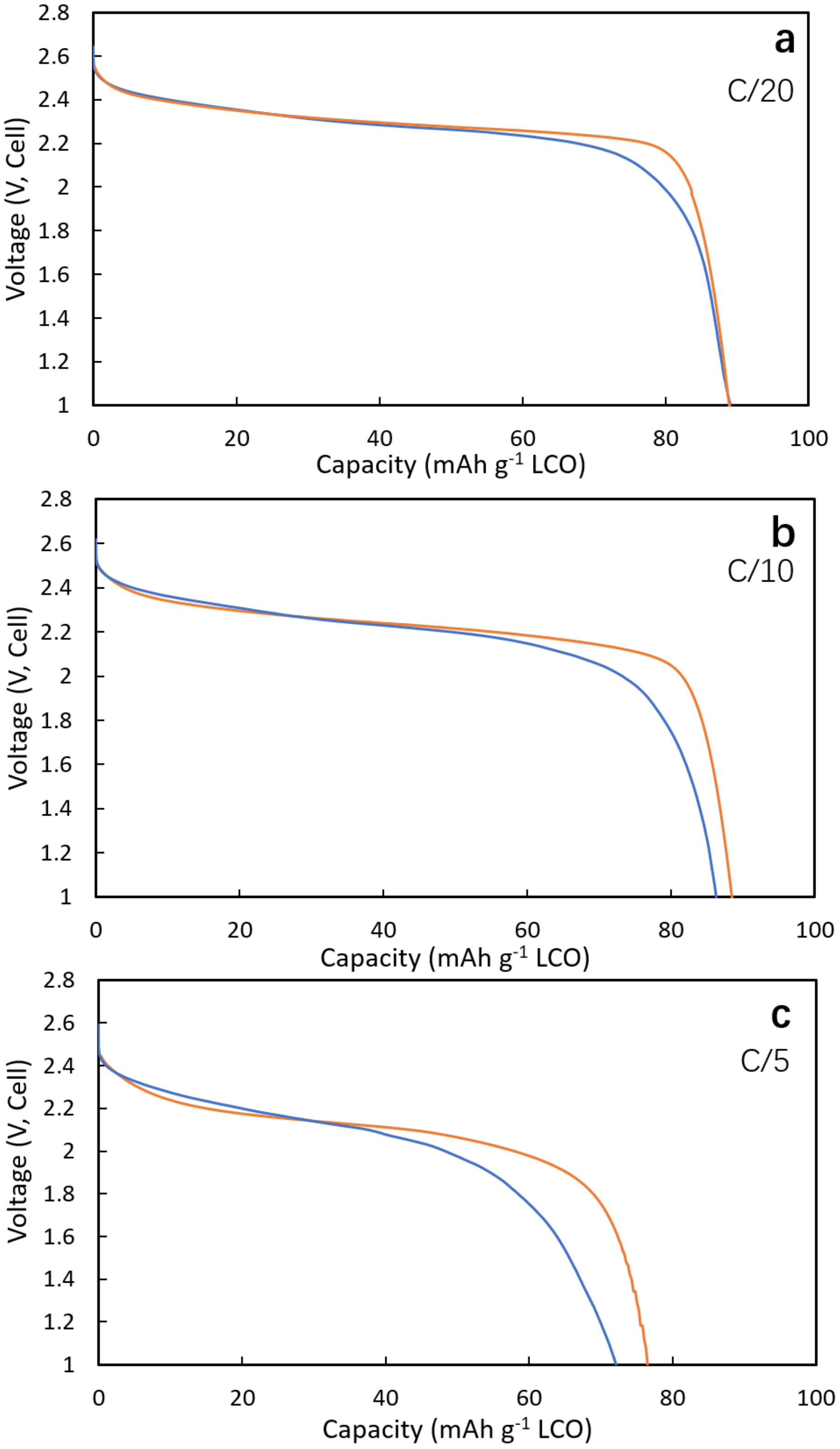

Fig. A3.7 Experimental (blue) and calculated (orange) discharge profiles at (a) C/20, (b) C/10 and (c) C/5 for LTO_{ICE}/LCO cell.

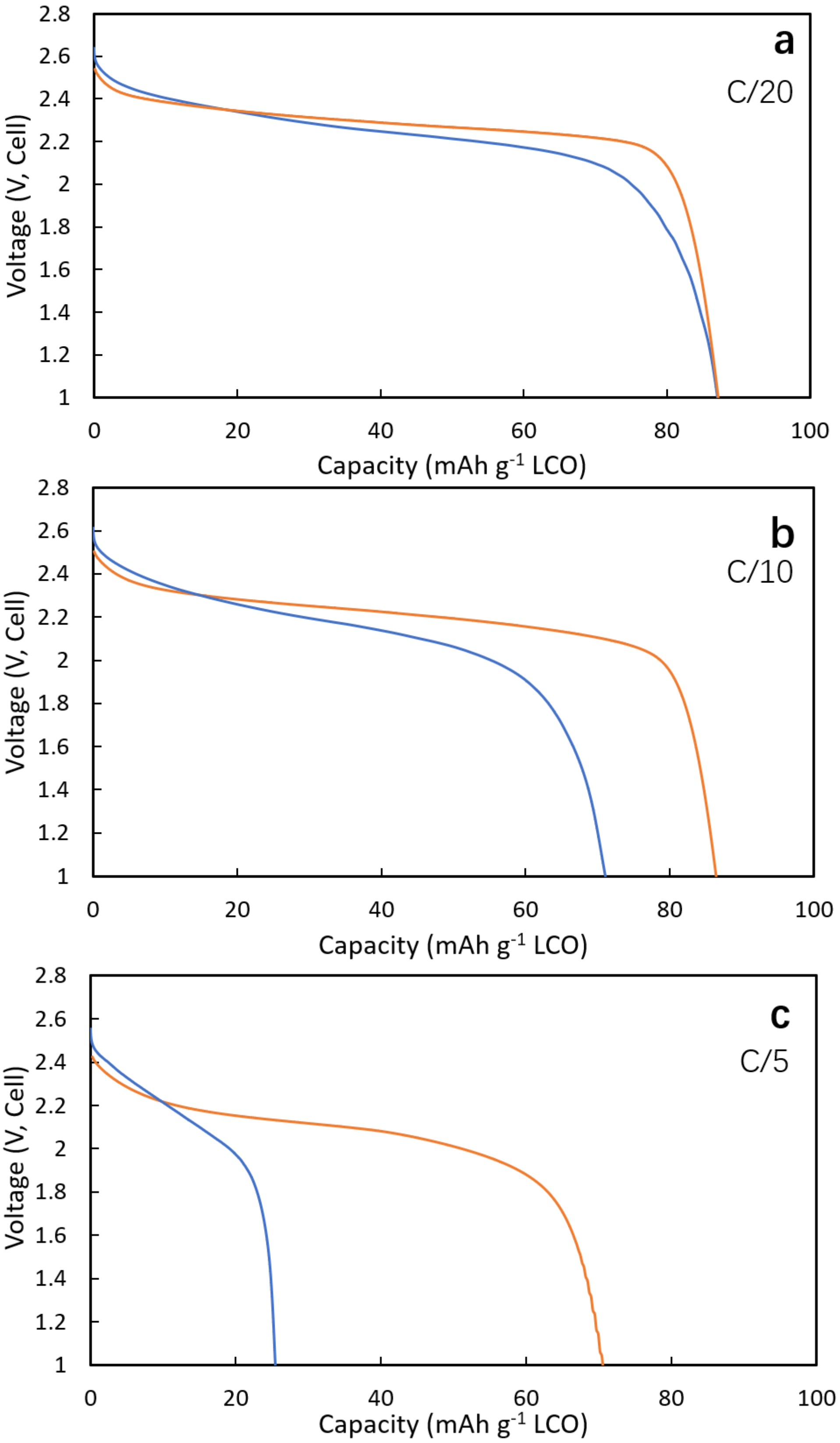

Fig. A3.8 Experimental (blue) and calculated (orange) discharge profiles at (a) C/20, (b) C/10 and (c) C/5 for LTO_{POR}/LCO cell.

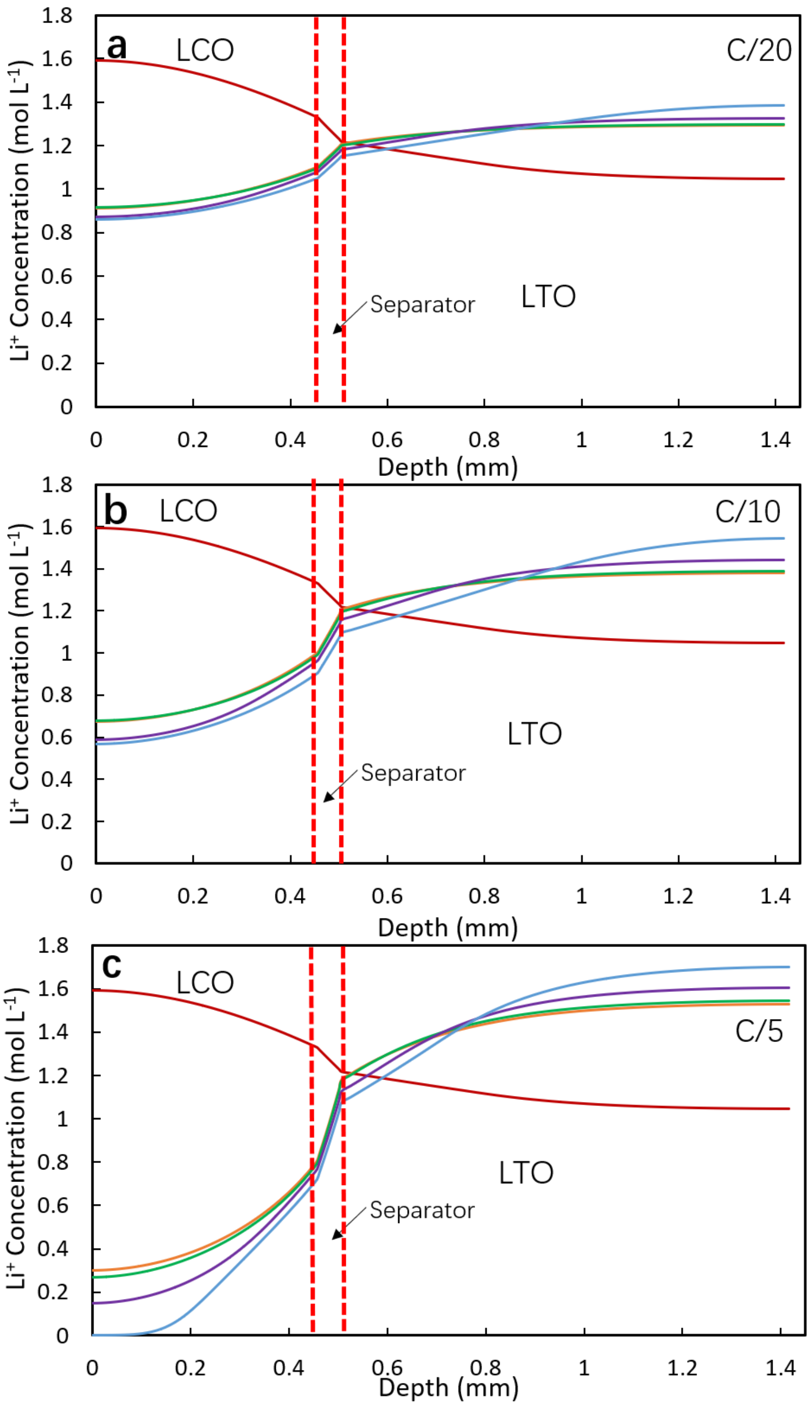

Fig. A3.9 Concentration profiles in electrolyte phase for LTO_{ICE}/LCO cell at (a) C/20, (b) C/10 and (c) C/5. The different curves correspond to the different extents of discharge capacity delivered, with the concentrations being shown for 0 % (magenta), 25 % (orange), 50 % (green), 75 % (purple), and 100 % (blue). The profile for 0 % capacity is right at the conclusion of the C/20 charge process.

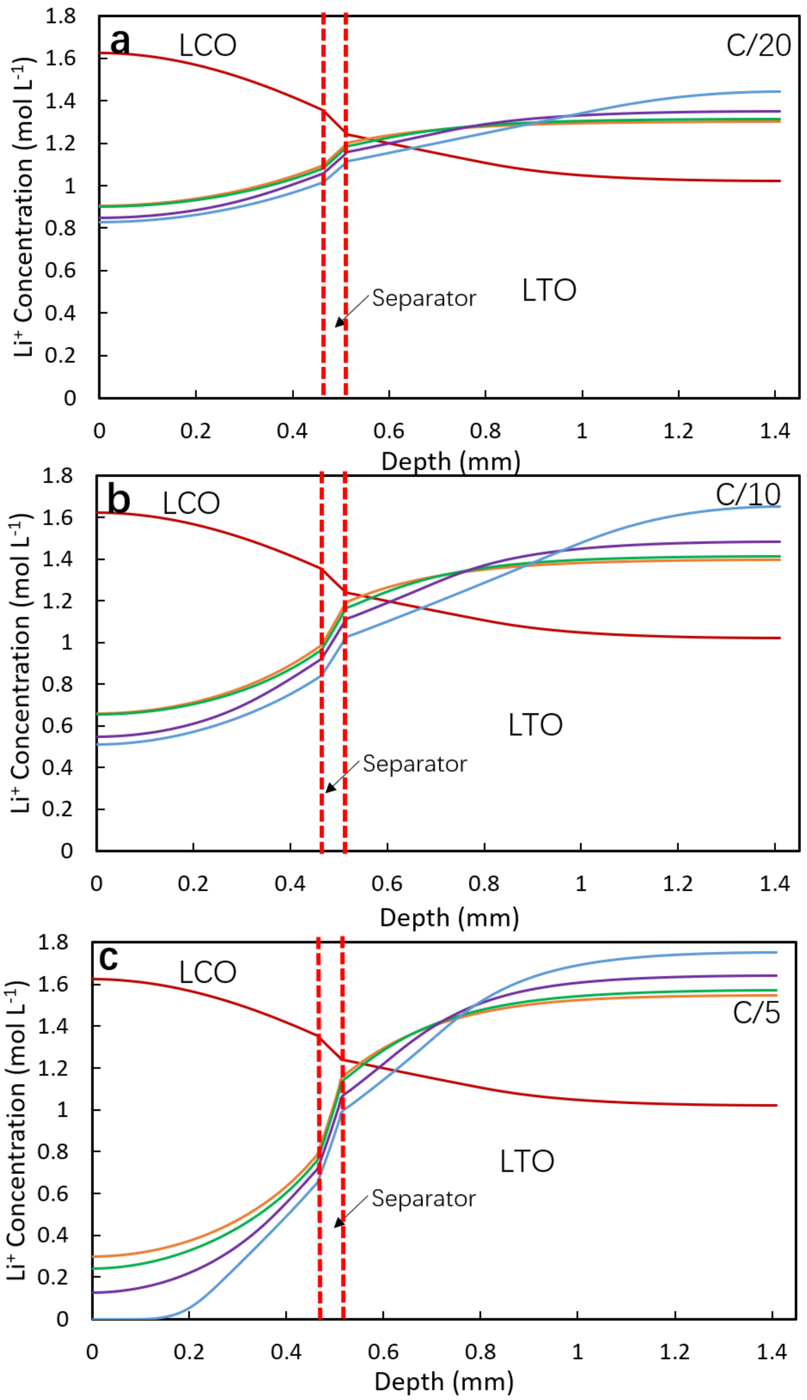

Fig. A3.10 Concentration profiles in electrolyte phase for LTO_{POR}/LCO cell at (a) C/20, (b) C/10 and (c) C/5 discharge process. The different curves correspond to the different extents of discharge capacity delivered, with the concentrations being shown for 0 % (magenta), 25 % (orange), 50 % (green), 75 % (purple), and 100 % (blue). The profile for 0 % capacity is right at the conclusion of the C/20 charge process.

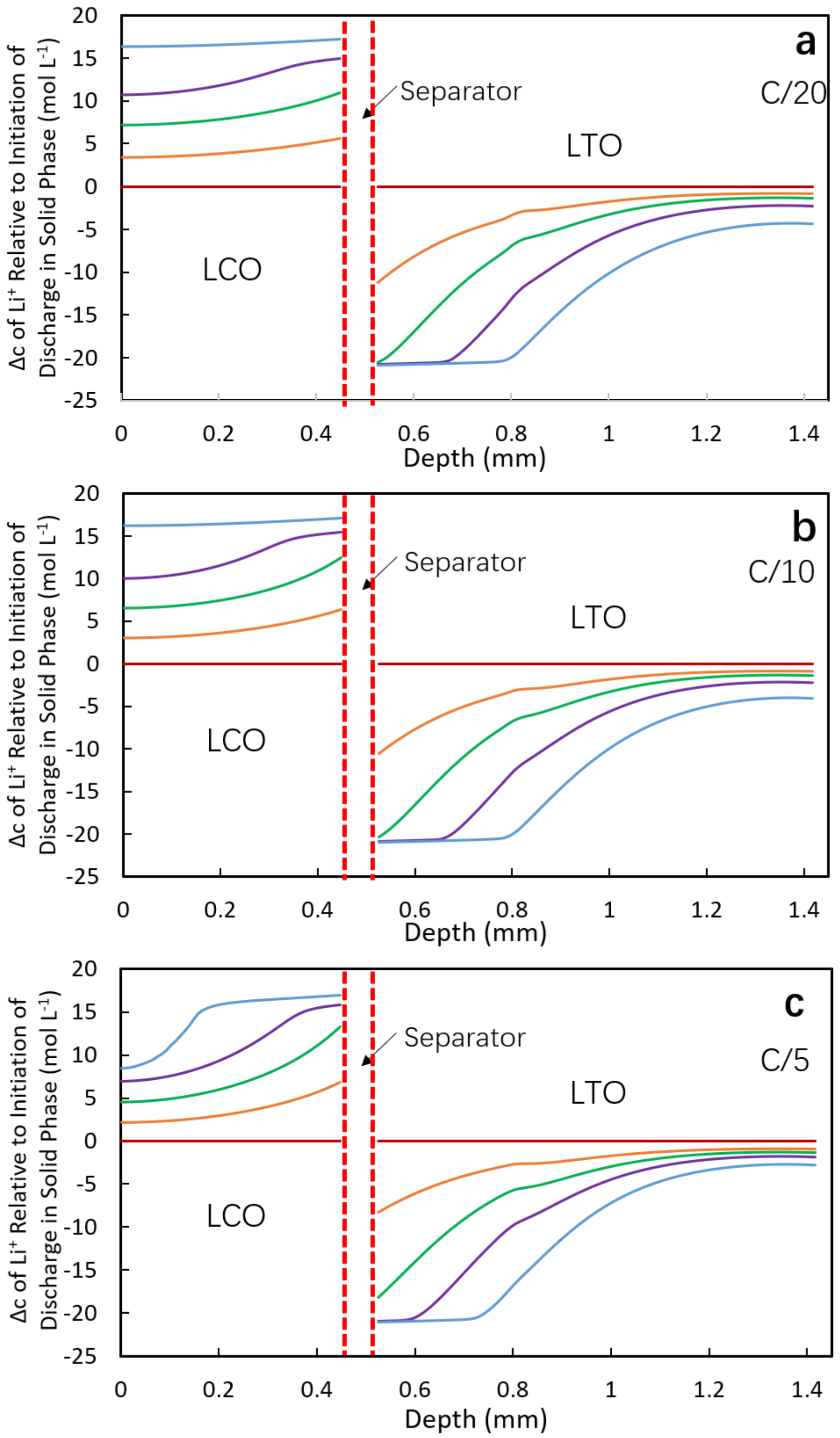

Fig. A3.11 Relative concentration profiles in solid phase for LTO_{ICE}/LCO cell at (a) C/20, (b) C/10 and (c) C/5. The different curves correspond to the different extents of discharge capacity delivered, with the concentrations being shown for 0 % (magenta), 25 % (orange), 50 % (green), 75 % (purple), and 100 % (blue).

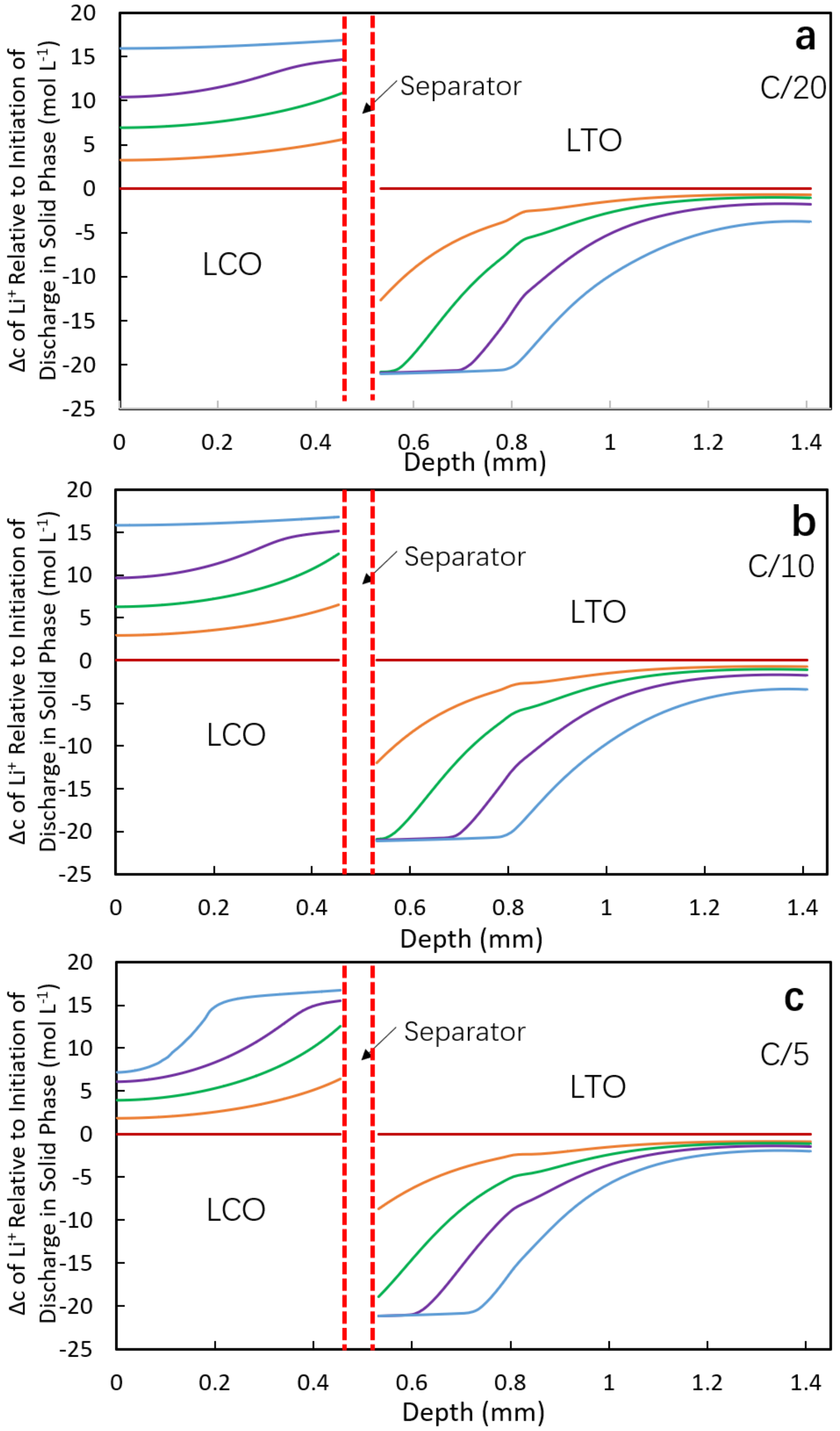

Fig. A3.12 Relative concentration profiles in solid phase for LTO$_{POR}$/LCO cell at (a) C/20, (b) C/10 and (c) C/5. The different curves correspond to the different extents of discharge capacity delivered, with the concentrations being shown for 0 % (magenta), 25 % (orange), 50 % (green), 75 % (purple), and 100 % (blue).

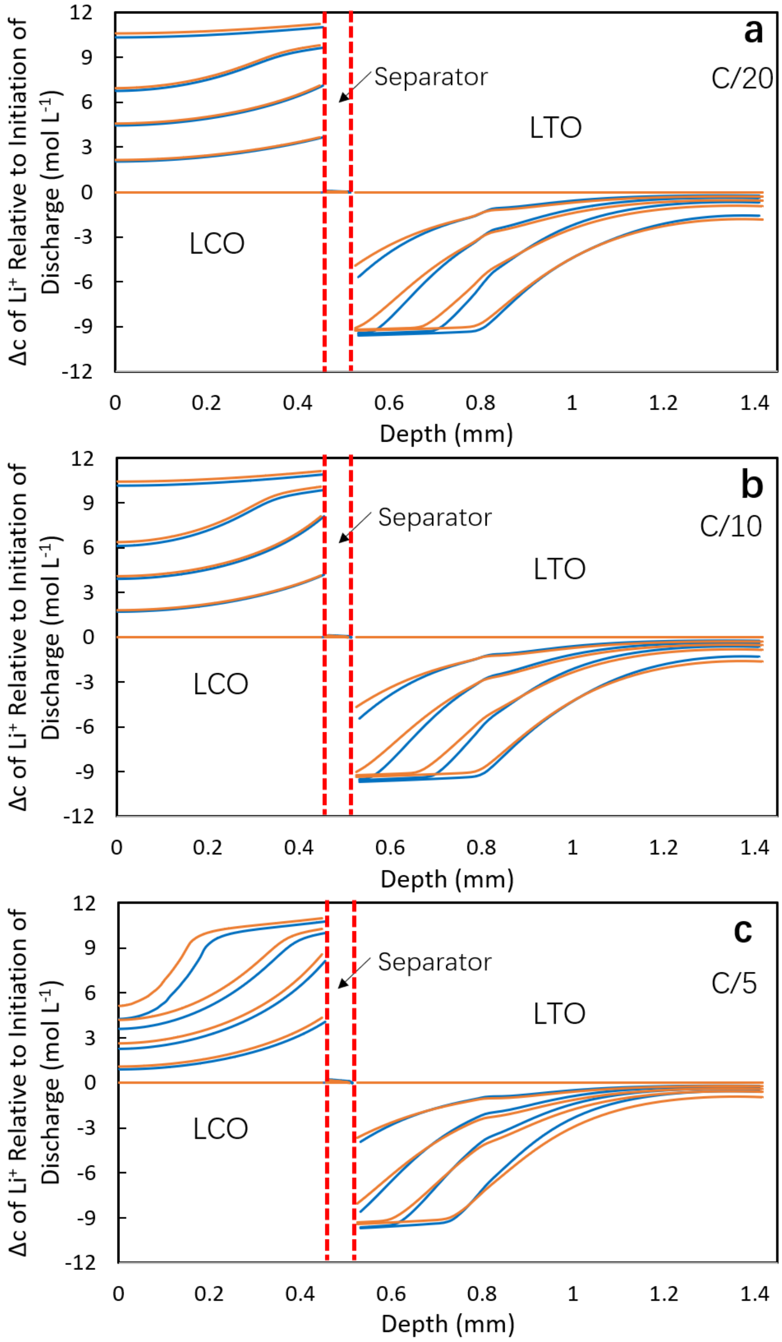

Fig. A3.13 Concentration profiles for LTO_{ICE}/LCO (orange) and LTO_{POR}/LCO (blue) cells that highlights the gradient comparison between two cells. The profiles for each cell are the same as those showed in Fig. 4.3 and Fig. 4.4 in main text.

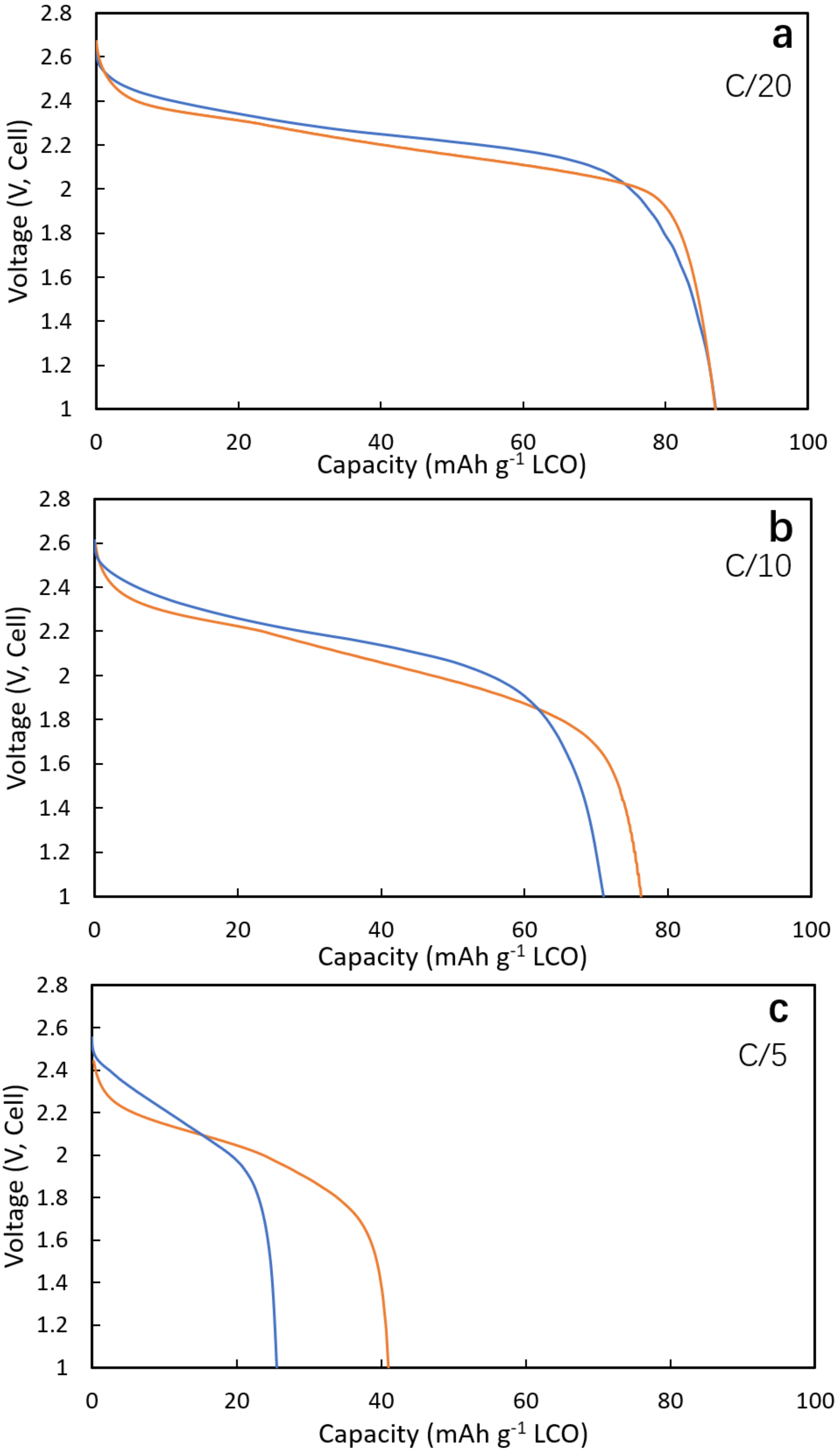

Fig. A3.14 Experimental (blue) and calculated (orange) discharge profiles at (a) C/20, (b) C/10 and (c) C/5 for LTO_{POR}/LCO cell with $\alpha(LTO_{POR})=4.0$.

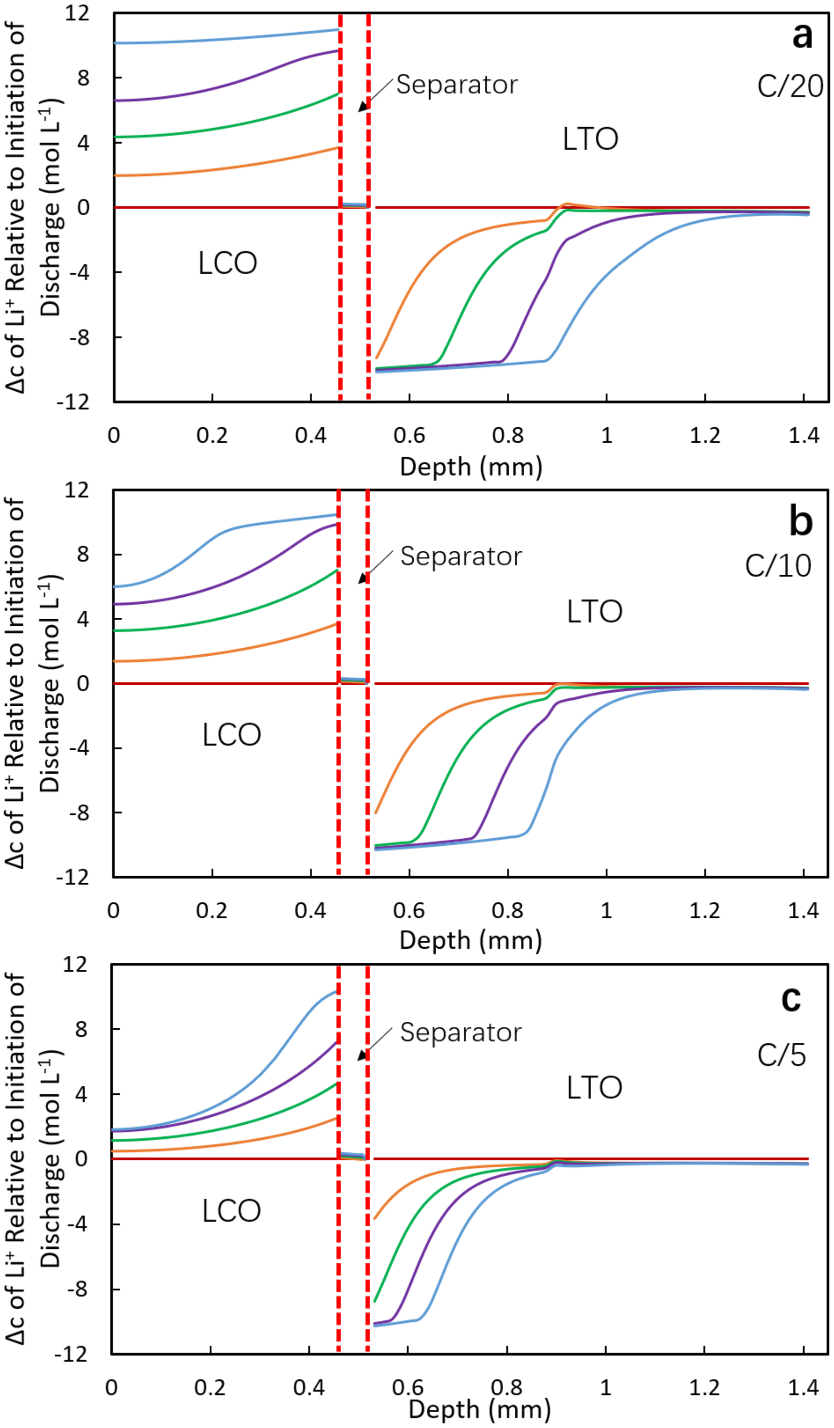

Fig. A3.15 Calculated change in total Li^{+} concentration profiles for LTO$_{\mathrm{POR}}$/LCO cell when α(LTO$_{\mathrm{POR}}$)=4.0 at (a) C/20, (b) C/10 and (c) C/5 discharge process. The different curves correspond to the different extents of discharge capacity delivered, with the concentrations being shown for 0 % (magenta), 25 % (orange), 50 % (green), 75 % (purple), and 100 % (blue).

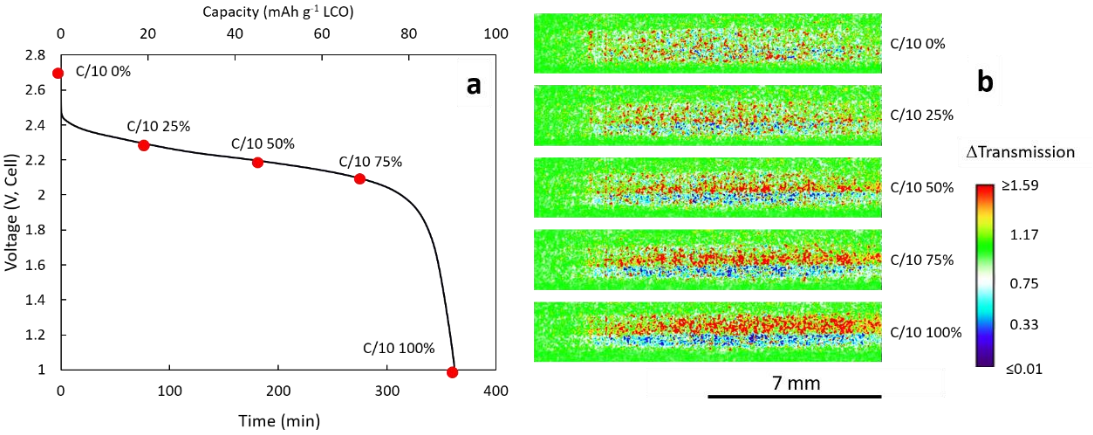

Fig. A3.16 (a) Discharge profiles of LTO$_{ICE2}$/LCO at C/10. (b) Changes in neutron transmission in the electrode region of the cell corresponding to the time points noted in (a).

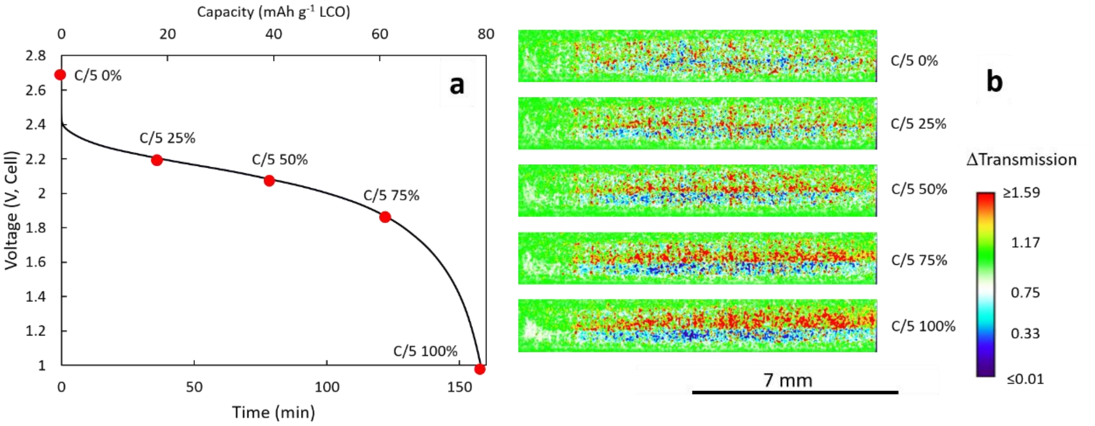

Fig. A3.17 (a) Discharge profiles of LTO$_{ICE2}$/LCO at C/5. (b) Changes in neutron transmission in the electrode region of the cell corresponding to the time points noted in (a).

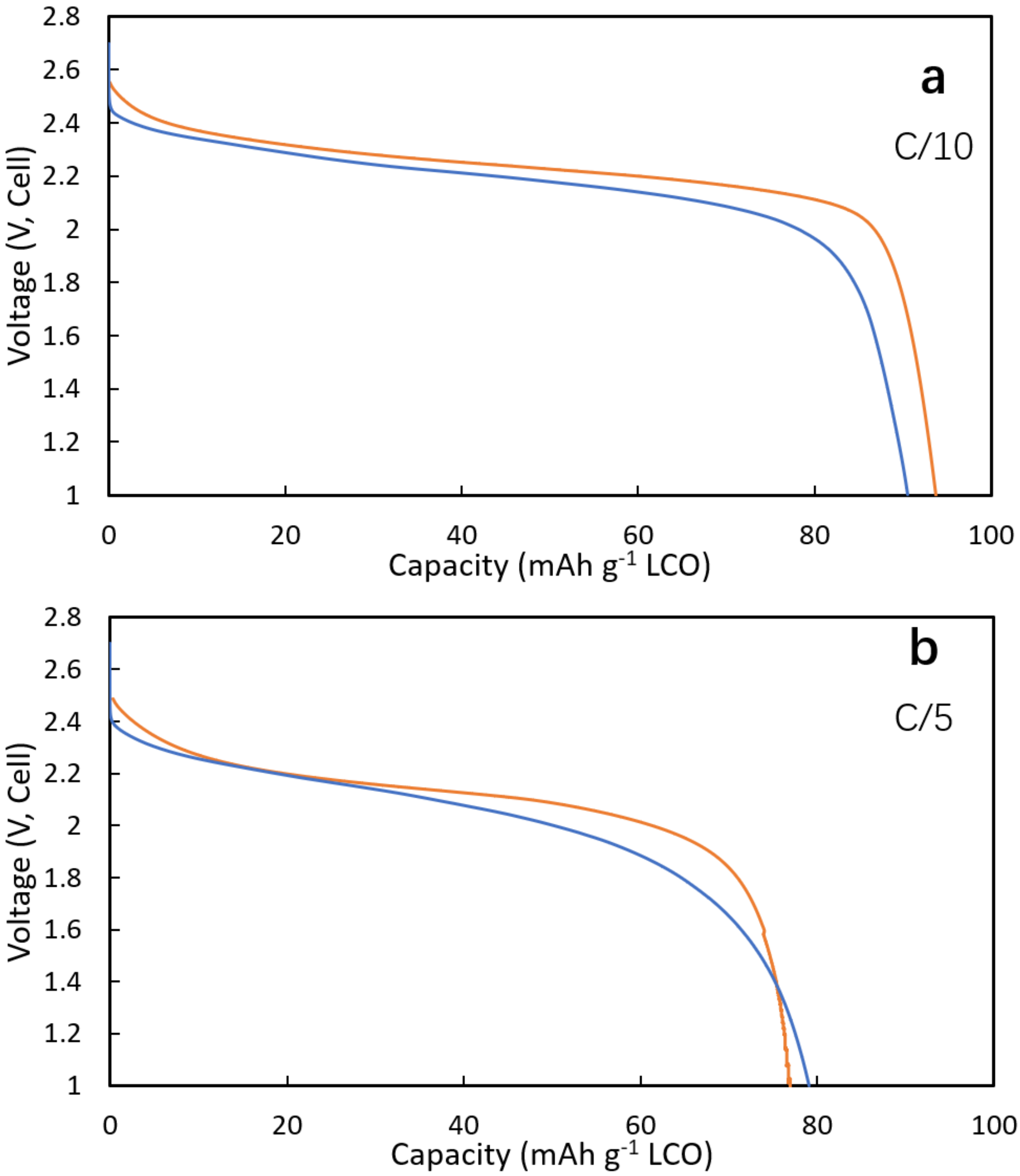

Fig. A3.18 Discharge profiles experimentally measured (blue) and calculated (orange) for discharge at (a) C/10 and (b) C/5 for LTO_{ICE2}/LCO cell.

References

(1) Qi, Z.; Koenig, G. M., Jr. A Carbon-Free Lithium-Ion Solid Dispersion Redox Couple with Low Viscosity for Redox Flow Batteries. *J. Power Sources* **2016**, *323*, 97–106.

(2) Doyle, M.; Fuller, T. F.; Newman, J. Modeling of Galvanostatic Charge and Discharge of the Lithium/Polymer/Insertion Cell. *J. Electrochem. Soc.* **1993**, *140*, 1526–1533.

(3) Fuller, T. F.; Doyle, M.; Newman, J. Simulation and Optimization of the Dual Lithium Ion Insertion Cell. *J. Electrochem. Soc.* **1994**, *141*, 1–10.

(4) Fuller, T. F.; Doyle, M.; Newman, J. Relaxation Phenomena in Lithium-Ion-Insertion Cells. *J. Electrochem. Soc.* **1994**, *141*, 982–990.

(5) Hussey, D. S.; Jacobson, D. L.; Arif, M.; Coakley, K. J.; Vecchia, D. F. In Situ Fuel Cell Water Metrology at the NIST Neutron Imaging Facility. *J. Fuel Cell Sci. Technol.* **2010**, *7*, 021024.

(6) Kardjilov, N.; Manke, I.; Hilger, A.; Strobl, M.; Banhart, J. Neutron Imaging in Materials Science. *Mater. Today* **2011**, *14,* 248–256.

(7) Zaghib, K.; Simoneau, M.; Armand, M.; Gauthier, M. Electrochemical Study of $Li_4Ti_5O_{12}$ as Negative Electrode for Li-Ion Polymer Rechargeable Batteries. *J. Power Sources* **1999**, *81–82*, 300–305.

(8) Xie, J.; Imanishi, N.; Matsumura, T.; Hirano, A.; Takeda, Y.; Yamamoto, O. Orientation Dependence of Li–Ion Diffusion Kinetics in LiCoO2 Thin Films Prepared by RF Magnetron Sputtering. *Solid State Ion.* **2008**, *179*, 362–370.

(9) Qi, Z.; Koenig, G. M., Jr. High-Performance $LiCoO_2$ Sub-Micrometer Materials from Scalable Microparticle Template Processing. *ChemistrySelect* **2016**, *1*, 3992–3999.

(10) Ménétrier, M.; Saadoune, I.; Levasseur, S.; Delmas, C. The Insulator-Metal Transition upon Lithium Deintercalation from $LiCoO_2$: Electronic Properties and ^{7}Li NMR Study. *J. Mater. Chem.* **1999**, *9*, 1135–1140.

(11) Levasseur, S. Evidence for Structural Defects in Non-Stoichiometric HT-$LiCoO_2$: Electrochemical, Electronic Properties and ^{7}Li NMR Studies. *Solid State Ion.* **2000**, *128*, 11–24.

(12) Young, D.; Ransil, A.; Amin, R.; Li, Z.; Chiang, Y.-M. Electronic Conductivity in the $Li_{4/3}Ti_{5/3}O_4$-$Li_{7/3}Ti_{5/3}O_4$ System and Variation with State-of-Charge as a Li Battery Anode. *Adv. Energy Mater.* **2013**, *3*, 1125–1129.

(13) Nitta, N.; Wu, F.; Lee, J. T.; Yushin, G. Li-Ion Battery Materials: Present and Future. *Mater. Today* **2015**, *18*, 252–264.

(14) Kataoka, K.; Takahashi, Y.; Kijima, N.; Akimoto, J.; Ohshima, K.-I. Single Crystal Growth and

Structure Refinement of $Li_4Ti_5O_{12}$. *J. Phys. Chem. Solids* **2008**, *69*, 1454–1456.

(15) Mao, J.; Tiedemann, W.; Newman, J. Simulation of Li-Ion Cells by Dualfoil Model under Constant-Resistance Load. *ECS Trans.* **2014**, *58*, 71–81.

(16) Habte, B. T.; Jiang, F. Microstructure Reconstruction and Impedance Spectroscopy Study of $LiCoO_2$, $LiMn_2O_4$ and $LiFePO_4$ Li-Ion Battery Cathodes. *Microporous Mesoporous Mater.* **2018**, *268*, 69–76.

(17) Chen, J.; Yang, L.; Fang, S.; Hirano, S.-I.; Tachibana, K. Synthesis of Hierarchical Mesoporous Nest-like $Li_4Ti_5O_{12}$ for High-Rate Lithium Ion Batteries. *J. Power Sources* **2012**, *200*, 59–66.

(18) Landesfeind, J.; Hattendorff, J.; Ehrl, A.; Wall, W. A.; Gasteiger, H. A. Tortuosity Determination of Battery Electrodes and Separators by Impedance Spectroscopy. *J. Electrochem. Soc.* **2016**, *163*, A1373–A1387.

(19) Capiglia, C.; Saito, Y.; Kageyama, H.; Mustarelli, P.; Iwamoto, T.; Tabuchi, T.; Tukamoto, H. ^7Li and ^{19}F Diffusion Coefficients and Thermal Properties of Non-Aqueous Electrolyte Solutions for Rechargeable Lithium Batteries. *J. Power Sources* **1999**, *81–82*, 859–862.

(20) Nyman, A.; Behm, M.; Lindbergh, G. Electrochemical Characterisation and Modelling of the Mass Transport Phenomena in $LiPF_6$–EC–EMC Electrolyte. *Electrochim. Acta* **2008**, *53*, 6356–6365.

Appendix 4. Supporting material for chapter 5

Materials and methods

1. Electrolyte preparation

Lithium bis(fluorosulfonyl)imide (LiFSI) was used as the primary salt in the electrolyte and dimethyl carbonate (DMC) was used as solvent. Three initial concentrations of electrolyte were selected. The target LiFSI concentration for three electrolytes were 1 mol L^{-1}, 2 mol L^{-1} and 3 mol L^{-1}, respectively. To suppress possible corrosion caused by trace Cl^- in LiFSI salt sample,[1,2] 0.5 mol L^{-1} $LiPF_6$ was added to all electrolytes. Thus, the total target Li^+ concentrations were 1.5 mol L^{-1}, 2.5 mol L^{-1} and 3.5 mol L^{-1} for three electrolytes, respectively. However, at high concentration regime, the volume increase caused by adding salts was no longer negligible. After volume measurements, the actual concentrations for three electrolytes were 1.3 mol L^{-1}, 2.0 mol L^{-1} and 2.5 mol L^{-1}, in which the LiFSI:$LiPF_6$ molar ratios were 2:1, 4:1 and 6:1, respectively. The conductivity of different blend electrolytes at different concentration was measured with a Mettler Toledo@ conductivity probe.

The commercial “GEN2” electrolyte (Gotion) was composed of 1.2 mol L^{-1} $LiPF_6$ in 3:7 (w/w) ethylene carbonate (EC)/ ethyl methyl carbonate (EMC) solvent and was used as received.

2. Powder material preparation

2.1 Active material powder

$LiCoO_2$ (LCO) was used as the cathode material. LCO was synthesized via firing a mixture of Li_2CO_3 powder and $CoC_2O_4\cdot 2H_2O$ precursor.[3] Coprecipitation was used to synthesize the precursor. First, 1800 mL of 62.8 $mmol\cdot L^{-1}$ $Co(NO_3)_2\cdot 6H_2O$ (Fisher Reagent Grade) solution (50 °C) was poured into 1800 mL of 87.9 mmol L^{-1} $(NH_4)_2C_2O_4\cdot H_2O$ (Fisher Certified ACS) solution (50 °C) all at once. After maintaining at 50 °C for 30 minutes with a stir bar stirring at 800 rpm, the solid precipitate was collected using vacuum filtration and rinsed with 4 L deionized (DI) water. The powder was then dried in an 80 °C oven for 24 h in air atmosphere. Then, the oxalate precursor powder was mixed with Li_2CO_3 (Fisher Chemical) powder with a molar ratio of 1.02:1 for Li:Co using mortar and pestle. The powder mixture was fired at a ramp rate of 1 $°C\cdot min^{-1}$ to 800 °C in air in a Carbolite CWF 1300 box furnace. The sample was cooled to room temperature without control of cooling rate after reaching 800 °C. The resulting LCO material was ground with mortar and pestle by hand and was further milled in a Fritsch Pulverisette 7 planetary ball mill using 57 zirconia beads (5 mm diameter) at 300 rpm for 5 hours. 5 g of LCO was used for each batch of the planetary ball milling.

$Li_4Ti_5O_{12}$ (LTO) was used as anode material. It was purchased from a commercial supplier (NANOMYTE BE-10 from NEI Corporation) and was used without any additional treatment. The characterization and electrochemical properties of both LCO and LTO material used in this study can be found in previous publications.[1,4]

2.2 Polystyrene powder

Colloidal polystyrene (PS) particles (diameters 300 nm to 500 nm) were synthesized using procedures adapted from literature.[5] Styrene (Sigma-Aldrich, ReagentPlus, with 4-tert-butylcatechol as stabilizer, ≥ 99.0%) was pretreated using a prepacked column (Sigma-Aldrich, inhibitor, prepacked column for removing tert-butylcatechol) to remove the polymerization inhibitor. First, a three-neck 500 mL round bottom flask was filled with 290 mL DI water with 8.86 g styrene added. The flask was heated to 70 ˚C in an oil bath and thermally equilibrated for 30 minutes. Next, 0.204 g potassium persulfate (Sigma-Aldrich) was added as catalyst for the styrene polymerization reaction. During the reaction, the head space was purged with nitrogen flowed at 1 mL s^{-1}. The two-phase system was stirred for 8.5 h with a stir bar, resulting in a final milky white suspension. After drying in the air at room temperature until all water was evaporated, the PS powder was collected.

3. Electrode preparation

3.1 Sintered LCO preparation

Sintered LCO electrodes were used as cathodes in this study. First, the LCO active material powder was mixed with 1 wt.% polyvinyl butyral (Pfaltz & Bauer) solution dissolved in ethanol (Acros). 1 g LCO powder was blended with 2 mL polymer binder solution with a mortar and pestle. After all the solvent was evaporated, the mixture was collected. Then, 0.2 g of the mixture was loaded into a 13 mm diameter Carver pellet die and pressed with 12,000 lbf for 2 minutes in a Carver hydraulic press. Next, the pellets were heated in a Carbolite CWF 1300 box furnace in an air atmosphere. The ramping rate was 1 °C min^{-1} from 25 °C to 600 °C and was held at 600 °C for 1 hour. After that, the pellets were cooled to 25 °C at a rate of 1 °C min^{-1}.

3.2 Sintered LTO preparation

The sintered LTO electrodes were prepared using a similar method for sintered LCO electrodes. However, if the identical processing was used, the resulting LTO pellets generally had a geometric pore/void volume of 40%. Thus, in order to match the geometric pore/void volume of the ice-templated LTO pellets (~55%), sacrificial PS particles were mixed with the LTO powder before the hydraulic pressing step. The mass ratio of LTO powder and PS powder was 5:1 for LTO:PS. Then, the powder mixture was blended with 1 wt.% polyvinyl butyral solution. 2 mL solution added to 1 g LTO powder in the mixture. After the solvent was evaporated, 0.24 g of the powder mixture was loaded in the 13 mm diameter pellet die and pressed with 12,000 lbf for 2 minutes. Then, the pellets were fired in a Carbolite CWF 1300 box furnace in air atmosphere at 600 °C for 1 h. The heating and cooling rate were set to be 1 °C min^{-1}. The resulting LTO pellets had a porosity of ~55%.

3.3 Ice-templated LTO preparation

Ice-templated LTO materials were fabricated from aqueous suspensions containing 30% by volume LTO particles. To prepare an aqueous suspension, as-received LTO powder was mixed with DI water and yttria stabilized zirconia (ZrO_2) spheres (5 mm diameter, Inframat Advanced Materials LLC) in a Nalgene bottle, with ceramic powder to milling media mass ratio of 1:4. Then, cetyl trimethyl ammonium bromide (CTAB) cationic dispersant, at a concentration of 0.02 g cm^{-3} of distilled water, was added to the aqueous LTO suspension. The addition of CTAB caused slight foaming in the suspension. To avoid foaming, an antifoaming agent Surfynol 104PG50 (0.003 g g^{-1} of LTO powder) was added to LTO suspension. Then, the LTO suspension was milled for 24 h at 30 RPM. Next, a binder solution was prepared by dissolving poly(2-ethyl-2-oxazoline) in distilled water, and the binder solution was added to the LTO suspension such that the binder amount was 4% of the LTO powder mass. LTO suspension was further ball milled for another hour at 10 rpm to ensure proper mixing of binder solution and LTO suspension and then the ZrO_2 spheres were separated from suspension.

A custom-made ice-templating device was employed to fabricate LTO electrodes with aligned pores.[6] This setup contains an assembly of a polytetrafluoroethylene tube (mold) placed on a thin copper plate (referred to here as “cold-finger”), which is filled with an aqueous ceramic suspension. Next, to freeze the suspension under the influence of unidirectional temperature gradient, the mold assembly containing ceramic suspension was inserted inside a liquid nitrogen Dewar, where the cold-finger was placed above the liquid nitrogen. The distance between cold-finger and liquid N_2 determines the unidirectional temperature gradient, and hence the growth velocity of the freezing front. In this work, a 1 mm gap between the cold-finger and liquid nitrogen was used to achieve a relatively high freezing front velocity (FFV) of about 28 $\mu m\ s^{-1}$. As the temperature of the cold-finger reaches below 0 °C, ice crystals nucleate at the bottom of the suspension in contact with the cold-finger and grow upward under the influence of the applied thermal gradient.

Unidirectionally solidified samples were freeze dried in a freeze-dryer (2.5 L, Labconco, Kansas City, MI) for 96 h at a pressure of 0.014 mbar and temperature of -50 °C. Freeze dried LTO pellets were then sintered using a tube furnace (NBD, T-1700-60IT). Samples were first heated to 450 °C at a rate of 5 $°C\ min^{-1}$ and held for 4 hours to burn out binders. Next, samples were heated to 950 °C at a rate of 2 $°C\cdot min^{-1}$ and sintered for 2 h. After that, samples were cooled down to room temperature using a cooling rate of 5 °C min^{-1}. Dimensions of sintered LTO samples were approximately 13 mm in diameter and 10 mm in height. From each sintered LTO sample, an electrode disk of 1 mm thickness was extracted from a 2 mm height above the bottom of the sample and was denoted as LTO_ICE in the following discussion.

4. Electrochemical cell fabrication

Electrochemical evaluation of sintered electrode LTO/LCO full cells was conducted using CR2032 coin cells. To fabricate the cell with Gen 2 electrolyte, the LCO pellets were pasted onto the bottom plate of the coin cell and LTO pellets were pasted on a stainless steel spacer (15.5 mm in diameter and 0.5 mm in thickness). To fabricate the cells with LiFSI-containing electrolytes, the LTO pellets were pasted onto the bottom plate and LCO pellets were pasted on an aluminum spacer (15.5 mm in diameter and 0.5 mm in thickness). The paste for attaching sintered electrodes to current collectors was composed of 1:1 weight ratio Super P carbon black (Alfa Aesar) to polyvinylidene difluoride (PVDF, Alfa Aesar) binder dissolved in N-methyl pyrrolidone (NMP, Sigma-Aldrich). After drying in an 80 ˚C oven for 12 hours in air atmosphere, the pellets were transferred into an Ar atmosphere glove box with both O_2 and H_2O content <1 ppm. Then, LTO and LCO electrodes were assembled into a coin cell with glass fiber separator (Fisherbrand, 09-804-24A) between the anode and cathode. In a coin cell, 18 total drops of electrolyte were added. Assembly of sintered electrode full cells was described in greater detail in previous publications.[7,8]

The rate capability of LTO/LCO sintered electrode coin cells was determined by galvanostatically cycling at different C rates using a MACCOR battery cycler. The C rate was based on the assumption that the capacity of LCO was 150 mAh g^{-1}, and thus 1C was assumed to correspond to 150 mAh g^{-1} and the current was adjusted based on the actual LCO mass in the cell and the desired C rate. For cells fabricated in this study with LCO loadings typical in sintered electrodes, 1C would also correspond to ~21.4 mA cm^{-2} (28.4 mA). The voltage range used for all LTO/LCO cells was 1.0 V to 2.8 V (cell voltage, relative to LTO anode).

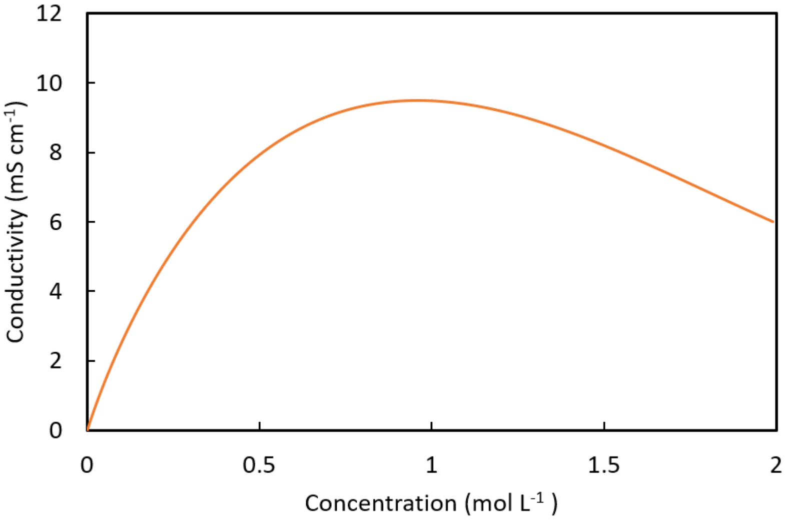

Fig. A4.1. $LiPF_6$ conductivity in 3:7 (w/w) EC/EMC electrolyte. (1.2 mol L^{-1} was the initial concentration of commercial Gen 2 electrolyte). The plotted line resulted from the experimental test and numerical fitting from ref. [9]. The fitted function is: $\kappa=1.297c^3 -25.1c^{1.5} + 33.29c$, where κ is the conductivity (mS cm^{-1}), c is the concentration (mol L^{-1}).

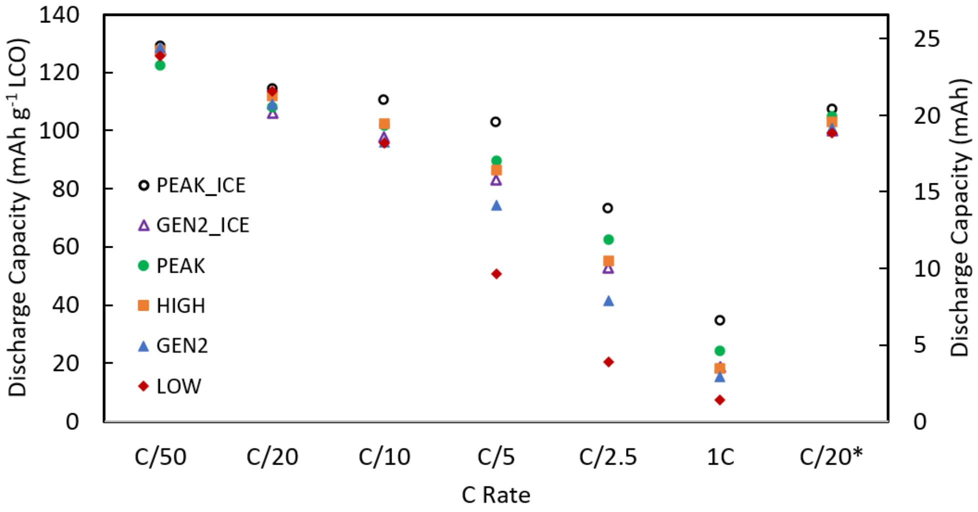

Fig. A4.2. Average discharge capacity at different discharge rates for each cell type reported in this manuscript. For C/50 discharge, the charge rate was C/50, and before all other discharge processes the charge rate was C/20. The last C/20* was the C/20 discharge process performed after all the cycles at increasing rates, indicating minimal capacity loss during the test.

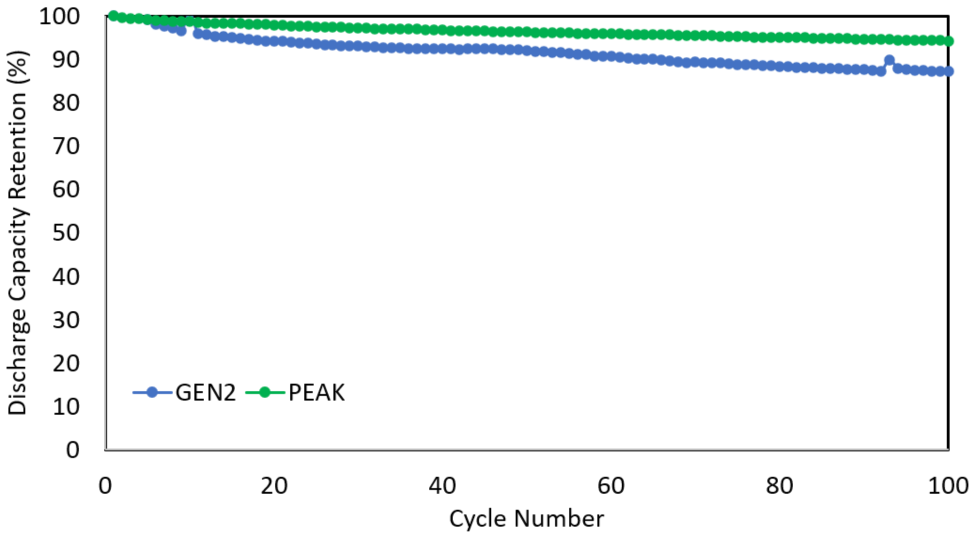

Fig. A4.3. Cycle life results for sintered LTO/LCO cells with GEN2 (blue circles) and PEAK (green circles) electrolyte, with the first cycle being the first cycle after the rate capability test (Fig. A4.2) was completed. The charge and discharge rate was C/20 for all of the cycle life test cycles.

References

(1) Kim, H. J.; Voronina, N.; Yashiro, H.; Myung, S.-T. High-Voltage Stability in KFSI Nonaqueous Carbonate Solutions for Potassium-Ion Batteries: Current Collectors and Coin-Cell Components. *ACS Appl. Mater. Interfaces* **2020**, *12*, 42723–42733.

(2) Han, H.-B.; Zhou, S.-S.; Zhang, D.-J.; Feng, S.-W.; Li, L.-F.; Liu, K.; Feng, W.-F.; Nie, J.; Li, H.; Huang, X.-J. Lithium Bis(Fluorosulfonyl)Imide (LiFSI) as Conducting Salt for Nonaqueous Liquid Electrolytes for Lithium-Ion Batteries: Physicochemical and Electrochemical Properties. *J. Power Sources* **2011**, *196*, 3623–3632.

(3) Qi, Z.; Koenig, G. M., Jr. High-Performance $LiCoO_2$ Sub-Micrometer Materials from Scalable Microparticle Template Processing. *ChemistrySelect* **2016**, *1*, 3992–3999.

(4) Qi, Z.; Koenig, G. M., Jr. A Carbon-Free Lithium-Ion Solid Dispersion Redox Couple with Low Viscosity for Redox Flow Batteries. *J. Power Sources* **2016**, *323*, 97–106.

(5) Tuin, G.; Peters, A. C. I.; van Diemen, A. J. G.; Stein, H. N. Preparation of Large Monodisperse Polystyrene Particles by a One Step Surfactant-Free Emulsion Polymerization. *J. Colloid Interface Sci.* **1993**, *158*, 508–510.

(6) Ghosh, D.; Dhavale, N.; Banda, M.; Kang, H. A Comparison of Microstructure and Uniaxial Compressive Response of Ice-Templated Alumina Scaffolds Fabricated from Two Different Particle Sizes. *Ceram. Int.* **2016**, *42*, 16138–16147.

(7) Robinson, J. P.; Ruppert, J. J.; Dong, H.; Koenig, G. M., Jr. Sintered Electrode Full Cells for High Energy Density Lithium-Ion Batteries. *J. Appl. Electrochem.* **2018**, *48*, 1297–1304.

(8) Nie, Z.; McCormack, P.; Bilheux, H. Z.; Bilheux, J. C.; Robinson, J. P.; Nanda, J.; Koenig, G. M., Jr. Probing Lithiation and Delithiation of Thick Sintered Lithium-Ion Battery Electrodes with Neutron Imaging. *J. Power Sources* **2019**, *419*, 127–136.

(9) Nyman, A.; Behm, M.; Lindbergh, G. Electrochemical Characterisation and Modelling of the Mass Transport Phenomena in $LiPF_6$–EC–EMC Electrolyte. *Electrochim. Acta* **2008**, *53*, 6356–6365.

Appendix 5. Supporting material for chapter 6

Materials and methods

1. Powder material preparation

$TiNb_2O_7$ (TNO) was synthesized via sol-gel method adapted from literature.[1] First, 0.01 mol $Ti(OC_3H_7)_4$ (Sigma-Aldrich) and 0.02 mol $NbCl_5$ (Sigma-Aldrich) was added into 40 mL ethanol with 300 rpm stirring. The solution was heated to 60 ˚C for 2 hours. Then, the solution was air dried in a fume hood overnight at room temperature to evaporate ethanol. The resulting gel was transferred to an 80 ˚C oven and dried for 24 hours in air. The resulting powder was washed with deionized (DI) water. Next, the material was fired at 700 ˚C for 2 h in a Carbolite CWF 1300 box furnace with the heating and cooling rate set to be 1 °C min^{-1}. Powder X-ray diffraction (Empyrean) of the product (Fig. A5.1) confirmed the crystal structure of the TNO material was consistent with previous reports.[1]

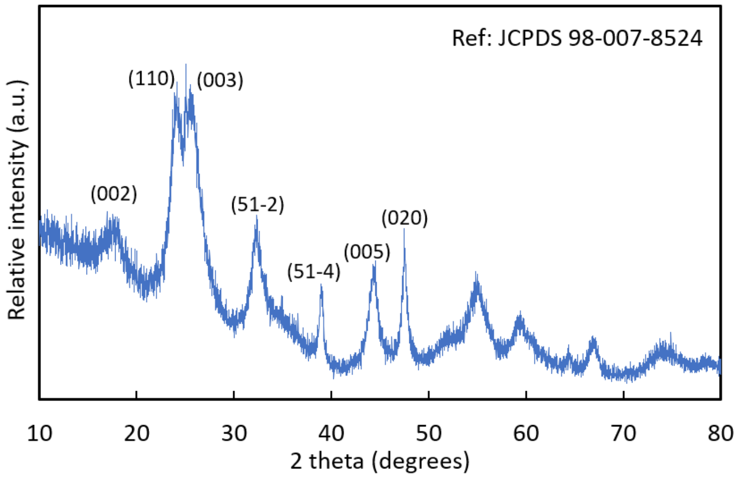

Fig. A5.1 X-ray diffraction pattern of the synthesized TNO material.

$LiCoO_2$ (LCO) was synthesized via coprecipitation of $CoC_2O_4 \cdot 2H_2O$ followed by lithiation of the precursor.[2] First, 1800 mL of 62.8 $mmol \cdot L^{-1}$ $Co(NO_3)_2 \cdot 6H_2O$ (Fisher Reagent Grade) solution and 1800 mL of 87.9 mmol L^{-1} $(NH_4)_2C_2O_4 \cdot H_2O$ (Fisher Certified ACS) solution was prepared and heated to 50 ˚C. Then the $Co(NO_3)_2$ was poured into $(NH_4)_2C_2O_4$ solution all at once with 800 rpm stirring to facilitate the mixing. After maintaining at the same temperature for 30 minutes, the solid precipitate was collected using vacuum filtration and rinsed with 4 L DI water. The powder was dried in an 80 °C oven for 24 h in air. The oxalate precursor was mixed with Li_2CO_3 (Fisher Chemical) with a molar ratio of 1.02:1 for Li:Co using mortar and pestle. Then, the powder mixture was fired at 800 °C in air in a Carbolite CWF 1300 box furnace with a ramp rate of 1 °C min^{-1}. The sample was cooled to room temperature without control of cooling rate after reaching 800 °C. The LCO product was then milled in a Fritsch Pulverisette 7 planetary ball mill using 57 zirconia beads (5 mm diameter) at 300 rpm for 5 hours.

$LiFePO_4$ (LFP) cathode powder was purchased from a commercial supplier (Xiamen TOB New Energy Technology) and used as received. Characterization and electrochemical properties of LCO and LFP material used in this study can be found in previous publications.[3,4]

2. Electrode preparation

2.1 Composite electrode fabrication

The composite electrode was made via slurry casting. The active material was mixed with Super P carbon (Alfa Aesar) and polyvinylidene difluoride (PVDF, Alfa Aesar) dissolved in n-methyl-2-pyrrolidone (NMP) solvent. The weight ratio of active material:carbon:PVDF was

8:1:1. The slurry was cast onto an aluminum foil and dried in an 80 °C oven in air atmosphere for 12 hours. The electrode sheet was transferred to a vacuum oven and further dried in 80 °C in vacuum for 3 hours. The resulting electrode was stored in a dry box.

The composite $LiNi_{0.8}Co_{0.15}Al_{0.05}O_2$ (NCA) electrode was provided by Argonne CAMP facility with a loading of 9.9 mg cm^{-2}. For cell fabrication, a 9/16’’ discs were punched from electrodes.

2.2 Sintered electrode fabrication

TNO or LCO powder was mixed with 1 wt.% polyvinyl butyral (Pfaltz & Bauer) solution dissolved in ethanol (Acros). 1 g powder was blended with 2 mL polymer binder solution with a mortar and pestle. After the solvent evaporated, 0.2 g of the mixture was loaded into a 13 mm diameter Carver pellet die and pressed with 12,000 lbf for 2 minutes in a Carver hydraulic press. The pellets were then heated in a Carbolite CWF 1300 box furnace in an air atmosphere at a ramp rate of 1 °C min^{-1} from 600 °C, held at 600 °C for 1 hour, then cooled at 1 °C min^{-1} to 25 °C.

3. Electrochemical cell fabrication

All electrochemical characterization was conducted using CR2032 coin cells. For TNO composite half cell, the TNO electrode was paired with a 100 μm thick, 9/16’’ diameter Li foil disc. For composite full cells, the TNO anode was paired with a composite cathode. 8 drops of electrolyte (1.2 mol L^{-1} $LiPF_6$ in 3:7 EC:EMC, Gotion) were added for each composite cell. For sintered full cell, the LCO pellets were pasted onto the bottom plate of the coin cell and TNO pellets were pasted on a stainless steel spacer (15.5 mm in diameter and 0.5 mm in thickness). The paste was composed of 1:1 weight ratio Super P carbon to PVDF dissolved in NMP. After drying in an 80 ˚C oven for 12 hours in air, the pellets were fabricated in to full cells with 16 drops of electrolyte added. Cell fabrication was conducted in an Ar atmosphere glove box with both O_2 and H_2O content <1 ppm and Celgard 2325 separators were used for all cells.

Galvanostatic charge/discharge cycling was conducted at different C rates using a MACCOR battery cycler. The C rate was based on the mass loading of the cathode material with an assumed capacity (150 mAh g^{-1} for LCO, 165 mAh g^{-1} for LFP and 180 mAh g^{-1} for NCA).

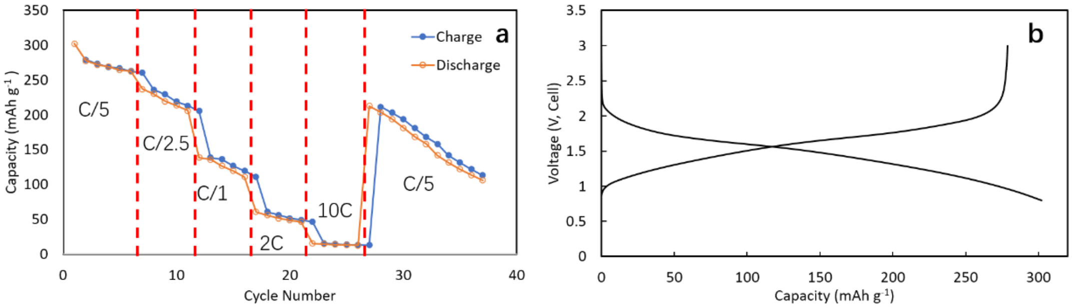

Fig. A5.2. (a) Charge/discharge capacity during cycling at different discharge rates for Li/TNO composite half cells with constant charge rate at C/5 (b) Voltage profiles for the 1st cycle of the cell from (a). C rates were based on an assumed capacity of 230 mAh g^{-1} TNO. The voltage window for all cycles was 0.8-3.0 V, and the current density for 1C corresponded to 1.6 mA cm^{-2}.

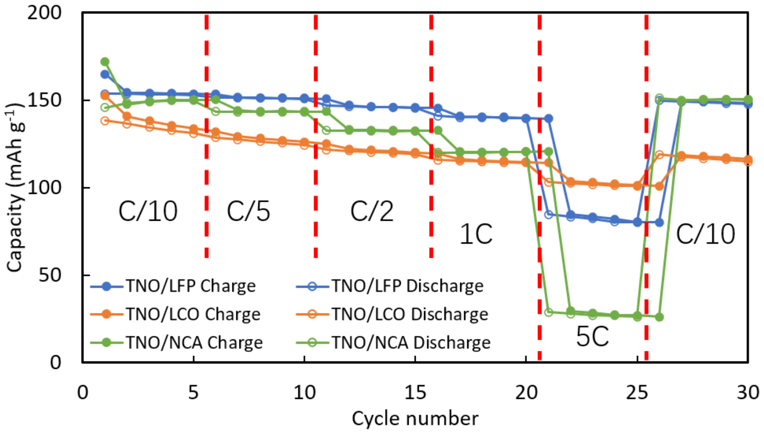

Fig. A5.3. Charge/discharge capacity during cycling at different rates for composite electrode full cells containing TNO anodes and LFP (blue), LCO (orange), or NCA (green) cathodes. Discharge data points are slightly lighter shade than the charge data points. The charge rate was C/10 for all cycles and the discharge rate is noted in the figure. The capacity was calculated based on the loading of the cathode material. The test parameters can be found in Table S1

Table A5.1 Test parameters for cells in Fig. A5.3

Cell	Assumed cell capacity (mAh)	Anode capacity: cathode capacity	Voltage window (V, cell)	1 C current density (mA cm^{-2})
TNO/LCO	1.4	2.0	0.4-2.6	0.88
TNO/LFP	1.6	1.6	0.4-2.2	1.03
TNO/NCA	2.6	0.9	0.4-2.9	1.63

References

(1) Lin, C.; Hu, L.; Cheng, C.; Sun, K.; Guo, X.; Shao, Q.; Li, J.; Wang, N.; Guo, Z. Nano-TiNb$_2$O$_7$/Carbon Nanotubes Composite Anode for Enhanced Lithium-Ion Storage. *Electrochim. Acta* **2018**, *260*, 65–72.

(2) Robinson, J. P.; Ruppert, J. J.; Dong, H.; Koenig, G. M., Jr. Sintered Electrode Full Cells for High Energy Density Lithium-Ion Batteries. *J. Appl. Electrochem.* **2018**, *48*, 1297–1304.

(3) Qi, Z.; Koenig, G. M., Jr. High-Performance LiCoO2Sub-Micrometer Materials from Scalable

Microparticle Template Processing. *ChemistrySelect* **2016**, *1*, 3992–3999.

(4) Qi, Z.; Dong, H.; Koenig, G. M., Jr. Electrochemical Characterization of Lithium-Ion Battery Cathode Materials with Aqueous Flowing Dispersions. *Electrochim. Acta* **2017**, *253*, 163–170.

Acknowledgement

The PhD study at Department of Chemical Engineering in University of Virginia is nearly at the end. This is an unforgettable experience with both challenge and pleasure. Hereby, I would like to thank those who have provided great help and kindness in these 5 years.

First, I would like to thank my advisor Prof. Gary Koenig. I know little about electrochemistry and battery when I joined the group. It is your guidance and patience that help me to be proceed in this field and become who I am today. Also, as an international student who come to this country for the first time, you help me a lot on adapting to a new culture. This help will be a lifetime lesson that I will never forget.

I would like to thank my current and former lab members: Dr. Pierce Robinson, Dr. Linxiao Geng, Dr. Hongxu Dong, Dr. Devanshi Gupta, Patrick McCormack, Chen Cai, Jing Wang, Dean Yost, Charlie Leroux and the undergraduate students who work with me: Samuel Ong, Ethan Bush and Sunya Qamar. Your companion and support have made my research life enjoyable.

Thank my collaborators Rohan Parai, Dr. Lucy Yoon, Milena Milich and their advisors Prof. Dipankar Ghosh, Prof. Joshua Choi and Prof. Patrick Hopkins. It is a pleasure working with you and make progress in our research project.

Thank my committee members: Prof. Gaurav Giri, Prof. Joshua Choi, Prof. David Green and Prof. James Smith. Thank you for reviewing my dissertation and provide your insights for this work to make it better.

I also want to thank my parents. Your support and understanding have made it possible for me to be a graduate student in a different country and help me focus on my work.

Finally, thank Department of Chemical Engineering at University of Virginia. Without the offer, the support from both department level and university level, I would not have such a wonderful experience that will definitely be a treasure in my life!